JSASS 14TH INTERNATIONAL SESSIONS IN 38TH AIRCRAFT SYMPOSIUM

October 11-13, 2000

Sendai Civic Auditorium
Sendai, Japan

The Japan Society for Aeronautical and Space Sciences (JSASS)

20001031 076

REPORT DOCUMENTATION PAGE

1. REPORT DATE *(DD-MM-YYYY)*	2. REPORT TYPE	3. DATES COVERED *(From - To)*
25-10-2000	Conference Proceedings	11-13 October 2000

4. TITLE AND SUBTITLE

JSASS 14th INTERNATIONAL SESSIONS in 38th AIRCRAFT SYMPOSIUM, held 11-13 Oct 00, in Sendai Civic Auditorium, Sendai, Japan

5a. CONTRACT NUMBER
F6256200M9191

5b. GRANT NUMBER

5c. PROGRAM ELEMENT NUMBER

6. AUTHOR(S)

Conference Committee

5d. PROJECT NUMBER

5e. TASK NUMBER

5f. WORK UNIT NUMBER

7. PERFORMING ORGANIZATION NAME(S) AND ADDRESS(ES)

Tohoku Univ., Institute of Fluid Science
2-1-1, Katahira, Aoba-ku
Sendai 980-8577
Japan

8. PERFORMING ORGANIZATION REPORT NUMBER

N/A

9. SPONSORING/MONITORING AGENCY NAME(S) AND ADDRESS(ES)

AOARD
UNIT 45002
APO AP 96337-5002

10. SPONSOR/MONITOR'S ACRONYM(S)

AOARD

11. SPONSOR/MONITOR'S REPORT NUMBER(S)
CSP-00-22

12. DISTRIBUTUION/AVAILABILITY STATEMENT

Approved for public release; distribution is unlimited.

13 SUPPLEMENTARY NOTES

14. ABSTRACT

Conference Proceedings Included 7 Sessions With Topics Which Included:
"An Improved Co-Evolutionary Method for Pursuit-Evasion Game"
"Analytic Solution of the Calculation of Turn Maneuver of Agricultural Aircraft"
"Control Law Design for Aircraft With Reduced Tail Size in Preliminary Design Phase"
"Aeroelastic Analysis of Active Twist Helicopter Rotor Blades"
"Acoustic Behaviour of Cavities Due to Fluid-Structure Interactions Problems"
"Numerical Simulation of a Dual-Combustor Scramjet Flow-Field"
"Deployment of a Beam in Plane Motion of a Body"

15. SUBJECT TERMS

Aerodynamics, Computational Aerodynamics, Computational Fluid Dynamics, Acoustics, Flight Control, Virtual Reality, Aeroelasticity

16. SECURITY CLASSIFICATION OF:			17. LIMITATION OF ABSTRACT	NUMBER OF PAGES	19a. NAME OF RESPONSIBLE PERSON
a. REPORT	b. ABSTRACT	c. THIS PAGE			Mark L. Nowack, Major, USAF
U	U	U	UU	637-816	**19b. TELEPHONE NUMBER** *(Include area code)* +81-3-5410-4409

Proceedings of
JSASS 14th International Sessions
in 38th Aircraft Symposium

October 11-13, 2000

Sendai Civic Auditorium
Sendai, Japan

The Japan Society for Aeronautical and Space Sciences
(JSASS)

Chairperson
Tetsuya Onishi
Manager, Structure Designing Section,
Defense Aircraft Engineering Department,
Nagoya Aerospace Systems Works,
Mitsubishi Heavy Industries Inc.
Nagoya 455-8515 Japan

Organizing Committee
Tomoko Iijima   National Aerospace Laboratory
Takumi Kobayashi   Kawasaki Heavy Industry
Shigeru Obayashi   Tohoku University
Masahiro Obukata   Fuji Heavy Industry
Noboru Sakamoto   Nagoya University

Acknowledgement

The organizing committee of the 14th International Sessions in the 38th Aircraft Symposium wishes to thank the following for their contribution to the success of this conference:

Table of Contents

1E1 AN IMPROVED CO-EVOLUTIONARY METHOD FOR PURSUIT-EVASION GAME

Han-Lim Choi* and Min-Jea Tahk**

Division of Aerospace Engineering, Department of Mechanical Engineering
Korea Advanced Institute of Science and Technology (KAIST)
373-1 Kusong-dong, Yusung-gu, Taejon, 305-701, Korea

Key Words: Guidance and control, pursuit-evasion game, co-evolution

ABSTRACT

Pursuit-evasion game is a representative minimax problem. Co-evolution optimization method is one of newly emerging techniques for addressing minimax problem obtaining the saddle point solution through simultaneous evolution of two opposite players. When applied to conventional pursuit-evasion game, it is reformulated due to the unprescribed final time condition. In this paper, an improved co-evolutionary method for pursuit-evasion game is proposed introducing a smoothing technique to generate a more elegant solution history.

1. INTRODUCTION

Co-evolutionary algorithm (CEA) is recently devised to solve minimax problems and it has shown reliable performance for various optimization problems. Park and Tahk[3] propose a CEA autopilot design method and Tahk and Sun[4] developed CEA for constrained optimization problems by adopting the benefits of the augmented Lagrangian method. The main advantage of CEA for minimax problems is that it optimizes the fitnesses of minimizer and maximizer simultaneously so that it has a low possibility of converging to local solutions.

Pursuit-evasion game is a typical minimax optimization situation dealing with the behaviors of the pursuer and the evader at the situation of interception[1]. In this game one player tries to minimize a prescribed payoff and the other to maximize it. The payoff, or the objective of the game is usually represented as the intercept time, or the final miss distance, or a combination of both of them[5].

When applying the CEA to the pursuit-evasion game, the payoff is hardly obtainable due to the unprescribed final time condition, which is essential for the calculation of the payoff as well as the flight trajectories of the pursuer and the evader.

This paper proposes an improved co-evolutionary method for addressing this problem by employing another evolving group representing the final time and a different game concept is implemented for fitness evaluation. Furthermore, a smoothing technique is applied in order to obtain more elegant input histories. The proposed algorithm is verified by a numerical example of 2-dimensional intercept situation.

2. ALGORITHMS

A. General Co-evolutionary Algorithm (CEA)

Conventional co-evolutionary algorithm (CEA) is a stochastic global search algorithm for obtaining a saddle point solution of a minimax problem. It is summerized as the following 6 steps[3]:

1. Initialization
The initial populations of the two evolving groups (minimizing group and maximizing one) are generated.

2. Offspring generation
The offspring populations of each group are generated through genetic operations such as recombination and mutation.

3. Match
The two evolving groups play full matches for cost evaluations.

4. Fitness evaluations and sorting.
The fitness of each individual of two groups is evaluated from the worst-case cost values of his (or her) match scores. And the two groups sort themselves for their sakes.

5. Selection
The two groups select new parent populations for the next generation from the sorted offspring populations for the present generation.

6. Termination criteria
If the termination criteria are satisfied, the co-evolution process is terminated. Otherwise, go to step 2.

B. Intercept Time Optimization

The intercept time of the pursuit-evasion game is usually unprescribed, which causes much trouble for obtaining payoff and the solution trajectories. When the final time, denoted as t_f, is employed as the payoff, the pursuit-evasion game is expressed as the following minimax optimization problem:

$$\min_{u_p} \max_{u_e} \; t_f \tag{1}$$

which is subject to the kinematics of the pursuer and the evader and u_p, u_e denote the pursuer and evader control

* Graduate Student, Division of Aerospace Engineering
** Professor, Division of Aerospace Engineering

input histories, respectively.

C. Control Input Parameterization

For the calculation of the payoff and the trajectories, the input histories of the pursuer and the evader are parameterized, which results in a direct optimization method. The control inputs are parameterized with the time step $\delta t = \dfrac{t_f}{N}$ as

$$\mathbf{u}_p = \begin{bmatrix} u_{p1} , u_{p2} , \cdots , u_{pN} \end{bmatrix}^T$$
$$\mathbf{u}_e = \begin{bmatrix} u_{e1} , u_{e2} , \cdots , u_{eN} \end{bmatrix}^T \tag{2}$$

The parameterized input vectors are treated as the parameter vector of the CEA where the pursuer input vector is the minimizer and the evader input vector is the maximizer.

D. Evolving Role Assignment

The pursuer input group (X) and the evader input group (Y) evolve simultaneously to the saddle point solution by the CEA. However, the unprescribed final time brings the need to introduce another evolving group considering the variations of the final time. We introduced an evolving group made up of the individuals of the final time and denote it as group Z.

Z also evolves through ordinary genetic operations and thus the candidates of the optimal final time are randomly generated. By the way, the evolution process of the group Z is somewhat different from the other groups. The fitness of each individual in the group Z is not determined independently but dependently on the other groups' fitness evaluations, which will be interpreted concretely in the followings.

E. Fitness Evaluation and Selection Scheme

For the situation that the pursuer is unable to capture the evader, it is unrealistic to optimize the intercept time. Therefore, we considered only the situation that the pursuer can catch the evader. The final intercept condition is expressed as the final miss distance (R_f) being smaller than the specified radius of capture (R_{cap}), which is treated as the constraint of the minimax problem. In the proposed method, a penalty function method is introduced to deal with this final miss distance constraint. Thus, the payoff functions become different for players like the below.

$$J_p = t_f + C R_f$$
$$J_e = t_f - C R_f \tag{3}$$

where C is a constant.

The penalty term W is first calculated in order to evaluate the fitness of each individual in the group X or Y. The penalty term for the i-th individual in the group X and j-th individual in the group Y, or W_{ij} is calculated as

$$W_{ij} = \begin{cases} R_f^{ij} = R_f(u_p^i, u_e^j, t_f^k = t_f^{ij}) & \text{if } R_f^{ij} > R_{cap} \\ 0 & \text{if } R_f^{ij} \le R_{cap} \end{cases} \tag{4}$$

Here t_f^k is k-th individual in the group Z. If i is smaller than μ,

the number of parent individuals, and $i = j$, k equals to i, otherwise it is randomly selected from [1 , $\mu+\lambda$], where λ is the number of offspring individuals. However, t_f^{ij} selected as stated before may be erroneous compared with the actual intercept time, because t_f^k is generated through random operations not through physically meaningful processes. Therefore, a modification term is added for the calculation of the final time and miss distance. The modified final time and miss distance can be evaluated using the final relative position vector and the final relative velocity vector.

$$dt_f^{ij} = -\frac{\vec{R}_{rel} \bullet \vec{V}_{rel}}{\left\| \vec{V}_{rel} \right\|^2} \tag{5}$$

$$t_{f,\text{mod}}^{ij} = t_f^{ij} + dt_f^{ij} \tag{6}$$

where $\vec{R}_{rel} = \vec{R}_e - \vec{R}_p$ and $\vec{V}_{rel} = \vec{V}_e - \vec{V}_p$.
Then, the miss distance is evaluated as follow:

$$R_f^{ij} = \left\| \vec{R}_{rel} + dt_f^{ij} \vec{V}_{rel} \right\| \tag{7}$$

Therefore, the payoff obtained from the match is expressed as

$$J_p^{ij} = t_{f,\text{mod}}^{ij} + C W_{ij}$$
$$J_e^{ij} = t_{f,\text{mod}}^{ij} - C W_{ij} \tag{8}$$

The performance index of each player is evaluated in a different way because the payoff of each player has a different form with the conventional CEA. It has been shown that Stackelberg game introducing the concept of *leader and follower* is applicable to co-evolution using bimatrix game[6]. According to this game theory, the performance indices of the leader players are determined in advance and then those of the follower players are evaluated[2]. For the pursuit-evasion game, the maximizing group is treated as the *leader* and the minimizing group as the *follower*.

The performance indices of the individuals in the maximizing group are calculated in the same way as the conventional CEA as

$$J_e^i = \min_j J_e^{ij} \tag{9}$$

The performance indices also imply the fitness of each individual in the maximizing group. The individual ($\mathbf{u}_e$) is sorted in descending order with respect to the fitness value and denoted as $\hat{\mathbf{u}}_e$. For the follower individuals, the sorted $\hat{\mathbf{u}}_p$ is expressed as

$$\hat{\mathbf{u}}_p^i = \{ \tilde{\mathbf{u}}_p \in \hat{X} : J_p(\tilde{\mathbf{u}}_p, \hat{\mathbf{u}}_e^i) \le J_p(\mathbf{u}_p^j, \hat{\mathbf{u}}_e^i), \forall \mathbf{u}_p^j \in \hat{X} \} \tag{10}$$

where $\hat{X}$ is a subset of X which excludes already selected $\mathbf{u}_p^i$'s.

After evaluating fitness using the presented method, ($\mu+\lambda$)-selection scheme is used for the selection processes of the group X and Y.

The selection scheme of the group Z is heavily dependent on the result of the selection process in the group X and Y. If $\mathbf{u}_p^i$ and $\mathbf{u}_e^j$ is selected as one of next parents, $t_{f,\text{mod}}^{ij}$ is selected as one of the parents individuals in the group Z. In other words, after evaluation fitness as the following:

$$\hat{t}_f^k = t_{f,\text{mod}}^{ij} \quad \text{if} \quad \hat{\mathbf{u}}_p^k = \mathbf{u}_p^i \quad \text{and} \quad \hat{\mathbf{u}}_e^k = \mathbf{u}_e^j \, .$$

and then, select $\hat{t}_f^k$ if k is smaller than μ.

F. Smoothing Technique

The cost function of a conventional pursuit-evasion game is expressed as an explicit function of the intercept time and the final miss distance. The resulting optimal control input histories produce the intercept trajectories. It is noted that the trajectory is quite insensitive to fluctuations of control inputs as long as the averaged input history remains same. For this reason the optimal control inputs obtained by co-evolution might be very irregular.

Therefore, a smoothing technique is necessary to obtain more elegant shapes of both players' controls. When applying the smoothing technique, parents group (X or Y) at the present generation consists of two different sub-groups, X_o (or Y_o) and X_s (or Y_s). The subscript o implies the original group and the subscript s the smoothed group. In other words,

$$\begin{aligned} X_o \text{ (or } Y_o) &= \left\{ \mathbf{u}_o^1, \cdots, \mathbf{u}_o^i, \cdots, \mathbf{u}_o^{\mu o} \right\} \\ X_s \text{ (or } Y_s) &= \left\{ \mathbf{u}_s^1, \cdots, \mathbf{u}_s^i, \cdots, \mathbf{u}_s^{\mu s} \right\} \end{aligned} \quad (11)$$

where $\mu_o + \mu_s = \mu$.

The individuals in the original group are selected from the sorted offspring group of the last generation and the selection scheme is the same as conventional CEA as

$$\mathbf{u}_o^i(k) = \hat{\mathbf{u}}_o^i(k-1), \quad \forall i \le \mu_o \quad (12)$$

where k denotes the generation number. On the contrary, the individuals in the smoothed group are determined from the smoothed sorted offspring group of the last generation as

$$\mathbf{u}_s^i(k) = \hat{\mathbf{u}}_s^i(k-1), \quad \forall i \le \mu_s \quad (13)$$

where

$$\hat{\mathbf{u}}_s = [u_{s1}, \cdots, u_{sn}, \cdots, u_{sN}]^T \quad (14)$$

$$u_{sn} = p \, u_{n-1} + q \, u_n + r \, u_{n+1} \quad (p+q+r=1) \quad (15)$$

In other words, the control input at the present time of smoothed individual is determined as a weighted average of the last, present and the next control inputs of the original individual.
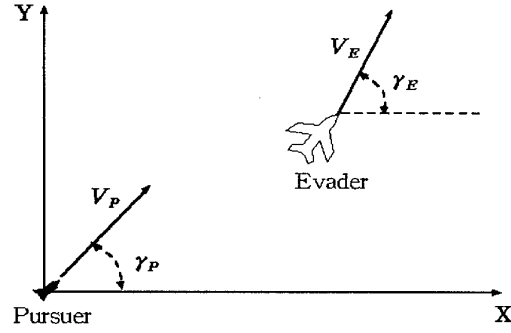
Fig. 1. Geometry of a 2-D pursuit-evasion situation

3. NUMERICAL EXAMPLE

A pursuit-evasion game for an intercept situation shown in Fig. 1 is considered. The gravitational effect is neglected by assuming the horizontal engagement. Thus only the control inputs and the aerodynamic forces drive the motion of both pursuer and evader. The control inputs are normalized angular accelerations. The kinematics relations of the pursuer and the evader are expressed as [5]

$$\begin{aligned} \dot{x} &= v \cos \gamma \\ \dot{y} &= v \sin \gamma \\ \dot{\gamma} &= \frac{v}{R} u \quad , \quad |u| \le 1 \\ \dot{v} &= -\frac{v^2}{R} (a + b u^2) \end{aligned} \quad (16)$$

where x, y are pursuer or evader's position and v is the speed and γ the flight path angle, respectively. u is the normalized control input and R denotes the minimum turn radius. a, b are the coefficients of the induced drag. a, b are determined from other aerodynamic coefficients as

$$a = \frac{C_{D0}}{C_{L\max}} \quad (17)$$

$$b = K \, C_{L\max}$$

where C_{D0} is the zero lift drag coefficient and $C_{L\max}$ is the maximum lift coefficient. The following data are used for numerical demonstration.

$$\begin{aligned} a_p &= 0.0875 \ , \ b_p = 0.40 \ , \ R_p = 1515(m) \\ a_e &= 0 \qquad \ , \ b_e = 0.40 \ , \ R_e = 600(m) \end{aligned} \quad (18)$$

The initial engagement is that the pursuer is launched at the origin in the positive x-direction at the speed of $600m/s$, and the evader, which is initially $1500m$ apart from the origin in the direction of positive x-axis, flies in the direction of positive y-axis at the speed of $200m/s$. The parameters used for the numerical verification are shown in Table 1.

The termination criterion is that the generation number exceeds the maximum generation limit, 10000 generations.

The trajectories of the pursuer and the evader are presented in Fig. 2. The pursuer maneuvers counterclockwise and the

evader clockwise, which looks feasible. Neither of them turns with its minimum turn radius, which is a reasonable result for the case of a pursuit-evasion model with aerodynamic drag[6].

Fig. 3 shows the pursuer's and the evader's control histories. In both plots the shapes of control histories are smooth enough not to seem to be irregular. The optimized final time is 3.64 sec.

4. CONCLUSION

An improved co-evolutionary method for pursuit-evasion game is proposed. The final time is employed as the payoff of the minimax problem and the pursuer (or evader) roles as a minimizer (maximizer) for this payoff. Only the situation in which the pursuer can catch the evader is assumed and the penalty term, or the final miss distance, is introduced in order to satisfy the interception condition. A new evolving group is introduced so as to treat the unprescribed final time problem. Fitness evaluation method based on Stackelberg bimatrix game theory is employed and a smoothing technique is implemented to obtain an elegant solution. For the verification of the proposed algorithm, a numerical example of a 2-D engagement situation is tested. The result demonstrates reasonable minimax solution trajectories of both players and the smoothing effect of input histories is observed.

ACKNOWLEDGEMENT

REFERENCES

[1] R.Issac, *Differential Games*, John Wiley and Sons, New York, 1975.
[2] T.Basar and G.J.Olsder, *Dynamic Noncooperative games*, Academic Press, London, 1982.
[3] C.S.Park and M.J.Tahk, "A co-evolutionary minimax solver and its application to autopilot design," *Proceeding of AIAA Guidance, Navigation, and Control Conference*, Boston, USA, pp.408-415, Aug. 1998.
[4] M.J.Tahk and B.C.Sun, "Co-evolutionary augmented Lagrangian methods for constrained optimization," *IEEE Transactions on Evolutionary Computation*, Vol.4, No.2, Jul. 2000.
[5] J.Kim and M.J.Tahk, "A direct method for constrained pursuit-evasion games," *Proceedings of JSASS Aircraft Symposium*, Yokosuka, Japan, Oct. 1998.
[6] M.J.Tahk, H.Ryu, and J.G.Kim, "An iterative numerical method for a class of quantitative pursuit-evasion games," *Proceedings of AIAA Conference on Guidance, Navigation, and Control*, Boston, Mass., USA, August 1998.
[7] J.Hur and M.J.Tahk, "Robust flight control design using co-evolution with considerations of design constraints," *Proceedings of the 3rd Asian Control Conference*, Shanghai, China, p.73, Jul.2000

Table 1. Simulation parameters

N	R_{cap}	C	μ	λ	μ_s	μ_o
30	3.0	1.0	4	20	2	2
(p, q, r)	(0.2, 0.8, 0.0) if $n = 1$					
	(0.0, 0.8, 0.2) if $n = N$					
	(0.2, 0.6, 0.2) otherwise					

Fig. 2. Trajectories of both players

Fig. 3. Control histories of both players

1E2　A Co-Evolutionary Computation for Constrained Min-Max Problems

Jegyom Kim* and Min-Jea Tahk**

Department of Aerospace Engineering
Korea Air Force Academy
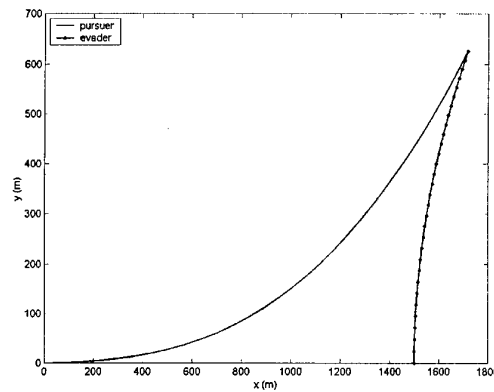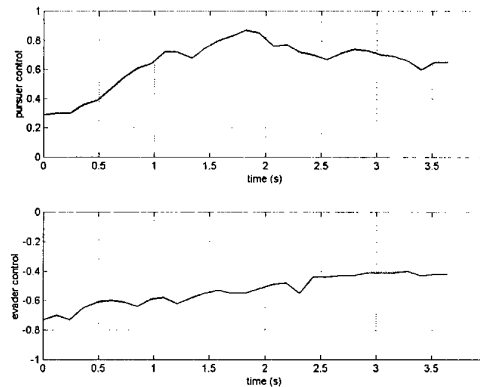P.O. Box 335-2, Chungwon, Chungbuk, 363-849, Korea

Department of Aerospace Engineering

Korea Advanced Institute of Science and Technology(KAIST)

373-1 Kusong-dong, Yusung-gu, Taejon, 305-701, Korea

Key Words: co-evolution, separable and inseparable constraints, and minimax problems

ABSTRACT

The co-evolutionary computation method is proposed for solving constrained min-max problems. Many engineering problems can be practically expressed as constrained min-max problems. Min-max problems have two groups of variables. Each group will minimize or maximize payoffs and is subject to equality and inequality constraints. Lagrange multipliers are implemented for handling constraints. Inseparable constraints are also involved in the proposed method. Previous co-evolutionary algorithms based on the penalty function can not be applied to minmax problems with inseparable constraints. Numerical examples are treated by the proposed method and their results are compared with exact solutions.

1. INTRODUCTION

Min-max problems are optimization between players with conflicting interests. Many engineering problems can be modeled with min-max optimization. Pursuit-evasion games between missile and aircraft, and design of robust controller against external disturbances and variations of plant parameters are min-max problems. For the more practical modeling, physical limitations of actual systems and design specifications have to be involved into problems as the form of constraints.

Recently, the issue of the evolutionary computation is handling of constraints in optimization problems. The algorithms for dealing with constraints are grouped into a few of categories[1]; 1)methods based on preserving feasibility, 2)penalty functions, 3)making a clear distinction between feasible and infeasible solutions and 4)hybrid methods. Tahk and Sun[2] suggested a co-evolutionary augmented Lagrangian method(CEALM) for solving constrained minimization problems. In CEALM, constrained minimization problems are converted into unconstrained min-max problems with Lagrangian multipliers. Solutions of unconstrained min-max problems are the saddle point of the parameter to be optimized and Lagrangian multipliers.

In this paper, the co-evolutionary computation method for solving constrained min-max problems is proposed. The Lagrange multipliers are implemented for handling various type of constraints; separable and inseparable constraints. The proposed method solves constrained min-max problems by solving their dual problems, alternatively. The strategy of Lagrange multipliers for separable constraints are determined by the duality relation of one-sided optimization problems. In case of inseparable constraints, the previous results can not inform Lagrange multipliers of the strategy. The duality properties of min-max problems with inseparable con-

straints are derived in the paper. They determine the strategy of the Lagrange multipliers for inseparable constraints.

This paper is organized as follows: Section 2 introduces the constrained min-max problems. In section 3 and 4, the co-evolution computation method and the properties of the algorithm for handling separable and inseparable constraints are derived. The proposed method is applied to min-max problems with inseparable constraints in section 5. Section 6 provides conclusion of the paper and further study.

2. CONSTRAINED MIN-MAX PROBLEMS

The constrained min-max problems are expressed as follows.

$$\max_{\mathbf{y}} \min_{\mathbf{x}} f(\mathbf{x}, \mathbf{y}) \tag{1}$$

subject to

$$\mathbf{g}(\mathbf{x}, \mathbf{y}) \leq 0 \tag{2}$$

$$\mathbf{h}(\mathbf{x}, \mathbf{y}) = 0 \tag{3}$$

The parameters to be optimized are classified into two groups. $\mathbf{x}$ and $\mathbf{y}$ are the vector of minimizing and maximizing payoffs, respectively. The feasible region is defined by a set of inequality and equality constraints. Domains of variables are determined by their lower and upper bounds.

$$L_i \leq x_i \leq U_i \qquad i = 1, 2, ..., n_x \tag{4}$$

$$L_j \leq y_j \leq U_j \qquad j = 1, 2, ..., n_y \tag{5}$$

The constrained min-max problems in the paper are assumed to satisfy the conditions below.

$$f(\mathbf{x}^*, \mathbf{y}) \leq f(\mathbf{x}^*, \mathbf{y}^*) \leq f(\mathbf{x}, \mathbf{y}^*) \tag{6}$$

$$\min_{\mathbf{x}} \max_{\mathbf{y}} f(\mathbf{x}, \mathbf{y}) = \max_{\mathbf{y}} \min_{\mathbf{x}} f(\mathbf{x}, \mathbf{y}) \tag{7}$$

The assumption for the interchangeability of min, max operation(7) is called as minimax assumption or Issacs condition[3]. If the payoff $f(\mathbf{x}, \mathbf{y})$ is separable in $\mathbf{x}$ and $\mathbf{y}$, the Issacs condition holds. In following two sections, inseparable and separable constraints is introduced and constraint-handling methods for them are derived.

3. SEPARABLE CONSTRAINTS

The minimizing and maximizing groups of min-max problems are subject to the separable constraints.

$\mathbf{x}$ is subject to

$$g_{x,i}(x) \leq 0 \qquad i = 1, 2, ..., m_x$$

$$h_{x,i}(x) = 0 \qquad i = 1, 2, ..., l_x \tag{8}$$

---

y is subject to

$$g_{y,i}(y) \leq 0 \qquad i = 1, 2, ..., m_x$$
$$h_{y,i}(y) = 0 \qquad i = 1, 2, ..., l_x \qquad (9)$$

'Separable' means the constraints (2) and (3) of min-max problems can be divided into constraints (8) and (9); the constraints of each group are functions of elements of its own group.
Min-max problems with separable constraints can be converted into unconstrained min-max ones.

$$\min_{\mu_{\mathbf{y}} \leq 0, \lambda_{\mathbf{y}}} \ \max_{\mathbf{y}, \mu_{\mathbf{x}} \geq 0, \lambda_{\mathbf{x}}} \ \min_{\mathbf{x}} \ L(\mathbf{x}, \mathbf{y}, \mu, \lambda) \qquad (10)$$

where the Lagrangian function is defined as

$$L(\mathbf{x}, \mathbf{y}, \mu, \lambda) = f(\mathbf{x}, \mathbf{y}) + \mu^T \mathbf{g} + \lambda^T \mathbf{h} \qquad (11)$$

μ and λ are Lagrange multipliers for inequality and equality constraints.

$$\mu^T = \begin{bmatrix} \mu_{\mathbf{x}}^T & \mu_{\mathbf{y}}^T \end{bmatrix} \qquad \lambda^T = \begin{bmatrix} \lambda_{\mathbf{x}}^T & \lambda_{\mathbf{y}}^T \end{bmatrix} \quad (12)$$

$$\mathbf{g}^T = \begin{bmatrix} \mathbf{g_x}^T & \mathbf{g_y}^T \end{bmatrix} \qquad \mathbf{h}^T = \begin{bmatrix} \mathbf{h_x}^T & \mathbf{h_y}^T \end{bmatrix} \quad (13)$$

The min-max-min problem can be expressed as min-max one by min-max assumption[3].

$$\max_{\mathbf{y}, \mu_{\mathbf{x}} \geq 0, \lambda_{\mathbf{x}}} \ \min_{\mathbf{x}, \mu_{\mathbf{y}} \leq 0, \lambda_{\mathbf{y}}} \ L(\mathbf{x}, \mathbf{y}, \mu, \lambda) \qquad (14)$$

Theorem 1 (No duality gap conditions for separable constraints)
If **g** is convex and **h** is affine , the solutions of the unconstrained min-max problems are equal to those of the constrained min-max ones, and there is no duality gap.

$$\min_{\mathbf{x}} \max_{\mathbf{y}} \{ f(\mathbf{x}, \mathbf{y}) : \mathbf{g_x} \leq 0, \mathbf{g_y} \leq 0, \mathbf{h_x} = 0, \mathbf{h_y} = 0 \}$$
$$= \min_{\lambda_y, \mu_y \leq 0} \ \max_{\lambda_x, \mu_x \leq 0} \{ \phi(\mu, \lambda) : \mu_x \geq 0, \mu_y \leq 0 \} \quad (15)$$

where
$$\phi(\mu, \lambda) = \min_{\mathbf{x}} \max_{\mathbf{y}} L(\mathbf{x}, \mathbf{y}, \mu, \lambda) \qquad (16)$$

Proof: Consider the two constrained minimization and maximization problems. Equality constraints are taken into account in the proof for simplicity.

Problem 1
$$\min_{x} \frac{1}{2} f(\mathbf{x}, \mathbf{y}^*) \qquad (17)$$

subject to
$$\mathbf{h_x}(x) = 0 \qquad (18)$$

Problem 2
$$\max_{y} \frac{1}{2} f(\mathbf{x}^*, \mathbf{y}) \qquad (19)$$

subject to
$$\mathbf{h_y}(y) = 0 \qquad (20)$$

By the strong duality theorem[4], the solutions of Problem 1 and Problem 2 satisfy conditions below.

$$\min \frac{1}{2} f(\mathbf{x}, \mathbf{y}^*) = \max_{\lambda} \min L_1(\mathbf{x}, \mathbf{y}^*, \lambda_x) \qquad (21)$$

$$\max_{\mathbf{y}} \frac{1}{2} f(\mathbf{x}^*, \mathbf{y}) = \min_{\lambda_y} \max_{\mathbf{y}} L_2(\mathbf{x}^*, \mathbf{y}, \lambda_y) \qquad (22)$$

From (21) and (22),

$$\begin{aligned} \max_{\mathbf{y}} \min_{\mathbf{x}} f(\mathbf{x}, \mathbf{y}) &= \max_{\lambda_x} \min_{\mathbf{x}} L_1(\mathbf{x}, \mathbf{y}^*, \lambda_x) \\ &\quad + \min_{\lambda_y} \max_{\mathbf{y}} L_2(\mathbf{x}^*, \mathbf{y}, \lambda_y) \\ &= \max_{\lambda_x} \min_{\lambda_y} \phi(\lambda) \qquad (23) \end{aligned}$$

where
$$\phi(\lambda) = \min_{\mathbf{x}} \max_{\mathbf{y}} L(\mathbf{x}, \mathbf{y}, \lambda) \qquad (24)$$

This completes the proof. □
Solutions of the min-max problems with separable constraint are acquired by solving the dual min-max ones.

Theorem 2 (Saddle-point optimality for separable constraints)
The solutions of constrained min-max problems $(\mathbf{x}, \mathbf{y}, \lambda, \mu)$ satisfy the following saddle-point optimality.

$$\begin{aligned} L(\mathbf{x}^*, \mathbf{y}, \lambda_x, \mu_x, \lambda_y^*, \mu_y^*) &\leq L(\mathbf{x}^*, \mathbf{y}^*, \lambda_x^*, \mu_x^*, \lambda_y^*, \mu_y^*) \\ &\leq L(\mathbf{x}, \mathbf{y}^*, \lambda_x^*, \mu_x^*, \lambda_y, \mu_y) \end{aligned}$$
$$(25)$$

Proof: Consider two optimization problems with constraints; Problem 1 and Problem 2. By the strong duality theorem[4] , the solutions of Problem 1 and Problem 2 satisfy conditions below.

$$L_1(\mathbf{x}^*, \mathbf{y}^*, \lambda_x) \leq L_1(\mathbf{x}^*, \mathbf{y}^*, \lambda_x^*) \leq L_1(\mathbf{x}, \mathbf{y}^*, \lambda_x^*) \quad (26)$$

$$L_2(\mathbf{x}^*, \mathbf{y}, \lambda_y^*) \leq L_2(\mathbf{x}^*, \mathbf{y}^*, \lambda_y^*) \leq L_2(\mathbf{x}^*, \mathbf{y}^*, \lambda_y) \quad (27)$$

where L_1, L_2 are the Lagrangian functions of Problem 1 and Problem 2, respectively.

$$\begin{aligned} &L(\mathbf{x}, \mathbf{y}^*, \lambda_x^*, \lambda_y^*) \\ &\leq \frac{1}{2} f(\mathbf{x}, \mathbf{y}^*) + \frac{1}{2} f(\mathbf{x}^*, \mathbf{y}^*) + \lambda_x^{*T} \mathbf{h_x} + \lambda_y^T \mathbf{h_y} \\ &\leq f(\mathbf{x}, \mathbf{y}^*) + \lambda_x^{*T} \mathbf{h_x} + \lambda_y^T \mathbf{h_y} \\ &= L(\mathbf{x}, \mathbf{y}^*, \lambda_x^*, \lambda_y) \qquad (28) \end{aligned}$$

The right part of (25) has been proved.

$$\begin{aligned} &L(\mathbf{x}^*, \mathbf{y}^*, \lambda_{\mathbf{x}}^*, \lambda_{\mathbf{y}}^*) \\ &\geq \frac{1}{2} f(\mathbf{x}^*, \mathbf{y}) + \frac{1}{2} f(\mathbf{x}^*, \mathbf{y}^*) + \lambda_x^T \mathbf{h_x} + \lambda_y^{*T} \mathbf{h_y} \\ &\geq f(\mathbf{x}^*, \mathbf{y}) + \lambda_x^T \mathbf{h_x} + \lambda_y^{*T} \mathbf{h_y} \\ &= L(\mathbf{x}^*, \mathbf{y}, \lambda_{\mathbf{x}}, \lambda_{\mathbf{y}}^*) \qquad (29) \end{aligned}$$

This completes the proof. □
If $\nabla_{xx} f$ is not positive semi-definite and $\nabla_{yy} f$ is not negative semi-definite, the Lagrangian function is defined as

$$L(\mathbf{x}, \mathbf{y}, \mu, \lambda) = f(\mathbf{x}, \mathbf{y}) + \sum_{k=1}^{m} p_{x \cdot k}(x, u_{x,k}, \rho_x)$$

$$+ \sum_{k=1}^{l} \lambda_{x,k} h_{x,k}(x) + \frac{\rho}{2} \| h_x(x) \|^2 + \sum_{k=1}^{m} p_{y,k}(y, u_{y,k}, \rho_y)$$

$$+ \sum_{k=1}^{l} \lambda_{y,k} h_{y,k}(y) - \frac{\rho}{2} \| h_y(y) \|^2 \qquad (30)$$

where

$$p_{x,k} = \frac{1}{2\rho_x}\{\{\max(0, \mu_{x,k} + \rho g_{x,k})\}^2 - \mu_{x,k}^2\} \quad (31)$$

$$p_{y,k} = -\frac{1}{2\rho_y}\{\{\max(0, \mu_{y,k} + \rho g_{y,k})\}^2 - \mu_{y,k}^2\}(32)$$

Note that the difference between quadratic penalty terms of minimizing and maximizing group is signs of penalty terms.

4. INSEPARABLE CONSTRAINTS

Inseparable constraints can not be divided into constraints of a group. In the case of inseparable constraints, the strategy of Lagrange multipliers for x's and y's constraints are maximizing and minimizing the Lagrangian function, respectively. This results from the duality relation of constrained one-sided optimization problems. The strategy of Lagrange multipliers of inseparable constraints can not be determined by the previous duality relation. In this section, the duality relation of min-max problems with inseparable constraints and the strategy are derived.

Theorem 3 (Weak duality theorem for min-max problems)

Let $(\mathbf{x}, \mathbf{y})$ and (μ, λ) be feasible solutions to primal and dual problems.
If $\phi(\lambda, \mu)$ is convex,

$$\min_{\mu \leq 0, \lambda} \phi(\lambda, \mu) \geq \min_{\mathbf{x}} \max_{\mathbf{y}} f(\mathbf{x}, \mathbf{y}) \quad (33)$$

If $\phi(\lambda, \mu)$ is concave,

$$\max_{\mu \geq 0, \lambda} \phi(\lambda, \mu) \leq \min_{\mathbf{x}} \max_{\mathbf{y}} f(\mathbf{x}, \mathbf{y}) \quad (34)$$

This theorem shows not only the lower or upper bounds of the primal problems' solution but also the strategy of Lagrange multipliers for the inseparable constraints.

Proof:

$$\phi(\lambda, \mu) = \min_{\mathbf{x}} \max_{\mathbf{y}}\{f(\mathbf{x}, \mathbf{y}) + \lambda^T \mathbf{h}(\mathbf{x}, \mathbf{y}) + \mu^T \mathbf{g}(\mathbf{x}, \mathbf{y})\} \quad (35)$$

For convex $\phi(\lambda, \mu)$,

$$\phi(\lambda, \mu) \geq \min_{\mathbf{x}}\{f(\mathbf{x}, \mathbf{y}) + \lambda^T \mathbf{h}(\mathbf{x}, \mathbf{y}) + \mu^T \mathbf{g}(\mathbf{x}, \mathbf{y})\}$$
$$\geq \min_{\mathbf{x}} f(\mathbf{x}, \mathbf{y}) \quad (36)$$

Since $\mu \leq 0$, $\mathbf{g}(\mathbf{x}, \mathbf{y}) \leq 0$, $\mathbf{h}(\mathbf{x}, \mathbf{y}) = 0$,

$$\min \phi(\lambda, \mu) \geq \min_{\mathbf{x}} \max_{\mathbf{y}} f(\mathbf{x}, \mathbf{y}) \quad (37)$$

For concave $\phi(\lambda, \mu)$,

$$\phi(\lambda, \mu) \leq \max_{\mathbf{y}}\{f(\mathbf{x}, \mathbf{y}) + \lambda^T \mathbf{h}(\mathbf{x}, \mathbf{y}) + \mu^T \mathbf{g}(\mathbf{x}, \mathbf{y})\}$$
$$\leq \max_{\mathbf{y}} f(\mathbf{x}, \mathbf{y}) \quad (38)$$

Since $\mu \geq 0$, $\mathbf{g}(\mathbf{x}, \mathbf{y}) \leq 0$, $\mathbf{h}(\mathbf{x}, \mathbf{y}) = 0$,

$$\max \phi(\lambda, \mu) \leq \min_{\mathbf{x}} \max_{\mathbf{y}} f(\mathbf{x}, \mathbf{y}) \quad (39)$$

This completes the proof. □

Theorem 4 (Strong duality theorem for min-max problems)

The solution of the primal (constrained min-max) problems can be acquired by solving the dual (unconstrained min-max) problems. Suppose $\mathbf{g}(\mathbf{x}, \mathbf{y})$ is convex and $\mathbf{h}(\mathbf{x}, \mathbf{y})$ is affine,
If $\phi(\lambda, \mu)$ is concave,

$$\max_{\mathbf{y}} \min_{\mathbf{x}}\{f(\mathbf{x}, \mathbf{y}) : \mathbf{g}(\mathbf{x}, \mathbf{y}) \leq 0, \mathbf{h}(\mathbf{x}, \mathbf{y}) = 0\}$$
$$= \max_{\lambda, \mu}\{\phi(\lambda, \mu) : \mu \geq 0\} \quad (40)$$

If $\phi(\lambda, \mu)$ is convex,

$$\max_{\mathbf{y}} \min_{\mathbf{x}}\{f(\mathbf{x}, \mathbf{y}) : \mathbf{g}(\mathbf{x}, \mathbf{y}) \leq 0, \mathbf{h}(\mathbf{x}, \mathbf{y}) = 0\}$$
$$= \min_{\lambda, \mu}\{\phi(\lambda, \mu) : \mu \leq 0\} \quad (41)$$

Proof: Let

$$\gamma = \min_{\mathbf{x}}\{\max_{\mathbf{y}} f(\mathbf{x}, \mathbf{y}) : \mathbf{g}(\mathbf{x}, \mathbf{y}^*) \leq 0, \mathbf{h}(\mathbf{x}, \mathbf{y}^*) = 0\} \quad (42)$$

If $\max_{\mathbf{y}} f(\mathbf{x}, \mathbf{y})$ and $\mathbf{g}(\mathbf{x}, \mathbf{y}^*)$ are convex, $\mathbf{h}(\mathbf{x}, \mathbf{y}^*)$ is affine, and the following system has no solution,

$$\max f(\mathbf{x}, \mathbf{y}) - \gamma < 0, \quad \mathbf{g}(\mathbf{x}, \mathbf{y}^*) \leq 0, \quad \mathbf{h}(\mathbf{x}, \mathbf{y}^*) = 0 \quad (43)$$

there exists a nonzero vector (u_o, λ, μ) with $(u_o, \lambda) \geq 0$ such that [4]

$$u_o[\max f(\mathbf{x}, \mathbf{y}) - \gamma] + \mu^T \mathbf{g}(\mathbf{x}, \mathbf{y}^*) + \lambda^T \mathbf{h}(\mathbf{x}, \mathbf{y}^*) \geq 0 \quad (44)$$

$$\max\{f(\mathbf{x}, \mathbf{y}) + \bar{\mu}^T \mathbf{g}(\mathbf{x}, \mathbf{y}) + \bar{\lambda}^T \mathbf{h}(\mathbf{x}, \mathbf{y})\} \geq \gamma \quad (45)$$

$$\phi(\lambda, \mu) \geq \min \max\{f(\mathbf{x}, \mathbf{y}) : \mathbf{g}(\mathbf{x}, \mathbf{y}) \leq 0, \mathbf{h}(\mathbf{x}, \mathbf{y}) = 0\} \quad (46)$$

If $\phi(\lambda, \mu)$ is concave,

$$\max \phi(\lambda, \mu) \geq \min_{\mathbf{x}} \max_{\mathbf{y}} f(\mathbf{x}, \mathbf{y}) \quad (47)$$

From (34),

$$\max \phi(\lambda, \mu) = \min_{\mathbf{x}} \max_{\mathbf{y}} f(\mathbf{x}, \mathbf{y}) \quad (48)$$

The strong duality theorem for the convex $\phi(\lambda, \mu)$ has been proved.
Let

$$\gamma = \max_{\mathbf{y}}\{-\min_{\mathbf{x}} f(\mathbf{x}, \mathbf{y}) : \mathbf{g}(\mathbf{x}^*, \mathbf{y}) \leq 0, \mathbf{h}(\mathbf{x}^*, \mathbf{y}) = 0\} \quad (49)$$

If $-\min_{\mathbf{x}} f(\mathbf{x}, \mathbf{y})$ and $\mathbf{g}(\mathbf{x}^*, \mathbf{y})$ are convex, $\mathbf{h}(\mathbf{x}^*, \mathbf{y})$ is affine, and the following system has no solution,

$$-\min f(\mathbf{x}, \mathbf{y}) - \gamma < 0, \quad \mathbf{g}(\mathbf{x}^*, \mathbf{y}) \leq 0, \quad \mathbf{h}(\mathbf{x}^*, \mathbf{y}) = 0 \quad (50)$$

there exists a nonzero vector (u_o, λ, μ) with $(u_o, \lambda) \geq 0$ such that

$$u_o[-\min f(\mathbf{x}, \mathbf{y}) - \gamma] + \mu^T \mathbf{g}(\mathbf{x}^*, \mathbf{y}) + \lambda^T \mathbf{h}(\mathbf{x}^*, \mathbf{y}) \geq 0 \quad (51)$$

$$\min\{f(\mathbf{x}, \mathbf{y}) + \bar{\mu}^T \mathbf{g}(\mathbf{x}, \mathbf{y}) + \bar{\lambda}^T \mathbf{h}(\mathbf{x}, \mathbf{y})\} \leq -\gamma \quad (52)$$

$$\phi(\lambda, \mu) \leq \min \max\{f(\mathbf{x}, \mathbf{y}) : \mathbf{g}(\mathbf{x}, \mathbf{y}) \leq 0, \mathbf{h}(\mathbf{x}, \mathbf{y}) = 0\} \quad (53)$$

If $\phi(\lambda, \mu)$ is convex,

$$\min \phi(\lambda, \mu) \leq \min \max f(\mathbf{x}, \mathbf{y}) \quad (54)$$

From (33),

$$\min \phi(\lambda, \mu) = \min_{\mathbf{x}} \max_{\mathbf{y}} f(\mathbf{x}, \mathbf{y}) \qquad (55)$$

This completes the proof. □
The solution set $(\mathbf{x}, \mathbf{y}, \lambda, \mu)$ of the unconstrained min-max problems satisfies the saddle-point optimality.
For convex $\phi(\lambda, \mu)$

$$L(\mathbf{x}^*, \mathbf{y}, \lambda^*, \mu^*) \leq L(\mathbf{x}^*, \mathbf{y}^*, \lambda^*, \mu^*) \leq L(\mathbf{x}, \mathbf{y}^*, \lambda, \mu) \qquad (56)$$

For concave $\phi(\lambda, \mu)$

$$L(\mathbf{x}^*, \mathbf{y}, \lambda, \mu) \leq L(\mathbf{x}^*, \mathbf{y}^*, \lambda^*, \mu^*) \leq L(\mathbf{x}, \mathbf{y}^*, \lambda^*, \mu^*) \qquad (57)$$

5. EXAMPLES

In this section, the proposed method is applied to numerical examples. The co-evolutionary algorithm based on evolution strategy for selection, recombination and mutation is used.

Example 1.
$$\min_{x} \max_{y} \{x^2 - y^2\} \qquad (58)$$

subject to
$$2x + y - 1 = 0 \qquad (59)$$

$$\begin{aligned}
\phi(\lambda) &= \min_{x} \max_{y} \{x^2 - y^2 + \lambda(2x + y - 1)\} \\
&= \min_{x} \{x^2 + 2\lambda x\} + \max_{y} \{-y^2 + \lambda y\} - \lambda \\
&= -\frac{3}{4}\lambda^2 - \lambda \qquad (60)
\end{aligned}$$

Since $\phi(\lambda)$ is concave,

$$\max_{\lambda} \phi(\lambda) = \min_{x} \max_{y} \{x^2 - y^2 : 2x + y - 1 = 0\} \qquad (61)$$

The solution of Example 1 is $x^* = \frac{2}{3}$, $y^* = -\frac{1}{3}$ and $\lambda^* = -\frac{2}{3}$.

Example 2. This example has the same payoff of Example 1 but a different constraint given below.

$$x + 2y - 1 = 0 \qquad (62)$$

$$\begin{aligned}
\phi(\lambda) &= \min_{x} \max_{y} \{x^2 - y^2 + \lambda(x + 2y - 1)\} \\
&= \min_{x} \{x^2 + \lambda x\} + \max_{y} \{-y^2 + 2\lambda y\} - \lambda \\
&= \frac{3}{4}\lambda^2 - \lambda \qquad (63)
\end{aligned}$$

Since $\phi(\lambda)$ is convex,

$$\max_{\lambda} \phi(\lambda) = \min_{x} \max_{y} \{x^2 - y^2 : x + 2y - 1 = 0\} \qquad (64)$$

The solution of Example 2 is $x^* = -\frac{1}{3}$, $y^* = \frac{2}{3}$ and $\lambda^* = \frac{2}{3}$.

Numerical results are compared with analytic ones in table 1 and table 2. The proposed method gives the accurate solutions. Example 1 has the concave Lagrangian function, and the Lagrange multiplier has the strategy of maximizing it. The Lagrangian function in Example 2, and the corresponding strategy is minimizing it.

	Example 1		
Exact	$x = \frac{2}{3}, y = -\frac{1}{3}, \lambda = -\frac{2}{3}$		
Numerical	x=0.666667, y=-0.333333, λ=- 0.666667		

TABLE 1
EXACT AND NUMERICAL SOLUTIONS OF EXAMPLE 1

	Example 2		
Exact	$x = -\frac{1}{3}, y = \frac{2}{3}, \lambda = \frac{2}{3}$		
Numerical	x=-0.333333, y=0.666667, λ=0.666667		

TABLE 2
EXACT AND NUMERICAL SOLUTIONS OF EXAMPLE 2

6. CONCLUSION

The co-evolutionary algorithm is presented to solve the constrained min-max problems. Dual problems of constrained min-max ones are derived using Lagrange multipliers. The solution of primal(constrained min-max) problem is acquired by solving the dual(unconstrained min-max) problems. The proposed method solves min-max problems with the separable and inseparable constraints. For inseparable constraints, the duality relation is derived and the strategy of Lagrange multipliers is also determined. The proposed algorithm is applied to the min-max problems with inseparable constraints. The numerical results acquired is equal to the analytic ones.

REFERENCES

[1] Z. Michalewicz and M. Schoenauer, "Evolutionary algorithms for constrained parameter optimization problems", *Evolutionary Computation*, Vol. 4, No. 1,1996.
[2] M.J. Tahk and B.C. Sun, "Co-evolutionary augmented Lagrangian methods for constrained optimization", *IEEE Transactions on Evolutionary Computation*, Vol.4, No.2, July 2000.
[3] T. Basar and G. J. Olsder, *Dynamic Noncooperative Game Theory*, Academic Press, London, 1982.
[4] M. S. Bazaraa, H. D. Sherali and C. M. Shetty, *Nonlinear Programming*, John Wiley & Sons Inc. , 1993.

1E3 A STUDY TO OBTAIN A REALISTIC GAME SOLUTION IN AN AIR COMBAT GAME (2)

Fumiaki Imado* and Josef Shinar**

* Shinshu University, 4-17-1 wakasato Nagano, Nagano 380-8553 JAPAN

** Israel Institute of Technology, Haifa 32000 ISRAEL

Key Words: Optimal Control, Differential Games, Aircraft

ABSTRACT

A method to obtain a game solution in a practical complex problem is proposed, and an example in an air combat game is presented. The principle of the method is, at first to obtain a feedback form suboptimal solution for both players. Next, by solving the one-sided optimal control problems for both players, and by improving the feedback form solution, we can get the approximate saddle point solution. An application for a minimum time pursuit-evasion air combat game is presented, and the accuracy achieved by the method is shown to be very good.

1. BACKGROUND

Many aerospace tasks belong to the class of pursuit-evasion problems and can be addressed either in an optimal control or in a zero-sum differential game formulation. The advantage of the differential game formulation is that it is robust with respect to the disturbances created by an adversary controlling agent. Because of the inherently complex nonlinear mathematical models used for representing aerospace problems, no closed form solutions are available and iterative numerical methods have to be used. Such methods solve, for each set of initial conditions, a nonlinear two-point

---

* Professor, Dept. of Mechanical
  Systems Engineering
** Professor, Faculty of Aerospace
  Engineering

boundary-value problem of high dimensions and yield the control functions in a feedback representation. There exist several algorithms that solve successfully the optimal control version of such problems, requiring the minimization (or maximization) of a cost function, denoted by J. The solution of a zero-sum differential game, that requires the simultaneous minimization and maximization of the same cost function, i.e. a simultaneous mini-max convergence, is much more difficult. For this reason many scientists refrain to address problems in a game formulation. In this paper, a fairly complicated practical air combat game is solved based on the idea of "the method of bounds", and some results are shown.

2. TEST CASE

In order to verify the algorithm, an example problem is employed about which the exact minimax solution is obtained in closed form functions of states. Consider the following two-dimensional minimum time pursuit-evasion problem.

$$\dot{x}_p = u_x \quad (1)$$
$$\dot{y}_p = u_y \quad (2)$$
$$\dot{x}_e = v_x \quad (3)$$
$$\dot{y}_e = v_y \quad (4)$$

where x_p, y_p and x_e, y_e are pursuer's and evader's coordinates, u_x, u_y and v_x, v_y are velocity components of both players with constraints,

$$(u_x^2 + u_y^2)^{\frac{1}{2}} \le u_{max} \quad (5)$$

$$(v_x^2 + v_y^2)^{\frac{1}{2}} \le v_{max} \quad (6)$$

where $\quad u_{max} > v_{max} \quad (7)$

The interception condition is defined by giving a proper capture range R_c, by

$$\Omega \equiv R - R_c = 0 \quad (8)$$

The cost function J is the time of capture, $J = t_f \quad (9)$

where

$$R = \{(x_e - x_p)^2 + (y_e - y_p)^2\}^{\frac{1}{2}} \quad (10)$$

In this case, the differential game solutions of both players can be solved and obtained as follows[1]

$$u^\circ(t) = \begin{bmatrix} u_{max}(x_e - x_p)/R \\ u_{max}(y_e - y_p)/R \end{bmatrix} \quad (11)$$

$$v^\circ(t) = \begin{bmatrix} v_{max}(x_e - x_p)/R \\ v_{max}(y_e - y_p)/R \end{bmatrix} \quad (12)$$

Figure 1 shows the pursuit-evasion geometry of two players, where "P" and "E" denote a pursuer and an evader, respectively. R is the relative distance, Vp and Ve are velocities of the pursuer and evader, and ϕ_p and ϕ_e show their directions, and ϕ shows the evader's direction.

3. MATHEMATICAL MODEL

Suppose that we don't know the exact game solution. However, as it is clear that both players will use their maximum performances, then

$$u_x = V_p \sin \phi_p$$
$$u_y = V_p \cos \phi_p$$
$$v_x = V_e \sin \phi_e$$
$$v_y = V_e \cos \phi_e \quad (13)$$

where

$$V_p = u_{max}$$
$$V_e = v_{max} \quad (14)$$

At first, we assume the pursuer's strategy as the following proportional + pure pursuit guidance,

$$\dot{\phi}_p = [N_p V_c \dot{\phi} + k(\phi - \phi_p)]/V_p \quad (15)$$

Table 1 shows the initial condition and parameters. Optimal control of the

evader ϕ_e are numerically calculated by a steepest ascent algorithm[2]. The cost function becomes smaller as k increases. The cost function J values for $k = 200, 300, 400, 500, 600$ are $16.79s$, $16.59s$, $16.38s$, $16.08s$ and $16.0s$, respectively. Fig.2 shows trajectories of both players for $k = 200, 400$ and 600.

As $k = \infty$ means $\phi_p = \phi$, which means the pure pursuit guidance.

Next, we solve the optimal control for pursuer's strategy, $\phi_p = \phi$ for several conditions. This can be done numerically (and even analytically in this case, but it is not in the usual case). Heuristically, we see that in every case, optimal ϕ_e equals to ϕ. The result means that the obtained solutions are same as (11) and (12). The saddle point characteristics can be established, but is not stated here.

4. A MINIMUM TIME AIR COMBAT GAME

The problem is stated in Ref.(3), but is explained for readers' convenience.

In Fig.1, we employ realistic aircraft models and polar coordinates, then system equations are given as follows,

$$\dot{R} = -V_p \cos(\phi_p - \phi) + V_e \cos(\phi_e - \phi) \quad (16)$$

$$\dot{\psi} = [-V_p \sin(\phi_p - \phi) + V_e \sin(\phi_e - \phi)]/R \quad (17)$$

$$\dot{V}_p = [\xi_p(T_{mp}) - D_{0p} - n_p^2 D_{Ip}]/m_p \quad (18)$$

$$\dot{V}_e = [\xi_e(T_{me}) - D_{0e} - n_e^2 D_{Ie}]/m_e \quad (19)$$

$$\dot{\phi}_p = g(n_p^2 - 1)^{\frac{1}{2}}/V_p \quad (20)$$

$$\dot{\phi}_e = g(n_e^2 - 1)^{\frac{1}{2}}/V_e \quad (21)$$

Where T_m is the maximum available thrust, D_o is the zero-lift drag, D_I is the induced drag, m is the aircraft mass, and n is the normal load factor. The following relations exist between drag and lift coefficients,

$$D = \frac{1}{2}\rho V^2 s[C_{D0} + k(C_L - C_{L0})^2] \quad (22)$$

$$L = \frac{1}{2}\rho V^2 s(C_L - C_{L0})^2 \quad (23)$$

$$D = D_0 + n^2 D_I \qquad (24)$$

$$D_0 = \tfrac{1}{2}\rho V^2 s C_{D0} \qquad (25)$$

$$D_L = 2k(mg)^2/(\rho V^2 s) \quad (26)$$

The control variables are the thrust T and lift coefficient C_L. The stopping condition and cost function are same as (8) and (9).

A feedback form of the approximation of the optimal control for both players are expressed as follows.[4]

$$\xi_i = 1,$$

$$\varsigma_i = (\dot\phi_s)_i \left(\frac{2V_i}{V^r_i - V_i}\right)^{\tfrac{1}{2}} \sin(\tfrac{\phi - \phi_i}{2})$$

$$i = p, e \quad (27)$$

Where ς is the optimal required turning rate, related to the aerodynamic load factor n by

$$\varsigma = \tfrac{g}{V}(n^2 - 1)^{\tfrac{1}{2}} \qquad (28)$$

$\dot\phi_s$ is the sustained turning rate with full thrust,

$$\dot\phi_s = \tfrac{g}{V}\left(\frac{J_m - D_0 - D_I}{D_I}\right)^{\tfrac{1}{2}} \qquad (29)$$

and V^r is the reference speed obtained from the reduced-order game solution. Originally the value of V^r is assumed to be the aircraft maximum speed.

5. IMPLEMENTATION

Table 2 shows parameters employed. Both aircraft are YF16, however the C_{D0} of the evader is intentionary increased than the actual one. The computation is performed through the following process.

a) Simulations are conducted by employing suboptimal law (eq.27) for both players, for several parameters of V_i^r. The histories of C_L's; C_{LP} and C_{Le} are stored, and the interception time t_f is registered.

b) Solve the minimum time optimal control of the pursuer, while the evader employs the suboptimal law (eq.27). The solution is obtained by steepest ascent method, and the time history of C_{LP} obtained in step a) is employed as the nominal control. The solutions are

obtained for several value of the evader's V^r; V_e^r, and the interception times are registered.

c) Solve the maximum time optimal control of the evader, while the pursuer employs the suboptimal law (eq.27) in the same way as step b). The time history of C_{Le} obtained in step a) is employed as the nominal control, and the interception times for several value of the pursuer's V^r; V_p^r are registered.

Let us denote the performance indices in step a); $J(u^*, v^*)$, Step b); $J(u^0, v^*)$ and step c); $J(u^*, v^0)$, where superscripts "$*$" and "0" mean suboptimal and optimal, respectively. It is clear that the following relation exists,

$$J(u^0, v^*) < J(u^*, v^*) < J(u^*, v^0) \quad (30)$$

If the difference between $J(u^0, v^*)$ and $J(u^*, v^0)$ is small enough, then, we can consider $J(u^*, v^*)$ as the approximate solution of this mini-max problem.

6. RESULTS

One result of ref.(4), which is corresponding to $\phi_0 = 60°$ in Table 2 is shown. The $J(u^0, v^*)$ and $J(u^*, v^0)$ for several values of V_e^r and V_p^r, are calculated respectively. These $J(u^0, v^*)$ and $J(u^*, v^0)$ are shown together in Fig.3. The optimal values of these are 52.9475sec and 53.0450sec, yielding $\Delta J = 0.0975$sec; which is less than 0.2% of the interception time. The corresponding $J(u^*, v^*)$, obtained by simulation, turned out to be 52.9614sec, which is within the expected range.

For the case of $\phi_0 = 90°$ and $120°$ are also studied, which show similar results. These results enforce the validity of our method.

7. CONCLUSIONS

The above given results demonstrate the feasibility to solve a pursuit-evasion game of interest with a satisfactory

accuracy by using the above outlined method. However, the accuracy that can be achieved in this way depends strongly on the validity of the functional form selected for the approximate strategies.

ACKNOWLEDGEMENT

Table 1. Parameters(Test case)

R	$3000m$
ϕ	$60°,90°,120°$
V_p	$240m/s$
V_e	$260m/s$
ϕ_p	$0°$
ϕ_e	$0°$
R_c	$2500m$

Table 2. Parameters(Air combat)

R	$3000m$
ϕ_0	$90°$
V_p	$300m/s$
V_e	$240m/s$
ϕ_p	$0°$
ϕ_e	$0°$
R_c	$60m$
N_p	3
k	$200,300,400,500,600$

REFERENCES
1)A.E. Bryson, Jr. and Yu-Chi Ho, "Applied Optimal Control" pp277-280, John Willey & Sons,1975
2)A.E. Bryson Jr., and W.F. Denham, "A Steepest Ascent Method for Solving Optimum Programing Problems", Journal of Applied Mechanics", Vol.29, No.6, pp.247-257, 1962
3)F. Imado, and J. Shinar, "A Study to obtain a Realistic Game Solution in an Air Combat Game", Proc. Of the 13th International sessions in the 37th Aircraft Symposium, pp.583-586, 1999
4)J. Shinar, "Evaluation of Suboptimal Pursuit-evasion Game Strategies for Air Combat Analysis", Journal of Guidance, Controls, and Dynamics, Vol.8, No.1, pp.9-15, 1985.
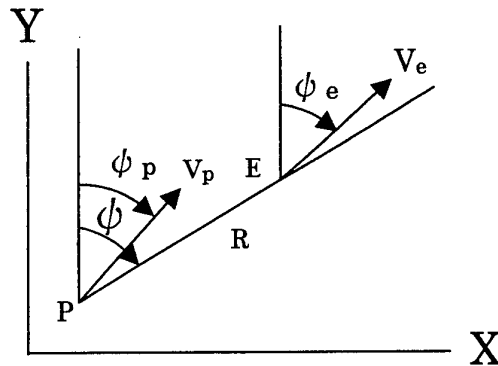
Fig.1 Horizontal interception geometry

Fig.2 Optimal trajectories of evader
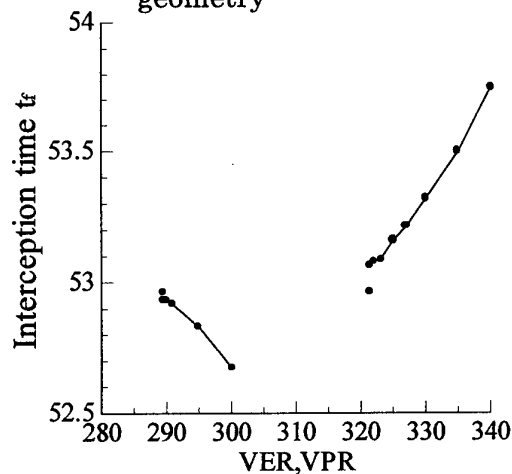
Fig.3 Optimal cost functions for Pursuer and evader

1E4　Spaceflight by Optimal Control with Theory of Relativity

Hiroyuki Takano[*], Yoriaki Baba[**]

Department of Aerospace Engineering, National Defense Academy

1-10-20 Hashirimizu, Yokosuka, 239-8686, JAPAN

(E-mail: htakano0@cc.nda.ac.jp)

Keywords: Guidance and Control, Trajectory Optimization

Abstract

In this paper, the interstellar trajectory optimization of a spacecraft whose velocity is close to the light speed is studied with several performance indices. Although the principle of relativity is famous, its dynamics is not so popular. Thus, this paper starts from collecting the equations of motion etc. The result shows interesting difference from ordinary optimal solutions.

Nomenclature

x, v, m　:spacecraft's position, velocity and mass in the absolute rest frame

m'　:spacecraft's mass in moving coordinates with the spacecraft (= proper mass)

a　:acceleration in the spacecraft's coordinates(= acceleration)

t, τ　:times in the absolute rest frame and the spacecraft's coordinates

c　: light speed(=$3.0 \cdot 10^8$m/s)

$0, f$　:(subscripts)at the beginning and at the end

1. Introduction

In the aerospace engineering, the effect of the principle of relativity near light speed is hardly taken account of. Although we can not fly at near light speed in our technology, it is difficult to find a text in which the equations of motion in the principle of relativity are introduced. In this paper, the formulation under the principle of relativity is introduced and is used in a simple example of numerical trajectory optimization with several performance indices.
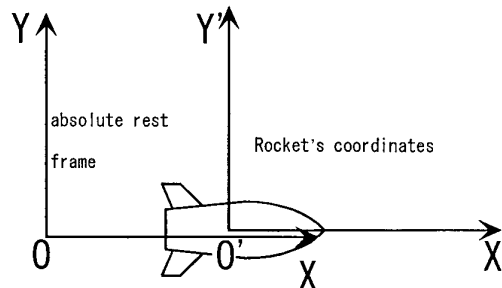

Fig. 1　coordinates

2. Formulation

Assuming one-dimensional straight motion, the spacecraft is a mass point and

---

[*] Associate Professor, Department of Aerospace Engineering

[**] Professor, Department of Aerospace Engineering

has a rocket engine which converts propellant mass perfectly into propulsion energy, ex. anti-matter propulsion. The observation from earth is considered as that from the absolute rest frame, and the coordinates fixed at the spacecraft near light speed is named the spacecraft's coordinates. There are no gravitational field distortions either by stars or planets and no influence from the interstellar matter, so the space is totally vacuum.

2.1 Equations of motion

$$\left.\begin{array}{l} \dfrac{d\tau}{dt} = \sqrt{1 - \dfrac{v^2}{c^2}} \\[2mm] \dfrac{dx}{dt} = v \\[2mm] \dfrac{dv}{dt} = a\left(1 - \dfrac{v^2}{c^2}\right)^{1.5} \\[2mm] \dfrac{dm}{dt} = -\dfrac{m|a|v}{c^2}\sqrt{1 - \dfrac{v^2}{c^2}} + \dfrac{mav}{c^2}\sqrt{1 - \dfrac{v^2}{c^2}} \end{array}\right\} \quad (1)$$

Although the second equation in eqs. (1) seems quite ordinary even in Newtonian mechanics, the third equation may not be familiar to engineers which leads from the equation below:

$$\frac{dm}{d\tau} = \frac{F}{m}$$

$$\left(m = \frac{m'}{\sqrt{1 - \dfrac{v^2}{c^2}}}, \quad \frac{d\tau}{dt} = \sqrt{1 - \dfrac{v^2}{c^2}} \right) \quad (2).$$

Here t is the time in absolute rest frame and t is the proper time in the rocket's coordinates.

The fourth equation in eqs. (1) is the change of rocket's mass in the absolute rest

frame, which equals zero if a > 0, i.e. the rocket accelerates. Since we assumed a rocket engine which converts propellant mass perfectly into propulsion energy, the mass of the propellant consumption equates the mass gain in the principle of relativity in the absolute rest frame. When a < 0, it loses twice mass and the mass in the absolute rest frame is the same as the proper mass in the rocket's coordinate when the rocket stops. In the rocket's coordinate, it loses propellant either in the acceleration or in the deceleration, as the mass is also relative in the principle of relativity. It differs from one coordinates to another.

Although we mainly use state variables in the absolute rest frame in this paper except acceleration, the position, the velocity, the mass or the proper time in the rocket's coordinates can be obtained from the Lorentz transformation, which is well-known.

2.2. Performance indices

In this paper, several ordinary trajectory optimizations like the minimum time problem are solved. In the minimum time problem, the performance indices are,

$$I = \tau_f = \int_0^{t_f} d\tau = \int_0^{t_f} \sqrt{1 - \frac{v^2}{c^2}}\, dt \quad (3).$$

Here the time in the rocket's coordinates will be minimized.

In the minimum fuel problem, we chose the performance indices

$$I = m_f \quad (4),$$

where the terminal mass of the rocket will be

maximized.

2.3. Inequality constraints

The acceleration of the spacecraft may continue for a long time, so it is limited within 10m/s², nearly 1 G, considering crew's health.

$$|a| \leq 10 \qquad (5)$$

2.4. Boundary conditions

The rocket flies to the point 10 light year away from the earth and it stops at the earth and the terminal position.

$$x_0 = 0, \quad x_f = 10 \text{ light year,}$$
$$v_0 = v_f = 0, \quad m_0 = 100\% \qquad (6)$$

The flight time in the maximum final mass problem is specified 5% more than that of the minimum time flight.

For the numerical analysis, EZopt[1) is utilized.

3. Numerical results

The solution for the minimum time problem is shown in Figure 2. The minimum flight time is 11.7 year in the absolute rest frame or 4.79 year in the rocket's coordinate. The acceleration seems quite normal bang-bang solution, ie. maximum thrust in the former half and maximum deceleration in the latter half.

Although the acceleration is constant in the rocket's coordinates, the closer the velocity in the absolute rest frame gets to the light speed, the smaller the acceleration in the absolute rest frame is because of the

relativistic effect. The velocity of the spacecraft reached 98.7% of light speed at the middle, so it can hardly accelerate in the absolute rest frame.

As mentioned before, the relativistic mass of the rocket does not change in the former half, since the loss by fuel consumption equals the gain by the relativistic mass. When it decelerates in the latter half, it loses twice mass in absolute rest frame. At the end only 2.67% mass remained. It seems really difficult to travel near at the light speed even with an idealistic engine whose $E=mc^2$.

The solution for the minimum squared integral of acceleration is shown in Figure 3. The flight time for it is specified 5% more than that of the minimum time flight. Its acceleration usage with Relativity is linear, although, with Newtonian mechanics, it is usually non-linear.

4. Conclusion

In this paper, the equations of motion in the principle of relativity are presented from the engineering point of view. The interstellar trajectory optimization is numerically analyzed with several preformance indices. The results show many difference from the results from Newtonian mechanics.

References

[1] http://www.ama-inc.com/product.html

[2] Л. Д. Ландау and Ю. Б. Румер, "ЧТО ТАКОЕ ТЕОРИЯ ОТНОСИТЕЛЬНОСТИ," 3rd. ed., (1975).

2-1 $x - t$

2-2 $v - t$

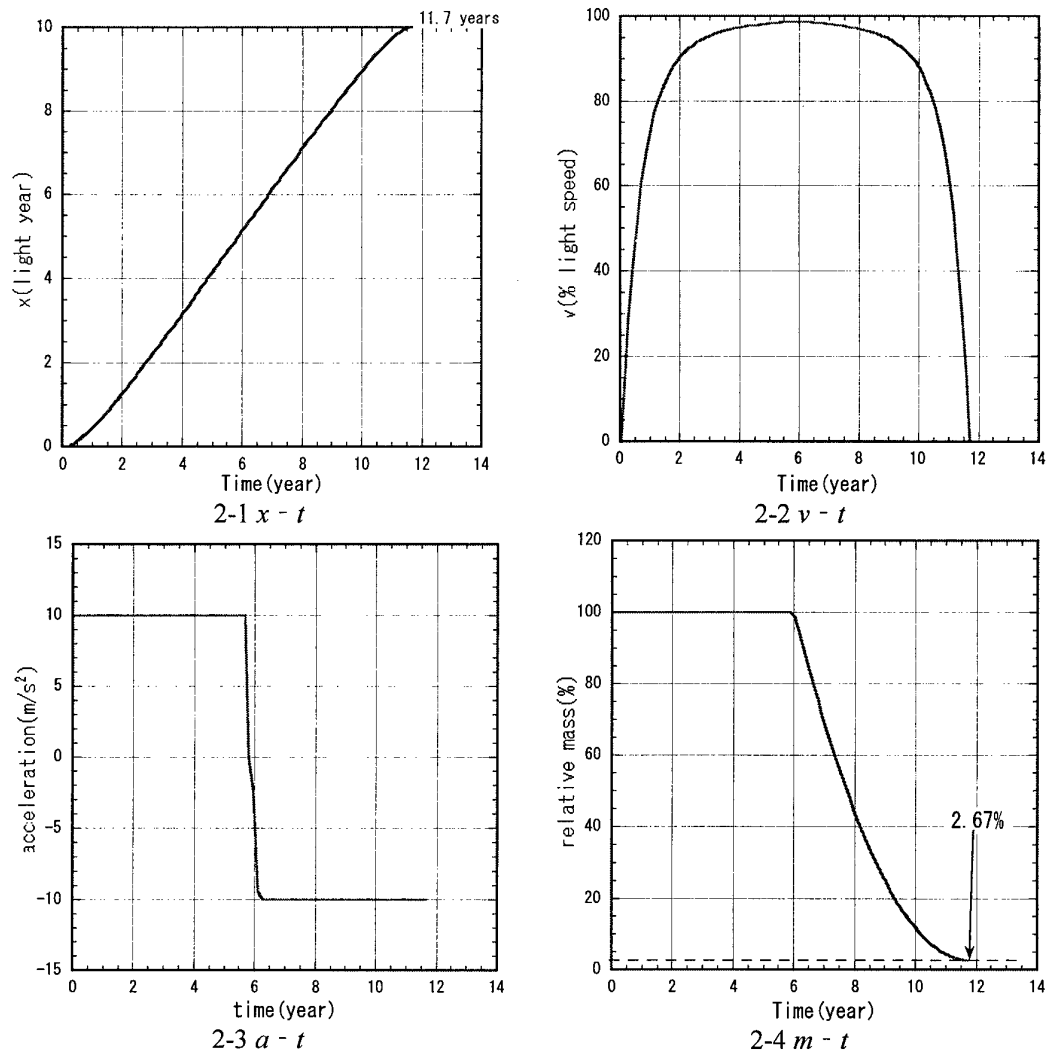2-3 $a - t$

2-4 $m - t$

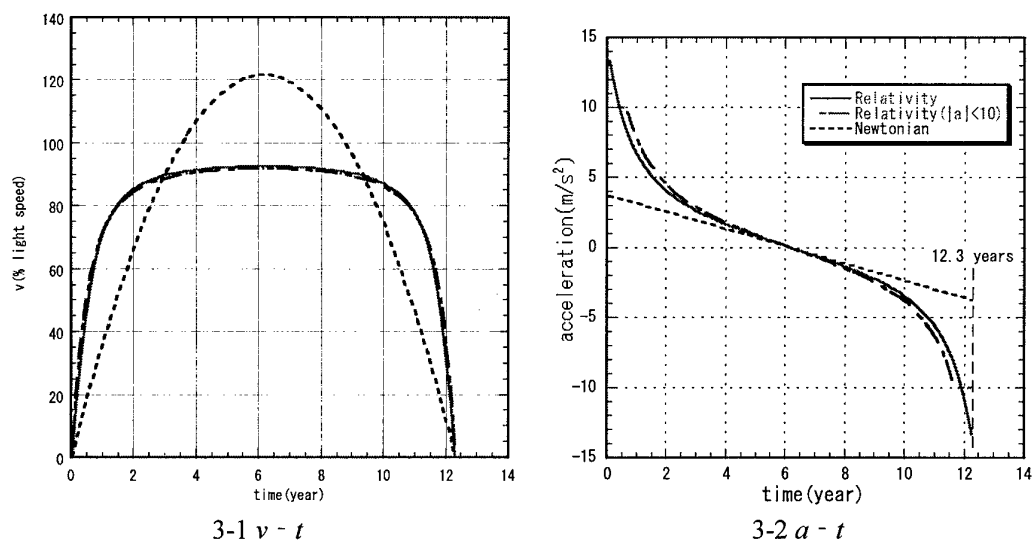Fig. 2　Time Minimization

3-1 $v - t$

3-2 $a - t$

Fig. 3　Minimum Squared Integral of Acceleration

IL1 INTELLIGENT SYSTEMS IN AEROSPACE APPLICATIONS

K. KrishnaKumar, Y. Hachisako, K. Nishita

Department of Aerospace Engineering and Mechanics
The University of Alabama, Box 870280
Tuscaloosa, AL 35487-0280, USA
e-mail: kkumar@coe.eng.ua.edu

ABSTRACT

Intelligent system technologies are gaining popularity due to their ability to solve many difficult problems of interest to aerospace engineers. In this paper, an overview of intelligent systems is presented. Next, several applications of intelligent system technologies to aerospace engineering discipline are highlighted. The applications include: aircraft control; jet engine estimation & control; aircraft combat tactics optimization; and helicopter training.

INTRODUCTION

Intelligent Systems are nature-inspired, mathematically sound, computationally intensive problem solving tools and methodologies that have become extremely ·important for advancing the current trends in information technology. Artificially intelligent systems currently utilize computers to emulate various faculties of human intelligence and biological metaphors. They use a combination of symbolic and sub-symbolic systems capable of evolving human cognitive skills and intelligence, not just systems capable of doing things humans do not do well. Intelligent systems are ideally suited for tasks such as search and optimization, pattern recognition and matching, planning, uncertainty management, control, and adaptation.

Intelligent Systems in general exhibit the following traits:

- Efficiency
- Robustness
- Self-improvement
- Learning
- Pattern recognition
- Long-term optimization
- Long-term planning

Several techniques inspired by nature have been proposed and extensively used to solve difficult engineering problems. Currently, neural networks, fuzzy logic, genetic algorithms, and evolutionary strategies have provided excellent computational intelligence tools for problem solving. Other areas of potential breakthrough include immune systems, DNA computing, and ecological modeling.

In the next several paragraphs, we present several applications of these technologies to various aerospace related problems conducted at the University of Alabama in the Intelligent Control Laboratory.

ENGINE ESTIMATOR

One of the common objectives of aircraft engine control is to enhance engine performance under deteriorated conditions. To maximize engine performance efficiently under degraded conditions, a fault tolerant engine control scheme can be applied. The first step to implement the fault tolerant engine control architecture is developing an engine performance estimator. This application focuses on developing an engine performance estimator using a combination of a genetic algorithm (GA) and a radial basis function neural network (RBFNN) for the implementation [1].

Generally, a traditional engine performance estimation, such as a Kalman filter estimator, involves intensive computational procedures because of engines' physical complexity which requires a large number of measurements to be taken and processed.

To overcome computational complexity, model estimation using neural networks has emerged. Neural network-based model estimation has been applied to areas such as optics, robotics, and system control. Attracted by the advantages of neural networks, the recent studies of fault tolerance have employed neural network architectures [2-4]. In these studies, the input selection is executed by simple inspection of data files. This manual inspection can be replaced by automatic inspection using GAs.

To apply GAs to an optimization problem, the parameter performance can be evaluated by an objective function (also, a performance index, PI). Regularly, a quadratic error measure is used for the objective function. The error is defined as the difference between desired performance measures and GAs' performance outputs.

Engine Details: The XTE46 engine used in this study consists of a fan, a compressor, burners, turbines, an afterburner, and an exhaust nozzle. Table 1 describes the twenty-one inputs from which the GA is to choose a small subset. The input variables are numbered 1 through 21.
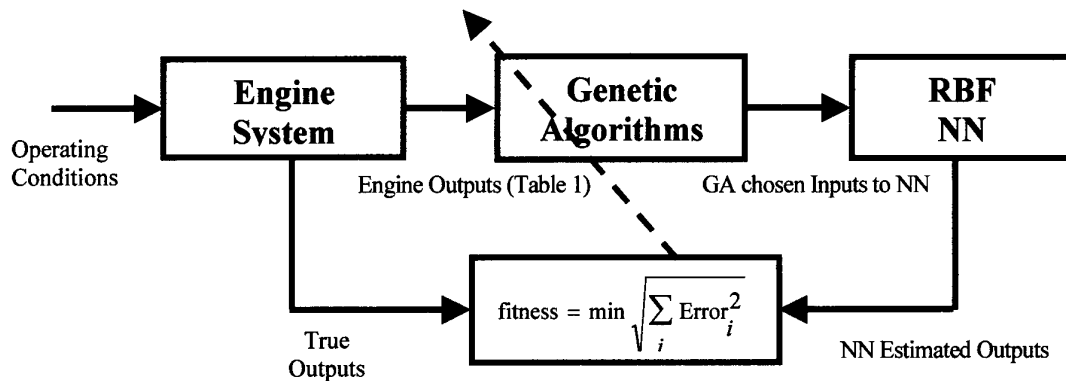
Figure 1. GA-RBFNN Architecture

Table 1. Estimator Input Variables

Ind	Var.	Description
1	xn2c	fan (and LP turbine) speed
2	xn25c	core speed (compressor and HP turbine)
3	t27c	core stream total temperature
4	t27dc	duct stream total temperature
5	t5bc	avg temp of compressor & turbine inlet
6	t56c	turbine total temperature
7	ps15c	average static pressure of HP compressor exit and forward bypass duct inlet
8	p27c	core stream total pressure
9	ps3c	compressor exit/burner inlet static temp
10	ps56c	turbine static pressure
11	p2c	fan inlet total pressure
12	t2c	fan inlet temperature
13	zwf36c	main burner fuel flow
14	za8c	variable nozzle area
15	za16c	rear bypass door variable area
16	zstp2c	fan inlet guide vane angle
17	epr	engine pressure ratio
18	lepr	linear engine pressure ratio
19	pc	power code
20	alt	altitude
21	mach	Mach number

The operating condition of the engine power code varied from 25 to 33. Similarly, the time history of altitude varied from 0 to 1000 ft and Mach number varied from 0 to 0.35.

GA-RBFNN Architecture: The GA-RBFNN architecture is shown in Figure 1. The Genetic Algorithms picks "n" inputs out of the possible 21 variables shown in table 1. The quantity "n" is a user choice. For example, if n=5, the GA has the following chromosome representation

10110	10011	11011	10111	00110
Input 1	Input 2	Input 3	Input 4	Input 5

We use a 5 bit representation to cover the 21 possibilities. Since 5 bits give us 32 possibilities, there will be multiple mapping for some of the variables.

The data from the first 150 seconds (300 data points with 0.5 seconds of step size) is used for the RBFNN's training. For the GA fitness, all the 500 data points are utilized. This way, we incorporate a combination of training and validation data into the GA fitness.

The RBFNN produces one output, either compressor **stall margin (*sm27*)** or **thrust (*fn*)**. The output is then compared with a desired performance of the corresponding performance measure (desired *sm27* or *fn*). The difference between the output from the RBFNN and the desired performance becomes the estimation error. Squaring the error and summing it up over the time range (500 data points) results in a fitness function of the entire system.

Application Results: For the *thrust* case, the GA-RBFNN selected input parameters are shown in Table 2 along with the corresponding fitness values. The numbers shown in the parameter set correspond to the parameters presented in Table 1. As seen in Table 2, the 3 inputs' (xn2c, xn25c, and p27c) case yields the best *fn* estimation. In reference 2, a similar study conducted by correlation analysis for the performance estimation of *fn*, yielded eight parameters zwf36c, xn2c, xn25c, alt, pc, za8c, t2c, and mach number.

Table 2. Best Parameter Set and Fitness (fn)

n	Parameter Set	Fitness
1 Input(s)	2	201.5091
2	3, 20	264.2763
3	1, 2, 8	172.7635
4	2, 3, 8, 20	399.6802
5	1, 2, 3, 8, 20	743.7452

The simulation of the RBFNN's output and the engine's desired output are plotted in Figure 2 for the three input

case for the training and testing data sets. Similar results were obtained for the stall margin.
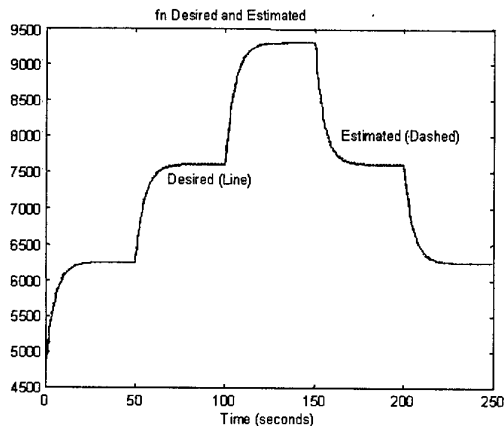

Figure 2. Thrust Estimation

AIR COMBAT TACTICS OPTIMIZATION USING GENETIC ALGORITHMS [5]

The complete design and specification of air combat tactics for many-vs.-many engagements poses a considerable challenge to tactical planners. While solutions have been developed for one-vs.-one or few-vs.-few encounters, the results may not generalize to larger engagements where formation tactics become increasingly important. The purpose of this research is to investigate the feasibility of large-scale air combat tactics optimization using genetic algorithms (ACTOGA).

The most effective **formation tactics** employ a basic fighting unit of two aircraft (called a *section* or *element*) [6]. Since this is how all fighter pilots learn their craft, it was determined early in this research that it would be most effective for optimized tactics not to deviate from established tactical doctrine. Accordingly, software tactics modules that employ basic fighting units of two aircraft have been developed. Since large numbers of fighter aircraft are difficult to control, formation tactics for large groups may be developed using a hierarchical structure consisting of smaller units or divisions; for example, a four-airplane division called the *fluid four* consists of two elements. Each element consists of two aircraft, but they are treated as a unit. This hierarchical concept is used to develop a GA-based approach to optimized air combat tactics development. Given a palette of air combat maneuvers and standard small-formation tactics as building blocks, GAs are used to determine how they can be integrated to produce large fighting groups that optimize overall combat effectiveness.

Tactics implementation in ACTOGA proceeds as follows:

1) Define a set of commonly-used element and division formations (see Table 3) as well as the underlying tactical maneuvers and attack tactics.
2) Develop a set of principles for aggregating the small formation tactics for large MvN engagements, and implement a method for doing so in the GA software. To illustrate, consider a team consisting of four aircraft. Using only the fighting wing and double-attack, the possible team formations are shown in Figure 3 (assuming both elements use the same two-ship formation). A similar approach can be used to develop large division formations from smaller 2-ship and 4-ship groupings.
3) Use the resultant formation tactics to drive the engagement, and evaluate the results via the performance metric generator.
4) Optimize the MvN engagement tactics with respect to the performance metrics.
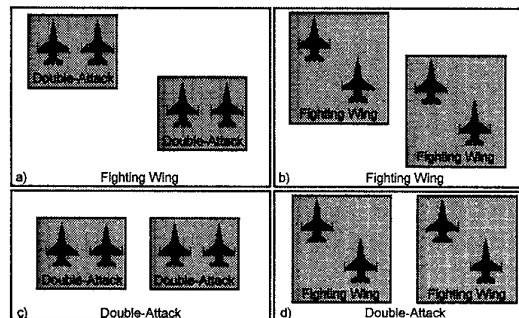
Figure 3. Potential Four-Aircraft Formations.

Table 3: Commonly used Formations [6]

Name	Symbol	Number of entities
Fighting Wing	FW	2
Left Double Attack	DAL	2
Right Double Attack	DAR	2
Fighting Wing	FW	2
Finger Four	FF	4
Left Sections in Trail	LST	4
Right Sections in Trail	RST	4
Wall Formation	WF	4

GA Fitness Functions

A cost function was developed to represent the weighted sum of several terms:

$$J = \sum_{i=1}^{6} k_i J_i; \quad 0 \le k_i \le 1, 0 \le J_i \le 1$$

The GA's objective is to minimize J. Each of the k_i coefficients enables weightings the relative importance of each of the J_i terms, which are defined as follows:

J_1 = Fraction of blue members killed
J_2 = Fraction of red team members surviving
J_3 = Fracn. of blue members violating separation criteria
J_4 = Mean blue team *relative advantage* assessment
J_5 = Standard deviation in blue team relative advantage
J_6 = Mean blue *risk assessment*

Considering first J_1 and J_2, a desirable solution would be one where none of the blue players are killed (i.e., $J_1 = 0$), and none of the red players survive (i.e., $J_2 = 0$). These are the basic performances desired from the optimization. However, by themselves, these considerations are insufficient to generate an effective tactical solution. The other terms address some key issues that characterize an effective tactical formation. The J_3 term captures the idea that team members should not come too close to each other, due to the potential collision risk. Thus, a penalty is applied when any two aircraft violate a separation constraint (set to 2,500 ft for the results that follow).

The J_4, J_5, and J_6 terms measure relative tactical advantage and situational risk, based on an assessment of the tactical situation. This assessment, in turn, is completed on the basis of *belief network* situation models [7]. The relative advantage belief network (not shown in the interest of brevity) quantifies a pilot's belief as to who possesses the instantaneous tactical advantage (*blue, neutral,* or *red*).

System evaluation

To demonstrate GA performance, two different tactical scenarios were considered, each with a given red team formation:

Scenario 1a. 16v16; Blue formation not optimized by GA

Scenario 1b. Red formation same as scenario 1; Blue formation optimized by GA

Scenario 2. Examine blue performance when at a numerical disadvantage

Scenario #1a
The first scenario allowed the examination of the blue team performance in a simulation where both blue and red tactics were specified manually -- the blue team's tactics were deliberately not optimized. Table 2 shows several performance measures for this scenario. Clearly, the blue team fared quite poorly. The relative advantage and risk measures refer to the belief network metrics described earlier. The mean relative advantage and risk measures are scaled between 0 and 1. Overall, the non-optimized blue tactics provided a poor solution.

Scenario #1b
For the next scenario, the red team formation and tactics used in scenario 1a is used. However, now the GA optimized the blue force tactics. This resulted in the configuration shown in Figure 4. The GA selected a *lead-trail* (LT4) formation for the blue team, consisting of (from front to back) a *finger four* (FF) followed by three *sections-in-trail* (ST).

Table 4 shows the scenario's outcome. It is clear that the GA had a profound impact on the blue team's tactical effectiveness: blue suffered zero casualties, while red suffered 16 casualties. The blue team had better relative advantage and risk measures than the red team. The margin was determined to be statistically significant by the T-test. Furthermore, the standard deviation in both risk and relative advantage was zero, meaning that every blue player obtained the same performance measures. These results indicate that even with perfectly even blue/red aircraft performance, proper selection of tactical formation and intercept geometry can make a substantial difference.

Scenario #2
With a set of successful evaluations of ACTOGA's performance in 16v16 engagements, its performance was assessed in a scenario where the blue team was outnumbered. Figure 4 shows the 12v16 engagement used for scenario 4, where the red team was given the

Table 4. Comparison of the three scenarios

Measure	Scenario 1a		Scenario 1b		Scenario 2	
	Blue	**Red**	**Blue**	**Red**	**Blue**	**Red**
Casualties	9	7	0	16	0	16
Mean Relative Advantage (Lower is better)	0.49	0.49	0.40	0.59	0.48	0.44
Standard Deviation in Relative Advantage	0.03	0.03	0.00	0.03	0.12	0.12
Mean Risk (Higher is better)	0.44	0.36	0.85	0.66	0.85	0.71
Standard Deviation in Risk	0.28	0.28	0.00	0.19	0.01	0.17

same configuration as in scenario 2. The GA fitness function weights were the same as those used in scenario #1b.

Table 4 shows the outcome of the second scenario, and it indicates that the GA once again obtained excellent results. Although there was no statistically significant difference in relative advantage and risk between the red and blue forces, the GA achieved a perfect result (in terms of kills and losses). Some blue players entered 1v2 engagements, which is unavoidable when the blue team is outnumbered.
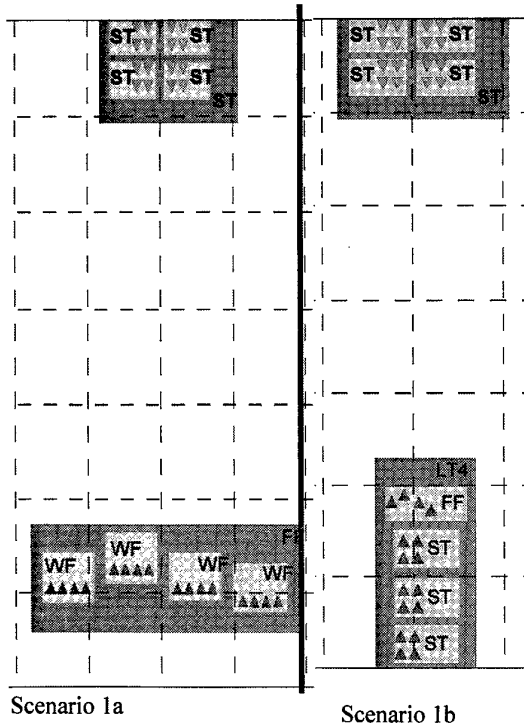

Scenario 1a

Scenario 1b

Figure 4. Optimal Formation

LEVELS OF INTELLIGENT CONTROL

Over the past decade, several innovative control architectures utilizing the intelligent control tools have been proposed. It therefore makes sense to classify these architectures in order to study their relative merits. Krishnakumar [8,9] has proposed a classification scheme

based on the ability of the control architecture for self-improvement (see Table 5). The classification scheme divides the control architectures among levels of intelligent control (LIC). For instance, most of the proposed architectures can be divided among level 0, level 1 and level 2 intelligent control schemes. Based on this classification scheme, several seemingly differing control architectures can be looked at as achieving similar goals.

In a general sense, an intelligent controller design can be stated as the following:

Given
the dynamic system as

$$X(t+1) = f(X(t),U(t),t)+\eta; \text{ where } \eta \text{ is an unknown disturbance}$$

a set of goals generated as a function of time as
$$X_g(t+1) = g(X_g(t),X(t),t)$$

a performance measure as:
$$J(t+1)= \Im(M(X_g(t),X(t),U(t),t));$$
where $\Im$ is an operator (usually summation over future time)

and a planning function as
$$P(t+1) = p(X(t),P(t),t,v);$$
where v is system faults and emergencies

the intelligent controller needs to arrive at a control, $U(t)$, such that the system (in the order of priority)

- is locally stable (includes safety of the system)
- follows closely the desired path (closeness defined by the performance measure)
- constantly optimizes long-term and short-term goals
- reacts to changing environments by properly adapting the planning functionality.

We believe that a practical way to accommodate the above needs is to approach the system as having various levels of capabilities for self-improvement. We emphasize here that self-improvement is an important goal of human intelligence. Self-improvement is

Table 5. Levels of Intelligent Control

Level	Self improvement of	Description
0	Tracking Error (TE)	Robust Feedback Control: Error tends to zero.
1	TE + Control Parameters (CP)	Adaptive Control: Robust feedback control with adaptive control parameters (error tends to zero for non-nominal operations; feedback control is self improving).
2	TE + CP + Performance Measure (PM)	Optimal Control: Robust, adaptive feedback control that minimizes or maximizes a utility function over time.
3	TE+CP+PM+ Planning Function	Planning Control: Level 2 + the ability to plan ahead of time for uncertain situations, simulate, and model uncertainties.

quantifiable and measurable in various ways. By defining Intelligent Control with various levels of intelligence, the definition is left 'open ended' such that it will not become obsolete, and it will accommodate easily the innovations that will inevitably come from the contributions of such fields as cognitive science, computer hardware, sensors and actuators, learning theory, and control architectures.

Level 0 intelligent control -- A Robust Controller

Level 0 intelligent control comprises control architectures that aim towards self-improvement of the tracking error. Robust feedback controllers that improve error with time belong to this group. Level zero excludes control architectures that adapt online to handle uncertainties associated with the system or the environment.

Level 1 intelligent control -- An Adaptive Controller

Level one intelligent control comprises control architectures that not only aim towards self-improvement of the tracking error but also involve online adaptation to accommodate for any changes in the system or the operating environment. Thus level 1 intelligent control stands out at a higher complexity level as compared to the level 0 intelligent control.

Level 2 intelligent control --An Optimal Controller

Level 2 intelligent control tries to incorporate the idea of

optimal control for the case of a known or an unknown plant that may be changing with time. It thus not only incorporates the intelligence of level one intelligent control but also tries to minimize or maximize a performance measure. As in the case of linear optimal control, control architectures incorporating these ideas rely on dynamic programming or its approximate form. Entities known as the adaptive critics form the heart of these architectures.

Level 3 Intelligent Control -- A Planning Module

In addition to level 2 capabilities, Level 3 Intelligent Control should include self- improvement of planning functions. Planning functions include contingency planning, planing for emergencies, planning for faults, etc. These planning functions could be static for Level 2 but needs to be self-improving for Level 3.

Application to Autonomous Aircraft Control [9,10]

The intelligent control architecture used for the autonomous aircraft control problem is presented in Figure 5. The architecture was implemented on a six-DOF numerical aircraft simulation with full-envelope nonlinear aerodynamics, as well as nonlinear kinematics, and a first order full-envelope thrust model. The aircraft modeled is a high-performance, supersonic vehicle representative of modern fighters. Excellent results were obtained and are documented in References 9 and 10.
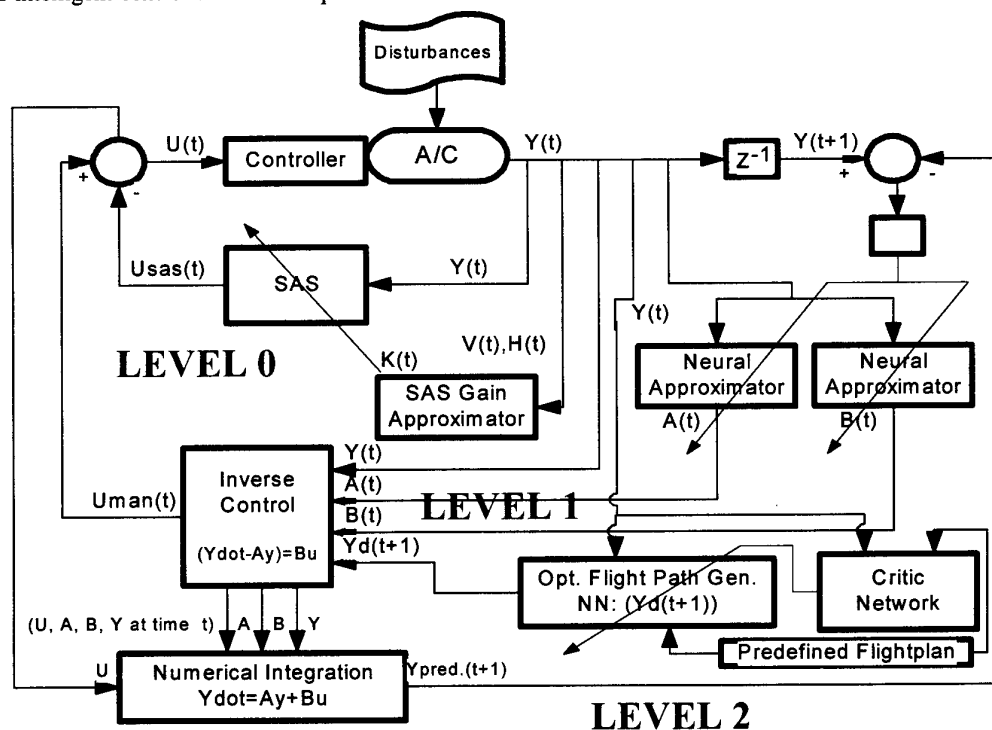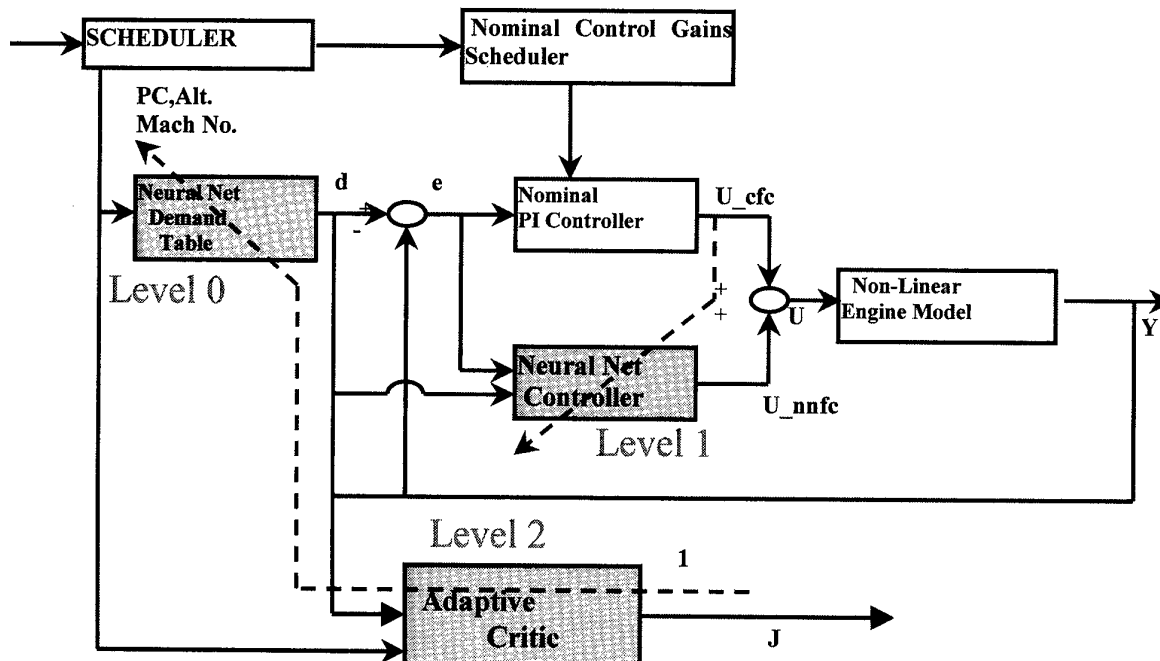
Figure 6. LIC framework for an engine control problem

In this application (see Figure 5), Level 0 was a neural-network based gain scheduler. In Level 1, a linear inverse controller with NN based system identification was used for adaptive control. In Level 2, an immunized critic was used to update the optimal path that was followed by the aircraft.

Application to Engine Control [11]

An engine (propulsion) system is a non-linear distributed system with complex interactions between sensors and

actuators, the dynamics of the system, and the dynamics of the environment. Many researchers have investigated control of engines with a motivation towards applying modern control techniques for improved engine performance. In this work, we concentrate on the need to harvest and interpret the information from the network of sensors and to apply it for control such that good engine performance is maintained under any of the following situations:

- Engine Component failure and damaged engine
- Plant characteristics change

Figure 7. Automated Hover trainer implementation

- Changing Air loads in actuators
- Changing operating conditions

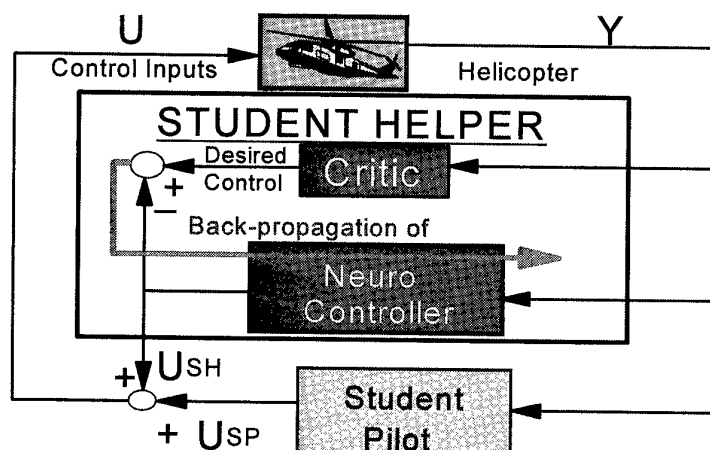We have successfully applied the LIC framework up to a level 2 controller for a non-linear General Electric Engine. In the level one intelligent controller, an inverse adaptive neuro-controller architecture is applied. In the level two intelligent controller, an adaptive critic is used to predict a performance measure, which is then used to train a neural net demand generator for minimizing the performance measure.

AUTOMATED TRAINING

Figure 7 presents an implementation of automated hover training system. This system was implemented in a fixed-base simulation facility and was shown to provide basic hover training skills with no human intervention [12]. The neural network based intelligent system adapts the helicopter dynamics to the student pilot and automatically changes the dynamics as learning progresses.

CONCLUSIONS

In this paper, several applications of intelligent systems to problems related to aerospace engineering are highlighted. References that detail these applications are provided.

ACKNOWLEDGEMENT

REFERENCES

1. K. KrishnaKumar & Y. Hachisako, Two Applications of Genetic Algorithms, GA for optimization in Aeronautics and Turbomachinery, von Karman Institute for Fluid Mechanics Lecture series 2000-07, Belgium, 2000.
2. Maggiore, Manfredi, Diao, Yixin, and Passino, Kevin M., *Intelligent Fault Tolerant Engine Control NASA/GEAE/OSU Project First Year Report*, The Ohio State University, Columbus OH, November 1998.
3. Rohloff, Thomas J., Whitmore, Stephan A., and Catton, Ivan, *Fault-Tolerant Neural Network Algorithm for Flush Air Data Sensing*, Journal of Aircraft, Vol.36, No. 3, pp. 541-549, May-June 1999.
4. Bettola, Simone and Piuri, Vincenzo, *High Performance Fault-Tolerant Digital Neural Networks*, IEEE Transactions on Computers, Vol. 47, No. 3, pp. 357-363, March 1998.
5. S. Mulgund, K. Harper, K. KrishnaKumar, and G. Zacharias, Air Combat Tactics Optimization using Stochastic Genetic Algorithms, IEEE Systems, Man, and Cybernetics Conference, San Diego, October, 1998.
6. Shaw, R. (1988). *Fighter Combat: Tactics and Maneuvering*, Annapolis, MD: Naval Institute Press.
7. Pearl, J. (1988). *Probabilistic Reasoning in Intelligent Systems: Networks of Plausible Inference*. San Mateo, CA: Morgan Kaufmann.
8. K. Krishnakumar, Intelligent Control for Aerospace Systems, Global Aerospace Technology, World Market Research Center, 2000.
9. J. Neidhoefer, K. Krishnakumar, Intelligent Control For Near-Autonomous Aircraft Missions, IEEE Systems, Man, and Cybernetics Conference, San Diego, October, 1998.
10. K. KrishnaKumar and J. Neidhoefer, Immunized Adaptive Critic for an Autonomous Aircraft Control Application, Artificial Immune Systems And Their Applications, Springer-Verlag, Inc, 1998.
11. Krishnakumar, K., Kulkarni, N., "Inverse Adaptive Neuro-Control for the control of a turbofan engine", Proceedings of AIAA conference on Guidance, Navigation and Control, Portland, OR, 1999.
12. *R. Wai, K. KrishnaKumar, Automated Manual Training Using Adaptive Neuro-controllers,* IEEE Systems, Man, and Cybernetics Conference, Vancouver, Canada, October 22-25, 1995.

SL1   HOW ACTIVE AEROELASTIC WINGS
are a
A RETURN TO AVIATION'S BEGINNINGS
AND A SMALL STEP TO FUTURE BIRD-LIKE WINGS

Ed Pendleton
Air Vehicles Directorate
Air Force Research Laboratory
Wright-Patterson Air Force Base, Ohio

We wished to employ some system whereby the operator could vary, at will, the inclination of different parts of the wings, and thus obtain from the wind forces the means to restore the balance the wind itself had disturbed. - Orville and Wilbur Wright

Introduction

The evolution of birds has brought to the world a series of magnificent, optimized flyers. Flyers optimized by nature for weight and energy. Flyers that use their feathers, bones, muscles, nerves, ligaments, *and wing flexibility* to soar through the air.

As we prepare for the centennial of powered flight in 2003, aviation historians are there to remind us that for man to first learn to fly, he had to abandon the quest to emulate these birds. Nevertheless, since we have learned to fly and have subsequently matured our current approach to flight, we must continue to consider the birds and the lessons they teach.

With nearly one hundred years of aviation development behind us, there are many that argue that aeronautics is a sunset technology. But consider this thought. Nature has always required that aerodynamic shapes must change to be optimum through various speed regimes. Until technologies similar to those used by the birds are developed, the ability to achieve true optimums in shape will never fully be achieved. Until technologies are developed that can optimally integrate aerodynamics, flight controls, with flexible lifting surfaces to maximize performance while minimizing energy and weight, aeronautics development is not at its sunset, it is not even noon

Wing flexibility -- A key to control during the first manned powered flight

The Wright Brothers realized that the key to their successful first flight was the appropriate aircraft stability and control. When Orville Wright got airborne during the Wright Brothers' historic flight on Dec. 17, 1903, he didn't have ailerons or flaps to control his airplane. Instead, the brothers chose to twist or "warp" the wings of their craft as a means to control its rolling motion. Rather than using one of the craft's two control sticks to make the wingtips twist, they devised a "saddle" in which the pilot lay.

→→ CABLES ATTACHED TO CRADLE - SLIDING CRADLE TO LEFT OF MACHINE PULLS TRAILING EDGE OF RIGHT WING DOWNWARD

→→ CABLE (NOT ATTACHED TO CRADLE) IS MOVED AUTOMATICALLY BY DOWNWARD MOVEMENT OF RIGHT WING

The accompanying picture of the Wrights' powered machine (with motor and propellers removed) shows the method of twisting the rear of the wings. A movement of only an inch or two, to the left or right, of the operators' hips resting on the little cradle was enough to give greater lift to whichever wing needed it, and to restore sidewise balance.
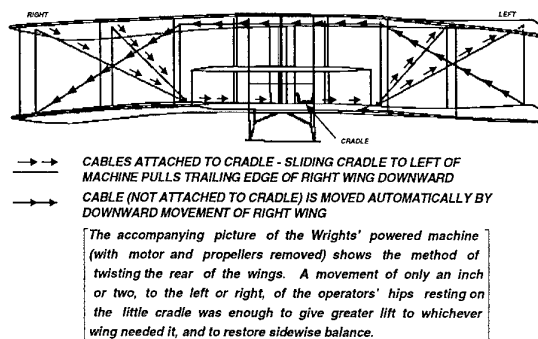
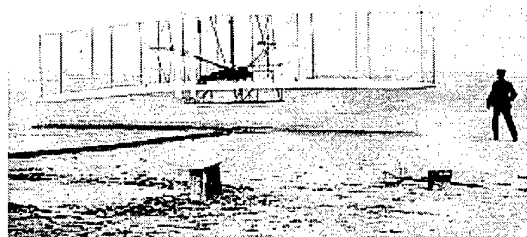Figure 1. Wing warping technique used by the Wrights

Figure 2. Wing flexibility was a key to control during the first manned flight

By moving his hips from side-to-side, the pilot tugged on a set of cables that warped either the left or right wingtip, providing the necessary flight control for the aircraft. So it was with man's earliest powered venture into the sky. The Wright brothers took advantage of wing flexibility to control their craft.

Wing flexibility - Used in the natural world for millions of years

Though the first successful manned aircraft used wing flexibility, mankind was not the first to employ wing flexibility. Eight separate fossil specimens tell us of the first living creature believed to have taken to the skies some 150 million years ago, the Archaeopteryx.

Archaeopteryx was part bird and part dinosaur. The creature had feathers and

Figure 3. Archaeopteryx fossil

bones with air sacs like a bird, but also had many reptile features like free trunk vertebra and a long bony tail. Archaeopteryx, shown in Figure 2, weighed little more than a half-pound and had a wing span of more than 20 inches. The fossil evidence suggests Archaeopteryx needed to use wing flexibility to generate enough lift to fly. As Archaeopteryx took off from a running start, it went airborne by rotating its wings by 45 degrees at the shoulder, angled forward like two large oars beating the air. Archaeopteryx 's wings acted more like an airplane's engines than wings, providing more thrust than lift. Once in the air, Archaeopteryx had to rotate its wings back to horizontal, to maintain altitude.

Figure 4. Artist's depiction of the proposed earliest bird - Archaeopteryx

In birds, wing flexibility is all in the wrist action

Since those days long ago, birds have evolved to the point where they can sustain powered flight over long distances. To do this, a modern bird needs feathers, muscle mass, a keeled sternum, and must employ anatomical wing flexibility.

In modern birds, the wing shoulder joint acts as a universal joint providing a high degree of mobility for downward wing movement, upward wing movement, extension, and retraction. It also allows significant rotation along the axis of the humerus. The elbow is a very restrictive joint that allows only planar extension and

flexure. The wrist joint is composed of two bony carpals that control the movement of the joint. Located beyond the wrist is a series of fused and incompletely fused carpal bones to which primary flight feathers are attached.

The wrist joint, articulating on two small, round carpals, allows an amazing range of movement and flexibility. This flexibility is vital to bird powered flight, since it allows the wrist to describe a lazy figure-of-eight during a complete flap. The elbow joint allows no rotation, but the wing must be able to present a solid open wing on the power stoke, but rotate during the recovery stroke to minimize resistance. The birds accomplish this by rotating the wrist and shoulder.

Wing flexibility – A negative in aircraft design for the 20th century

Though wing flexibility was a key to control during the first successful manned powered flight, wing flexibility affected other early designs adversely. Perhaps, the first designer to be affected was Dr. Langley. The unfortunate wing failure that wrecked his machine in 1903 was likely due to wing torsional divergence. The success of the Wright Brothers and the failure of the
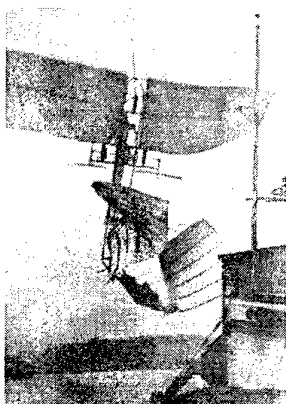

Figure 5. Dr. Langley's flying machine was subject to an early disaster caused by wing flexibility

Langley monoplane provided one of the original reasons for early designer preference for biplanes.

By the mid-1930s, the quest for higher performance and speed led designers to promote monoplanes designs with semi-monocoque structures. As these designs were built and flown, aircraft encountered a wide variety of problems, which we now classify as aeroelastic problems. Wing flutter, wing divergence, buffeting, control effectiveness, and control reversal are examples of aeroelastic problems that have plagued aircraft designs ever since.

Today, aircraft lifting surfaces are designed to be strong enough to meet loading requirements and material is added to provide stiffness adequate to keep them free from flutter, divergence, and bucking. And as pilots and passengers on aircraft, we are glad this is so.

But this added stiffness usually means adding structural weight, so design trades are made between weight and aerodynamic performance for a given set of aerodynamic requirements. As speeds increase, designers often have opted to reduce wing span, increase wing thickness and live with the subsequent reduced aerodynamic performance in an attempt to save weight.

Wing flexibility used as a benefit... The first step towards a new era in aeronautics?

As we enter the second one hundred years of aeronautics development, we are poised to enter a potentially new era in aircraft design. To take full advantage of this, it will take vision and new aircraft materials and new ways of integrating wing design with adaptive control strategies to take advantage of it.

The AFRL Air vehicles Directorate and NASA have taken a first step by developing a novel technology that offers weight competitive wing designs and improved aerodynamic performance. It is called the Active Aeroelastic Wing or

AAW. AAW Technology is a synergistic technology that integrates air vehicle aerodynamics, active controls, and structures together to maximize air vehicle performance. The concept turns wing aeroelastic flexibility into a net benefit by using of multiple leading and trailing edge control surfaces activated by a digital flight control system.

AAW techniques employ the energy of the air stream to achieve this desirable wing twist with very little control surface motion. The wing then creates the needed control forces with outstanding effectiveness. At higher dynamic pressures, AAW control surfaces are used as "aerodynamic tabs" that promote wing twist for added control force capability instead of trying to overcome control surface losses due to wing elastic twist. At these high dynamic pressures, large amounts of control power can be generated using this approach. In the same design the AAW control can minimize drag at low wing strain conditions and/or minimize structural loads at high wing strain conditions. The AAW concept was successfully by a Air Force / NASA / Rockwell North American team tested in the transonic dynamics wind tunnel. Now, another joint Air Force /NASA/Boeing team is preparing to take it to flight in California at NASA Dryden.
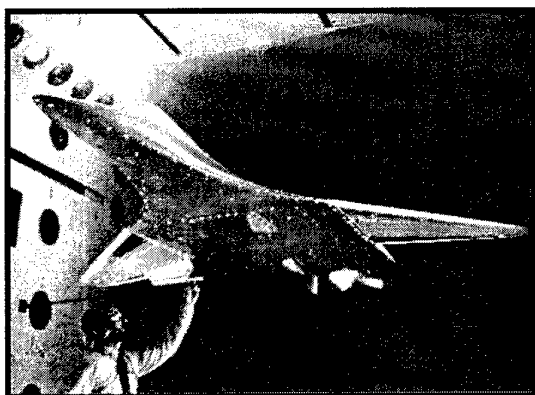

Figure 6. The Active Flexible Wing Transonic Dynamics Wind Tunnel Model proved the viability of the AAW concept

On the original F/A-18, wing flexibility was a negative. AAW will turn it into a positive.

Our joint Air Force, NASA, and Boeing team is modifying an F/A-18 fighter to demonstrate the feasibility of the AAW concept. To do this, we are taking advantage of some historical aspects of the F/A-18 wing development.

The early prototype F/A-18 wings were designed with stiffness adequate for strength, buckling, and flutter with no stiffness added for roll effectiveness. At high dynamic pressures where wing flexibility effects are most pronounced, the early F/A-18s prototypes were unable to roll sufficiently. Therefore, the aircraft's wing covers were stiffened and wing aft spars were beefed up to provide improve roll effectiveness.

The AAW modification returns the wings on one of the prototype aircraft to their original stiffness, which is representative of an Active Aeroelastic Wing. The existing wing panels along the trailing edge aft box of the wing have been replaced with original-type F/A-18 wing panels.

Other modifications include changes to the leading edge actuation system and a set of new flight control laws. A high rate leading edge control actuation system has been installed to drive the outboard leading edge flap as a control surface independent of the inboard flap. The inboard flap will also be used as a control surface.

New AAW control laws have been developed using an optimization algorithm called the "Integrated Structure-Maneuver Design (ISMD) Procedure". The AAW control laws actively command the control surfaces to optimal trim settings to control the aeroelastic twist of the wing and minimize loads at high speeds.

These basic AAW control laws are designed for the AAW F/A-18 flight test as "point designs" at 20 transonic and supersonic flight conditions. These control laws were designed using ISMD and

MATLAB using a linear flight test corrected aerodynamic database. The control laws provide large amounts of control power while minimizing a weighted percentage combination of induced drag and maneuver load. The control laws control the aircraft in all axes using control surfaces in an optimal manner by using combinations of leading and trailing edge control surfaces in their best direction, aeroelastically reversed or not. The control laws use basic roll, yaw, and pitch rate, Nz and lateral acceleration feedback and provide control surface output.

The control surface outputs are gearing functions that are linear with fixed gain constant coefficients. The gearing functions are scheduled with Mach and dynamic pressure. Current F/A-18, low Level I handling qualities are also a goal to be achieved using these control laws.

By using the trailing edge control surfaces and leading edge flaps to control the aeroelastic twist of the wing, the aerodynamic forces on the wing provide the roll forces desired. A lightweight flexible wing will now have a positive control benefit rather than a negative one.
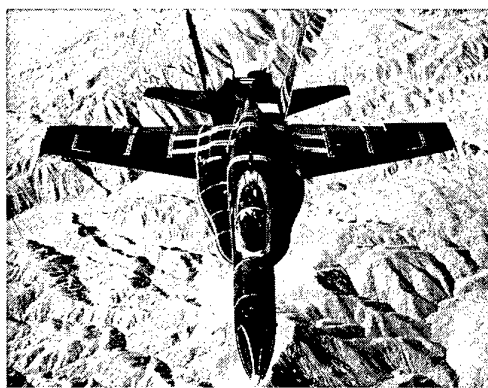

Figure 7. F/A-18 Active Aeroelastic Wing Testbed will prove the AAW concept in full-scale

Wing flexibility used as a benefit is a shift in the aircraft wing design paradigm

Active Aeroelastic Wing (AAW) Technology is a novel way of providing powerful rolling control forces for high performance aircraft. AAW Technology is especially synergistic with thin, flexible wings and allows designers more freedom to exploit highly efficient, thin, higher aspect ratio aerodynamic wing planforms. The technology can be used not only to improve the capabilities of existing wing planforms, but to reduce the conflict in requirements for new wing design. The conflicting requirements between stiff versus flexible wings are removed for aircraft that must provide competitive performance for multiple design conditions.

Potential benefits to future air vehicles as a result of application of AAW technology include substantially increased control power from conventional control surfaces by maintaining their effectiveness, reduced aerodynamic drag through programmed optimum control surface deflections, and reduced aircraft structural weight due to relaxed stiffness and hinge moment requirements. Other benefits include reduced wing and control surface deflections by allowing the wing deflections to help in the control function and an overall increased design latitude in terms of wing span, sweep, and thickness due to relaxed stiffness requirements. These benefits come for little added hardware complexity.

The AAW Program - A first, small step toward the development of bird-like wings

The AAW Flight Research Program is a first, small step toward the development of bird-like wings. But there is much more to be considered and to be done. New adaptive control algorithms and optimization techniques must be developed that take advantage of wing flexibility.

With respect to the AAW design approach, maneuver load controllers need to be developed to help keep control surface

rates within bounds when load constraints are active in the optimal gearing function. Load constraints can cause significant changes to control surface output versus feedback input and can result in large actuator rates. More research needs to be conducted to determine the best way to design the gearing functions to maximize performance without exceeding rates, or to minimize rates within a performance goal.

Research needs to be conducted to determine how to appropriately "mix" load feedback with the AAW a-priori control approach. The mixing of feedback control could easily undo the a-priori controls objective, effectively resulting in a "fighting" of the a-priori and feedback controllers. Development of an adaptive controller that monitors load feedback signals and adjusts the a-priori gains accordingly could be one possible approach.

Adaptive controller research also needs to be conducted to determine both the controller architecture and the adaptive algorithms used to adjust the gains during flight. Research needs to be conducted to develop a robust processes to solve for and implement the gearing functions in a controller.

Toward the Future

In thinking toward a future where aircraft and their lifting surfaces are optimized for energy as well as performance and weight, lifting surfaces capable of emulating some aspects of flexible birds' wings will be highly desired. To achieve this idea, new materials that are strong, but flexible and provide new levels of flexibility will need to be developed. In addition, new ways of sensing wing deformation will need to be developed as "nerves" to feedback to the controller so that the adaptations can be made to the structure.

The propulsion "muscle" will probably always be provided by a jet-type or pulse type of propulsion system since they are so efficient.

But, the ability to change the aerodynamic shape to alleviate load, reduce drag, and improve lifting efficiency is still a worthy and needed capability.

Through the integration and optimization of new materials, structures, controls with aerodynamics, new highly efficient lifting surfaces can be devised that change aerodynamic shape as they traverse the low and high subsonic, transonic, supersonic, and hypersonic aerodynamic regimes. These active lifting surfaces will change shape through active twisting and morphing to provide optimal lift throughout the flight envelope while minimizing drag, and controlling loads such as a bird does.

Nature shows us the benefits of doing so. New air vehicles will require the performance and energy savings that can be achieved. They will be lighter and cost effective, while answering the performance challenges that inevitably lie ahead in the 21st century.

Aeroelastic Wing

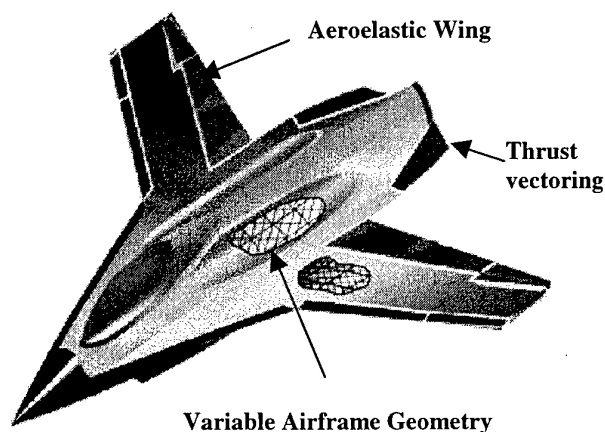**Thrust vectoring**

Variable Airframe Geometry

Figure 8. Active Aeroelastic Wing along with other innovative features will enable novel new air vehicle designs
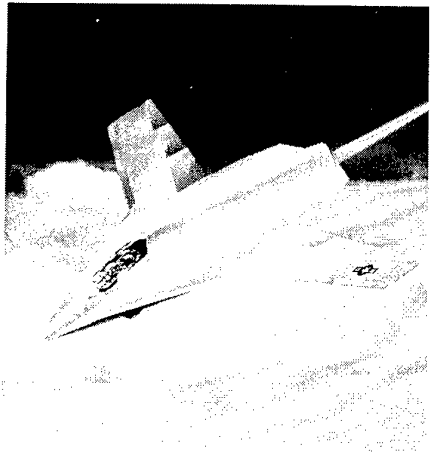
Figure 9. A vision for the future ---
Lightweight air vehicle with an active
aeroelastic wing / multifunctional lifting
surfaces

REFERENCES

1. Wright, O. and W., The Wright
   Brothers' Aeroplane, 1903.

2. Chris Nedin , "All about
   Archaeopteryx", Origins Archive, 1999.

3. Miller, G.D., "Active Flexible Wing
   (AFW) Technology," Air Force Wright
   Aeronautical Laboratories TR-87-3096,
   February, 1988.

4. Miller, G.D., "An Active Flexible Wing
   Multi-Disciplinary Design Optimization
   Method," AIAA Paper No. 94-4412-CP.

5. Perry III, B., Cole, S.R., and Miller,
   G.D., "A Summary of an AFW
   Program," Journal of Aircraft Vol. 32,
   No. 1.

6. Pendleton, Lee, and Wasserman,
   "Application of AFW Technology to the
   Agile Falcon", Journal of Aircraft Vol.
   29, No. 3, May-June, 1992.

7. Yurkovich, R., and Miller, G.D., "An
   F/A-18 Wing Modification Study for
   Active Aeroelastic Wing",
   McDonnell/Rockwell/Air Force, TBP.

8. Yurkovich, R., "Optimum Wing Shape
   for an AFW", 36th AIAA Structures,
   Structural Dynamics and Materials
   Conference, New Orleans, La., April,
   1995.

9. Pendleton, E., Griffin, K.E., Kehoe, M,
   and Perry, B. "A Flight Research
   Program for Active Aeroelastic Wing
   Technology," AIAA Paper No. 96-1574,
   37th AIAA Structures, Structural
   Dynamics and Materials Conference,
   Salt Lake City, Utah, April, 1996.

10. Pendleton, E., Bessette, D., Field, P.,
    Miller, G., and Griffin, K., "The Active
    Aeroelastic Wing Flight Research
    Program, Technical Program & Model
    Analytical Development", Journal of
    Aircraft, publish date pending.

1E5 ANALYTIC SOLUTION OF THE CALCULATION OF TURN MANEUVER OF AGRICULTURAL AIRCRAFT

Boško Rašuo*

Faculty of Mechanical Engineering, University of Belgrade,
27 Marta 80, Belgrade, Yugoslavia

Key Words: Turn maneuver, Agricultural Aircraft

ABSTRACT

In this paper a theoretical study of turn maneuver of an agricultural aircraft is presented. The problem of climb turning flight has been described with the system of differential equations which describe the influence of normal and tangential load factors on derivation velocity, path angle in the vertical plane and the rate of turn as a function of the bank angle during turning flight. The first equation determines derivative of velocity, the second one derivative of path angle in the vertical plane, and the third one derivative of flight altitude as a function of path angle in the horizontal plane. The system of differential equations of motion has been solved by analytic method. Some results of this calculation are presented in this paper.

1. INTRODUCTION

Aerial treating has become an integral part of modern agriculture. However, agricultural flying has been plagued by a great number of accidents. The maneuvers of an agricultural aircraft are divided into those carried out while entering or while leaving the spraying line. Despite low height of the airplane while spraying, this part of the flight is considered to be the safest because of an appreciable flight velocity. Upon completing a spraying run the aircraft enters a turn maneuver procedure. Pilots assert that the procedure is the most dangerous maneuver and most of the accidents occur while this maneuver is being performed. There are many secondary factors that influence the safety of agricultural flying; some of them will be treated in this paper.

In accordance with the above mentioned considerations, two segments of the procedure turn are considered to be critical: climb while turning, and rolling. In these phases of the maneuver the aircraft may encounter stalling. The aim of this paper is to determine those factors that provoke the appearance of stall and to estimate their magnitude.

The analysis has been restricted to the climb turn maneuver only. A special types of the turn maneuver has also been analyzed, i.e. the case in which the x-direction forces are balanced. This case involves a balance between thrust and drag $(T = D)$. Analytical solutions for the climb turn maneuver at a constant normal load coefficient have been obtained and analyzed.

The usual treat (spray) run is carried out along the larger dimension of the field. At the end of a treating run a turn procedure is made, and the pilot enters the following treating line (Fig. 1).

The turn maneuver procedure of agricultural aircraft may be performed in different ways, however, the maneuvers have a common feature reflecting in the requirement that a flight altitude increase have to be realized, clearly, for safety reason. In order to avoid a too high flight altitude (which is undesirable as well) resulting from the changes of field treating (spraying) conditions, the altitude increase can be combined with flight descent in the second part of turn maneuver (when the path angle in the horizontal plane $\psi \geq 90°$) [1-3].
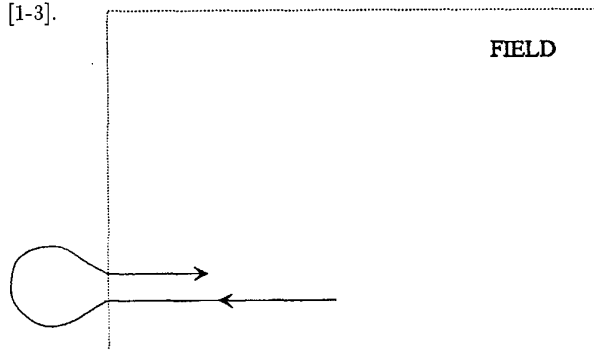

Figure 1: - Turn procedure

2. MATHEMATICAL MODEL

Using the stability-axes system for the nonsteady turning flight the following equations of motion may be written [4]:

$$m\frac{dV}{dt} = T\cos(\alpha - \alpha_s) - D - mg\sin\gamma$$

$$mV\frac{d\gamma}{dt} = [T\sin(\alpha - \alpha_s) + L]\cos\varphi - mg\cos\gamma \quad (1)$$

$$mV\frac{d\psi}{dt}\cos\gamma = [T\sin(\alpha - \alpha_s) + L]\sin\varphi$$

where are: γ path angle in the vertical plane, ψ path angle in the horizontal plane and φ bank angle.

By introducing tangential and normal load factors:

$$n_x = \frac{1}{mg}[T\cos(\alpha - \alpha_s) - D] \quad (2)$$

$$n = \frac{1}{mg}[T\sin(\alpha - \alpha_s) + L] \quad (3)$$

the system of equations of motion (1) are transformed into:

$$\frac{1}{g}\frac{dV}{dt} = n_x - \sin\gamma$$

$$\frac{V}{g}\frac{d\gamma}{dt} = n\cos\varphi - \cos\gamma \quad (4)$$

$$\frac{V}{g}\frac{d\psi}{dt}\cos\gamma = n\sin\varphi$$

The system of differential equations (4) describes the influence of normal and tangential load factors on derivation velocity V, the path angle in the vertical plane γ and the rate of turn $d\psi/dt$ as a function of the bank angle φ during turning flight.

Generally, the normal and tangential load factors vary within some limits during turn maneuver performance. However, variations of these factors during turn maneuver may be taken as constants in the first approximation for such an analysis [1-3].
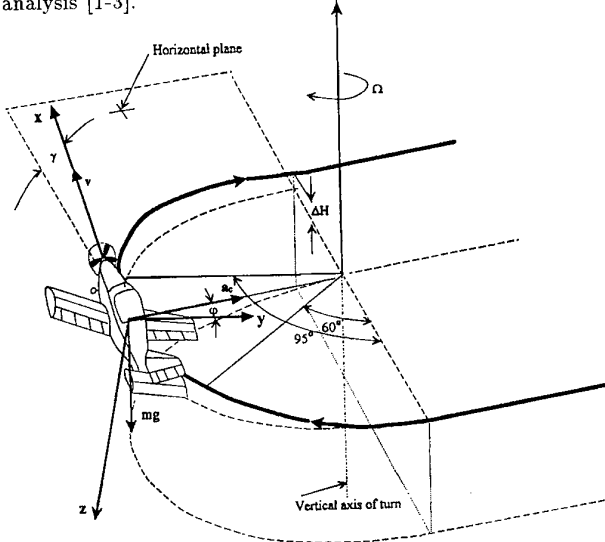

Figure 2: - The climb turn of agricultural aircraft

Substituting relation $dh/dt = V \sin\gamma$ into the system of differential equations of motion (4) we eliminate time from the system and obtain the following system of differential equations:

$$\frac{dV}{d\psi} = \frac{V \cos\gamma}{n \sin\varphi}(n_x - \sin\gamma)$$

$$\frac{d\gamma}{d\psi} = \frac{\cos\gamma}{n \sin\varphi}(n \cos\varphi - \cos\gamma) \qquad (5)$$

$$\frac{dh}{d\psi} = \frac{V^2 \sin\gamma \cos\gamma}{ng \sin\varphi}$$

as a function of path angle in the horizontal plane (ψ).

A fourth equation, that results directly from the last equation of the system (4) can also be added to the system of equations. The equation yields the time to turn, t:

$$\frac{dt}{d\psi} = \frac{V \cos\gamma}{ng \sin\varphi} \qquad (5a)$$

The system of differential equations of motion (5) are solved with numerical methods with normal and tangential load factors and bank angle as parameters [1-3].

The first equation determines derivative of velocity, the second one determines derivative of path angle in the vertical plane, and the third one gives derivative of flight altitude as a function of path angle in the horizontal plane.

Using the usual assumptions: that $\cos(\alpha - \alpha_s) \approx 1$, density of air $\rho \approx constant$ (small altitude change during turning) and $mg \approx constant$ (small change of airplane mass resulting from fuel consumption during turning), the tangential load factor can be expressed in form:

$$n_x = \frac{T \cos(\alpha - \alpha_s) - D}{mg} \cong \frac{T}{mg} - \frac{D}{mg} \qquad (6)$$

and, for small values of path angle in the vertical plane $(L \cong mg)$, we obtain:

$$n_x \cong \frac{T}{mg} - \frac{C_D}{C_L} \qquad (7)$$

Thus, tangential load factor expresses the influence of airplane thrust (power plant) and polar on characteristics of turn maneuver.
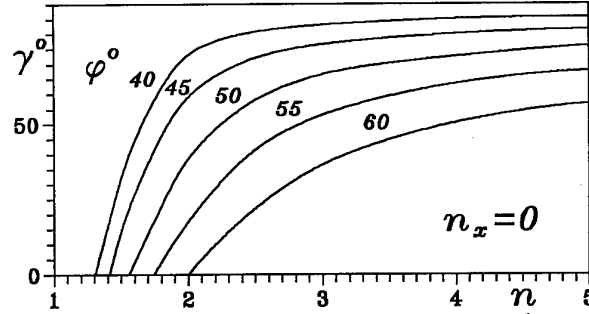

Figure 3: - Angle of flight path at the end of turn $(\psi = \pi)$ as a function of normal load coefficient
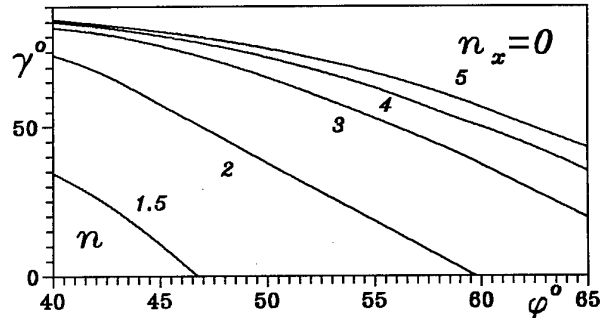

Figure 4: - Angle of flight path at the end of turn $(\psi = \pi)$ as a function of the bank angle φ

3. ANALYTIC SOLUTION

From all the variety of the turn maneuver performance a very interesting case of turning is for $n_x = 0$, i.e. when the thrust T is equal or almost equal to the aerodynamic drag D. The special feature of the case is that analytical solution can be obtained.

The system of equations of motion (4) in this case is transformed into:

$$\frac{1}{g}\frac{dV}{dt} = -\sin\gamma$$

$$\frac{V}{g}\frac{d\gamma}{dt} = n \cos\varphi - \cos\gamma \qquad (8)$$

$$\frac{V}{g}\frac{d\psi}{dt}\cos\gamma = n \sin\varphi$$

Dividing the first equation by the second one, one obtains a differential equation with separated variables:

$$\frac{dV}{V} = -\frac{\sin\gamma}{n \cos\varphi - \cos\gamma}d\gamma \qquad (9)$$

Integrating the equation from initial condition , i.e. initial values for $\gamma_1 = 0$ and V_1 to some arbitrary point γ and V the solution is obtained:

$$\frac{V}{V_1} = \frac{n \cos\varphi - 1}{n \cos\varphi - \cos\gamma} \qquad (10)$$

This equation describes speed variation during turn maneuver for given values of normal load factor and bank angle φ. Since the altitude as well as the angle of flight path γ

increases during turn, it is evident that the airplane's speed continuously decreases at the same time. Hence, lift coefficient increases.

The highest altitude increase would have been obtained when the airplane speed were lowest, i.e. when the lift coefficient would have been increased to its maximal value. However, as the flight at $C_{L_{max}}$ is unsufficiently safe, the lift coefficient is limited, as it is the case with many other performances, to a safe value $C_{L_s} = (0.7 - 0.9)\,C_{L_{max}}$.
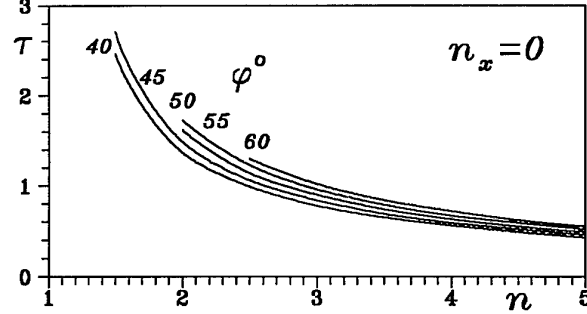

Figure 5: - Factor $\tau = t(g/V_1)$ as a function of the normal load coefficient
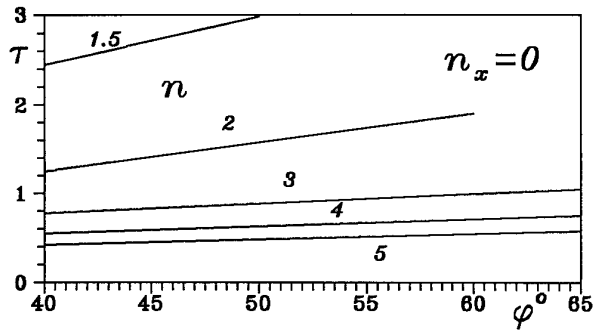

Figure 6: - Factor $\tau = t(g/V_1)$ as a function of the bank angle φ

The flight duration up to a point on the turning path, determined by the angle γ, can be obtained from the second equation of the system (8) and by substituting the solution (10):

$$t = \frac{1}{g}\int\limits_{\gamma_1=0}^{\gamma} \frac{V d\gamma}{n cos\varphi - cos\gamma} = \frac{V_1}{g}(ncos\varphi - 1)\int\limits_{\gamma_1=0}^{\gamma} \frac{d\gamma}{(ncos\varphi - cos\gamma)^2} \quad (11)$$

Hence,

$$t = \frac{(V_1/g)}{n\,cos\varphi + 1}\left[\frac{sin\gamma}{n\,cos\varphi - cos\gamma} + \frac{2n\,cos\varphi}{\sqrt{n^2\,cos^2\varphi - 1}}arctg\left(\sqrt{\frac{n\,cos\varphi + 1}{n\,cos\varphi - 1}}tg\frac{\gamma}{2}\right)\right] \quad (12)$$

For further analytical determination of the turn characteristics it is necessary to establish a relation between angle of yaw and angle of flight path. If we divide the third equation of the system (8) by the second one, we obtain:

$$cos\gamma\frac{d\psi}{d\gamma} = \frac{n\,sin\varphi}{n\,cos\varphi - cos\gamma} \quad (13)$$

The integral of the equation between limits $\gamma_1 = 0$ and γ is:

$$\psi = n\,sin\varphi \int\limits_{\gamma_1=0}^{\gamma} \frac{d\gamma}{(n\,cos\varphi - cos\gamma)cos\gamma} \quad (14)$$

which yields:

$$\psi = tg\varphi\left\{ln\left[tg\left(\frac{\gamma}{2}+\frac{\pi}{4}\right)\right] + \frac{2}{\sqrt{n^2cos^2\varphi - 1}}arctg\left(\sqrt{\frac{n\,cos\varphi + 1}{n\,cos\varphi - 1}}tg\frac{\gamma}{2}\right)\right\} \quad (15)$$

The expression (15) gives the dependence of the angle of flight path γ_2 at the end of turn maneuver ($\psi = \pi$) on the bank angle φ and normal load coefficient n. The curves $\gamma_2 = f(n)$ are shown in Fig. 3 for several values of bank angle φ. Points of intersection of this curves with abscissa ($\gamma_2 = 0$) correspond to a horizontal regular maneuver for which, as it is known: $n = 1/cos\varphi$.
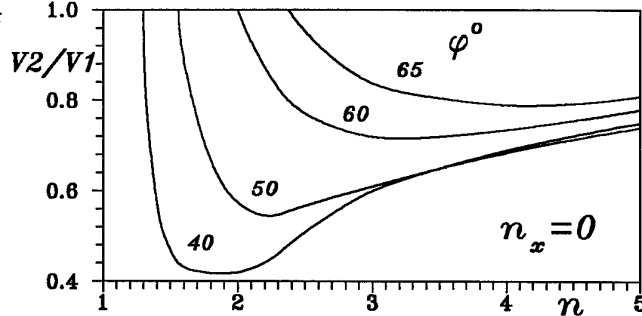

Figure 7: - Speed ratio V_2/V_1 as a function of normal load coefficient
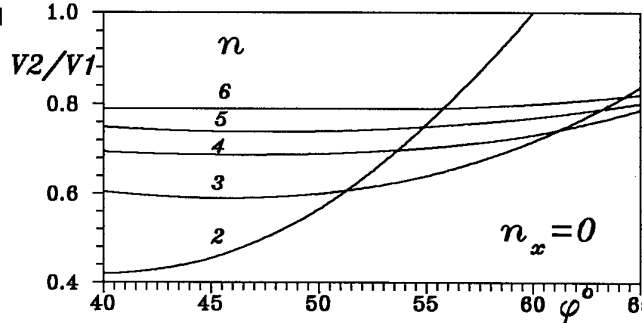

Figure 8: - Speed ratio V_2/V_1 as a function of the bank angle φ

From Fig. 3 it is evident that the flight path becomes steeper when the normal load coefficient n increases, especially for relatively moderate values of the bank angle φ ($< 45°$). This is logical, as the increase of the normal load coefficient n results from kinetic energy. Reduction in the energy results in an altitude increase and, consequently, in an increase in flight path slope.

Based on Equation (15), we may derive the relation $\gamma_2 = f(\varphi)$ for different values of normal load coefficient n and ($\psi = \pi$). These solutions are shown in Fig. 4, from which one can see that the angle of flight path at the end of turn maneuver γ_2 drops rapidly with an increase of aircraft bank angle φ. This is pronounced especially at lower values of normal load coefficient n, what is in full agreement with the above conclusions.

Now, we can determine the time needed to carry out the turn from equation (12):

$$t = \frac{(V_1/g)}{n\,cos\varphi + 1}\left[\frac{sin\gamma_2}{n\,cos\varphi - cos\gamma_2} + \frac{2n\,cos\varphi}{\sqrt{n^2cos^2\varphi - 1}}arctg\left(\sqrt{\frac{n\,cos\varphi + 1}{n\,cos\varphi - 1}}tg\frac{\gamma_2}{2}\right)\right] \quad (16)$$

The time of turn t resulting from the above equation is shown in a nondimensional form $\tau = t(g/V_1)$ as a function of the normal load coefficient with the bank angle φ as a parameter by taking $\gamma = \gamma_2$ and $\psi = \pi$ (see Fig. 5).

From Fig. 5 one can see a large decrease of time of turn maneuver when the normal load coefficient increases and less pronounced effect of the bank angle on the time of turn. This last conclusion is illustrated by low slope of curves, especially

for the values of normal load coefficient which are greater than three (see Fig. 6).

The equation (10) gives the aircraft speed at the end of turn maneuver:

$$\frac{V_2}{V_1} = \frac{n\cos\varphi - 1}{n\cos\varphi - \cos\gamma_2} \tag{17}$$

Dependence $V_2/V_1 = f(n)$ for several values of bank angle φ is shown in Fig. 7 and $V_2/V_1 = f(\varphi)$ for several values of the normal load coefficient in Fig. 8.

It is necessary to check the speed at the end of turn. Since the lift is equal to:

$$L = nW = \frac{1}{2}\rho_2 V_2{}^2 C_{Ls} S \tag{18}$$

the speed at the end of turn should be:

$$V_2 \geq V_s\sqrt{n} \tag{19}$$

where V_s is the lowest allowable (safe) horizontal speed at altitude h_2 and which is equal to:

$$V_s = \sqrt{\frac{2mg}{\rho_2 C_{Ls} S}} \tag{20}$$

By using the relation for equivalence of potential and kinetic energy we may obtain the altitude increase $\Delta h = h_2 - h_1$ at the turn:

$$\Delta h = \frac{V_1^2 - V_2^2}{2g} = \frac{V_1^2}{2g}\left[1 - \left(\frac{V_2}{V_1}\right)^2\right] \tag{21}$$

By substituting the relation for speed ratio V_2/V_1 given by equation (17), the altitude increase during turn maneuver may be written as:

$$\Delta h = \frac{V_1^2}{2g}\left[1 - \left(\frac{n\cos\varphi - 1}{n\cos\varphi - \cos\gamma_2}\right)^2\right] \tag{22}$$

The altitude increase Δh shown in Fig. 9 in a nondimensional form $\eta = \Delta h(2g/V_1^2)$ is given as a function of the normal load coefficient and the bank angle as parameters and in Fig. 10 $\eta = f(\varphi)$ and the normal load coefficient as parameters.

This special case, when the tangential load factor $n_x = 0$, also confirms the above conclusions about the influence of main parameters on the agricultural airplanes' turn characteristics [1-3]; in the domain of optimum bank angles and for the typical values of normal load coefficient the altitude increase becomes higher with the normal load coefficient decreasing, but at the same time, the time of turn increases. And vice versa, with an increase of the normal load coefficient the altitude increase becomes smaller as well as the time of turn.

4. CONCLUSION

The calculation results for the particular case of the agricultural aircraft climb turn maneuver when the tangential load coefficient is $n_x = 0$ is plotted in Fig. 3 to 10 as a function of the normal load coefficient and of the bank angle. The results of the angle of flight path change, time of turn, initial and final speed ratio and altitude increase during turning maneuver are shown for different airplane bank angles within the range $\varphi = 40 - 65°$.

Derived analytic solution is unique for its universality, because it gives analytic solutions for main flight parameters during climb turn maneuver performance. It also enables one to point out and to evaluate the most favorable conditions for the maneuver during field treating run in agriculture.

This analysis, as well as some previous investigations [1-3] shows that the solutions for the turn maneuver are to be sought primarily for the case when the basic turn-defining parameters for this type of airplane have moderate values. Thus, some moderate and variable normal and tangential load factors values result in some moderate and acceptable altitude increase, speed and bank angles. Of course, the flight parameters at the entry in a new flight path, i.e. a new treating line shall take values that correspond to the optimal treating conditions. In other words, the new-path flight parameters shall duplicate the previous treating line flight condition (Fig. 1).

The analysis and calculation of the climb turn maneuver by involving the normal and tangential load factors provide general results. In this way, observation and analysis of behavior of all types of agricultural aircraft are possible. The analysis shows that the stalling speed and the start altitude at the beginning of the turn maneuver are limiting factors. For this kind of aircraft the stalling speed of approximately $30\,m/s$ is a typical value. Accordingly, at the end of the treating (spraying) run (beginning of turn maneuver) the velocity should exceed $40\,m/s$.
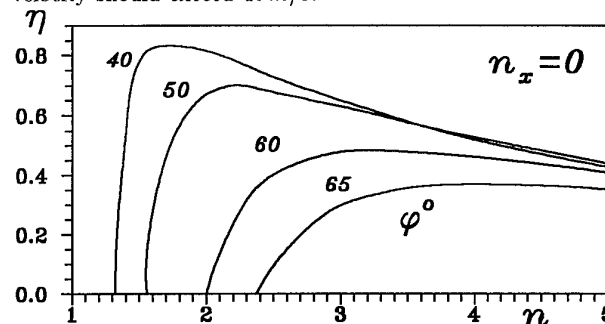
Figure 9: - Factor $\eta = \Delta h(2g/V_1^2)$ as a function of normal load coefficient
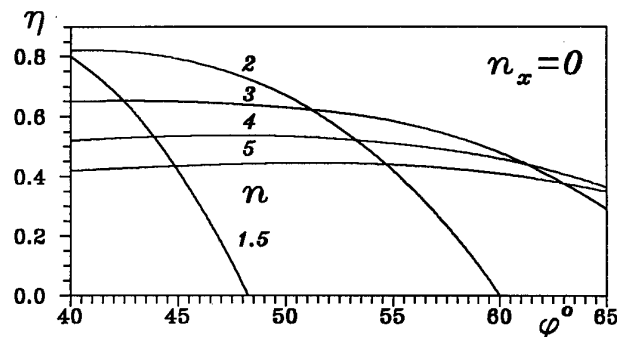
Figure 10: - Factor $\eta = \Delta h(2g/V_1^2)$ as a function of the bank angle and the normal load coefficient as parameters

REFERENCES

[1] Rašuo, B., "Effect of Load Factors on Turn Maneuver of Agricultural Aircraft", 21st ICAS, CD-ROM, Melbourne, 1998.

[2] Rašuo, B., "Numerical Modelling of the Safe Turn Maneuver of Agricultural Aircraft", 1st UNCONF, Budapest, 1997.

[3] Rašuo, B., "Theoretical Study about Turn Maneuver of Agricultural Aircraft", ISASTI, pp. 361-376, Jakarta, 1996.

[4] Etkin, B. - Reid, L.D., "Dynamics of Flight", John Wiley & Sons, pp. 238-242, New York, 1996.

1E6   A New Optimal Guidance Law for Homing Missiles with Varying Velocity

Ching-Show Lin*,   Lu-Ping Tsao**
Department of System Engineering, Chung Cheng Institute of Technology
Tahsi, Taoyuan, 33509, Taiwan, R.O.C.
Keywords: Optimal guidance law,   proportional guidance law

Abstract
An optimal guidance law (OPG) for varying velocity missiles, based on minimizing the control energy cost, is presented. The time-varying linear optimization problem is formulated and then solved analytically in a closed form by the maximum principle. The proposed guidance law demonstrates a desirable property needed for the guidance design that the commanded acceleration requirement decreases monotonically with time. The simulation studies show that the performance of the OPG is superior to that of the true proportional navigation law (TPN) and augmented proportional navigation law (APN) in terms of the miss distance and interception time.

I.   Introduction

Guidance law of homing missiles has been a topic of intensive research over the past four decades. Many of the popular guidance laws cited in open literature are based on the proportional navigation law and its variants[1-7]. It is well known that the proportional navigation law gives best results against non-maneuvering targets. In other cases, such as smart target maneuvers, the proportional navigation scheme always leads to the saturation of the commanded acceleration and then yields unacceptable miss distance. Therefore, various optimal guidance laws for missiles have been suggested extensively for many years in an attempt to replace the proportional navigation law in order to intercept the highly maneuvering targets. Most optimal guidance laws have been derived from the linear quadratic optimal control theory to obtain feedback-form solutions, and many of them take target maneuver into account to cope with the evasive target. However, the main drawback of the linearized approach is that the results only apply to a relatively small region of the state space, where the trajectory linearization is valid[8-10].

In a significantly different approach, an optimal solution to the guidance problem for a maneuvering target, using the exact nonlinear equations of motion in relative polar coordinates, was derived [11].

The optimality criterion is a weighted combination of the time of interception for a given miss distance and the expenditure of maneuvering energy. The equations of motion are solved in a closed form in terms of elliptic integrals. The obtained closed-form solution can be applied to the problems where the target information can be predicted or when a continuous update of the guidance parameters, based on the updated target model, can be implemented. A typical example is the interception of a ballistic missile in the boost phase, wherein, the target model can be estimated and its future behavior is predictable. However, the study only focuses on the cases of constant-velocity targets and missiles. In fact, the target and missile can not keep the constant velocities throughout the engagement.

The purpose of the present study is to derive an optimal guidance law for homing missiles with varying velocity against the highly maneuvering and varying velocity targets without any trajectory linearization. It is assumed that a perfect

knowledge of the target motion is available to the missiles. The optimal capture criterion, based on the constant bearing theory, is to nullify the change rate of LOS in the final time of engagement, i.e., the missile can go straight to strike the target with any control energy expenditure. The proposed guidance law can also modify the weakness of the conventional proportional navigation law against the highly evasive targets, that always results in the commanded acceleration saturation in the final phase of engagement.

The rest of the paper is organized as follows: In Section II, the optimal guidance control problem is formulated by the linear time-varying differential equations. The optimization problem is then solved in Section III and the implementation of the resulting optimal guidance scheme is analyzed. In Section IV, the results of the simulation studies conducted to evaluate the performance of the OPG and a comparison with that of the TPN and the APN schemes are presented. Discussions are also included. Finally, the study is concluded in Section V.

II. Problem Formulation

Fig.1 shows the intercept geometry of a missile intercepting a target. M and T represent the actual position of the missile and the target, respectively. The two dimensional engagement model can be represented by the following equations :

$$\dot{\theta} = [V_M(t)\sin\beta_M - V_T(t)\sin\beta_T]/R,$$
$$\theta(0) = \theta_0 \tag{1}$$

$$\dot{R} = -V_M(t)\cos\beta_M + V_T(t)\cos\beta_T,$$
$$R(0) = R_0 \tag{2}$$

$$\beta_M = \theta - \gamma_M, \tag{3}$$

$$\beta_T = \theta - \gamma_T, \tag{4}$$

$$\dot{\gamma}_M = \frac{u}{V_M(t)}, \gamma_M(0) = \gamma_{M0} \tag{5}$$

$$\dot{\gamma}_T = \frac{a_T}{V_T(t)}, \ \gamma_T(0) = \gamma_{T0} \tag{6}$$

where R is the relative distance between the missile and the target, $V_M(t)$ and $V_T(t)$ are the varying velocities of the missile and the target, respectively, θ is the angle of the line of sight, β_M and β_T are the angles between the line of sight and the current heading of the missile and the target, u and a_T are the lateral accelerations of the missile and the target, while γ_M and γ_T are the flight directions of the missile and the target with respect to the inertial reference system.

If we formulate the optimal guidance problem from Eq.(1)-(6), we have to handle the exact nonlinear differential equations and then have difficulty in solving the problem

---

* Ph.D candidate, Department of System Engineering
** Associate Professor, Department of System Engineering

analytically. Hence, we find a new approach to treat the optimal guidance problem via Eq.(1). By differentiating Eq.(1), we obtain the following time-varying linear differential equation

$$\ddot{\theta} = A(t)\dot{\theta} + B(t)u + C(t) \qquad (7)$$

where

$$A(t) \underline{\underline{\Delta}} -2\frac{\dot{R}}{R}$$

$$B(t) \underline{\underline{\Delta}} -\frac{\cos\beta_M}{R}$$

$$C(t) \underline{\underline{\Delta}} \frac{a_T\cos\beta_T + \dot{V}_M\sin\beta_M - \dot{V}_T\sin\beta_T}{R}$$

Defining the states as $\theta = x_1$, and $\dot{\theta} = x_2$, the state equations can be written as follows.

$$\dot{x}_1 = x_2, x_1(0) = x_{10} \qquad (8)$$

$$\dot{x}_2 = A(t)x_2 + B(t)u + C(t), x_2(0) = x_{20} \qquad (9)$$

Hence, the problem which needs to be solved is to find a control u such that the capture defined by

$$x_2(t_f) = 0 \qquad (10)$$

is assured while the performance index J

$$J = \frac{1}{2}\int_0^{t_f} u^2 dt \qquad (11)$$

is minimized, which means the control energy expenditure is minimized. It is assumed that $\dot{V}_M$, V_T, $\dot{V}_T$ and a_T are known in this study. Whereas, the capture condition in Eq.(10) shows that the missile is driven on the collision course in the final phase of the engagement; i.e., the missile can go straight to hit the target without any control effort. Thus, such a problem leads to a time-varying linear optimization problem.

III. Optimal Control Solution

The optimization problem formulated in the previous section can be solved by applying the maximum principle[12]. Therefore, we now write the Hamiltonian H for the system in Eq.(8)-(11).

$$H = \frac{1}{2}u^2 + \lambda_1 x_2 + \lambda_2(Ax_2 + Bu + C) \qquad (12)$$

where λ_1 and λ_2 are the adjoint variables. The adjoint variables are defined by the equations

$$\dot{\lambda}_1 = -\frac{\partial H}{\partial x_1} = 0, \qquad (13)$$

$$\dot{\lambda}_2 = -\frac{\partial H}{\partial x_2} = -A\lambda_2 - \lambda_1, (14)$$

while their boundary values are derived from their transversality condition:

$$\lambda_1(t_f) = 0; \qquad (15)$$

$$\lambda_2(t_f) = v; \qquad (16)$$

where v is an unknown constant.

By solving Eq.(13)-(16), we get

$$\lambda_1 = 0 \qquad (17)$$

$$\lambda_2 = ve^{\int_t^{t_f} Adt} \qquad (18)$$

Defining $f(t) \underline{\underline{\Delta}} e^{\int_t^{t_f} Adt} = \frac{R^2}{R_f{}^2}$, we then have

$$\lambda_2 = vf(t) \qquad (19)$$

Next, the control function $\frac{\partial H}{\partial u} = 0$ gives

$$u = -B\lambda_2 \qquad (20)$$

Substituting Eq. (19) into Eq.(20) yields

$$u = -vBf(t) \qquad (21)$$

Thus, Eq.(9) becomes

$$\dot{x}_2 = Ax_2 - vB^2 f(t) + C \qquad (22)$$

Then, solving Eq.(22) yields

$$x_2(t) = \frac{f(0)}{f(t)}\left\{\int_0^t \left[C - vB^2 f(t)\right]\frac{f(t)}{f(0)}dt + x_{20}\right\} \qquad (23)$$

Eq.(23) has to satisfy the capture criterion in Eq.(10); thus, we derive

$$x_2(t_f) = \frac{f(0)}{f(t_f)}\left\{\int_0^{t_f}\left[C - vB^2 f(t)\right]\frac{f(t)}{f(0)}dt + x_{20}\right\} = 0 \qquad (24)$$

After some arrangement, we obtain

$$v = \frac{x_2(0) + \int_0^{t_f} C\frac{f(t)}{f(0)}dt}{\int_0^{t_f} B^2\frac{f(t)^2}{f(0)}dt} \qquad (25)$$

By substituting Eq.(25) into Eq.(21) and changing the variable from 0 to t, we then derive the resulting control law as follows

$$u(t) = \frac{R^3\cos\beta_M\dot{\theta} + R\cos\beta_M\int_t^{t_f} R(a_T\cos\beta_T + \dot{V}_M\sin\beta_M - \dot{V}_T\sin\beta_T)dt}{\int_t^{t_f} R^2\cos^2\beta_M dt}$$

$$(26)$$

The resulting control law has the following interpretation. First, if the constant velocity missile intercepts a non-maneuvering target with the constant velocity, Eq.(26) becomes

$$u(t) = \frac{R^3\cos\beta_M\dot{\theta}}{\int_t^{t_f} R^2\cos^2\beta_M dt} = -K(t)R\ddot{\theta} \qquad (27)$$

where $K(t) \underline{\underline{\Delta}} \frac{-R^3\cos\beta_M}{\dot{R}\int_t^{t_f} R^2\cos^2\beta_M dt}$

Eq.(27) shows that, under such condition, the OPG is nothing but a proportional navigation law with a time-varying navigation gain $K(t)$. Second, while against a maneuvering target, the OPG must make use of the extra information, namely, knowledge of the target maneuver, target velocity variation, target flight direction and missile velocity variation. Obviously, this explicit knowledge enables the missile to maneuver in a more efficient manner.

Moreover, for guidance implementation, the values of the time to go t_{go} and integration parts in Eq.(26) remain to be

determined. First, the time to go t_{go} can be calculated approximately from the following.

$$tgo = t_f - t \cong -\frac{R(t)}{\dot{R}(t)} \qquad (28)$$

However, the standard technique of dividing range by range rate information performs very poorly when both the missile and the target are accelerating. Fortunately, the nearer the missile approaches the target, the more accurate is the value of time to go. Therefore, Eq.(28) can be used as one of the parameters to carry out this guidance scheme. Second, the values of the integration parts in Eq.(26) are for predicting the future trajectory of the target and the missile. These values can be obtained by solving together Eq.(1)-(6), Eq.(26) and Eq.(28) with a numerical method and then, the optimal control law can be implemented.

In order to gain an insight into the characteristics of the OPG, we now simplify Eq. (26). Assuming that V_T and V_M are constant, $\beta_M \cong 0$, $\beta_T \cong 0$, and the relative closing velocity V_C is constant, we then obtain

$$\dot{V}_M = 0 \qquad (29)$$

$$\dot{V}_T = 0 \qquad (30)$$

$$\cos\beta_M \cong 1 \qquad (31)$$

$$\cos\beta_T \cong 1 \qquad (32)$$

$$R = -\dot{R}(t_f - t) = V_C(t_f - t) \qquad (33)$$

Substituting Eq. (29)-(33)into Eq .(26) yields the surprising result as

$$u = \frac{Vc^3(t_f - t)^3 + Vc(t_f - t)\int^{t_f} Vc(t_f - t)a_T dt}{\int^{t_f} Vc^2(t_f - t)^2 dt}\dot{\theta} = 3Vc\dot{\theta} + \frac{3}{2}a_T \qquad (34)$$

In fact, Eq. (34) is the optimal augmented proportional navigation law with the navigation constant of 3. If the target does not execute any maneuver, Eq. (34) becomes

$$u = 3Vc\dot{\theta} \qquad (35)$$

Eq. (35) is the optimal proportional navigation law with the navigation constant of 3. The results are similar to those of studies proposed by Bryson and Zarchan[12][13]. As a result, the optimal augmented proportional navigation law and optimal proportional navigation law are the simplified versions of the OPG.

IV. Simulation Results
1.Simulation scenarios

In order to evaluate the performance of the proposed optimal guidance law encountering the highly maneuverable targets, simulation studies are conducted and presented here for two different engagement scenarios. In Scenario 1, the target flies straight at the beginning of the interception and, 3 seconds later, executes a 9G left turn with a $\dot{V}_T = -0.5G$ longitudinal deceleration and maintains such a maneuver till the end of the interception (see Fig. 2). Here, the missile flies with a $\dot{V}_M = 0.5G$ longitudinal acceleration throughout the engagement. In Scenario 2, the target first initiates a 9G

right turn and, 3 seconds later, takes a sustained 9G left turn till the end of the interception (see Fig. 3). The target has a 0.5G longitudinal deceleration throughout the engagement. Whereas, the missile flies with a 0.5G longitudinal acceleration. Furthermore, in this deterministic study, we assume no lag in the guidance system and all data needed for the implementation of the guidance laws are available without any measurement errors. The remaining simulation data are presented in Table 1.

For the purpose of comparison, the following versions of the true proportional navigation law and the augmented proportional navigation law are employed in the simulation studies:

$$u_{TPN} = -N\dot{R}\dot{\theta} \qquad (30)$$

$$u_{APN} = -N\dot{R}\dot{\theta} + \frac{N}{2}a_T \qquad (31)$$

Here u_{TPN} and u_{APN} denote the commanded accelerations with the TPN and APN, respectively. And, the navigation constant N of 3 has been selected in both schemes. In addition, the maximum normal acceleration of the missile is limited to 30G (1G= $9.8\,m/sec^2$).

2. Simulation results

Fig. 4 and Fig.6 describe the engagement trajectories of the missile and target for Scenario 1 and Scenario 2, respectively. Fig. 5 and Fig. 7 show the commanded acceleration histories of the missile for Scenario 1 and Scenario 2, respectively. Table 2 lists the miss distance and the interception time data considered for the two engagement scenarios. It is seen that the performance of the OPG is superior to that of the other two schemes in terms of the interception time and miss distance

3. Discussions

In Scenario 1, the missile is to attack the target with a hard turn strategy. We observe that the APN and TPN slightly turn the missile heading toward the collision course at the beginning of the interception, and then make a hard turn towards the target in the final phase of the engagement. Fig.5 shows that as the target begins to perform an evasive maneuver, the commanded acceleration of the TPN increases monotonically with time and almost saturates in the end. On the other hand, the OPG quickly drives the missile heading toward the collision course as it senses the target maneuver, thereafter, the missile nearly goes straight to hit the target. Moreover, the OPG ensures a decreasing acceleration demand which almost reduces to zero as the missile approaches the target. As a result, the OPG induces the least miss distance with a minimum interception time among the three schemes.

In Scenario 2, the missile is to intercept a jink-like maneuvering target. Fig. 6 shows that even while dealing with the highly maneuverable targets, the OPG quickly steers the missile heading into the collision course in the final phase of the engagement, thereafter, the geometry is nearly a constant bearing course to intercept the target. In this case, Fig. 7 shows that the required acceleration of the OPG decreases monotonically with time in the final phase of the engagement and approaches zero at the time of the impact. These results justify the capture criterion of the proposed guidance law.

The simulation results show that the TPN requires an increasing acceleration command and almost leads to the saturation in the final phase of the engagement. In a realistic environment, missiles often run out of fuel in the duration and performing such a large normal acceleration is usually not feasible. As a consequence, the TPN may yield a large miss distance. This is the reason why the conventional proportional

navigation law gives poor performance in the presence of target maneuver.

V. Conclusion

In the present study, an optimal guidance problem for a time-varying velocity missile to intercept a maneuvering target with varying velocity, while minimizing the energy cost, has been solved analytically. The resulting optimal control law is expressed as an explicit function of the current and the future behavior of both the missile and target. We also prove that the optimal proportional guidance law and augmented proportional guidance law, where both the navigation constants are 3, are the special cases of the OPG.

The performance of the OPG is demonstrated by two engagement scenarios in which that of the APN and the TPN is also presented for the purpose of comparison. Simulation results show that the OPG gives the best performance among the three schemes both in the interception time and in the miss distance. The study also verifies that using $-\dot{R}/R$ to estimate the value of time to go is acceptable. Besides, the proposed guidance law shows the desirable property of a guidance system wherein, the required missile acceleration decreases monotonically with time.

From a mathematical point of view, the OPG is the promising candidate for the future guidance design. However, for the purpose of guidance implementation, the missile has to necessitate an additional requirement to estimate : a) the forward acceleration of the target, b) the lateral acceleration of the target and c) the value of time to go. Furthermore, the OPG has to be carried out step by step, based on the real time estimation of the target's and the missile's current state and the prediction of their future behavior. This not only demands excessive computational effort but also makes the guidance law more complex. This is the most common disadvantage of all existing optimal guidance laws and remains to be improved in the future.

Reference

(1) Murtaugh, S. A., and Criel, H. E., "Fundamentals of Proportional Navigation", *IEEE Spectrum*, Vol. 3, No. 6, pp.75-85, 1966.

(2) Cottrell, R. G., "Optimal Intercept Guidance for Short Range Tactical Missile", *AIAA Journal*, Vol. 9, pp. 1414-1415, 1971.

(3) Kreindler, E., "Optimality of Proportional Navigation", *AIAA Journal*, Vol.11, pp. 878-880, 1973.

(4) Pastric, H.J., Setlzer, S., and Warren, M. E., "Guidance Laws for Short Range Homing Missiles", *Journal of Guidance , Control, and Dynamics*, Vol. 4, No. 2, pp. 1161-1166, 1989.

(5) Yang, C.D., Yeh, F.B. and Hsiao, F.B., "Generalized Guidance Law for Homing Missiles", *IEEE Transactions on Aerospace and Electronic Systems*. Vol. AES-25, No. 2, pp.197-212, 1989.

(6) Yuan, P.J., and Chern, J.S., "Solution of True Proportional Navigation for Maneuvering and Nonmaneuvering Targets", *Journal of Guidance , Control, and Dynamics*, Vol. 15, No. 1, pp. 268-271, 1992.

(7) Yuan, P.J., and Chern, J.S., "Ideal Proportional Navigation", *Journal of Guidance , Control, and Dynamics*, Vol. 15, No. 5, pp. 1161-1166, 1992.

(8) Gutman, S., "On Optimal Guidance for Homing Missiles", *Journal of Guidance , Control, and Dynamics*, Vol. 2, pp. 296-300, 1979.

(9) Li, Z.Y., and Li, Q.Y., "The Optimal Guidance Law of Air-to-air Missiles Attacking in All-direction", *Acta Aeronautica Et Astronautica Sinica*, Vol.12, No.3, 1991.

(10) Cho, H.J, Ryoo, C.K., and Tahk, M. J., "Closed Form Optimal Guidance Law for Missile of Time-varing Velocity", *Journal of Guidance, Control, and Dynamics*, Vol. 19, No. 5, pp. 1017-1022, 1996.

(11) Guleman, M., and Shina, J., "Optimal Guidance Law in The Plane", *Journal of Guidance, Control, and Dynamics*, Vol. 7, No. 4, pp. 471-476, 1984.

(12) Bryson, A. E., Jr., and Ho, Y., *Applied Optimal Control*, Hemisphere, Washington, DC, 1975.

(13) Zarchan, P., *Tactical and Strategic Missile Guidance*, 2nd ed., AIAA, Washington, DC, Chaps.8, 1994.

Table 1 Simulation data

R	5000 m
θ	0 rad
V_M	$660\,m/s^2$
V_T	$300\,m/s^2$
$\dot{V}_M$	0.5G
$\dot{V}_T$	-0.5G
γ_T	Scenario 1 : 1.047rad Scenario 2 :: 2.62rad
γ_M	Scenario 1 : 0.8rad Scenario 2 : 0.77rad

Table 2 Simulation results

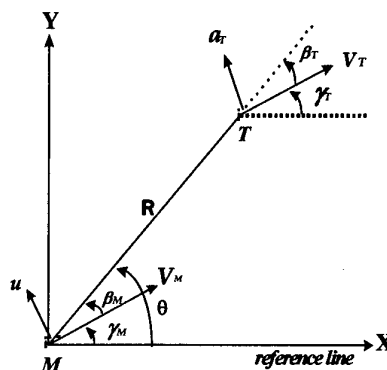| Scenario	Performance	TPN	APN	OPG
1	Miss distance(m)	2.91	0.73	0.25
	Interception time(sec)	8.40	8.40	8.12
2	Miss distance(m)	4.15	0.80	0.32
	Interception time(sec)	6.49	6.55	6.38

Fig 1. Intercept geometry

1E7 Rocket Trajectory Tracking Guidance Using Adaptive Predictive Control

Joosang Eom* and Youdan Kim**

Seoul National University, Seoul 151-742, Korea

Key Words: Guidance, Predictive Control, Adaptive Control, Trajectory Tracking

ABSTRACT

A new control law is presented to make the rocket follow the nominal trajectory. The predictive control law is used, and the linear time varying system is adopted as the predictive model. To deal with the varying of the flight environment, an adaptive predictive model is introduced, and the convergence analysis for the adaptive law is performed. The proposed adaptive predictive control law is applied to Korea Sounding Rocket III, especially for the pitch program. External disturbances and the internal uncertainties such as the wind effects, model uncertainties and thrust error are considered. To show the effectiveness of the proposed guidance law, numerical simulation is performed.

1. INTRODUCTION

In the real rocket flight, a rocket trajectory usually deviates from the pre-determined reference trajectory mainly due to the disturbances, model uncertainties, and thrust error. This will deteriorate the overall performance of the rocket system. Therefore, the control system that compensates tracking error is required.

In this paper, an adaptive tracking control law is proposed using predictive control method. The predictive control method is usually implemented in a discrete form, but the proposed control law is based on the continuous system. The predictive model is designed to apply the predictive control method to trajectory tracking problem. The predictive model should estimate the values of future state variables. That is very critical in the predictive control. In this paper, the linear time varying system is adopted as the predictive model, and is adapted to a real rocket states. During the rocket flight, the flight environment varies rapidly. The nominal system can be adopted as a predictive model, however, the nominal system cannot reflect the environment change well. To cope with the varying of the flight environment, an adaptive predictive model is introduced. The convergence analysis for the adaptive law is also shown.

The proposed adaptive predictive control law is applied to Korea Sounding Rocket (KSR) III.[1] The reference trajectory is designed by using a pitch program. In the numerical simulation,

the wind effects, model uncertainties and thrust error are considered. The simulation results show that the proposed guidance law is effective in the rapid environment change.

2. LAUNCH VEHICLE SYSTEM

In this paper, two different rocket systems are used. To design the nominal trajectory as well as the guidance law, a point-mass rocket system is used. And to evaluate the designed guidance system, the attitude dynamics including the rigid body motion and the flexible motion is considered. Liquid fuel sloshing effects and the engine moment of inertia effects are also considered.

For the point mass system, the launch vehicle is modeled as a point mass flying over a spherical nonrotating Earth. Motion is confined to a two-dimensional plane as shown in Fig.1.
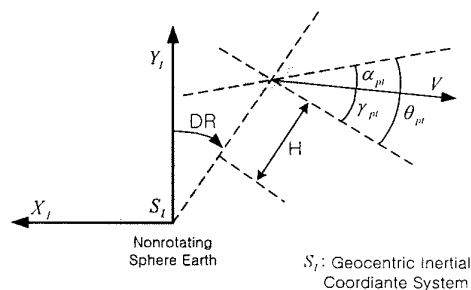

Fig.1 Coordinate system of point-mass model

The obtained equations of motion are as follows[2]:

$$m_T \dot{V} = T\cos\alpha_{pt} - D - m_T g \sin\gamma_{pt} + \Delta \tag{1}$$

$$m_T\left(\dot{\gamma}_{pt} - \frac{V}{R_m + H}\cos\gamma_{pt}\right) = T\sin\alpha_{pt} + L - m_T g\cos\gamma_{pt} + \Delta \tag{2}$$

$$\dot{H} = V\sin\gamma_{pt} \tag{3}$$

$$\frac{d}{dt}(DR) = \frac{R_m}{R_m + H}V\cos\gamma_{pt} \tag{4}$$

where T is thrust, Δ is external disturbance, and L and D are lift force and drag force, respectively, defined as

$$D = \frac{1}{2}\rho V^2 A_{ref} C_D(n_{mach}) \tag{5}$$

$$L = \frac{1}{2}\rho V^2 A_{ref} C_{L_\alpha}(n_{mach})\alpha \tag{6}$$

with $n_{mach} = V / c$. Note that the relative velocity of the launch vehicle with respect to the wind is considered.

3. DESIGN OF NOMINAL TRAJECTORY

Most launch vehicles are launched vertically and shortly after liftoff, a programmed initial pitch maneuver begins. For the atmospheric region of high dynamic pressure, the steering program is chosen to fly with a near zero angle of attack to reduce bending moments caused by aerodynamic loads. When the launch vehicle is flying in the exo-atmospheric region, the controlled injection maneuver and optimized closed-loop guidance are performed. Taking account of these constraints, during the flight of the first stage, the angle of attack is held to be zero. Shortly after liftoff, when the velocity is low, kick turn maneuver (a small programmed turn downrange at a very low pitch rate) begins. Then, a gravity turn with zero angle of attack and zero lift is performed until the launch vehicle is out of the sensible atmosphere. The gravity turn is a maneuver in which thrust vectoring is used to keep the velocity vector aligned with the body fixed axes and the vertical component of gravity is used to rotate the launch vehicle slowly about its center of gravity. The pitch program sequence is summarized in Table 1.[3]

Table 1 Pitch program sequence

Event	Time[sec]	Remarks
Vertical Liftoff	0-3	$q_{pt} = 0$ ($\theta_{pt} = 90$ at $t = 0$)
Kick Turn	3-12	$q_{pt} = -0.6$
	12-t_g	$q_{pt} = 0$ $\theta_{pt} = \gamma_{pt}$ (at t_g)
Gravity Turn	t_g-59	$\theta_{pt} = \gamma_{pt}$

Figures 2 and 3 shows the simulation results performed by pitch program. 1976 standard atmospheric model is used. Figure 2 shows the designed nominal trajectory that the rocket should follow. As shown in Fig. 3, the gravity turn begins at $t_g = 14.2$ sec.
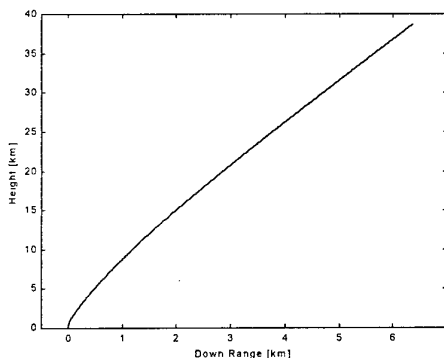

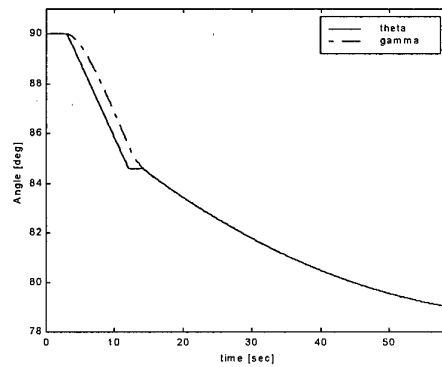Figure 2 Designed nominal trajectory

Figure 3 Pitch angle and flight path angle (nominal trajectory)
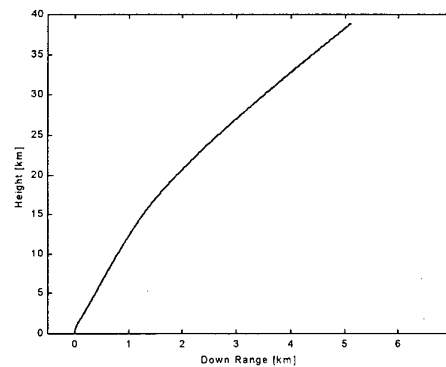

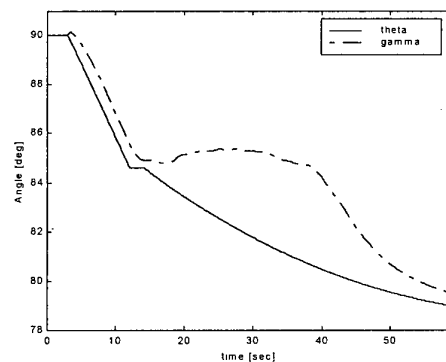Figure 4 Launch vehicle trajectory (with wind effects)

Figure 5 Pitch angle and flight path angle (with wind effects)

Figures 4 and 5 shows the trajectory, pitch angle and flight path angle histories, respectively, when the external wind disturbance is considered. Figure 4 shows that the pitch angle of the launch vehicle follows the nominal pitch angle history by the pre-programmed pitch maneuver. However, the flight path angle

deviates from the desired values due to the wind effects, therefore the real flight trajectory does not follow the nominal trajectory. Note from Figures 5 that the angle of attack is not zero during the gravity turn phase. This may produce bending moments and result in the catastrophic failure of the launch vehicle structure. To avoid this, the launch vehicle guidance system is required.

4. GUIDANCE SYSTEM DESIGN

In this study, the predictive control system is used to design the launch vehicle guidance system. Usually, the performance of the predictive control law is dependent on the prediction of state variables in future. Therefore, it is required a good predictive model that will be used as nominal system in the predictive control system. However, the nominal system may not be relevant to the estimation of the state variables because of system uncertainties and disturbances. In this study, the time-varying system is designed for the predictive model.[4] And to obtain more reliability, the adaptive scheme is adopted to the time-varying model. The computing process of the guidance command can be simplified by using the adaptive predictive model.

Predictive model
The predictive model considered in this study is as follows:
$$\dot{x} = A(t)x + B(t)u \tag{7}$$
where
$$x = [V, \gamma_{pt}]^T, \quad u = \alpha_{pt}$$

Since the uncertainty terms are included in the kinetic parts, system matrices in Eq. (7) cannot be determined precisely. Therefore, the estimation process of the system matrices is needed. To estimate the state variables, the following series-parallel model is used.[5]
$$\dot{\hat{x}} = A_m(t)\hat{x} + (\hat{A}(t) - A_m(t))x + \hat{B}(t)u \tag{8}$$
where $\hat{x} = [\hat{V}, \hat{\gamma}_{pt}]^T$, $\hat{A}(t)$ and $\hat{B}(t)$ are the system matrix estimates, respectively.

Adaptive law
Let us introduce the error states and matrix estimate errors as follows
$$e = x - \hat{x}, \quad \tilde{A}(t) = \hat{A}(t) - A(t), \quad \tilde{B}(t) = \hat{B}(t) - B(t) \tag{9}$$
Then, the error dynamics can be obtained by using Eqs. (7) and (8) as follows:
$$\dot{e} = A_m(t)e - \tilde{A}(t)x - \tilde{B}(t)u \tag{10}$$
In this study, the following adaptation rule is used to update the system matrices.[5]

$$\dot{\hat{A}}(t) = Pex^T \tag{11}$$

$$\dot{\hat{B}} = Peu^T \tag{12}$$

where

$$A_m^T(t)P + PA_m(t) = -Q \tag{13}$$

Assuming slow varying systems, the convergence of the time-varying adaptive system can be proved by using the following Lyapunov function.
$$V = e^T Pe + tr(\tilde{A}^T \tilde{A}) + tr(\tilde{B}^T \tilde{B}) \tag{14}$$
Differentiating the above equation with respect to time yields
$$\dot{V} = \dot{e}^T Pe + e^T P\dot{e} + tr(\dot{\tilde{A}}^T \tilde{A} + \tilde{A}^T \dot{\tilde{A}}) + tr(\dot{\tilde{B}}^T \tilde{B} + \tilde{B}^T \dot{\tilde{B}})$$
$$= -e^T Qe - 2tr(\tilde{A}^T \dot{A}) - 2tr(\tilde{B}^T \dot{B}) \tag{15}$$
As seen in Eq. (15), for the slow varying system, the convergence of $\hat{x}$ to x is guaranteed.

Predictive control law
Now, the guidance command is computed based on the predictive adaptive model.[6] The equations of motion have been normalized, and the normalized predictive model is obtained as
$$\dot{x}_{n1} = A_n(t)x_{n1} + B_n(t)u$$
$$\dot{x}_{n2} = f_n(x_n) \tag{16}$$
where, $x_{n1} = [V/V_f, \gamma/\gamma_{ptf}]^T$, $x_{n2} = [H/H_f, DR/DR_f]^T$, and $x_n = [x_{n1}^T, x_{n2}^T]^T$. Taylor series expansion is used to estimate the state variables as follows:

$$x_{n1}(t+h) = x_{n1}(t) + h(A_n(t)x_{n1} + B_n(t)u)$$
$$x_{n2}(t+h) = x_{n2}(t) + hf_n(x)$$
$$+ \frac{1}{2}h^2\left(\frac{\partial f_n(x)}{\partial x_{n1}}(A_n(t)x_{n1} + B_n(t)u) + \frac{\partial f_n(x)}{\partial x_{n2}}f_n(x)\right) \tag{17}$$

where h is the step size. To make the current state variables track the predictive model variables, a following performance index is adopted.

$$J = \frac{1}{2}(x_{1n}(t+h) - x_{1n}^*(t+h))^T Q(x_{n1}(t+h) - x_{n1}^*(t+h))$$
$$+ \frac{1}{2}(x_{2n}(t+h) - x_{2n}^*(t+h))^T Q(x_{n2}(t+h) - x_{n2}^*(t+h))$$
$$+ \frac{1}{2}(u(t) - u^*(t))^2$$
$$\tag{18}$$

The first and second terms are introduced for good tracking performance, and the third term is used for less control efforts. By applying optimality condition, the guidance law is obtained as follows:

$$u(t) = \left(1 + q_{n1} + q_{n2}\right)^{-1}$$
$$\times \left[u^*(t) - e_{n1}'^{\,T} QhB_n(t) - e_{n2}'^{\,T} Q \times \frac{1}{2}h^2 \frac{\partial f_n(x)}{\partial x_{n1}} B_n(t) \right] \quad (19)$$

where

$$q_{n1} = \left(hB_n(t)\right)^T Q\left(hB_n(t)\right)$$

$$q_{n2} = \left(\frac{1}{2}h^2 \frac{\partial f_n(x)}{\partial x_{n1}} B_n(t)\right)^T Q\left(\frac{1}{2}h^2 \frac{\partial f_n(x)}{\partial x_{n1}} B_n(t)\right)$$

$$e_{n1}' = x_{n1} + hA_n(t)x_{n1} - x_{n1}^{\,*}$$

$$e_{n2}' = x_{n2}(t) + hf_n(x) + \frac{1}{2}h^2 \frac{\partial f_n(x)}{\partial x_{n1}} A_n(t)$$
$$+ \frac{1}{2}h^2 \frac{\partial f_n(x)}{\partial x_{n2}} f_n(x) - x_{n2}^{\,*}(t+h)$$

5. NUMERICAL SIMULATION

In this study, the proposed guidance law is applied to the KSR III Rocket.[6]. Figures 6 show the launch vehicle trajectory and flight path angle using the closed-loop guidance law under the wind disturbance.
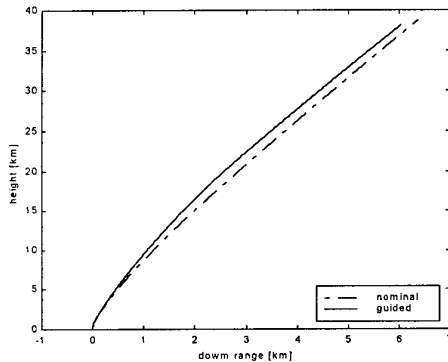
(a) Launch vehicle trajectory
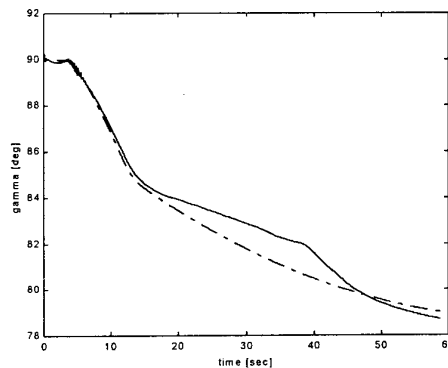
(b) Flight path angle

Figure 6 Time histories using predictive adaptive guidance law
(dotted line: nominal, solid line: guided)

Comparison of Fig. 4 and Fig. 6(a) shows that the performance of the guided (closed-loop) trajectory using adaptive predictive control law is better than the open-loop pitch maneuver. In Fig.6(b) nominal flight path angle and guided flight path angle are shown. Comparison of Fig. 5 and Fig. 6(b) shows that the difference between the nominal flight path angle and the guided flight path angle is reduced. Also, the magnitude of angle of attack was less than the proscribed values.

6. CONCLUSIONS

In this paper, a new control law is proposed for rocket trajectory tracking guidance system. An adaptive predictive control law is used to compensate for the wind effects. The proposed guidance law makes the rocket follow the nominal trajectory. In the numerical simulation, the wind effects, model uncertainties and thrust error are considered. Numerical simulations show that the proposed guidance law exhibits better performance than the open-loop pre-programmed maneuver.

ACKNOWLEDGEMENT

REFERENCES

1. Final Report, Research and Development of KSR-III (II), Korea Aerospace Research Institute, 1999.
2. Greensite, A.L., Analysis and Design of Space Vehicle Flight Control Systems, Spartan Books, New York, 1970.
3. Cho, H., A Study on the Rocket Autopilot Design Using Neural Network, MS Thesis, Dept. of Aerospace Engineering, Seoul National University, Feb. 2000.
4. Sanchez, J.M.M., and Rodellar, J., Adaptive Predictive Control : from the Concepts to Plant Optimization, Prentice Hall, New York, 1996, pp23-65.
5. Ioannou, P.A., and Sun, J., Robust Adaptive Control, Prentice Hall, New Jersey, 1996.
6. Lu, P., "Nonlinear Trajectory Tracking Guidance with Application to a Launch Vehicle", Journal of Guidance, Control, Dynamics, Vol.19, No.1, 1996, pp.99-106.

1E8 NONLINEAR FLIGHT NEURO-CONTROLLER DESIGN USING SLIDING MODE BASED NEURAL NETWORK

Dongho Shin*, Youdan Kim** and Dohyun Kim***

* Department of Aerospace Engineering, Seoul National University, Seoul 151-742, Korea
** Department of Aerospace Engineering, Seoul National University, Seoul 151-742, Korea
*** Department of Automobile Engineering, Woosuk University, Chonbuk 565-701, Korea

Key Words: Sliding Mode, Neural Network, Lyapunov, Aircraft Dynamics

ABSTRACT

Neural networks based adaptive controller is designed for nonlinear aircraft system. Neural networks controller is used to implement feedback linearization control law. And sliding mode control design methodology is adopted to suppress the approximation error of nonlinear function and guarantee the robustness to uncertainties. The proposed controller guarantees the global stability of the resulting closed loop system and the tracking objective is achieved asymptotically. The effectiveness of the proposed method has been verified using an example of aircraft pitch rate tracking problem.

1. INTRODUCTION

Modern aircraft dynamics is highly nonlinear at high angle of attack and at high angular rates. Therefore researches on nonlinear controllers that provide superior closed-loop performance to the linear controller designed at a various operating region have been widely performed during a past few decades. However, most of nonlinear controllers require an accurate analytic aircraft dynamics that is hard to obtain because aerodynamic and thrust coefficients in aircraft model are highly nonlinear. Neural network is an attractive alternative for the identification and control of unknown dynamic systems because it has a good property of representing complex nonlinear function, which is known as universal approximation. [1]

Recently, the neural network based control of nonlinear aircraft through inverse dynamics has received much attention, [2-4], which is based on the off-line training of neural network using back-propagation algorithm or modified back-propagation algorithm through mathematical dynamic model and experimental data. The off-line trained neural controller cannot yield consistent performances when there exist aerodynamic coefficient variations and/or unpredictable uncertainties. Several papers on adaptive neural network based controller design to cope with various uncertainties are reported. [5-6] They provided the stable controllers for a class of nonlinear systems based on

feedback linearization technique on the assumption that the absolute first derivative value of nonlinear input function is bounded by a known positive constant to make the control input bounded. Yesidirek and Lewis introduced sliding mode term for the same objective [7], but the proposed control strategy became very complicated. In this paper, the adaptive neural controller is proposed by combining neural networks with sliding mode control technique. Neural network approximates the nonlinear functions in the feedback linearization controller. Sliding mode variable is introduced in the feedback linearization controller to compensate for the approximation error and guarantee the robustness with respective to the uncertainties by adjusting the gain of sliding mode variable adaptively.

This paper is organized as follows: Section II deals with the basic concepts and preliminaries for neural networks. Section III describes the problem statements, and in sec. IV we present an adaptive control law based on neural network. In sec.V, numerical simulation is performed to show the feasibility and performance of the proposed design method are presented and discussed.

2. PRELIMINARIES

In this study, Neural networks (NN) with a three-layer network structure is used for approximating nonlinear continuous functions. Let $h(x):R^{N_1+1} \to R$ be a smooth function. The following three-layers NN is used to represent $h(x)$.

$$h(x) = W^T \vec{\sigma}(V^T x) \qquad (1)$$

where $W = [w_1, w_2, \cdots, w_{N_1}]^T \in R^{N_1}$ is a weight vector between hidden layer and output layer, $V = [v_1, v_2, \cdots, v_{N_1}] \in R^{(N_1+1) \times N_2}$ is a weight matrix between input layer and hidden layer, $x = [x_1, x_2, \cdots, x_{N_1}, 1]^T \in R^{N_1+1}$, and $\vec{\sigma}(z) = [\sigma(z_1), \sigma(z_2), \cdots, \sigma(z_{N_1})]^T$ with $\sigma(z) = \tanh(z)$.

It is well known that the neural network can approximate any continuous functions to any desired accuracy over a compact set. Therefore there exist W^* and V^* such that

$$h(x) = W^{*T} \vec{\sigma}(V^{*T} x) + \mu_h \text{ and } |\mu_h| \le \mu_{0h} \text{ with constant } \mu_{0h} > 0.$$

* Ph.D Student, Department of Aerospace Engineering
** Associate Professor, Department of Aerospace Engineering
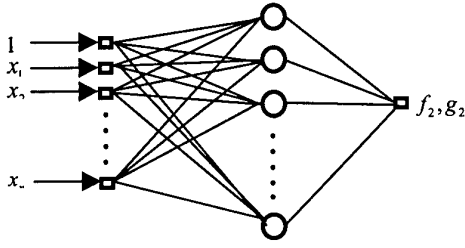*** Assistant Professor, Department of Automobile Engineering

Fig.1 Neural network structure

Fig. 2 The neural network controller scheme

Lemma 1 [8] For neural network approximator (1), the NN estimation error can be expressed as

$$W^{*T}\bar{\sigma}(V^{*T}x) - \hat{W}^T\bar{\sigma}(\hat{V}^Tx) = \tilde{W}^T(\hat{\bar{\sigma}} - \hat{\bar{\sigma}}'\hat{V}^Tx) + \hat{W}^T\hat{\bar{\sigma}}'\tilde{V}^Tx + d_h$$

(2)

where $\hat{W}$ and $\hat{V}$ are the estimates of W^* and V^*, $\tilde{W} = W^* - \hat{W}$, $\hat{\bar{\sigma}} = \bar{\sigma}(\hat{V}^Tx)$ $\tilde{V} = V^* - \hat{V}$, , $d_h = W^{*T}\bar{\sigma}(V^{*T}x) - W^{*T}(\hat{\bar{\sigma}} - \hat{\bar{\sigma}}'\hat{V}^Tx)$ $-\hat{W}^T\hat{\bar{\sigma}}'V^{*T}x$, and $\hat{\bar{\sigma}}' = d\bar{\sigma}(z)/dz\big|_{z=\hat{v}^Tx}$

And the residual term $d_h + \mu_h$ is bounded by

$$|d_h| + |\mu_h| \leq [\|W^*\|_1 + \mu_{0h}, \|W^*\|, \|V^*\|_F] \begin{bmatrix} 1 \\ \|\hat{\bar{\sigma}} - \hat{\bar{\sigma}}'\hat{V}^Tx\| \\ \|x\hat{W}^T\hat{\bar{\sigma}}'\|_F \end{bmatrix} \equiv K_h^{*T}\varphi_h$$

(3)

3. PROBLEM STATEMENT

Let us consider the following longitudinal aircraft dynamic system, which is simplified by neglecting the effect of the gravity. [9]

$$\dot{\alpha} = Z_{\alpha0} + Z_\alpha\alpha + (Z_q + 1)q + Z_{\delta e}\delta e$$
$$\dot{q} = M_{\alpha0} + M_\alpha\alpha + M_q q + M_{\delta e}\delta e$$

(4)

where $M_{\alpha0}$ and $Z_{\alpha0}$ are the aerodynamic moment and force coefficients at zero angle of attack, respectively, α is the angle of attack, q is the pitch rate, and δe is elevator deflection. The coefficients $Z_\alpha, Z_q, Z_{\delta e}, M_\alpha, M_q$ and $M_{\delta e}$ are nonlinear functions of angle of attack.

Let the dynamic equation (4) be rearranged as follows to make it convenient to derive adaptive neural control law.

$$\dot{\alpha} = f_1(\alpha, q) + g_1(\alpha)\delta e$$
$$\dot{q} = f_2(\alpha, q) + g_2(\alpha)\delta e$$

(5)

In this study, the control objective is to obtain control law and an updating law of the controller parameters to make pitch rate follow the given desired pitch rate trajectory,
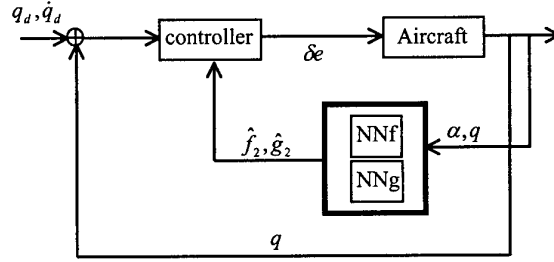
i.e., $\lim_{t\to\infty}|q(t) - q_d(t)| \leq \varepsilon$ for some specific constant $\varepsilon > 0$. It is assumed that all of the state values, $q_d(t)$ and $\dot{q}_d(t)$ are available.

4. ADAPTIVE NEURAL CONTROLLER DESIGN

Define the state error as $e = q - q_d$. Then, error dynamics can be written as

$$\dot{e} = f_2(\alpha, q) + g_2(\alpha)\delta e - \dot{q}_d$$

(6)

The proposed control law based on feedback linearization method is defined as follows:

$$\delta e = \hat{g}_2^{-1}\{-\hat{f}_2 + \dot{q}_d - \rho\,\text{sgn}(e) - K_e e\}$$

(7)

where the estimated nonlinear functions $\hat{f}_2$ and $\hat{g}_2$ are approximated by neural networks (1), sgn($\bullet$) is a sign function, ρ is a switching gain and K_e is a positive constant gain.

By substituting Eq.(7) into Eq.(6), we have the closed loop error dynamics as follows:

$$\dot{e} = f_2 + g_2\hat{g}_2^{-1}\{-\hat{f}_2 + \dot{q}_d - \rho\,\text{sgn}(e) - K_e e\} - \dot{q}_d$$
$$= f_2 + \{g_2 + \hat{g}_2 - \hat{g}_2\}\hat{g}_2^{-1}\{-\hat{f}_2 + \dot{q}_d - \rho\,\text{sgn}(e) - K_e e\} - \dot{q}_d$$
$$= (f_2 - \hat{f}_2) + (g_2 - \hat{g}_2)\delta e - \rho\,\text{sgn}(e) - K_e e$$

(8)

$$= (f_2 - f_2^*) + (f_2^* - \hat{f}_2) + (g_2 - g_2^*)\delta e + (g_2^* - \hat{g}_2)\delta e$$
$$- \rho\,\text{sgn}(e) - K_e e$$

where

$$f_2 = f_2^* + \mu_f = W_f^{*T}\bar{\sigma}(V_f^{*T}x_f) + \mu_f$$

(9)

$$g_2 = g_2^* + \mu_g = W_g^{*T}\bar{\sigma}(V_g^{*T}x_g) + \mu_g$$

(10)

$$\hat{f}_2 = \hat{W}_f^T\bar{\sigma}(\hat{V}_f^Tx_f) , \hat{g}_2 = \hat{W}_g^T\bar{\sigma}(\hat{V}_g^Tx_g)$$

(11)

and μ_f and μ_g are approximation errors of f_2 and g_2, respectively, $x_f = [1, \alpha, q]^T$ and $x_g = [1, \alpha]^T$.

Neural network weights $\hat{W}_f, \hat{W}_g, \hat{V}_f$ and $\hat{V}_g$ are updated by the following adaptation rule.

$$\dot{\hat{W}}_f = \Gamma_{wf}(\hat{\sigma}_f - \hat{\sigma}_f{}'\hat{V}_f{}^T x_f)e^T$$

$$\dot{\hat{W}}_g = \Gamma_{wg}(\hat{\sigma}_g - \hat{\sigma}_g{}'\hat{V}_g{}^T x_g)\delta e \cdot e^T$$

$$\dot{\hat{V}}_f = \Gamma_{vf} x_f e^T \hat{W}_f{}^T \hat{\sigma}_f{}' \qquad (12)$$

$$\dot{\hat{V}}_g = \Gamma_{vg} x_g e^T \hat{W}_g{}^T \hat{\sigma}_g{}' \delta e$$

where $\Gamma_{wf}, \Gamma_{wg}, \Gamma_{vf}$ and Γ_{vg} are positive definite weight matrices with appropriate dimension.

According to the sliding mode control, it is required to assign the switching gain ρ to the appropriate value in order to compensate for the effect of neural network approximation errors of nonlinear functions f_2 and g_2. However the bounds of these approximation errors are usually unknown. Therefore, it is necessary to estimate the bounds. Using Eq.(3) of Lemma 1, the switching gain ρ can be set as follows.

$$\rho = \hat{K}_f{}^T \varphi_f + \hat{K}_g{}^T \varphi_g |\delta e| \qquad (13)$$

where the $\hat{K}_f$ and $\hat{K}_g$ are updated by the following adaptation rules.

$$\dot{\hat{K}}_f = \Gamma_{fk}\varphi_f|e| \ , \ \dot{\hat{K}}_g = \Gamma_{gk}\varphi_g|e||\delta e| \qquad (14)$$

Now, the following main result of this paper can be summarized.

Theorem 1 Consider the aircraft dynamic system given by Eq.(5). Let the neural network weight be provided by Eq.(12) and the switching gain ρ be given by Eqs.(13) and (14). Then, the control law (7) makes the tracking error converge to zero asymptotically. In addition, all of the signals in the closed loop system are bounded.

Proof) Let us take the Lyapunov function candidate as

$$V = \frac{1}{2}e^2 + \frac{1}{2}\{\tilde{W}_f{}^T \Gamma_{fw}{}^{-1}\tilde{W}_f + \tilde{W}_g{}^T \Gamma_{gw}{}^{-1}\tilde{W}_g + tr(\tilde{V}_f{}^T \Gamma_{fv}{}^{-1}\tilde{V}_f)\}$$
$$+ \frac{1}{2}tr(\tilde{V}_g{}^T \Gamma_{gv}{}^{-1}\tilde{V}_g) + \frac{1}{2}\{\tilde{K}_f{}^T \Gamma_{fk}{}^{-1}\tilde{K}_f + \tilde{K}_g{}^T \Gamma_{gk}{}^{-1}\tilde{K}_g\} \qquad (15)$$

Substituted Eq.(2) into the time derivative of V evaluated along the trajectories of system (8)-(14), and noting that $tr[yx^T] = x^T y$, the time derivative of V can be expressed as

$$\dot{V} = e(\mu_f + d_f) + e(\mu_g + d_g)\delta e + \tilde{K}_f{}^T \Gamma_{fk}{}^{-1}\dot{\tilde{K}}_f + \tilde{K}_g{}^T \Gamma_{gk}{}^{-1}\dot{\tilde{K}}_g$$
$$- e\rho \,\text{sgn}(e) - K_e e^2$$

Therefore, we have

$$\dot{V} \le |e|(|\mu_f| + |d_f|) + |e|(|\mu_g| + |d_g|)|\delta e| + \tilde{K}_f{}^T \Gamma_{fk}{}^{-1}\dot{\tilde{K}}_f$$
$$+ \tilde{K}_g{}^T \Gamma_{gk}{}^{-1}\dot{\tilde{K}}_g - e\rho \,\text{sgn}(e) - K_e e^2$$

Taking account of the Eqs (3),(13) and (14), the upper bound of the time derivative of V can be obtained as

$$\dot{V} \le -K_e e^2 \qquad (16)$$

Thus, if Eqs.(15) and (16) hold and the initial values of weights, tracking error and gain parameters are bounded, then $\hat{W}_f, \hat{V}_f, \hat{W}_g, \hat{V}_g, \ \hat{K}_f, \hat{K}_g$ and $e \in L^\infty$.

Note that $\int_0^\infty e^2 dt < \infty$ and $0 \le V(t) \le V(0)$, $\forall t > 0$, therefore, we can say that $e \in L^2$.

From Eqs.(7) and (8) the control input is bounded and $\dot{e} \in L^\infty$. Now, because $\dot{e} \in L^\infty$ and $e \in L^2 \cap L^\infty$, it can be shown from Barbalat's lemma that $e \to 0$ as $t \to 0$, which means that the tracking error converges to zero asymptotically. **Q.E.D.**

5. SIMULATION

In this study, the proposed adaptive neural network control law is applied to the longitudinal aircraft dynamic system at Mach NO. 0.5 and altitude 5km. Table 1 gives the aerodynamic and force moments in the form of look up tables. [9] The stability derivative M_α, which is the measure of pitch axis static stability, has the positive sign when the aircraft becomes statically unstable. The table shows that the aircraft becomes statically unstable in the region of $9.0°$ to $14.5°$ of angle of attack.

Table 1 Variation of Aerodynamic Coefficients

Angle of attack (deg)	M_α 1/sec²	M_q 1/sec	Z_q	Z_α 1/sec	$M_{\delta e}$ 1/sec²	$Z_{\delta e}$ 1/sec
5.289	-0.571	-0.869	0.029	-0.600	-13.07	-0.309
0.800	-0.603	-0.869	0.029	-0.674	-13.11	-0.311
6.960	-0.631	-0.869	0.029	-0.789	-13.27	-0.320
9.004	-0.774	-0.869	0.029	-0.871	-13.33	-0.327
9.970	0.453	-0.869	0.029	-0.860	-13.38	-0.331
11.790	2.256	-0.869	0.029	-0.820	-13.02	-0.326
13.639	1.113	-0.869	0.028	-0.811	-12.32	-0.312
14.588	-0.190	-0.869	0.028	-0.804	-12.37	-0.310
16.577	-2.562	-0.869	0.028	-0.803	-12.25	-0.313
21.489	-5.926	-0.869	0.028	-0.841	-11.56	-0.325

To obtain numerical results, we choose the following simulation parameters:

$$\Gamma_{fw} = \Gamma_{fv} = \Gamma_{gw} = \Gamma_{gv} = 10 , \ \Gamma_{fk} = \Gamma_{gk} = 0.01 , K_e = 5$$

The eight hidden neurons are used to approximate the nonlinear functions f_2, g_2. We approximate the sign function by a saturation function with boundary layer thickness 0.01 usually used to avoid the chattering phenomenon. The initial weight matrices elements of neural network representing function f_2 are taken randomly in the interval [-0.001,0.001] and the elements of $\hat{W}_g(0)$ and $\hat{V}_g(0)$ are chosen randomly in the region of –2 to 2. To prevent the parameter drift phenomenon, during simulation, if the tracking error is less than specified value, the weight matrices and the switching gain parameters are not

updated.

It can be seen from figure 3 that the pitch rate tracks the desired reference trajectory asymptotically. The control input, elevator deflection shown in figure 4 remains in the reasonable scope.

6. CONCLUSIONS

An adaptive control law using sliding mode based neural network has been presented. A stable controller parameter adjustment scheme is derived using Lyapunov stability theory. To cope with neural network approximation errors, the sliding mode term is introduced. To show the effectiveness of the proposed control law, Numerical simulation was executed for nonlinear aircraft model. The future work will be directed to control the angle of attack using neural network through the reasonable elevator deflection.
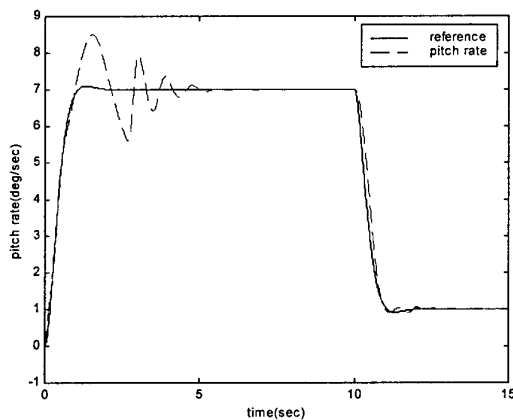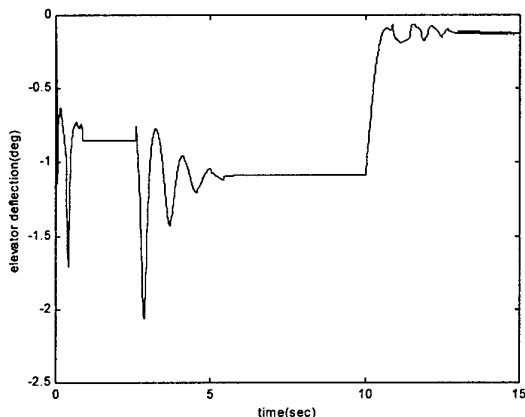
REFERENCE

1.Hornik, K., Stinchcombe, M., and White, H., "Multilayer Feedforward Networks are Universal Approximators," Neural Networks, Vol.2, No.5, pp. 359-366, 1989.
2.Adams, R. J., Buffington, J.M., and Banda, S.S., "Design of Nonlinear Control Laws for High-Angle-of-Attack Flight," Journal of Guidance, Control, and Dynamics, Vol.17, No.4, pp.737-746, 1994.
3.Zhiqang, Z., "Nonlinear Decoupling Control of Aircraft Motion," Journal of Guidance, Control, and Dynamics, Vol.8, No.4, pp.812-816, 1995.
4.Reiner, J., Balas, G.J., and Garrard, W.L., "Flight Control Design Using Robust Dynamic Inversion and Time- Scale Separation," Automatica, Vol.32, No.11, pp.1493-1504, 1996.
5.Spooner, J.T. and Passino, K.M., "stable adaptive control using Fuzzy System and Neural Networks," IEEE Transactions on Fuzzy Systems, Vol.4, No.3, pp.339-359, 1992.
6.Sanner, R.M. and Slotine, J.E., "Gaussian Networks for Direct Adaptive Control," IEEE Transactions on Neural Networks, Vol.3, No.6, pp.837-863, 1992.
7.Yesidirek, A. and Lewis, F.L., "Feedback Linearization using Neural Networks," Automatica, Vol.31, No.11, pp.1659-1664, 1995.
8.Ge, S.S., Hang, C.C., and Zhang, T., "A Direct Approach to Adaptive Controller Design and Its Application to Inverted Pendulum Tracking," Proceedings of the American Control Conference, Philadelphia, Pennsylvania, pp.1043-1047, 1998.
9.Somakumar, R. and Chandrasekhar, J. "Neural Network Based Nonlinear Inverse Dynamics for Flight Controller Design," Proceedings of the 1998 IEEE International Conference on Control Applications, Trieste, Italy, pp.187-191, 1998.

Fig.3 NNs output – pitch rate

Fig.4 Elevator deflection

1E9　Threshold Setting and Failure Monitoring in Multi-Lane Aircraft Control Surface Actuators

DR. FAWAZ Y. ANNAZ

MECHANICAL ENGINEERING LABORATORY,
BIOMIMETICS DIVISION, NAMIKI 1-2, TSUKUBA, IBARAKI, 305-8564 JAPAN. EMAIL: MV260@MEL.GO.JP

KEY WORDS: Multi-Lane Actuator, Motor Failures, Zero Aerodynamic Load Angles, Force Fight

1. ABSTRACT

The essential requirements to realise high integrity in safety critical systems are hardware redundancy and intelligent monitoring. Earlier studies suggest that motor failures (in multi-lane actuators) resulted in the largest failure transient envelopes (when compared to RVDTs or Tachometers failures) causing large aircraft roll disturbances. The study here is based around a four-lane (torque summed) electric actuation system, capable of driving aerodynamic and inertial loads of an aircraft aileron control surface, with 2 lanes failed. Each lane contains its own dedicated microprocessor/s to perform control and comprehensive monitoring tasks. An aircraft model of a relatively small combat aircraft, similar to that of the Sea Harrier, will be utilized to examine the aircraft performance.

The aim of this paper is to present a Simulation-Graphical based Monte Carlo, SGMC, method as a threshold setting technique. Its advantages over other possible techniques, such as, Decision Theory, Analysis of Variance or a Purely Numerical Monte Carlo will be highlighted. A general methodology of this method to multi-lane safety critical redundant systems (with particular emphasis on the 4-lane actuator) will be derived. Schedule and unscheduled threshold setting concepts to a multi-mode combat aircraft system will also be presented.

To account for Torque Ripple Effects and hence any associated inherent lane disparities contributed by the individual lanes (as phase switching takes place) three phase motor equivalents were considered in the analysis. Furthermore, the paper will address an aspect of major concern in torque-summed architectures, that is, the possibility of force fight between mismatched lanes. Zero Aerodynamic Aileron Load Angles (at which the force fight is considered to be maximum) will be identified for different aircraft speeds and as an example the aircraft performance at a particular flight case will be examined. Efforts to minimise force fight between mismatched lanes are achieved by incorporating a simple Monitoring-Voting-Averaging Devices, MVADs, in the Fault Detection and Fault Isolation System. The effectiveness of these devices in minimizing the force fight will be proven.

2. INTRODUCTION

The advantages electromechanical actuator systems have over hydraulic actuators include weight reduction, elimination of hydraulic fluid leakage (consequently reduction in fire hazards) and offer reduction in system's complexity which makes them cheaper to install and maintain. Architecture descriptions of overall actuation systems (single and dual) and their performance may be found in [1]-[13]. The authors reported programs carried out by Boeing, Grumman, Lockheed-Georgia, Sundstrand Corporation, the USAF Flight Dynamics Laboratory and the Virginia Polytechnic Group. A quadruple system was presented in [14]-[16], where the author examined different architecture consolidation methods which assumed lumped models for the brushless dc motors, Fig.1. The author utilised and examined a Simulation-Graphical Monte Carlo as a threshold setting technique. This paper, will extend these findings by considering 3-phase model equivalents to allow for the examination of torque ripple effects, hence the possibility of force fight between mismatched lane.

Fig.1 Quadruplex Torque Summed Architecture
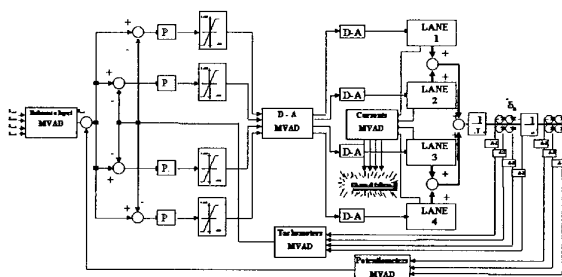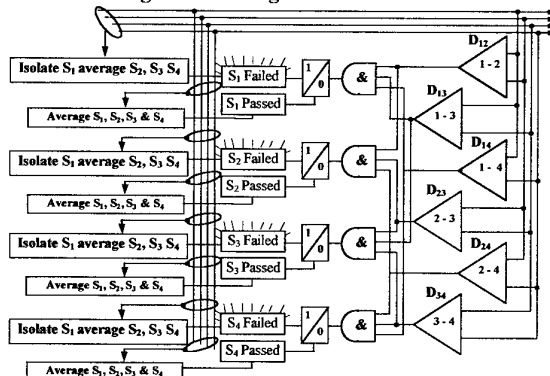

3. HARDWARE CROSS MONITORING

To monitor motors for failures in a 3-phase configuration, the input signals (to monitor the currents in the motors) to the MVADs, Fig.2, are represented by the filtered sum of the absolute measured individual phase currents. This eliminates the need for motors alignment, which is practically undesirable.

Fig.2 Block Diagram of the MVADs

The motors were driven in closed node configuration, therefore, for positive torque, the voltages applied to the nodes have to follow the switching sequence 7, 3, 4, 2, 6 and 5, [17] & [18]. For negative torque, the switching sequence is 2, 6, 5, 7, 3 and 4. To clarify this, nodes' voltages at a particular electrical angle range are listed in Table 1. Vs_{+ve} and Vs_{-ve} take the values of 100 and 0.0 Volts, for positive torque, and 0.0 and 100.0 volts, for negative torque. Therefore, the switching sequences 2, 6, 5, 7, 3 and 4 (for negative torque) is exactly the same sequence as the sequence 7, 3, 4, 2, 6 and 5 (for positive torque) except that the node voltages are interchanged.

Table 1   Delta node closed node and phase voltages

| State	Nodes Voltage			Phases voltage			Electrical Angle
	V_a	V_b	V_c	V_1	V_2	V_3	
7	V_{s+}	V_{s-}	V_{s+}	0	-100	100	$330 \leq \theta \leq 30$
3	V_{s+}	V_{s-}	V_{s-}	100	-100	0	$30 \leq \theta \leq 90$
4	V_{s+}	V_{s+}	V_{s-}	100	0	-100	$90 \leq \theta \leq 150$
2	V_{s-}	V_{s+}	V_{s-}	0	100	-100	$150 \leq \theta \leq 210$
6	V_{s-}	V_{s+}	V_{s+}	-100	100	0	$210 \leq \theta \leq 270$
5	V_{s-}	V_{s-}	V_{s+}	-100	0	100	$270 \leq \theta \leq 330$

Where $V_1 = V_a - V_c$, $V_2 = V_b - V_a$, and $V_3 = V_c - V_b$

4. FAILURE MODES

Utilisation of 3-phase models to represent the motors in the multi-lane actuator made it possible to test for additional and different types of lane failure modes such as line, commutation chips, drive transistors and motor failures, Fig.3. However, sudden introduction of commutation or switching transistor failures may not result in an immediate isolation or even failure recognition, hence the failures are dormant. To illustrate this, assume that the system is stable with the lanes driven at the first commutation state, hence, $Va_{1..4}=V_{s+}$, $Vb_{1..4}=0$ and $Vc_{1..4}=V_{s+}$. Also, assume that all failures occur in lane 1, hence, dormant failures may be realised if the following is considered;

1. A short circuit between Va_1 and Vc_1
2. The transistors supplying the nodes Va_1 or Vc_1 were latched to V_{s+} or if the transistor supplying node Vb_1 were to be latched to zero volts.
3. Commutation chip continuously outputs 1st commutation.

Fig.3: Motor and Power Conditioner Failure
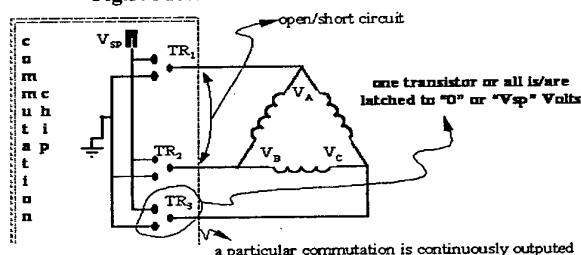
For a dormant failure to become apparent, a change in input command signal (by the pilot or on board computers) should take place first. However, the occurrence of such unnoticed dormant failures is a highly unlikely event, which may be eliminated by simple in-time-monitoring based upon reasonableness testing. For example, if any of the phase currents were to remain constant for 10 micro or more processor cycles, then an amber warning is declared.

5. DESCRIPTION OF SGMC METHOD

When compared to Decision Theory the SGMC does not require knowledge of observations distribution (in presence or absence of failures), knowledge of prior probabilities (in presence and absence of failures) or knowledge of cost functions for correct and incorrect decisions [19]. When compared to the Analysis of Variance, then, problems treated with this method could be set up in different forms depending on the number of control parameters [20]. The simplest form of this method is the No-way ANOVA, which does not consider any control parameters. Other higher forms of ANOVA may be conducted depending on the number of control parameters. In the multi-lane actuator, the control parameters could be reduced to aileron deflections at specific aircraft speeds (for a given set of servos and feedback transducers). Regardless of the form of ANOVA used, the method has the following limitations; it is linked with the analysis of purely experimental observations; its confidence level depends on the confidence level of the data used, which could be improved by increasing the sample size; and its complexity is directly related to the number of control parameters. The advantages of the SGMC method lies in the fact that it does not suffer from any of the above disadvantages and that it has the following additional advantages; it can be used with the same ease of application to any finite region (not essentially Gaussian); and It requires smaller sample of simulation or experimental tests, hence its more efficient. Furthermore, a purely simulation based Monte Carlo approach is also inefficient, since simulation time is governed by the false alarm rate.

Fig.4: Probability graph paper
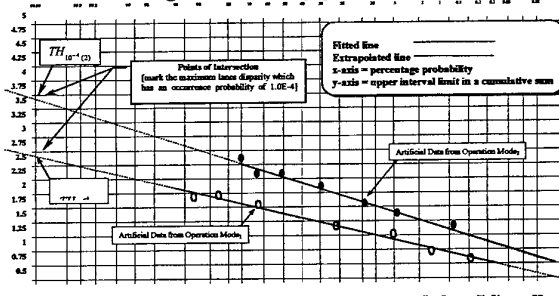
Description of the SGMC may be summarized by these steps

1. The thresholds values on the MVADs should be set to high values to observe lane disparities without triggering any alarms.
2. Peak lane disparities, from discrete modes of operation, are generated and the flight case of interest is identified.
3. Data banks for the chosen sample are then set up and the range over which the data spread over is divided into intervals containing counts of the number of events of occurrence within each interval.
4. Cumulative sum and the probability percentage of occurrence are then calculated.
5. Probability percentages are plotted on probability graph paper, Fig4. The x-axis is the percentage probability, while the y-axis represents the upper interval limit.

6. A graph is fitted to the plotted data and extrapolated to intersect with the y-axis (10^{-4} probability-axis). The fitted graph will be very close to a straight line if the percentage probabilities were normally distributed. For non-Gaussian distributions a smooth curve is expected, which may also be extrapolated, [21].

7. If a threshold were to be scheduled, then it will take the values of the $TH_{10}^{-4}(TH_{10}^{-4}{}_{(1)}$ or $TH_{10}^{-4}{}_{(2)}$ etc.) depending on the mode of operation, Fig.4.

8. If the threshold is to be unscheduled, then only the maximum value of the different TH_{10}^{-4} points should be considered, i.e. $TH_{10}^{-4}{}_{(max)}$. In Fig.4 $TH_{10}^{-4}{}_{(max)} = TH_{10}^{-4}{}_{(2)}$.

In this particular application, the flight case that yields maximum peak lane disparity is $\delta_a = 18^o$-low aircraft speed is the flight case of interest (δ_a is the aileron deflection) and by following a similar approach to the above steps, the current threshold was found to be 4.5Amps.

6. AIRCRAFT RESPONSE

Fig.5 reveals that the maximum failure transient due to repeated motor/power conditioner failures was 1° in amplitude lasting over a period of 0.8 seconds (at the maximum authority limit in δ_a for low aircraft speed flight case). To examine the aircraft roll and roll rate response, failures were simulated as aileron pulse disturbances to the aircraft model, [22] & [23]. Fig.6 shows that the resulting aircraft response in roll meets the aircraft response requirement (after absorbing two failures) of a maximum roll rate of 5°/sec and bank angle 3°.
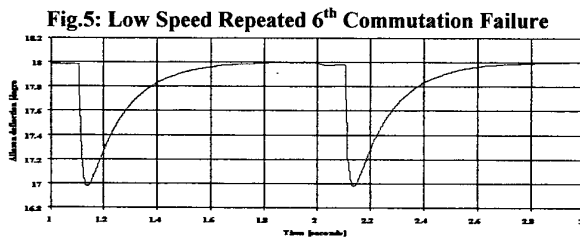
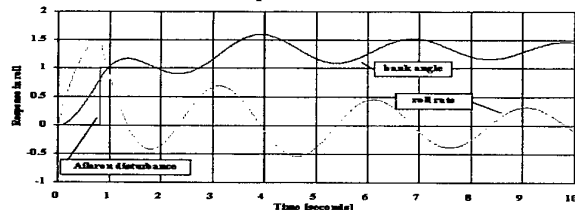**Fig.5: Low Speed Repeated 6th Commutation Failure**

Fig.6: Aircraft Roll Response to an Aileron Disturbance

7. FORCE FIGHT BETWEEN LANES

The possibility of force fight between mismatched lanes is an aspect which causes major concern in torque summing architectures. In the most pessimistic case, it could result in a small "dead zone". In this design, efforts to minimise force fight between lanes were made by averaging the D-A converter output signals, which feed the power conditioner. This section will assess the effectiveness of

these efforts at regions where the force fight will be maximum. At these regions, the net aerodynamic load is zero; that is the steady component of the aerodynamic load cancels out with the variable component at a specific angle of aileron deflection. These aileron angles are unique for each particular flight case, Fig.7, and will be referred to as the Zero Aerodynamic Load Angles, ZALAs. The force fight between lanes could be examined at any of these points, however, for the purpose of illustration the low aircraft speed flight case will only be considered, where the ZALA is -9° approximately, Fig.8.

Fig.7: Zero Aerodynamic Angles
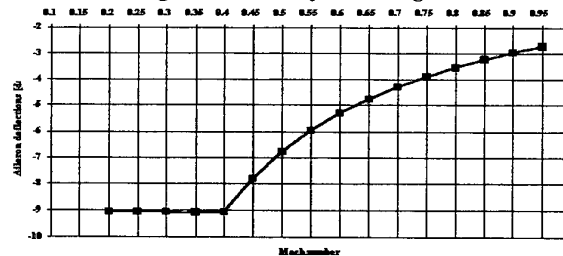
Fig.8: Net Aerodynamic Load and its Component
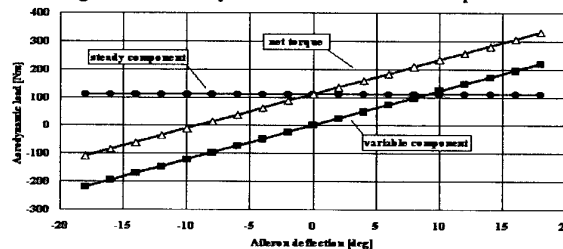
7.1 TOLERANCE VARIATIONS

The unique combination of component tolerance variations (resistance, inductance, torque constant and voltage constant) to yield maximum and minimum torques for one motor were identified to assess the maximum force fight between motors. It was assumed that the parameters of two of the motors are set to yield maximum torque, 8.6Nm, while the parameters of the remaining two are set to yield minimum torque, 3.7Nm. Although this variation in the torque outputs is large, this difference is reduced considerably when channel equalisation is applied.

Fig.9: Total and Individual Lane Torques at -9.0^o

Fig.9 shows the absence of any dead zones in the net torque contribution, T_o. This is because the individual lane contributions

are almost identical. A further test was carried to examine the actuator output impedance to mismatched lanes, Fig.10 and 11. In Fig.10, the aileron was deflected to the -9° position and once steady state was reached, an additional sinusoi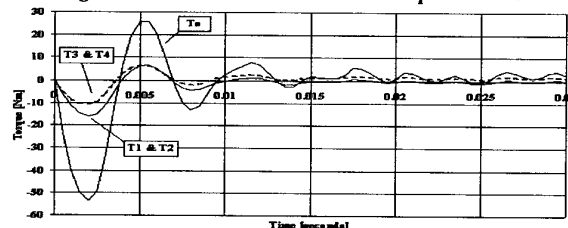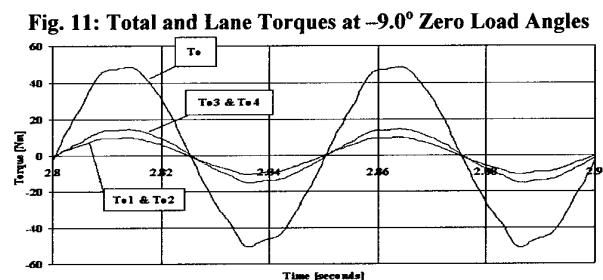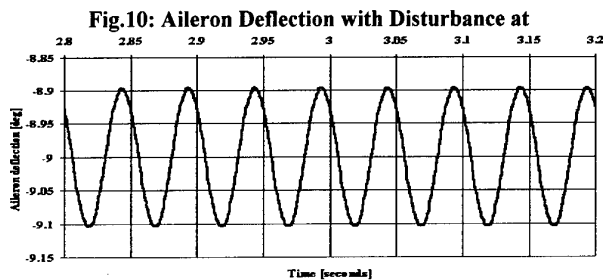dal disturbance was introduced to the variable component. The disturbance has a magnitude equivalent to the maximum nominal torque delivered by the actuator at frequencies of up to 20 Hz. The figure clearly shows that control was maintained around the δ_a=-9° with absence of any non-linearities in the individual and net torques.

Fig.10: Aileron Deflection with Disturbance at

Fig. 11: Total and Lane Torques at –9.0° Zero Load Angles

8. CONCLUSION

Utilisation of three phase motor equivalents in the above analysis permitted the examination of lane disparities in the presence of the torque ripple effects. It also allowed for detailed inspection of different failure modes in either the motors or power conditioner components. A Simulation Graphical Monte Carlo was used to set the thresholds on the Monitoring Voting Averaging Devices, which were used to identify and isolate failed Channels. The above study showed that with the current design all aircraft performance requirements were successfully met after absorbing two failures at false alarm rate of 1.0E-4. It was also proven that despite the poorly matched servos used, force fight between lanes was minimal and is not viewed as a performance problem. In fact, it may be dismissed as a limitation concept (in the torque summing architecture) as any force fight will merely appear as negligible strain on the summing gearbox teeth.

9. REFERENCES

[1] Hair, K.A., "Electromechanical actuation reliability and survivability", NAECON, 1983, page 74.

[2] Ward, D.,"The all electric helicopter", NAECON, 83, p104.

[3] Whitaker, R., Harmon, A. and Haynes, L., "A survivable fly-by-wire spoiler actuation system featuring non-flammable fluid, 8000 psi hydraulics and direct drive valves", NAECON, 1985, page 633.

[4] Holmdahl, M., "Putting all new electric technology development to the test", NAECON, 1983, page 74.

[5] Leonard, J.B., "A system look at the electromechanical actuation for primary flight control", NAECON, 83, p. 80.

[6] Thompson, K., Eitenmiller, K., and Hunter, L., "Demonstration for electromechanical actuation technology for military air cargo transport", NAECON, 1983, page 87.

[7] Thompson, K., Alden, R., and Hunter, L., "Lockheed-Georgia and electric primary flight control systems", NAECON, 1985, page 588.

[8] Thompson, K., "Notes on the electric control of large aeroplanes", NAECON, 1987, page 595.

[9] Bradbury G., "Development of an advanced primary flight control electromechanical actuator", NAECON, 87, p. 602.

[10] Demerdash, N.A. and Nehl, N.H., "Dynamic modelling of brushless dc motor power conditioner unit for electromechanical actuator application", IEEE Transaction on Industry Application, 1979.

[11] Demerdash, N.A. and Nehl, N.H., "Dynamic modelling of brushless dc motors for aerospace actuation", IEEE Transaction on Industry Application, 1980.

[12] Demerdash, N.A., Nehl, N.H. and Maslowski, E., "Dynamic modelling of brushless dc motors in electric propulsion and electromechanical actuation by digital techniques". IEEE Transaction on Industry Application, 1980.

[13] Pond, C.L. and Wyllie, C.E., "Test results of a unique high power electric motor actuator designed for space shuttle application", IEEE, 1983

[14] Annaz, F. Y., "Architecture and monitoring methods in high integrity multi-lane smart electric control surface actuators", Ph.D. Thesis, QMW, University of London, 96.

[15] Annaz, F. Y., "Architecture and monitoring philosophy in multi-lane high integrity electric actuators", Proceedings of the IASTED International Conference Control 97, May 28-31, Cancun Mexico, ISBN:0-88986-223-0.

[16] Annaz, F.Y., "Threshold setting methodologies in high integrity systems", IASTED International Conference, Control and Application, August98, Honolulu, USA.

[17] Taft, C. K. and Gauthier, R., "Brushless motor torque speed curves", IMCS, June 1985.

[18] Taft, C.K. and Huard, S.R., "Brushless motor torque-curves for open drives", IMCS, June 1988.

[19] Sage, A.P. & Melsa, J.L., "Estimation theory with applications to communications and Control" (McGraw-Hill Book Company, New York, 1971).

[20] Ross, P.J., "Taguchi Techniques for quality engineering", McGraw-Hill Book Company, 1989.

[21] Chambers, J.M., Cleveland, W.S., Kleiner, B. and Tukey, P.A. *Graphical methods for data analysis* (California: Wadsworth International Group, Duxbuy Press, 1983).

[22] Mil-F-83300, "Flying qualities of piloted aircraft", 1970.

[23] Teper, G.L., "Aircraft stability and control data, STI Technical Report 176-1", Ames Research Centre, April 69.

1E10　Control Law Design for Aircraft with Reduced Tail Size in Preliminary Design Phase

Endang S. L. Handayani[*], Mudjijanto[**], Cees Bil[***]

RMIT University, Melbourne, Australia

Key word : ACT, stability and control

ABSTRACT

The design of a longitudinal stability augmentation system (SAS) for an aircraft with reduced tail size in preliminary design phase is presented. Reducing tail size will reduce drag and result in better fuel consumption, but it will reduce the level of stability. A control law is designed to give the aircraft the same stability level as that with the initial tail size. The feedback gains of the control law are computed with the equivalent stability derivative criteria of C_{m_α} and C_{m_q}. This paper also gives an overview of classical root locus and pole placement method and demonstrates that the equivalent stability derivative criteria is suitable for preliminary aircraft design applications.

1. Introduction

The task of finding the best aircraft design to fill a given role is extremely complicated. Even if a satisfactory criterion of merit can be defined, the designer is faced with a problem composed of a large number of interacting technical factors drawn from several different engineering and scientific disciplines, and by the need to satisfy numerous mission requirements and constraints. His/her difficulties are compounded by the rapid rate of technical progress in the aeronautical sciences, which forces the designer to either work with uncertain data from the frontiers of knowledge or to use proven technology and risk producing an obsolescent aircraft ([1], [2]).

One of the modern technologies applied to the design of aircraft is the fly-by-wire technology. FBW replaces mechanical linkages from the cockpit through control surfaces with electrical signal resulting in reduction in flight control system weight. Also the inherent application of active-control technology (ACT), such as stability augmentation system, flutter suppression system, within the FBW increases aircraft performance [5].

Traditionally, transport aircrafts airplanes are equipped with mechanical flight control system and are usually designed to have inherent static stability. This design approach dictates the size of the horizontal tail plane. However, in many high performance aircrafts the inherent static stability margin may be decreased to reach zero or even negative (the so called relax static stability) [6]. This results in the reduction of horizontal tail plane size which means a reduction in weight and trim drag. A significant reduction of fuel consumption will be achieved [5].

Having a relax static stability, a stability augmentation system should be incorporated to maintain the stability. It is very desirable that the control law can be determined from the very early phase of design to anticipate the design of the flight control system. In this paper the equivalent stability derivative criteria is proposed since it deals with the very early design parameters such as C_{m_α} and

C_{m_q}. To verify this method the classical root locus for multiple loops and the pole-placement methods will also be discussed.

2. Requirement and Objective

The designed control law should be able to maintain the stability level of the aircraft with the initial size of the horizontal plane. The control law synthesis was performed based on cruise flight condition with center of gravity 22 % MAC since it has the least short period damping ratio.

3. Aircraft Dynamic Model

The linear longitudinal aircraft dynamic model is used for control law synthesis. The complete model is given in the following.

$$\begin{bmatrix} 4\mu_c & 0 & 0 & 0 \\ 0 & 4\mu_c - C_{Z_{\dot\alpha}} & 0 & -4\mu_c \\ 0 & 0 & 1 & 0 \\ 0 & -C_{m_{\dot\alpha}} & 0 & 8\mu_c \frac{I_y}{m\bar c^2} \end{bmatrix} \begin{bmatrix} D_c\hat u \\ D_c\alpha \\ D_c\theta \\ D_c\frac{q\bar c}{2V} \end{bmatrix} =$$

$$\begin{bmatrix} C_{X_u} & C_{X_\alpha} & C_{Z_o} & C_{X_q} \\ C_{Z_u} & C_{Z_\alpha} & -C_{X_o} & C_{Z_q}+4\mu_c \\ 0 & 0 & 0 & 1 \\ C_{m_u} & C_{m_\alpha} & 0 & C_{m_q} \end{bmatrix} \begin{bmatrix} \hat u \\ \alpha \\ \theta \\ \frac{q\bar c}{2V} \end{bmatrix} + \begin{bmatrix} C_{X_{\delta_e}} \\ C_{Z_{\delta_e}} \\ 0 \\ C_{m_{\delta_e}} \end{bmatrix} \delta_e$$

$$(1)$$

where $\quad D_c = \frac{c}{2V}\frac{d}{dt}$

By performing some matrix manipulation the above equation may be written in state space description as:

$$\dot{\bar x} = A\bar x + B\bar u \qquad (2)$$

where matrix $\begin{bmatrix} \hat u & \alpha & \theta & \frac{q\bar c}{2V} \end{bmatrix}'$ is the state vector matrix $\bar x$ and $[\delta_e]$ is the input vector $\bar u$.

The output of the system can be written as :

$$y = Cx + Du \qquad (3)$$

Close-loop State Feedback Model

After deriving the state space representation of the aircraft, it is now possible to apply modern control theory state feedback design. State feedback can be used to design a control system with a specific eigenvalue. Consider the system represented by the state

[*]　　Postgraduate Researcher, Department of Aerospace Engineering, RMIT University
[**]　 Flight Dynamics and Control Manager, Indonesian Aircraft Industry
[***]　Associate Professor, Department of Aerospace Engineering, RMIT University

equations given in Equations (2) and (3), by taking D = 0.
It can be shown from optimal control theory that if the system is state-controllable, then it is possible to use a linear feedback control law given by

$$\eta = -k^T x + \eta' \qquad (4)$$

to achieve a specific eigenvalue structure. The matrix k is called the feedback gain matrix and η' is the original control system input. Combining Eqs. (2) and (4), the closed loop system is given by

$$\dot{x} = (A - Bk^T)x + B\eta' \qquad (5)$$

where $A - Bk^T$ is the augmented matrix. For the case where the A matrix may have had undesirable eigenvalues, the augmented matrix $(A - Bk^T)$ can be made to have specific eigenvalues by properly selecting the feedback gains [4].

4. Effect of Horizontal Tail Area on Stability Derivatives

The effect of changes in horizontal tail area on some important stability and control derivatives will be illustrated with the 50-seater turboprop airplane, N250. Table A1 (Appendix) lists the important characteristics.

In the analysis to follow, the following expressions are known [1]:

$$C_{L_\alpha} = C_{L_{\alpha WB}} + C_{L_{\alpha H}} \frac{S_H}{S_W}(1 - \frac{d\varepsilon}{d\alpha}) \qquad (6)$$

$$C_{m_\alpha} = C_{m_{\alpha WB}}(\overline{X}_{cg} - \overline{X}_{acWB})$$
$$- C_{L_{\alpha H}} \frac{S_H}{S_W}(\overline{X}_{acH} - \overline{X}_{cg})(1 - \frac{d\varepsilon}{d\alpha}) \qquad (7)$$

$$C_{m_{\delta e}} = -C_{L_{\alpha H}} \frac{S_H}{S_W} \frac{l_H}{\bar{c}} \tau_E \qquad (8)$$

$$C_{m_q} = -2.0 C_{L_{\alpha H}} \frac{S_H}{S_W}\left(\frac{l_H^2}{\bar{c}}\right) \qquad (9)$$

$$C_{m_{\dot{\alpha}}} = 0.433 C_{m_q} \qquad (10)$$

Using the data in Table A1 the derivatives of Equations (6) through (10) can be expressed as a functions of S_H, in the following manner:

$$C_{l_\alpha} = 6.0653 + 0.0404 S_H$$

$$C_{m_\alpha} = 6.1982 - 0.59015 S_H$$

$$C_{m_{\delta e}} = -0.1995 S_H \qquad (11)$$

$$C_{m_q} = -4.8782 S_H$$

$$C_{m_{\dot{\alpha}}} = -1.194 S_H$$

Figure 1 shows how the important derivatives C_{m_q} and C_{m_α} are affected by these changes in horizontal tail area (S_H).
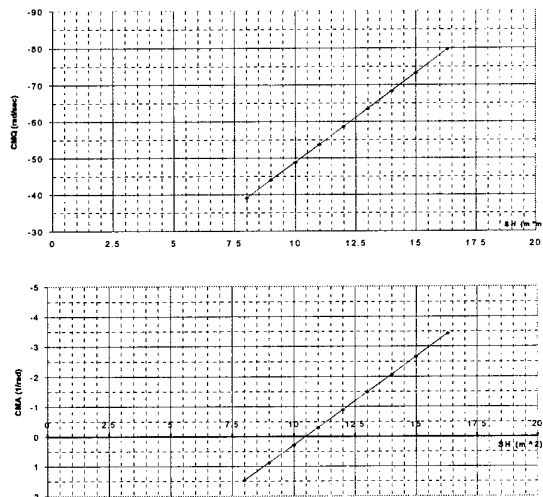

Fig.1 C_{m_α} and C_{m_q} as a function of horizontal tail area.

5. Achieving Artificial stability by Feedback

It is now be assumed that any reduction of S_H from the existing value of 16.31 m² will require stability augmentation to restore the inherent value of C_{m_q} and C_{m_α}. The stability augmentation will be obtained by α- and q- feedback through elevator deflection. Figure 2 shows a typical system arrangement for α- and q-feedback.
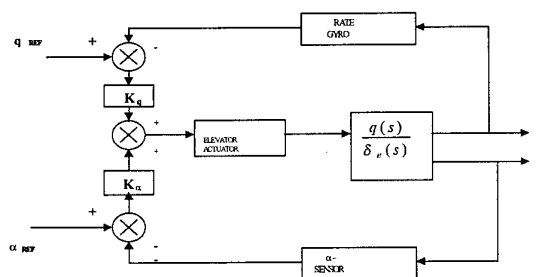
Fig. 2 Typical arrangement of α and q Feedback

The gain K_α and K_q may be determined using the concept of equivalent stability criteria. This concept will be discussed in the following section.

5.1 Equivalent Stability Derivative Criteria

Equivalent stability criteria concept is a method to determine how much stability augmentation is needed to achieve certain desired level of handling qualities. In this particular case is how much stability augmentation is needed if S_H is reduced to obtain the same level stability of the original S_H.

C_{m_q} has a very powerful effect on the short period damping ratio ζ_{SP} without affecting the phugoid characteristics. To obtain the required value of C_{m_q} for the original S_H if S_H is reduced a

pitch damper will have to be used.

A pitch damper consists of a rate gyro which senses airplane pitch rate q and then moves the elevator in a manner proportional to q as to oppose q. Assuming that such a 'perfect' pitch-damper can be built it is seen that the incremental pitching moment obtained by such a device can be written as:

$$\underset{q-SAS}{\Delta} C_m = C_{m_{\delta_e}} K_q \tag{12}$$

where K_q is called the pitch damper gain constant, or elevator per unit pitch rate. The corresponding increase in C_{m_q} is therefore:

$$\underset{q-SAS}{\Delta} C_{m_q} = \frac{2V}{\bar{c}} C_{m_{\delta_e}} K_q \tag{13}$$

As a result of this 'perfect' pitch damper, the airplane now has a new value of C_{m_q} equal to:

$$\underset{SAS-ON}{C_{m_q}} = \underset{BASIC}{C_{m_q}} + \underset{q-SAS}{\frac{2V}{\bar{c}} C_{m_{\delta_e}} K_q} \tag{14}$$

where $\underset{SAS-ON}{C_{m_q}}$ is called equivalent stability derivative.

The amount of required pitch damper gain can now be calculated from

$$K_q = \left[\frac{\underset{Desired}{C_{m_q}} - \underset{Basic}{C_{m_q}}}{C_{m_{\delta_e}}} \right] \frac{\bar{c}}{2V} \tag{15}$$

Feedback gain K_α and K_q

After deriving K_α and K_q, now they can be easily calculated by substituting values of variables (see appendix) and they are given in figure 3.
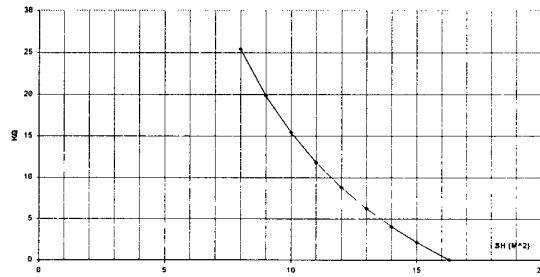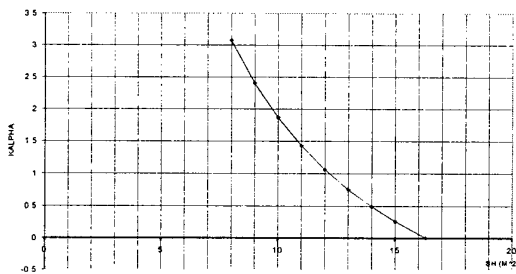

Fig. 3 Feedback gain K_α and K_q as a function of S_H

5.2 Root Locus Design

The control law design with classical control method using root locus is performed with short period approximation. Applying multiple loop as shown in the system in Fig. 2 in root locus design is somewhat cumbersome, however with some simplification it can be done quite elegantly.

First, the transfer function of $\dfrac{\alpha}{\delta_e}$ and $\dfrac{q}{\delta_e}$ should be determined [1]. The stability behavior of these transfer function is determined entirely by the characteristics equation:

$$1 + K_\alpha G_a \frac{\alpha}{\delta_e} + s K_q G_a \frac{\theta}{\delta_e} = 0 \tag{16}$$

Using the short period approximation for $\dfrac{\alpha}{\delta_e}$ and $\dfrac{q}{\delta_e}$ and representing G_a by $\dfrac{a}{s+a}$, the characteristic equation can be expanded into:

$$s^3 + s^2 (2\zeta \omega_n + a) + s(\omega_n^2 + 2a\zeta \omega_n + K_\alpha a K_{\alpha_\delta} \omega_n^2 T_\alpha$$
$$+ K_q a K_{\theta_\delta} T_\theta \omega_n^2) + \tag{17}$$
$$+ \left(a\omega_n^2 + K_\alpha a K_{\alpha_\delta} \omega_n^2 + K_q a K_{\theta_\delta} \omega_n^2 \right) = 0$$

Figure 4 presents a root-locus of the system of Fig. 2. It is seen that the system is apparently also capable of stabilizing an inherently unstable airplane.
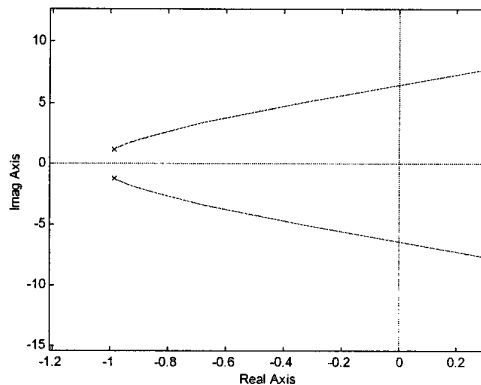
Fig. 4 Root locus for multiple loop

5.3 Pole-placement Method

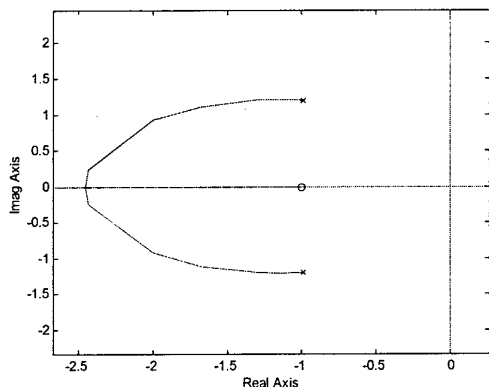The pole-placement method is a broadly explained in [4]. This method deals with the feedback gain required if the desired poles position is given. For practical calculation the function *place* in MATLAB can be used directly.

The comparison of the gains obtained from the equivalent stability criteria, root locus and pole-placement is given in Table 1 if S_H is reduced to 12 m².

Equivalent Stability Derivative criteria		Root locus		Pole-placement	
k_α	k_q	k_α	k_q	k_α	k_q
1.0626	8.784	1.012	9.797	1.053	9.337

Table 1 Comparison of the gains for the three different methods

6. Applying control law into airplane with reduced tail size

The goal of this study is to investigate the use of stability augmentation system into the aircraft with reduced tail size. The control law obtained from the equivalent stability derivatives criteria is used as a feedback controller. The open and closed loop characteristics as a function of S_H is shown in Figure5.
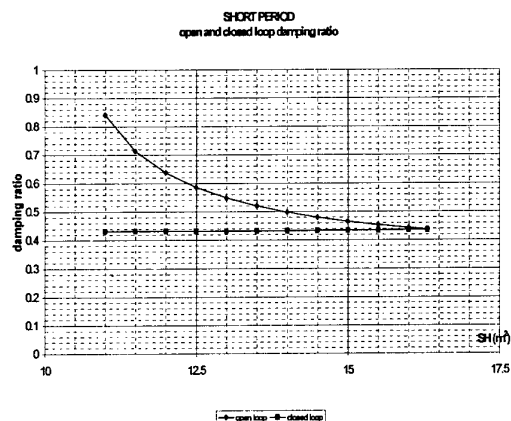

Fig. 5 Damping ratio of open and closed-loop system

7. Conclusion

The equivalent stability derivative criteria presented in this paper forms a very useful method to design the control law to be used as a stability augmentation system for an aircraft with reduced tail size in the preliminary design phase. The gains calculated using this method is comparable to those designed with root locus and pole placement methods. However, the control law should be verified with more accurate calculation in the detail design of flight control system.

8. References

[1]. Roskam, 'Aircraft Design', University of Kansas, 1986
[2]. Torenbeek, E, Synthesis of Subsonic Airplane Design', Martinus Nijhoflaan/Delft University Press, 1976
[3]. Roskam, J., 'Airplane Flight Dynamics and Automatic Flight Control Systems', Roskam Aviation and Engineering Corp., Kansas, 1981
[4]. Nelson, R. C., 'Flight Stability and Automatic Control', McGraw-Hill Book Company, 1989
[5]. 'Integrated Application of Active Control (IAAC) Technology to an advanced Subsonic Transport Project – Initial ACT Configuration Design Study', NASA CR – 159249, July 1980
[6]. Blight, J. D., Gangsaas, D., Richardson, T. M., Control Law synthesis for an Aircraft with Relaxed Static Stability, AIAA Jounal of Guidance, Control and Dynamics (Special Issue on Handling Qualities) , Vol. 9, no. 5, 1986, p. 546-554

Appendix

Table A1 Characteristics of N250

S = 65 m²; S_H initial = 16.31 m²; $\bar{C}$ = 2.417 m; W = 22000 kg

Xcg = 22 % mac; V = 220 keas; H = 20000 ft

Power setting : cruise flight

$C_{X_o} = -0.0013$

$C_{Z_o} = -0.4231$

$C_{X_u} = -0.1006$

$C_{Z_u} = -0.8196$

$C_{m_u} = 0.0172$

$C_{X_\alpha} = 0.2762\ rad^{-1}$

$C_{Z_\alpha} = -6.7258\ rad^{-1}$

$C_{Z_{\dot\alpha}} = -3.2269$

$C_{m_\alpha} = -3.4267\ rad^{-1}$

$C_{m_{\dot\alpha}} = -19.4736$

$C_{X_q} = 0$

$C_{X_{\delta_e}} = 0.0159\ rad^{-1}$

$C_{Z_q} = -13.3242$

$C_{Z_{\delta_e}} = -0.5223\ rad^{-1}$

$C_{m_q} = -79.5637$

$C_{m_{\delta_e}} = -3.2532\ rad^{-1}$

1E11   Flight Control System Design Using Neural Networks and Genetic Algorithms

K. D. Kumar*   and Y. Miyazawa[†]

Flight Division, National Aerospace Laboratory, Osawa 6-13-1, Tokyo, Japan 181 0015

Key Words: Flight Control System, Neural Networks, Genetic Algorithms

Abstract

Here, we presents a design methodology to develop flight control system using neural networks and genetic algorithms. The flight simulation model considered here has various types of uncertain parameters i.e. aerodynamics, actuator dynamics, sensor dynamics, environmental conditions, time delay etc., the stochastic properties of which are defined a priori. The flight control system requirements are defined based on the flight simulation results, and the neural networks with a preselected architecture is used to develop flight control laws. The training of neural networks is accomplished through genetic algorithms. In order to determine the performance of the trained neural networks, Monte Carlo method is applied to the results of large number of simulated flights to estimate the probability of satisfying the requirements, or the probability of total mission achievement. Simulation results for a benchmark problem of pitch attitude control of a flight vehicle are presented to illustrate the performance of the proposed methodology. The results of proposed NN structure is compared with the proportional-integral-derivative structure.

1. INTRODUCTION

Robustness against uncertainty is must for the success of flight control systems. The flight simulation is an essential tool for evaluation of the control system's performance. It generally includes uncertainty which are used in a wide variety of simulation components such as aerodynamics, actuator dynamics, sensor dynamics, environmental conditions, and so on. In order to consider the effects of these uncertain parameters, the stochastic methods must be applied to evaluate the total system performance. It is then necessary to define the probability distribution functions of uncertain parameters. Once they are assumed appropriately, it is possible to estimate the stochastic properties of the flight control system by the Monte Carlo flight simulation. As the flight simulation determines whether the vehicle satisfies requirements and specifications, Monte Carlo flight simulation is used to obtain the probability of total mission achievement, which is the most critical objective to be maximized in flight control system design.

[1]Science & Technology Agency Fellow, Guidance and Control Laboratory

[†]Head, Guidance and Control Laboratory

Stochastic evaluation and optimization of flight control systems was first discussed by Stengel et al.[1] who introduced the technical term "stochastic robustness". The basic idea of this approach was proposed by Marrison and Stengel[2-3]. Schubert and Stengel[4] have suggested flight control optimization using parallel computation. Recently, Miyazawa and Motoda[5] has applied proportional-integral-derivatiive controller based on stochastic gain tuning method and mean tracking technique to tune the feedback/feedforward gains on a benchmark problem. In the present work, a methodology for nonlinear controller design based on neural networks (NN), genetic algorithms (GAs) and stochastic optimizations is presented and it is tested on the same benchmark problem with a view to develop robust controller.

2. BENCHMARK PROBLEM

We consider a simple example of pitch attitude control of a flight vehicle with NN controller as shown in Fig.1. Here, the padé (1,1) approximant to time delay is considered. The uncertain parameters are a, b, k and time delay, T. The stochastic properties of these parameters are independent of each other, their probability distribution functions are assumed to be normal, and their means and variances are given as follows :

$$K \sim N(\mu_k, \sigma_k^2), \quad T \sim N(\mu_T, \sigma_T^2), \quad a \sim N(\mu_a, \sigma_a^2), \quad b \sim N(\mu_b, \sigma_b^2)$$

where, $\mu_k = 0$; $\mu_T = 0.2$; $\mu_a = 0$; $\mu_b = 0$; $\sigma_k = 0.5$; $\sigma_T = 0.5$; $\sigma_a = 3$; $\sigma_b = 0.05$ (base-line).if $T \leq 0$, $T = \varepsilon$; $\varepsilon = 10^{-6}$.

The control design objective is defined in the following quadratic function, where the initial state of the system is null and the command is non-zero and constant:

$$J \leq J_o; \quad J_o = 10 \text{ (s)}$$

$$J = \int_0^{80} (\frac{y(t) - y_c}{y_c})^2 dt$$

(1)

It is to be noted that the integration here is carried out till 80 sec only. This is because of larger computational resources involved in running the simulation for longer duration. However, this introduces the problem of convergence of the solution. To do away with this problem, an another constraint has been considered as follows:

$$(dy/dt)_{t=60 \text{ sec}} < 0.01 \tag{2}$$

3. DEVELOPMENT OF NONLINEAR CONTROL LAW

The motivation for considering a NN for this problem was to develop a nonlinear controller. A feedforward multilayer NN is used to synthesis nonlinear feedback laws (Fig. 2). The NN takes y_c, y, $\dot{y}$, $\int y dt$ as inputs and control variable, u as output. The tansigmoidal activation function is used. A single hidden layer with n_{neuron} number of neurons as a design parameter has been added between the input and output layers. As the input-output mapping of the plant involving uncertainty is difficult, the NN is trained on-line using GAs.

4. DESIGN OPTIMIZATION

The NN controller involves many design parameters. In the order to obtain these parameters so as to maximize the objective function or fitness i.e., probability of satisfying the requirement given by equation (1), GA is used. Control problems in which the system dynamics or the performance measures are discontinuous, non-smooth, or non-convex are difficult to solve with conventional methods. GA is extremely useful for these types of problems, as it is not gradient-based and can operate regardless of the complexity of the problem dynamics or performance specifications. However, the GA procedure in general involves especially much computational efforts towards the optimal solution and therefore some modifications have been suggested so as to tackle this problem. The modified GA Algorithm involves the following steps:

Step 1 Choose binary coding to represent design parameters. Select a tournament selection operator, a uniform crossover operator, jump and creep mutation operators. Take population size, n_p, number of children per pair of parents, n_{child}, crossover probability, p_c (i.e., 0.5) and jump and creep mutation probability, p_{mj} and p_{mc}. Initialize a random population of strings of size $n_{param}l_p$, where n_{param} and l_p are the number of design parameters and their respective number of chromosomes (binary bits). Choose a maximum allowable generation number t_{maxgn}. Set $t_{gn}=0$.

Step 2 Evaluate each string in the population.

Step 3 If $t_{gn}>t_{maxgn}$ or other termination criteria is satisfied, Terminate.

Step 4 Perform niching (sharing) on the population.

Step 5 Perform reproduction on the population.

Step 6 Perform crossover on random pairs of strings.

Step 7 Perform mutation on every string.

Step 8 Evaluate strings in the new population. Set $t_{gn}=t_{gn}+1$.

Step 9 If the fitness value remains same for n_{gn} number of generations, consider next population consisting of only string of highest fitness value. Still if the fitness value does not improve for p_{gn} number of generations, terminate, otherwise go to Step 3.

5. RESULTS AND DISCUSSION

With a view to assess the efficacy of the proposed methodology, it has been applied on the benchmark problem explained earlier. The detailed system response is numerically simulated using Runga-Kutta forth order method with a step size of integration as 0.02 sec. We assumed the following numerical data for GAs: $n_p=50$, $n_{child}=1$, $p_{mj}=0.02$, $p_{mc}=0.04$, $l_p=15$, $n_{gn}=20$, $p_{gn}=10$, $t_{maxgn}=100$. The niching (sharing) is done through Goldberg's multidimensional phenotypic[6] sharing scheme with a triangular sharing function. Here, the GA driver developed by David L. Carroll, University of Illinois, Urbana, Illinois, USA has been used.

We first consider the case of fixed set point. For convenience, we take $y_c=1$. The results of this case are shown in Table 1. The results for the PID are also presented in Table 1 for comparison. It has been found that the use of PID results in 24 unsuccessful cases whereas the NN has only 13 unsuccessful cases. Thus, NN could roughly make half of PID failure cases into successful cases. Fig. 3 shows some of these successful responses. It is important to note that some of the NN responses involves initial oscillations. This is due to sudden change in controller output in initial stage.

Table 1. Comparison between the Performance of NN and PID Controllers for fixed set point.

Case (2000 Monte Carlo Simulation) $y_c=1$	Performance		
	Base-line	1.5 x σ	2 x σ
PID with padé (1,1) approximant to time delay model	98.8% (tuned)	88.25%	72.7%
with pure time delay model	96.5%	83.05%	66.85%
NN (1-3-1) with padé (1,1) approximant to time delay model	99.35% (tuned)	90.9%	75.1%
with pure time delay model	97.15% 98.1% (tuned)	86.8%	73.05 %

In the case of pure time delay, the results for both PID and NN have detoriated as expected. The NN still performed better than PID. When we increase standard deviations of uncertain parameters with respect to the base-line, we get the

similar resultls showing the robustness of NN compare to PID.

Table 2. Design Parameters obtained through GAs.

PID Model	$K_F = 0.8145$, $K_p = 2.6139$, $K_D = 2.8190$, $K_I = 0.3269$,
NN Model (1-3-1):S^1=3	$W^1 = \begin{bmatrix} 1.5572 & -2.7532 & 2.0397; \\ -1.2789 & 1.9912 & -0.9087; \\ -1.9561 & 1.7647 & 2.6193; \\ -0.1515 & 1.0601 & -1.9381 \end{bmatrix}^T$ $b^1 = [\ 0.0003\ 0.0003\ 0.0003\ ]^T$ $W^2 = [\ -2.0104\ 4.3149\ 2.9904\ ]^T$ $b^2 = 0.0003$
NN Model (1-4-1):S^1=4	$W^1 = \begin{bmatrix} 1.5877 & 1.2889 & 1.3549 & -0.5196; \\ 4.4720 & -1.4779 & 2.1554 & 1.8377; \\ 0.8498 & -1.9118 & 1.3555 & 0.7927; \\ -0.5303 & -0.2629 & 0.4387 & 3.2983 \end{bmatrix}$ $b^1 = [\ 0.0001\ 0.0001\ 0.0001\ 0.0001]^T$ $W^2 = [\ 0.2104\ -1.7904\ -0.5312\ 0.0954\ ]^T$ $b^2 = 0.0001$

Next, we consider the the case of variable set point. We vary y_c uniformly in the range from -1 to 1. For base-line case, PID gives performance of 98.8%, whereas NN with structure 1-4-1 has the performance of 98.55%. In this situation of variable set point, the NN could not perform better than PID.

6. CONCLUSIONS

Here, we investigated the nonlinear controller based on NN. The design optimization is carried out through GAs. The numerical performance results for a benchmark problem of pitch attitude control of a flight vehicle is presented. It is found that the performance of NN controller is better than the PID controller for the fixed set point. However, in case of variable set point the controller could not perform better than the PID controller. It is suggested to carry out further research so as to remedy this problem. The proposed approach involves extensive computation. However, with expanding computational power the methodology presented may be useful for designing flight control systems.

REFERENCES

1. Ray, L. R., and Stengel, R. F., "Application of Stochastic Robustness to Aircraft Control Systems," *J. Guidance, Control and Dynamics*, Vol.14, No.6, 1991, pp. 1251-1259.
2. Marrision, C. I., and Stengel, R. F., "Synthesis of Robust Control Systems for a Hypersonic Aircraft," *Proc. 33rd Conf. Decision and Control*, 1994, pp.3324-3329.
3. Marrision, C. I., and Stengel, R. F., "Design of Robust Control Systems for Hypersonic Aircraft," *J. Guidance, Control and Dynamics*, Vol. 21, No.1, 1998, pp. 58-63.
4. Schubert, W. M., and Stengel, R. F., "Parallel Synthesis of Robust Control Systems," *IEEE Trans. on Control Systems Technology*, Vol.6, No.6, 1998, pp. 701-706.
5. Miyazawa, Y., and Motoda, T., "Stochastic Gain Tuning Method Applied to Unmanned Space Vehicle Flight Control Design," AIAA-99-4309, *AIAA GNC Conf.*, August 1999.
6. Goldberg, D. E., Genetic Algorithm in Search, Optimization, and Machine Learning, Addison-Wesley Publishing Company, Inc., 1989.
7. Hang, M. T., and Demuth, H. B, "Neural Networks for Control," *Proc. American Control Conf.*, June 1999, pp. 1642-1656.
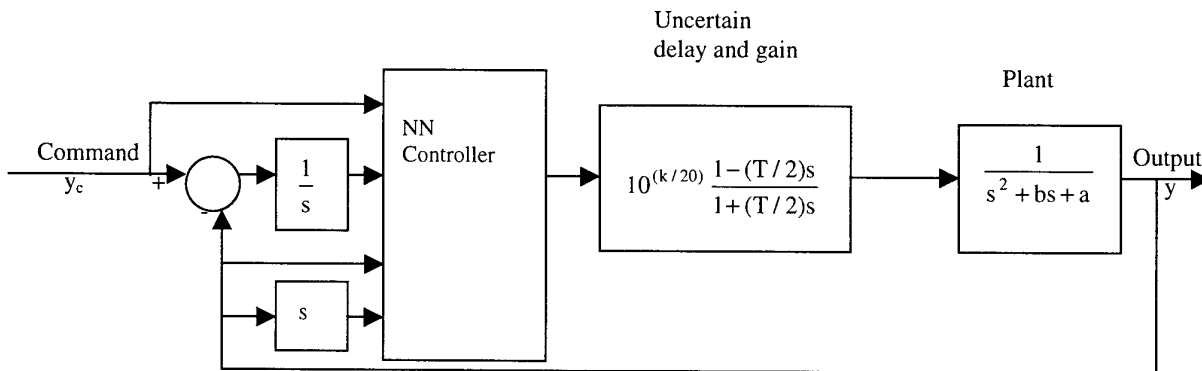
Fig.1 Neural Network Controller for the benchmark problem.

Input Layer   Hidden Layer   Output Layer
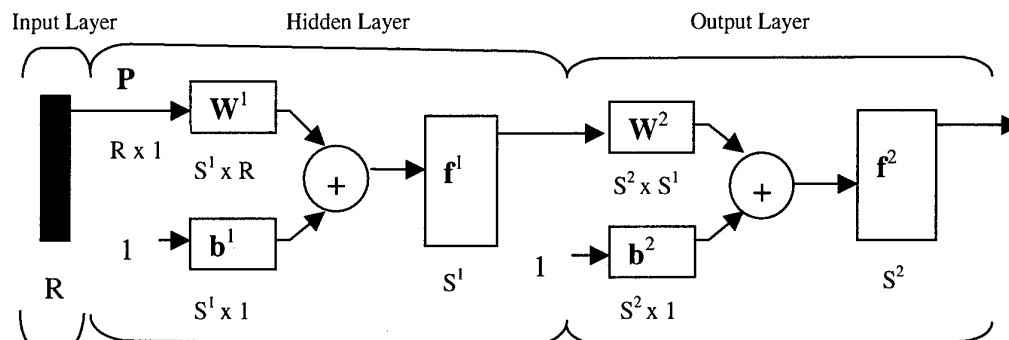
where, R=4; S^2=1; $f^1(n)= (1-e^{-n})/(1+e^{-n})$; $f^2(n)=n$

Fig.2 Neural Network Structure.

PID   NN

Fig 3. Typical Response Plots showing the effectiveness of NN controller for y_c=1 and the sets of uncertain parameters are (a) K =-6.9710, T =0.2875, a=-1.0550, b=0.4556; (b) K =-8.3310, T =0.2193, a= -1.1850, b=-0.0843;   (c) K =5.6590, T =0.2982, a=-0.1033, b=-0.3029; (d) K =-7.2860, T =0.1838, a=0.7879, b=-1.0020.

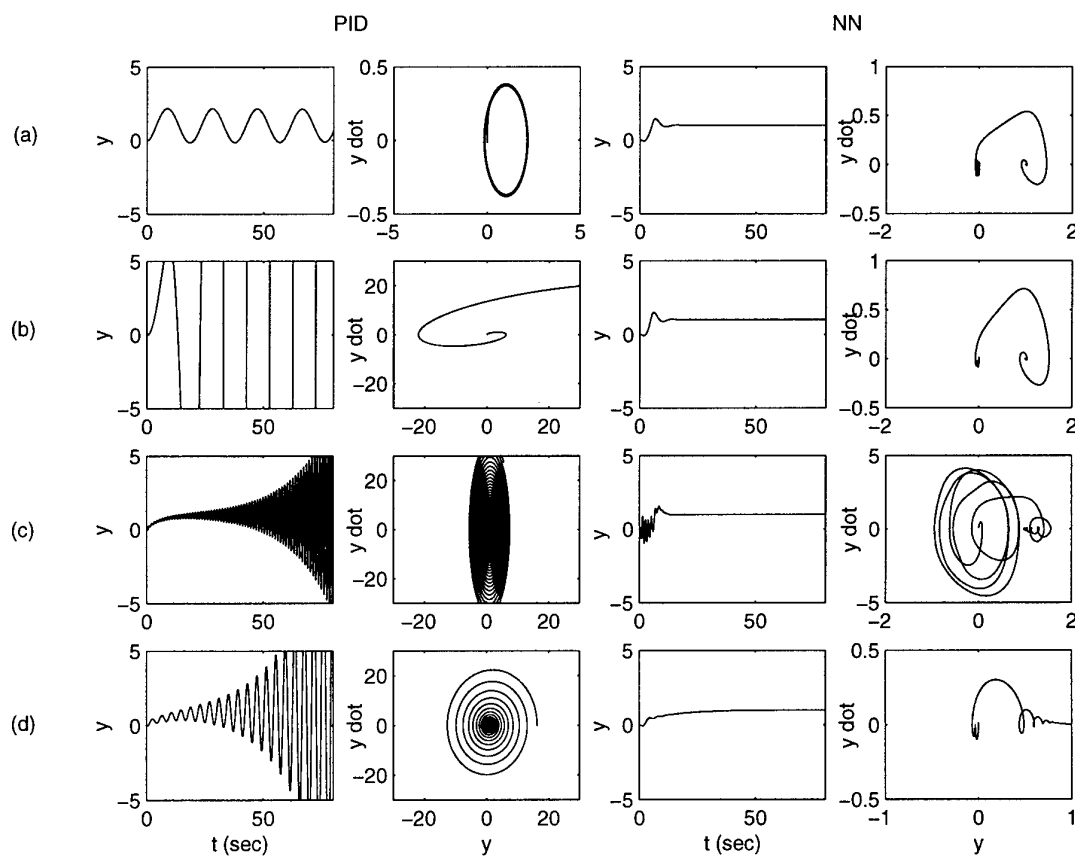APPLICATION OF MOVING HORIZON METHOD TO STATES ESTIMATION
FROM FLIGHT TEST DATA

Ari Legowo[*], *Hiroshi Okubo*[**], *Eiichi Muramatsu*[***], *Hiroshi Tokutake*[****]

Department of Aerospace Engineering, Osaka Prefecture University, 1-1 Gakuen-cho, Sakai, Osaka 599-8531

Keywords: Flight Dynamics, Flight Testing, Moving Horizon State Estimation, System Identification

ABSTRACT

This paper presents the application of moving horizon states estimation (MHSE) method to estimate states of non-linear aircraft equation of motion from dynamic maneuver's flight test data. To determine the optimum solution of minimizing the performance index a Quasi-Newton or gradient method is used. The present method also uses the Armijo's line search gradient to guarantee the solution/estimation to converge faster. The MHSE method is applied to flight test data of N250 PA-1 aircraft for parameter identification and flight path reconstruction. The result of estimation is also used to evaluate the accuracies of the measurement systems.

1. INTRODUCTION

For analyzing a prototype and/or series aircraft, the nonlinear model states and/or parameters estimator is critical to the success of identification process of stability and control derivatives in the linearized equation of motion. Identification process, states space model generating, and some robust controller designing require estimation of model states and/or parameters that often are unmeasurable directly. For example, application of state-feedback controller for longitudinal modes uses unmeasurable states, such as velocity on axes-x and axes-z, whereas the states to be transformed become angle of attack on aircraft center of gravity axes-system.

In the state estimation process, the stochastic model for states and/or parameters is proposed, and then the optimization method provides the algorithm to find the best values to represent unmeasurable states.

The application of Kalman filter is well used for state estimation, which provides a recursive solution to the minimum variance estimation problem for linear system with Gaussian variables. And then the extended Kalman filter (EKF) extends to nonlinear system by linearizing the non-linear model with a first order Taylor expansion around the current estimate. However, when the higher order terms neglected by linear model are significant, the EKF cannot converge to unbiased estimation.

This paper focuses on the implementation of a non-linear moving horizon state estimation (MHSE) from on board measurements aircraft's flight test data, similar to that proposed by Ari [1], and Robertson and others [2] combined with use the Armijo line search gradient.

[*] *Graduate Student*
[**] *Professor*
[***] *Lecturer*
[****] *Research Associate*

The MHSE is an interactive method to estimate unmeasured states, which optimizes a performance index subject to dynamic model of states and defined model of observation using a set of observation data. The data size that used to find the optimal estimation is called as horizon size.

Using real flight test data of parameters identification flights mission, this method is applied to reconstruct the aircraft flight path.

2. DYNAMIC MODEL

Consider the system described by non-linear dynamic model:

$$\begin{aligned}
\dot{x}(t) &= f_1(x(t), P(t), U(t)) \\
y(t) &= g_1(x(t), P(t)) + V(t)
\end{aligned} \tag{1}$$

where $x = [u\ v\ w\ \theta\ \varphi\ \psi\ h]^T$ is state vector,

$U = [p\ q\ r\ a_x\ a_y\ a_z]^T$ is input vector,

$y = [\alpha_v\ \beta_v\ \theta\ \varphi\ \psi\ h\ V_T]^T$ is measurement vector, $V(t)$ is measurement systems error assumed as a zero-mean, uncorrelated random process. The states model f_1 is similar to the kinematics equation model of nonlinear aircraft equations of motion in Etkin, [5]

$$\begin{aligned}
\dot{u} &= a_x - g\sin\theta - qw + rv \\
\dot{v} &= a_y + g\cos\theta\sin\phi + pw - ru \\
\dot{w} &= a_z + g\cos\theta\cos\phi - pv + qu \\
\dot{\varphi} &= p + q(\sin\varphi + r\cos\varphi)\tan\theta \\
\dot{\theta} &= q\cos\varphi - r\sin\varphi \\
\dot{\psi} &= (q\sin\theta + r\cos\varphi)\sec\theta \\
\dot{h} &= u\sin\theta - v\cos\theta\sin\varphi - w\cos\theta\cos\varphi
\end{aligned} \tag{2}$$

and the measurement model g_1 is described by nonlinear equation, as follows:

$$\begin{aligned}
\alpha_{cg} &= \tan^{-1}\left(\frac{w}{u}\right) \\
\beta_{cg} &= \sin^{-1}\left(\frac{u}{V_T}\right) \\
V_T &= \sqrt{u^2 + v^2 + w^2}
\end{aligned} \tag{3}$$

$$\begin{aligned}
\alpha_v &= P_1 + P_2\alpha_{cg} + P_3q \\
\beta_v &= P_4 + P_5\beta_{cg} + P_6r
\end{aligned} \tag{4}$$

$P = [P_1\ P_2\ P_3\ P_4\ P_5\ P_6]^T$ is vector representing unmeasured parameters of the instrumentation model of relationship between stability angles measured at vane (α_v and β_v) and at the center of gravity axes-system (α_{cg} and β_{cg}).

Where P(t) has a dynamic model

$$\dot{P}(t) = W(t) \qquad (5)$$

and W(t) is a zero-mean, uncorrelated random process.
In this dynamic model, the measured data of acceleration and angular velocity are taken as the inputs, whereas stability angles, attitude angles, altitude and airspeed are taken as the outputs, just because the former measurements give good precisions in the result of flight data measurements system.

  Equations (1) and (5) are combined to represent the augmentation model :

$$\begin{aligned}\dot{X}(t) &= f(X(t),U(t)) + W(t) \\ y(t) &= g(X(t)) + V(t)\end{aligned} \qquad (6)$$

where

$$X(t) = \begin{bmatrix} x(t) \\ P(t) \end{bmatrix} \qquad (7)$$

is augmented state vector.

3. MOVING HORIZON STATE ESTIMATION

  The moving horizon state estimation (MHSE) problem with *horizon size m* can be formulated as follows [1][2] :

$$\min_{X(t)} J(X(t)) = \frac{1}{2} V^T(t)\, Z\, V(t) \qquad (8)$$

in range time $[t, t+mT_S]$ subject to :

$$V(t) = y(t) - g(X(t)) \qquad (9)$$

where the initial value at t=0

$$X(0) = X_0 \qquad (10)$$

is known, and T_s is sampling time of measurement data, and Z is weighting matrix.

3.1 Optimization using Newton-Armijo Method

  To minimize performance index in equation (8), we have to find estimated $\hat{X}(t)$ such that

$$\left.\frac{\partial J(X(t))}{\partial X(t)}\right|_{\hat{X}(t)} = 0 \qquad (11)$$

If derivative of J(X(t)) with respect to X(t) above is defined as G(X(t)), thus the optimization of MHSE problem is to solve system of non-linear equation of the form :

$$G(X(t)) = 0 \qquad (12)$$

  Many methods have been proposed to solve this problem. In this paper Quasi-Newton method is used because it gives a convergence to the optimal estimate. Quasi-Newton

method is method of unconstrained optimization, which approximates the Newton search direction. And in order to improve the method to obtain 'globalized convergence', an Armijo type step-size will be added to this algorithm (called as Newton- Armijo method).

Assume that :
  (i) performance index J(X(t)) is twice Lipschitz continuously differentiable on bounded sets.
  (ii) second order derivatives of J(X(t)) or Hessian matrix is positive definite.

Then, the Newton-Armijo method to solve the problem as in eq. (12) can be formulated iteratively as follows [4].

$$\hat{X}_{n+1} = \hat{X}_n + \lambda_n H(\hat{X}_n)^{-1} G(\hat{X}_n) \qquad (13)$$

where $\hat{X}_n$ is the estimated value of X(t) on n-th step, $H(\hat{X}_n)$ is Hessian matrix of J(X(t)) on estimated value $\hat{X}_n$, and λ_n is Armijo step-size is formulated as follows :

$$\lambda_n = \max_{k \in N} \left\{ \beta^k \mid J(\hat{X}_n - \beta^k H(\hat{X}_n) G(\hat{X}_n)) - J(\hat{X}_n) \le \alpha \beta^k \left\| G(\hat{X}_n) \right\|^2 \right\}$$
$$(14)$$

where k is an integer and $\alpha \in \left(0, \frac{1}{2}\right)$ and $\beta \in (0,1)$ are known.

3.2 MHSE Algorithm

  To solve the MHSE problem subject to conditions in Eq. (8) – (10) of dynamic model in Eq. (6) numerically, firstly we define the initial values of states in time horizon $t = t_0$, X_0 such as in Eq. (10), define the constants α, β and precision parameters $\varepsilon, \varepsilon_1$, and then execute recursive algorithm as follows :

 (a) set i = 0.
 (b) check if $G(\hat{X}_i) \le \varepsilon$, then go to (c).
   compute λ_i as in Eq. (14), and Hessian :
$$H(\hat{X}_i)_j = \frac{1}{\varepsilon_1}[G(\hat{X}_i + \varepsilon_1 e_j) - G(\hat{X}_i)]$$
   where e_j is the jth column of the N X N identity matrix and N is state size.
   update :
$$\hat{X}_{i+1} = \hat{X}_i + \lambda_i H(\hat{X}_i)^{-1} G(\hat{X}_i)$$
   i = i + 1
   go to (b).
 (c) set $t = t+T_S$ and
$$\hat{X}_i = \hat{X}_i + \int_{t-T_S}^{t} f(X(\tau), U(\tau)) d\tau$$
   go to (a).
   (*repeat until* $t = t_0 + mT_S$)

4. FLIGHT PATH RECONSTRUCTION USING MHSE METHOD

  The calculation of the aircraft state trajectory from recorded input and output measurements is called as an aircraft state estimation or aircraft state reconstruction problem. Because in this case data of airspeed and altitude

output measurements are used, the aircraft state reconstruction problem is subsequently called as flight path reconstruction problem. [6]

The purpose of aircraft flight path reconstruction is to provide a check on instrument accuracy and data consistency apart from generating estimates of unmeasured variables. The instruments accuracy is to provide some measured variables of calibration model, e.g. airspeed, angle of attack, side-slip angle, altitude etc. and estimating of unmeasured variables is to provide generating of optimum or robust control law that's results some automatic control designs [3].

In order to reconstruct the aircraft flight path, dynamics motion type of flight test is required. Some methods to conduct the dynamics motion with optimum input are proposed. One of most popular methods is using doublet pilot input command. Flight test data of the N250 PA-1 aircraft is used for purpose of parameter identification. In case of lateral-directional dynamic modes, aileron and rudder doublets are inputted, and in case of longitudinal dynamic modes, elevator and engines power lever doublets are inputted. With respect to the available range of control surface deflection, engine power, PIO, and stability of aircraft, required amplitude and time period of each doublet input for various aircraft conditions (airspeed, altitude, and flaps setting) are evaluated using flight simulator.

For 150 knots of equivalent airspeed, 10000 feet of altitude and cruise condition, in case of lateral-directional dynamic modes, the doublet rudder is inputted 1 degree of amplitude, 4 seconds of time period and it takes 25 seconds until steady state condition occurred, and then followed by the doublet aileron with 2 degrees of amplitude and 4 seconds of time period. For longitudinal dynamic modes, the doublet elevator is inputted 2.5 degrees of amplitude, 4 seconds of time period and 5 seconds until steady state condition occurred, and then followed by the inputted engine power lever with 12% of amplitude, 4 seconds of time period (see Figure 1).

The aircraft responses are shown by measured variables: side-slip angle (AOS), roll angle, heading angle (lateral-directional), and angle of attack (AOA), pitch angle, altitude, true airspeed (longitudinal) in Figure 2 (left side) where flight test data are recorded using 20 Hz data sampling rate. An execution of the MHSE using the present algorithm is almost converging to optimum estimated states in different number of iterations. The number of iterations required is depending on how big a precision parameter ε is given, and also how fine the initial condition of dynamic model in Eq. (6) is available.

In this case the value of ε is 0.00001, the size of horizon time is 13, and initial condition is determined by deriving states in steady condition at a few seconds before pilot command is inputted. The results of estimation using MHSE are shown in Figure 2 (right side) for states and in Figure 3 for parameters. The result of calibration model of AOS and AOA in Equation (4) is represented by convergence points:

- offset angle : 2.5 degrees (P_1), -0.4 degrees (P_4),
- gradient : 0.8 (P_2), 1.2 (P_5)
- time delay due rate angle: 0.06 seconds (P_3, P_6)

In Figure 2, we can see that the consistency of data between flight test data measurement system with reconstructed data using dynamics and instruments model in Eqs. (2) – (4) are good, where time histories of the estimated observations agree well with the measured observations. The measurements

system accuracy can be evaluated as not greater than 0.5 degree (in dynamic), or 0.1 degree (in steady) for angle measurements, 0.5 knot for true airspeed and 20 feet for altitude.

5. CONCLUSIONS

An application of MHSE method to aircraft flight path reconstruction is presented. In order to find the optimal estimation, the nonlinear optimization using Quasi-Newton combined with Armijo type step-size method is proposed. The result of this optimization showed that the present MHSE method is useful for system parameter estimation and flight path reconstruction.

References:

1. Ari, S.,"Non-linear System Process Estimation using MHSE method", Research Progress Report, Institute of 10th November Surabaya, 1999.
2. Robertson D.G., J.H. Lee, and J.B. Rawlings, "A Moving Horizon-based Approach for Least Squares Estimation", AICHE J.,Vol.42, No.8, pp. 2209-2224, 1996.
3. Ohtsuka, T., and Fujii, H., "Non-linier Receding horizon State Estimation by Real-Time Optimization Technique", J. Guide, Contr., and Dyn., Vol.19, No.4, pp. 863-890, 1996.
4. Polak, E., "Optimization : Algorithms and Consistent Approximations", Springer – Verlag, New York, 1997.
5. Etkins, B., "Dynamics of Flight : Stability and Control", John Wiley & Sons, 1995.
6. Mulder, J.A, Chu, Q.P., Sridhar, J.K., Breeman, J.H., Laban, M., "Non-linear Flight Path Reconstruction review and New Advances", Progress in Aerospace Sciences 35, pp. 673-726, 1999.
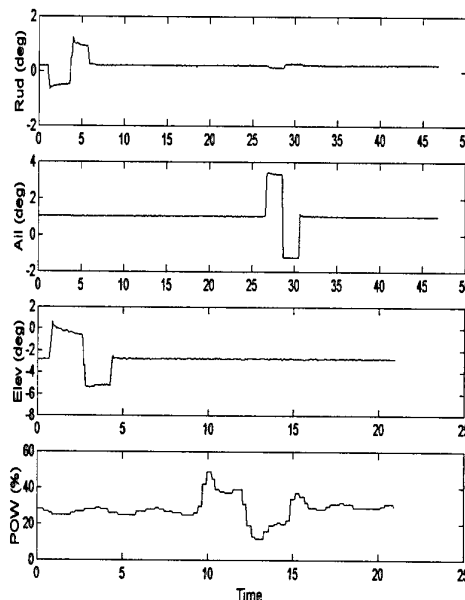
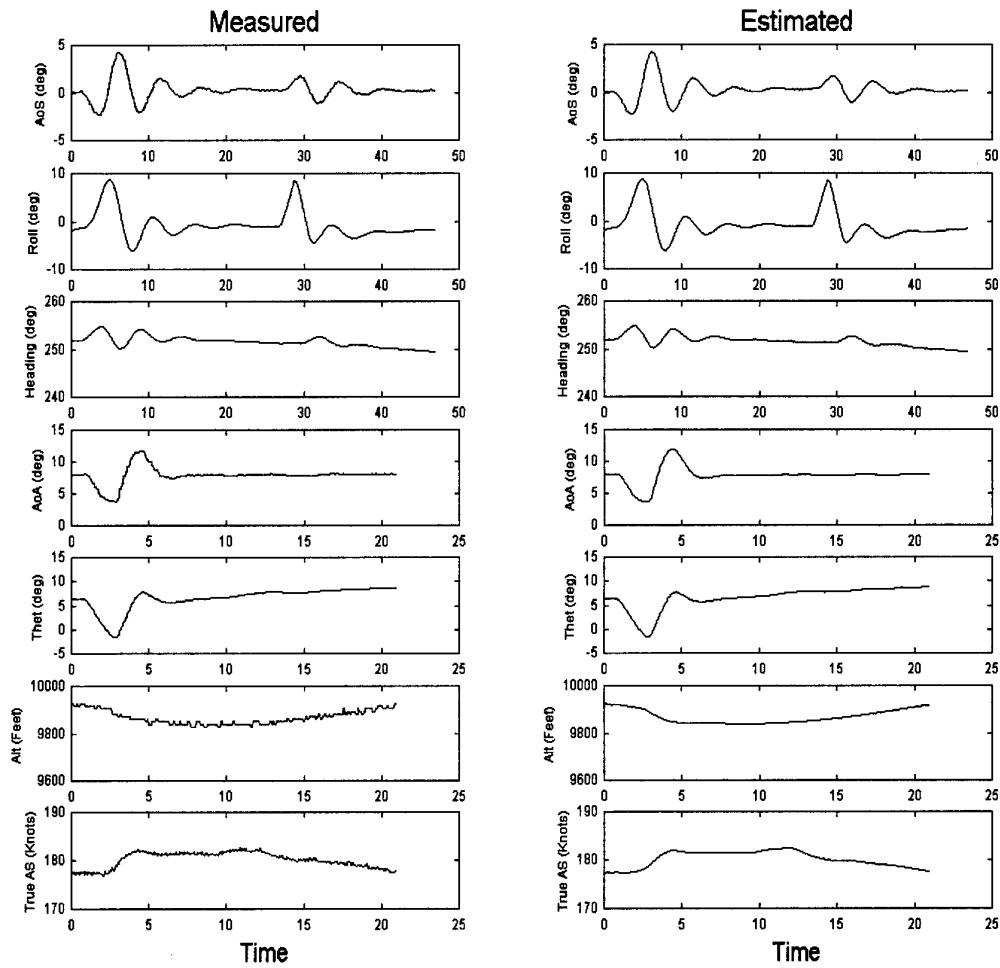Figure 1. Aileron, rudder, elevator and engine power doublet
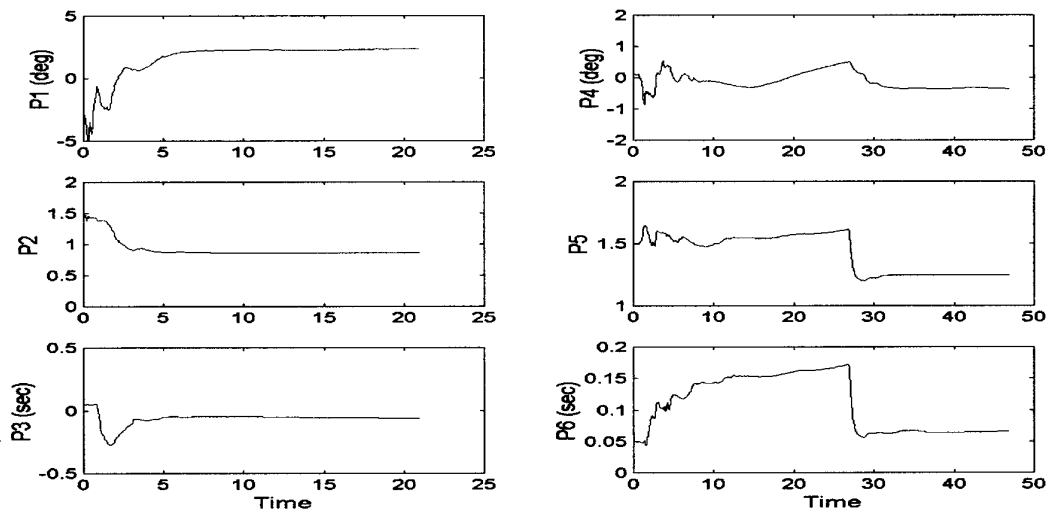
Figure 2. Measured and estimated observations

Figure 3. Estimated parameters

1E13 A GRAPHICAL USER INTERFACE FOR AN ADAPTIVE EXTENDED KALMAN FILTER PROGRAM FOR AIRCRAFT PARAMETER ESTIMATION STUDIES

R.M.O.Gemson[*], M.R.Ananthasayanam[**], M.R.Muralidharan[**]

[*]Hindustan Aeronautics Limited, Bangalore, INDIA
[**]Indian Institute of Science, Bangalore, INDIA

Key Words: Estimation Theory, Aircraft Parameter Estimation, Extended Kalman Filter

ABSTRACT

The implementation of the Method of Maximum Likelihood Estimation (MMLE) in estimation theory can be by optimisation or the filtering approach. This paper describes the implementation of a variant of the latter namely the Extended Kalman Filter (EKF) with an adaptive technique for tuning the filter parameters implemented in FORTRAN with an MS Windows based user friendly front end. This helps to analyse with ease, rapidity, and efficiency a range of simple to complex systems. This has been found to be an effective tool for teaching and research in the filtering technique in estimation theory.

1. INTRODUCTION TO EKF

The most general problem in state and parameter estimation technique consists of qualitatively modelling the system, measurement, process and measurement noise characteristics and to quantitatively determine all the unknown parameters in the above by combining the information in the model output with the measurement in some suitable optimal sense. A general nonlinear continuous system and discrete measurement model can be described by

$$\dot{X} = F(X, U, \Theta, t) + w(t); \quad X(0) = X_0$$

$$Z = G(X, U, \Theta, t_k) + v(t_k); \quad k = 1,2,\ldots\ldots N$$

where X, Z, Θ, U, w, and v denote the states, measurements, unknown parameters, control inputs, state and measurement noise matrices of appropriate order. The measurements at a time step are denoted by a subscript. The process and measurement noise have zero mean with covariance Q and R respectively. The time evolution of the estimate and covariance of state variable X in terms of the transition matrices ϕ and ψ obtained by suitable local linearisation are

$$X_k^- = \phi_{k-1} X_{k-1} + \psi_{k-1} U_{k-1}; \quad X(0) = X_0$$

$$P_k^- = \phi_{k-1} P_{k-1} \phi_{k-1}^T + Q_k; \quad P(0) = P_0$$

$$Z_k = H_k x_k + v_k$$

---

* Additional General Manager
** Associate Professor and Senior Scientific Officer

The superscript (-) indicates the estimate before using the measurement information. Thus we have at time t_k an estimate

$$X_k^- \text{ with covariance } P_k^-$$

and another from the measurement namely

$$Z_k \text{ with covariance } R_k$$

when combined optimally provides

$$X_k^+ = X_k^- + K_k[Z_k - H_k X_k^-] = X_k^- + K_k v_k$$

$$P_k^+ = [I - K_k H_k] P_k^- [I - K_k H_k]^T + K_k R K_k^T$$

where v_k is the innovation and the Kalman Gain

$$K_k = P_k^- H_k^T [H_k P_k^- H_k^T + R_k]^{-1}$$

When a linear system is driven by white noise the Gaussian distributed state X^- evolve with modified mean and covariance. The linear measurement equation also provides a Gaussian distributed Z. Then the conditional probability distribution of X given Z namely $p(X|Z)$ is also a Gaussian. Thus linear systems, measurements, and white noise match to keep X and Z as a Gaussian. But if either the system or the measurement is nonlinear the Gaussian structure is changed and one resorts to quasilinearization at every point, or over the full data to deal with the problem. The innovation follows a Gaussian distribution whose probability when maximised leads to the cost function

$$J = (1/N) \sum_{i=1}^{N} v_k [H_k P_k^- H_k^T + R_k] v_k^T$$
$$= J (X_0, P_0, Q, R, \Theta)$$

which is basically a batch processing nonlinear optimisation problem and the numerical effort cannot be avoided. For minimising J, we have to tune the statistical noise covariances which are usually assumed to be diagonal. This is the filter 'tuning' approach. Among the unknowns Q is the most 'notorious' one. When $Q = 0$, the above reduces to the so called output error method. If the unknown parameter Θ is also considered as an additional state then the formulation is known as the Extended Kalman Filter (EKF).

2.ADAPTIVE ESTIMATE OF P_0, Q AND R.

The general methodology of any filter estimation algorithm is to update the X_0, P_0, Θ, R and Q at a point, over a window, after a pass or after multiple pass by applying some corrections to them based on changes, iterations or sample statistics such that the numerical procedure does not diverge but converges to the best possible estimates based on the information contained in the data.

The residual sequence r_k is a measure of the measurement noise $r_k = Z_k - H_k x_k$ for which an unbiased estimate for R is taken as[1]

$$R_{est} = (1/N) \sum [\{r_k - r_m\}\{r_k - r_m\}^T - H_k P_k^- H_k^T]$$

where the subscript 'm' denotes the mean. The summation is over the window of time points.

Similarly a measure of the state noise sample $q_k = X_k^+ - X_k^-$ and an estimate for Q is given by[1]

$$Q_{est} = (1/N) \sum [\{q_k - q_m\}\{q_k - q_m\}^T - (P_k^+ - P_k^-)]$$

The initial covariance matrix P_0 is given by[2]

$$P_0 = [(1/N) \sum \{\phi_k H_k^T R_k^- H_k \phi_k]^{-1}$$

where the quantity inside the bracket denotes the information matrix. The following are the suggested steps[2] to obtain P_0, Q and R.

1. An initial value of diagonal R is assumed.

2. Set Q identically equal to zero.

3. Make a scouting first pass with a reasonable P_0 or even a unity matrix and obtain P_0 from the inverse of information matrix of this pass.

4. With P_0 from Step 3 iterate for Q till the cost function J converges.

5. With the above converged Q obtain R.

6. Initialize the filter with the above value of R and repeat from Step 2 till R does not change between two estimates obtained in Step 5.

3. WINDOW BASED EKF SHELL

1. After entry into the SHELL, the first menu is the MAIN containing the algorithm and this helps the user to select the main FORTRAN program, list the subroutines, function, edit them or even exit.

2. The next menu SYSTEM has to be provided by the user characterising his particular system to be analysed. It can list the routines and also edit them.

3. The INPUT menu also provided by the user helps to analyse his system and changes in it can be made by the EDIT menu.

4. The VIEW menu shows the input data in the EKF FORTRAN program format.

5. The COMPILE/RUN menu helps to compile MAIN and SYSTEM later link and create the executable file. Before commencing the RUN, checks if all the earlier output files are to be deleted or not and runs the program.

6. The OUTPUT menu item has all the FORTRAN output files which can be plotted and visualised.

7. Further experiments can be carried out by changing the parameters in the various routines and in particular the INPUT and analysing the results.

Typical dialogue boxes and the menu are shown in Figure 1. It is possible to obtain a large number of outputs using suitable programs available to the user. In Figure 2 among many that are possible, one sample plot of the results from the lateral dynamics of an airplane involving 3 states, 5 measurements, and 13 unknown parameters have been shown. Any large sized system or data can be handled when a suitable compiler is available.

4. SYSTEM REQUIREMENTS

- An IBM personnel computer or 100 percent compatible running MS DOS ver 4.0 or later.
- A VGA or SVGA monitor.
- An 80386 or higher processor.
- Microsoft Windows 95.
- A Fortran Compiler.

5. CONCLUSIONS

A user friendly software helpful in teaching and research activities in parameter estimation studies through EKF has been developed. This enables one to experiment rapidly on a large number of systems with varying complexity and in particular real flight test data of aerospace vehicles[2].

REFERENCES

1. Myers, K.A. and Tapley, B.D. "Adaptive Sequential Estimation with unknown Noise Statistics", IEEE Trans Automatic Control, Vol. AC 21, pp 520-525, (1976).

2. Gemson R.M.O. and Ananthasayanam. M.R. "Importance of Initial State Covariance Matrix for the Parameter Estimation using an Adaptive Extended Kalman Filter". AIAA-98-4153 (1998).
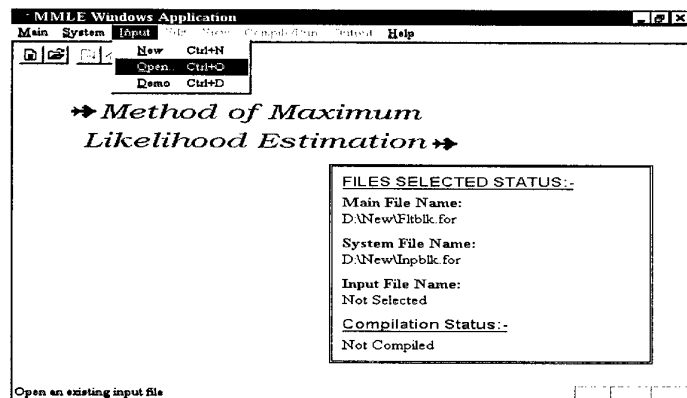
FIGURE 1A. THE MAIN, SYSTEM, AND INPUT DIALOGUE BOXES AND MENUS.
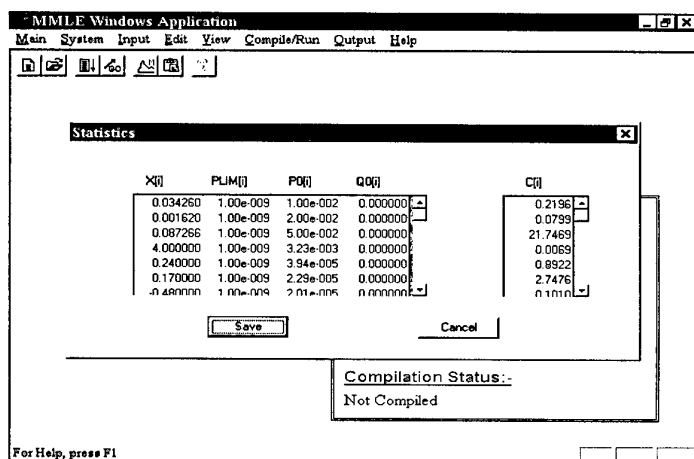

FIGURE 1B. GRIDS SHOWING TYPICAL INPUT STATISTICS.
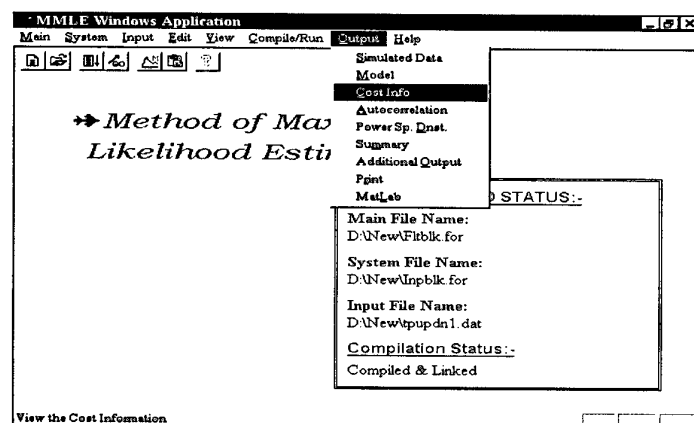

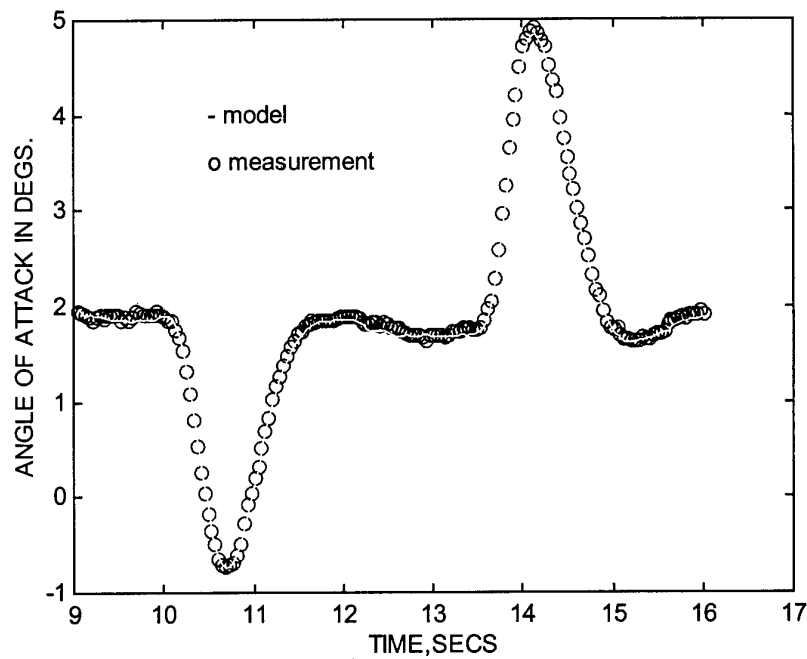FIGURE 1C. DIALOGUE BOX SHOWING TYPICAL OUTPUTS.

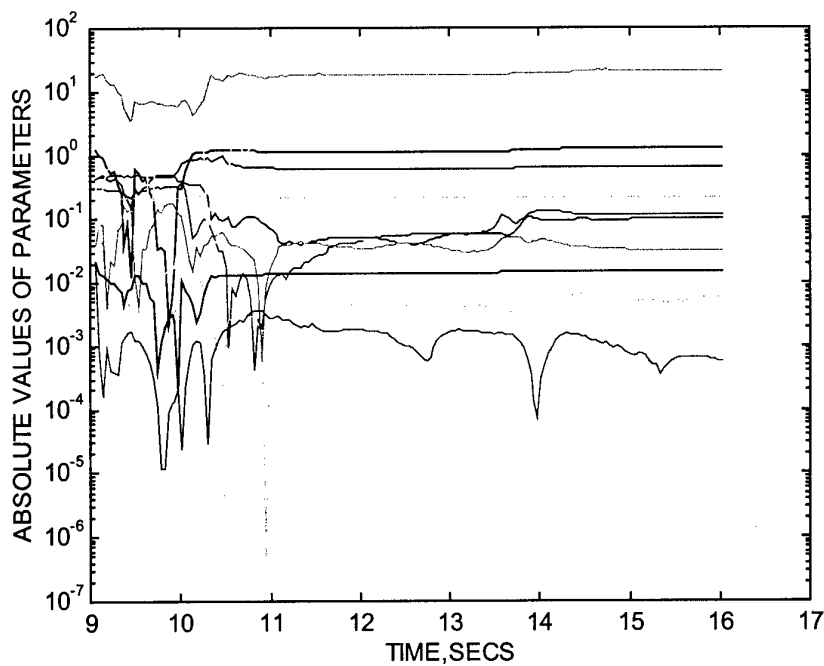FIGURE 2A. COMPARISON OF ONE OF THE MEASUREMENTS WITH MODEL OUTPUT.

FIGURE 2B. TYPICAL VARIATION OF THE PARAMETER ESTIMATES WITH
TIME FOR THE LATERAL MOTION OF AN AIRPLANE.

1E14   APPLICATION OF PROBABILITY, STATISTICS, RANDOM PROCESS AND ESTIMATION THEORY CONCEPTS IN AEROSPACE ENGINEERING

M. R. Ananthasayanam[*]

Indian Institute of Science, Bangalore, INDIA, 560012

Key Words: Aerospace Education, Probability, Statistics, Random Process, Estimation Theory

ABSTRACT

This paper discusses the concepts in probability, statistics, random process, and estimation theory from an engineering viewpoint and their use in aerospace engineering. Some illustrative examples highlight the useful features from the above topics.

1. PROBABILITY

Determinism dominated science since the earliest times of Newton. The seeds of probabilistic approach also cast around that time has now percolated to almost all branches of science and technology. Some of the compulsive reasons in many situations for a probabilistic approach are uncertainty, variability, complexity, and enormity. A simple coin tossing has all these in the nature of the initial conditions and the interaction of the large number of air molecules among themselves and with the coin. If ontology refers to the nature of the system and epistemology refers to our knowledge of the system, then coin tossing is ontonic determinism but epistemic indeterminism. Only quantum mechanics is truly probabilistic. Examples of random behaviour are the molecular, brownian, atmospheric motions, queues, voltage fluctuation in an electron tube, or a turbulent fluid flow.

Almost any deterministic numerical method can be carried out alternatively by a probabilistic approach involving randomness called Monte Carlo techniques. In many cases the latter could be a better approach. But there are also occasions when it is perhaps compulsive. Examples necessitating the compulsive use of randomness are the random location of correct answers in a multiple choice question paper, game theory, introduction of random noise to track aerospace vehicles when their equations of motion and/or the input cannot be modelled perfectly.

The analysis of systems displaying randomness is possible due to some of their stable characteristics over many outcomes in spite of any given outcome being random. Then what is the use of the prediction with a probability of 60% for it to rain tomorrow? Tomorrow either it rains or does not rain! The point is with the above prediction, different persons could take a variety of decisions such as not to go out, or go out with an umbrella, go out and borrow an umbrella, or stay outside overnight. Note that without a specific prediction of the probability regarding the arrival of rain the decisions could not have been made.

There are broadly three or more approaches to probability theory depending on which book you read! An interesting feature is the assignment of the probability for the occurrence of an event itself is extra probabilistic! The classical approach enumerates all possible outcomes and assigns equal probability for all. The axiomatic approach provides a certain freedom for the above assignment in a precise event scenario and the frequency approach takes the fraction of success by repeated experimentation. However there are difficulties in all the above. Enumeration may not be always possible uniquely, the subjective assignment of probability may not be quite correct and repeated experiments may just be impossible as for accidents or for landing a man on the moon. The Figure 1 shows how the above approaches as various hypothesis whose probability of being true can be updated by utilising the Baye's theorem of probability. Another way to consider the above is with increasing amount of information. Thus in the absence of any information the first is equally likely, and with the background or previous knowledge an improved probability assignment is possible and lastly with observational data a refined assessment of the probability can be made. If nothing else one can take a purely operational attitude namely based on the rules of the probability theory the results from it work in practice never mind if the meaning of probability or any other concepts in it are understood or not!

All practical useful inferences from probability are based on events whose probability is close to zero or one implying respectively practically impossible or certain occurrence. The theorems of weak and strong law of large numbers pertaining to such events have a great epistemological value. In fact the strong law is a connecting link between the probability theory and the real world though there are difficulties of conducting repeated experiments under identical conditions, independently and an infinite number of times. Further one can note that in probability theory the term 'probability' as it implies intuitively or really so refers to occurrences but based on a large number of repeated trials which is an 'ensemble'. It is only in statistics one deals with a single outcome or a member of the above 'ensemble' and wish to draw inferences about the fundamental event probabilities of the system.

---

[*] Associate Professor

2. STATISTICS

One simple way to view statistics is as an inverse problem to probability. As shown in Figure 2a the later predicts the outcome of events in an ensemble and the former based on the sample events infers the probability. A unique solution with finite data is generally possible only with some additional subjective criteria. Even the central tendency for a probability distribution is not unique leading to estimates like mean, median, and mode which are themselves useful in many different contexts. Hence statistics is highly subjective! Next consider the problem of fitting a linear relationship to two random variables X and Y as in Figure 2b. When the data is plotted there are a few points called outliers which are far away, and statistics cannot tell us if they should be included or not in the analysis. Some additional subjective criteria is needed to include or preclude them from the analysis. Further even after such outliers are removed the linear relationship cannot be made unique without a subjective criterion such as minimising the sum of the square of the departure from the fitting line should be a minimum or any other reasonable criteria.

Further even to determine the quantity 'A' in a simple linear relationship between X and Y as X = A Y when noisy measurements of X and Y are available is not easy. The least squares estimate will tend to the correct value if only the noise in the measurements of Y is zero. Thus in practical sophisticated dynamical problems one can see the necessity of having sound theoretical methods to obtain estimates which asymptotically approach the correct values. The Method of Maximum Likelihood Estimation (MMLE) was developed in statistics by Fisher in 1922. This estimator has sound desirable statistical properties such as being asymptotically unbiased, efficient, consistent and sufficient. These ensure that as the sample size increases the estimates approach the true value, be within smaller region, is the best possible from the data, and utilise all the information in the sample.

Since statistical samples are used to draw inferences about a population, it is necessary (i) to model the population, (ii) propose a criteria to fit the sample data with the assumed model, (iii) an algorithm to carry out the above matching to draw probabilistic inferences and lastly (iv) a consistency check of the above features, thus generally four steps in all. The task of modelling is based on some previous feel, experience or information about the system. Many systems are deterministic being governed by well known Newton's laws of mechanics or gravity, or laws in electricity, and magnetism and so on. If some systems are stochastic in nature like the population, flow in rivers, stock market, then appropriate stochastic models have to be considered. Among the models there could be true, best, or adequate and generally the last one is used. The second of the above steps leads to a large number of possible estimators like the moment method or the well known MMLE. This latter is the most widely used technique for the state and parameter estimation problems in the field of aerospace engineering. The algorithms utilised to satisfy the criterion could be in batch, sequential, or even in real time as most present day activities demand and the middle one is possible due to the filtering techniques, and the last due to the availability of enormous computing power and speed. The fourth of the steps utilises statistical hypothesis to check and draw inferences about the results from the estimation process. This helps in general mainly to decide if the behavior of a certain quantity is due to statistical fluctuation or due to a deterministic change. Once again the choice of the confidence level with which the inference can be made is not provided by statistics by by extra-statistical considerations! If the confidence level is large (or small) then the uncertainty in the estimates will be large (or small) making them useless (or unreliable). Hence in each application one has to decide the level based on the further extra-statistical consequences that would follow by the choice.

3. RANDOM PROCESS

The time dependent behaviour of a probabilistic system is a random process. Since most of present day activities generally involve the time dependent evolution of the state x of a dynamical system with random inputs also, the random processes have to be modelled. The distribution function describing the probability of a random variable possessing values for all times t becomes mathematically highly intractable and so to impart an element of dynamics a joint distribution function characterising x at two different time points is introduced. To simplify further only the behaviour in terms of an autocorrelation function $R(\tau)$ where τ is the time difference is introduced. Typical random processes with slow and fast time scales together with their autocorrelations are shown in Figure 3. The rate with which the above decays provides a clue to the various time scales involved in a given physical process involving randomness. The distribution of the amplitudes of the above scales denotes the energy content called the power spectral density.

Interestingly there is an advantage when a random variable is characterized instead of being left as random without any characterization. This is like providing some rules of a game which makes it interesting to study a system. Compare a game of 'draught' and 'chess'. There is an optimum, simple set of rules providing an excitement to deal with systems be it in aerospace or society. The simplest description of a random process is a Gaussian distribution at any time t and across time is white, meaning $R(\tau)$ is a Dirac delta function with unity for zero lag and zero everywhere else meaning uncorrelated. These assumptions provide a very good mathematical tractability. The reason for using a normal distribution is that a large number of situations involving random variations in nature follow it though are many others where it does not. Under fairly general conditions, the distribution of the sum of many independently distributed random variables each obeying arbitrary distribution but with finite variance, approaches

a normal distribution. From the point of view of information theory knowing only the mean and the variance, namely the least amount of information or the maximum entropy then the distribution obeyed by the constituents can be shown to follow a normal distribution. However since white noise has constant energy at all frequencies the total energy becomes infinite which is physically not possible. Since physical systems have inertia (in whatever sense it could be) changes cannot be instantaneous leading to correlation in their behaviour for a finite amount of time difference τ. Hence instead of a white noise which is a Gauss-Markov (GM) process of zeroth order higher order GM processes are introduced. These can be generated as outputs of suitable linear systems called shaping filters by white noise as the input.

4. ESTIMATION THEORY

The estimation theory (ET) can be viewed similar to what statistics is to probablity as an inverse problem to random process. All the four steps from statistics as above have been completely taken over in estimation theory. The MMLE has become the workhorse for all estimation problems involving dynamical systems in the field of aerospace engineering be it a spring, mass, and damper system or a space shuttle. In ET one generally chooses suitable qualitative models for the system and the measurement and their noise characteristics and quantitatively estimate the parameters Θ in them by optimizing a suitably chosen cost function J which is a function of the model output and the measurements. The above J can be in time or frequency domain. The processing of the measurement data can be in a batch mode of optimisation or through a sequential processing mode of Kalman filter or its variants. ET estimates the 'unobservable' parameters Θ and can also further expand the system states or even estimate the 'unmodellable' inputs. The ET provides better estimates from more and more noisy data by statistical estimation by probabilistically mixing the data from various sources at different rates with varying accuracies by appropriate weight depending on their uncertainties. Thus one achieves improved state as well as measurements, filters the noise and smoothes the measurements. Further it can be shown that ET is also capable of handling deterministic errors, deficiencies in the system and the measurement models or numerical errors by the addition of random noise. Some important benchmarks in the evolution of ET are shown in Figure 4.

5. EXAMPLES OF APPLICATIONS

The question of whether road or air travel is safer is ambiguous. If the number of fatalities are considered per kilometer then both are about equally safe. But based on per hour of travel road travel is more safe. Though for all practical purposes people can be safely advised to fly there are many who have sworn never to fly! Such people think of the situation subsequent to an engine or control failure whereas the airworthiness codes are based on the probability of engine failure and subsequently the performance going below an acceptable level. Thus one may note the scenario has to be precisely stated which shows the importance of axiomatic approach. It is the former situation subsequent to an engine failure that is implicitly accounted for in the ETOPS of airplanes. The unavoidable subjective differences in the approach in meeting the safety standards can be seen in the design of large long range airplanes with twin engines by Boeing and with four engines by Airbus.

A large number of regression relations connecting the mass, geometric, aerodynamic, structural and propulsive characteristics are very useful for the preliminary design sizing of airplanes. The confidence level with which launch vehicles are designed for wind loads depend on the cost effectiveness. If one desires to design an airplane or a launch vehicle capable of operating under all atmospheric conditions it would not be economical at all.

The fleet performance of an airplane type with airframe and engine maintenance checks at various times is a random process. The probability distributions of the performance behavior of airplanes in fleet service help to formulate the airworthiness codes. Turbulent flow is a random process whose understanding and control is highly beneficial for the drag standards and economy of airline operations.

The flight test data analysis based on the MMLE or the Kalman filter techniques for the stability and control derivatives of an airplane provides a very important input for simulation, envelope expansion, control law design, and handling characteristics. The point mass radar measurements of an airplane when combined with a suitable dynamical airplane model helps to expand the state scenario to infer the three dimensional motion and the control actuation to study an accident. There are many ways in which the data from a variety of sources such as the radar, telemetry, star, and GPS can be effectively combined in offline or online mode. This helps to study the operational characteristics such as the position and attitude of a satellite. These are typical applications of the concepts in probability, statistics, random process, and estimation theory in aerospace and in particular in the topic of flight mechanics.

REFERENCES

1. M.R. Ananthasayanam, Lecture Notes on 'State and Parameter Estimation Techniques'. Hindustan Aeronautics Limited, Bangalore, November 1999.
2. C.R. Rao, 'Statistics and Truth' (Putting Chance to work). Ramanujan Memorial Lectures. Council of Scientific and Industrial Research, India. 1989.
3. A. Papoulis, 'Probability, Random Variables, and Stochastic Processes' Third Edition. McGraw-Hill International Editions. 1991.
4. R.G. Brown, and P.Y.C. Hwang. 'Introduction to Random Signals and Applied Kalman Filtering. Third Edition. John Wiley and Sons. 1997.
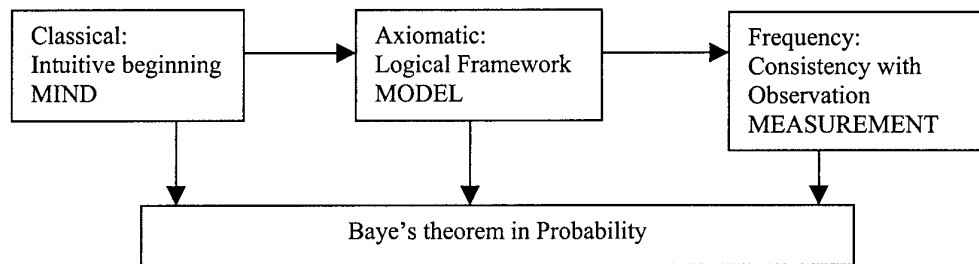
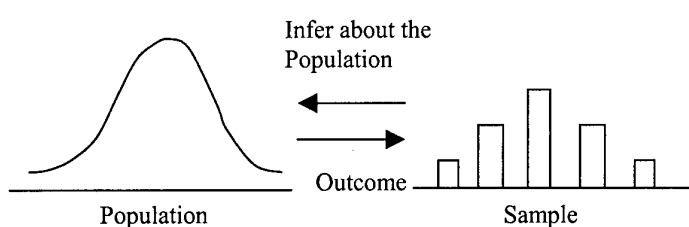Fig 1. Different Approaches to Probability theory and their Connections.

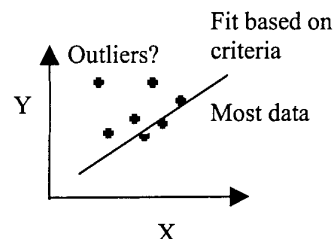Fig 2a. Statistics as Inverse to Probability.
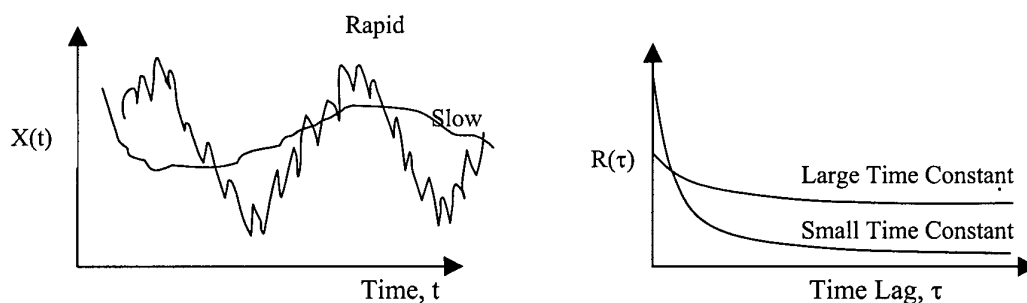
Fig 2b. Some _____res of Data analysis.

Fig 3a. Time Variation of Random Processes and their Autocorrelation Functions.

Newton	Gauss	Fischer	Kalman	Present Day
1687	1795	1922	1960	
Deterministic MODEL	Deterministic/ PROBABILISTIC APPROACH	STATISTICAL ESTIMATION MMLE	SEQUENTIAL PROCESSING of Data by OPTIMIZATION	BATCH PROCESSING OF MASSIVE DATA from uncertain model , measurement with random inputs to be handled BY FILTERING IN REAL TIME

Fig 4. Some Important Benchmarks in Estimation Theory.

IL2 Towards Accuracy and Efficiency for Practical CFD Simulations

Meng-Sing Liou*

NASA Glenn Research Center, MS 5-11, Cleveland, OH 44135, USA

(216) 433-5855, fsmsl@yinyan.grc.nasa.gov

Abstract

Enormous progress in computational fluid dynamics (CFD) has been made in the past towards achieving accurate solutions efficiently for flows in complex configurations. However, the solution still requires an advanced computing system, a fast and general grid generation capability, reliable numerical algorithms, as well as physical modelling to make CFD a routine engineering approach for analysis and design. Nevertheless, the goals of making CFD as a tool from research to common engineering practice and providing usable solutions in a timely manner appear to be within our reach. In this paper, we will address our efforts in addressing the efficiency and accuracy aspects in practical CFD simulations. In this regards, we shall specifically discuss the recent development of numerical flux scheme, AUSM$^+$and grid generation technique, DRAGON grid.

1 Introduction

In addressing the issues of accuracy and efficiency, we will demonstrate how they are affected by the advances in numerical algorithm and grid generation. Following the development of the AUSM-family schemes [1-3], we proposed the concept of numerical speed of sound [4], allowing an easy extension to low Mach number flow and multiphase flow [5,6]. It leads to improvements not only in convergence rate, but also in solution accuracy. To drastically shorten the time spent by the current methods on grid generation, we have developed a novel hybrid grid, called the DRAGON grid approach. This approach improves the overset grid approach by preserving conservation property and the unstructured grid approach by reducing its intensive memory requirement and automatically allowing high-quality hexahedral cells for resolving viscous layers at the walls.

We solve the Reynolds-averaged Navier-Stokes equations written in curvilinear coordinates (ξ, η, ζ) and conservation form:

$$\mathbf{Q}_t + \mathbf{F}_{l,l} + \mathbf{F}^{(v)}_{l,l} = 0, \quad l = 1, 2, 3 \ (\xi, \eta, \zeta). \quad (1)$$

The conservative variables are given in $\mathbf{Q}$ and the inviscid and viscous fluxes are $\mathbf{F}_{l,l}$ and $\mathbf{F}^{(v)}_{l,l}$. Since they are standard, their definition is omitted herein.

Discrete forms of these equations are solved numerically. To accelerate convergence to steady or unsteady solutions, several appraoches can be taken. In the 80s, a great deal of effort was devoted to the study of implicit methods in which either ADI [7] or LU [8,11] factorization is commonly used to solve the linearized set of matrix equations. In addition, multigrid methods [9] have also developed to top the convergence rate off the baseline iteration methods.

During the 90s, interest has been focused on the development of (local) preconditioning method to improve convergence rate in the low Mach number regime. This is accomplished by premultiplying the time-derivative term with a conditioning matrix $\boldsymbol{\Gamma}$,

$$\boldsymbol{\Gamma}\tilde{\mathbf{Q}}_t + \mathbf{F}_{l,l} + \mathbf{F}^{(v)}_{l,l} = 0, \quad \tilde{\mathbf{Q}} = (p, u, v, w, T)^T / J. \quad (2)$$

Several forms for the local preconditioning matrix $\boldsymbol{\Gamma}$ have been proposed. We have chosen the one proposed by Weiss and Smith [10].

---

*Senior Scientist

As for the numerical flux, immense interest was generated in the 80s, in developing methods under the category of flux vector and flux difference splittings. These notably include the Steger-Warming [11], van Leer [12] flux vector splitting schemes, and the Roe [13] and Osher-Solomon [14] flux difference schemes. In the 90s, we saw a continuing interest in improving these schemes. The AUSM family of schemes have been proposed and received considerable attention. Now they have been incorporated in many research, as well as commercial, codes. Among the several desirable features bestowed on the schemes, the most notable one is the capability of producing solutions free from the so-called "carbuncle" phenomena, see Fig. 1 [15].

2 Numerical Flux: AUSM$^+$Family

In this section, we will give a brief description of the algorithm involved in the AUSM$^+$scheme and the new development for low-speed flows. Concerning detailed numerical properties and detailed analysis, the reader should consult the above-cited references.

For illustration purpose, we shall begin by considering the 1D flux. The inviscid flux $\mathbf{F}$ is written as a sum of convective and pressure fluxes:

$$\mathbf{F} = \rho u \begin{pmatrix} 1 \\ u \\ H \end{pmatrix} + \begin{pmatrix} 0 \\ p \\ 0 \end{pmatrix} = \overset{\bullet}{m} \begin{pmatrix} 1 \\ u \\ H \end{pmatrix} + \begin{pmatrix} 0 \\ p \\ 0 \end{pmatrix} = \overset{\bullet}{m} \boldsymbol{\Phi} + \mathbf{p}. \tag{3}$$

The vectors $\boldsymbol{\Phi}$ and $\mathbf{p}$ are introduced respectively as shown. It is noted that a common mass flux $\overset{\bullet}{m}$ appears in all equations. This is also true for multidimensions. Hence, it is desirable that this fact at the discrete level be enforced. This leads to an easy extension to add other equations, such as chemical species or turbulence models equations.

Firstly, a simple upwinding is applied to the convected quantity $\boldsymbol{\Phi}$ to yield the numerical flux at the cell interface (denoted by subscript 1/2)

straddling cells j and $j + 1$.

$$\mathbf{f}_{1/2} = \frac{1}{2}[\overset{\bullet}{m}\ (\boldsymbol{\Phi}_j + \boldsymbol{\Phi}_{j+1}) + |\ \overset{\bullet}{m}\ |(\boldsymbol{\Phi}_j - \boldsymbol{\Phi}_{j+1})] + \mathbf{p}_{1/2}. \tag{4}$$

The mass flux is also defined by a simple upwind formula,

$$\overset{\bullet}{m}_{1/2} = \frac{\tilde{a}_{1/2}}{2}[M_{1/2}(\rho_j + \rho_{j+1}) + |M_{1/2}|(\rho_j - \rho_{j+1})], \tag{5}$$

where $\tilde{a}_{1/2}$ is a novel parameter in the formulation and will be described shortly.

The interface Mach number and pressure flux are expressed in the following forms,

$$M_{1/2} = \mathcal{M}^+(\tilde{M}_j) + \mathcal{M}^-(\tilde{M}_{j+1}), \tag{6}$$

and

$$p_{1/2} = \mathcal{P}^+(\tilde{M}_j)p_j + \mathcal{P}^-(\tilde{M}_{j+1})p_{j+1}, \tag{7}$$

where $\mathcal{M}^\pm$ and $\mathcal{P}^\pm$ are polynomials whose details can be found in [2].

The Mach number $\tilde{M}$ based on $\tilde{a}$ is

$$\tilde{M}_{j/j+1} = \frac{u_{j/j+1}}{\tilde{a}_{1/2}} = \frac{M_{j/j+1}}{f_a}. \tag{8}$$

A concept of numerical speed of sound is introduced in [4] to make the flux formulation valid for the entire speed regime. Here, we let the speed of sound be scaled by a scaling factor $f_a(\bar{M}; M_*)$,

$$\tilde{a}_{1/2} = f_a(\bar{M}; M_*)a_{1/2}, \tag{9}$$

where for simplicity,

$$a_{1/2} = (a_j + a_{j+1})/2, \tag{10}$$

and

$$\bar{M} = (M_j + M_{j+1})/2. \tag{11}$$

The scaling function f_a is defined as,

$$f_a(\bar{M}; M_*) = \frac{\sqrt{(1 - M_*^2)^2 \bar{M}^2 + 4M_*^2}}{1 + M_*^2} \leq 1, \tag{12}$$

with

$$M_*^2 = \min(1, \max(\bar{M}^2, M_{co}^2)). \tag{13}$$

This scaled Mach number will revert to the local physical Mach number at supersonic speeds. In fact, the scaling factor becomes essential only

in the low Mach range, as shown in Fig. 2. Hence, what the numerical speed of sound does is to make the Mach number appear larger in determining the numerical fluxes in the low speed regime. The cutoff parameter $M_{co} \ll 1$ is introduced to prevent a singularity at the stagnation point.

For the purpose of identification, we now call this extended method, AUSM$^+$-a, to highlight the role of the numerical speed of sound $\tilde{a}$.

To see the effect of this numerical speed of sound, we evaluate the condition number at low speed,

$$\kappa = \frac{|u| + \tilde{a}}{|u|} \to O(1), \qquad (14)$$

because

$$\tilde{a} \to 0, \quad \text{as } |u| \to 0. \qquad (15)$$

Hence, the condition number remains of order unity for all speed ranges. Also, the numerical dissipation based on this new speed of sound now scales with local speed $|u|$, instead of the local speed of sound a as $|u| \to 0$.

To further improve the residual convergence in the low speed range, it is found beneficial in Edwards and Liou [6] if a pressure diffusion term $\overset{\bullet}{m}_p$ is included in the mass flux. The scheme is now denoted as AUSM$^+$-ap.

2.1   Results and discussion

As noted at the outset, we shall demonstrate with examples the performance of the AUSM$^+$schemes by focusing on two issues: (1) convergence rate and (2) accuracy.

Darracq et al. [16] made a detailed investigation into the accuracy of the AUSM$^+$scheme and concluded that "the AUSM$^+$scheme predicts lift and drag values in better agreement experimental data than the Roe scheme." Furthermore, it was found that the AUSM$^+$scheme is much less gridsensitive than the Roe scheme, capable of yielding accurate solutions on relatively coarse grids. Figure 3 shows the surface pressure in excellent agreement with the data at various pitch angles. The solutions are seen to be strongly affected by the turbulence models employed; the Baldwin-Lomax model appears to give better prediction than the Granville-Cebeci (GRC) model.

We now come to show the effectiveness of using the numerical speed of sound, AUSM$^+$-a, with respect to the accuracy and convergence efficiency.

Firstly, we consider the flows over the Shuttle external tank with a sharp nose and blunt base, downstream of which there is a significant separation zone. The free stream Reynolds number was fixed at 10,000. We have tested conditions from low Mach, transonic, to supersonic flows. Several schemes were considered, consisting of the standard AUSM$^+$, AUSM$^+$-a, and AUSM$^+$-ap, with and without the Weiss-Smith preconditioner for $\boldsymbol{\Gamma}$.

For low Mach numbers (approximately $M_\infty < 0.3$), it was found necessary to use the time-derivative preconditioner $\boldsymbol{\Gamma}$ so that the numerical dissipations in both the implicit and explicit operators are compatibly scaled. For flows at transonic speeds or higher, the time-derivative preconditioner, as given in Eq. (2), provides no benefits whatsoever.

In Fig. 4, we display the convergence history for various Mach numbers using AUSM$^+$, but without the preconditioner $\boldsymbol{\Gamma}$. The residuals for the low Mach-number cases stall after a drop of four orders of magnitude. These drops in many calculations, although not especially admirable, would have been acceptable. However, a close examination of the solution reveals that it is completely unacceptable, as shown in Fig. 5. It appears that there is a false boundary (exactly aligned with a grid line) at which information is unable to get passed. This phenomenon is quite typical in the low Mach-number calculations using an unmodified compressible code, also seen in [4]. On the other hand, the solution obtained from the use of AUSM$^+$-a is well behaved and near the surface are revealed smooth contours, unlike the standard AUSM$^+$which has been known to yield unwanted pressure oscillations in viscous layers.

Also, the convergence histories with the use of

the numerical speed of sound display improvement over those without it, as shown in Fig. 4. The convergence rates for these two calculations nearly coincide with each other, indicating Mach-number independence. Finally the effect of including the pressure diffusion term on the convergence histories is also included in Fig. 4, indicating independence of Mach number and gaining another order of reduction for the low Mach numbers.

Moreover, we remark that in Fig. 4 the convergence rate is even improved in the transonic ranges by simply using the numerical speed of sound alone.

Next, the classical problem of incompressible flow past a backward-facing step in a channel is considered. The initial pressure and temperature are 1 atm and 300 K, and a parabolic velocity profile with an average velocity of 1 m/s is specified at the inlet of the channel. The Reynolds number based on the channel height D and the average velocity is 800.

The dominant features of the backward-facing step flowfield are the two large recirculation zones, positioned aft of the step and along the top wall of the channel, see Fig. 6. Upon reattachment, the flow slowly recovers toward a fully-developed Poiseuille flow near the exit of the domain. To predict the structure of the recirculation zones properly, the numerical formulation must capture the response of the pressure field correctly and must not introduce non-physical artificial diffusion. Normalized shear stress plots along the upper and lower surfaces of the channel, Fig. 7, shows an excellent agreement of the AUSM$^+$-a and AUSMDV-a results with the "benchmark" solution of Gartling [17], particularly in the capturing of the separation and reattachment points.

We now summarize major findings from the study of the above problems: (1) The numerical speed of sound concept is an effective means of extending the AUSM-type discretization to solve low Mach number flows in an accurate and efficient manner. (2) Since the numerical speed of sound is reduced with the flow speed, the numer-

ical dissipation changes accordingly, and a compatible implicit operator is required. (3) Incorporation of the numerical speed of sound helps remove pressure oscillations in the viscous layers.

In the next two examples, we consider 3D configurations, namely the ONERA M6 wing and wing-body problems. In the case of the ONERA M6 wing, we computed flows of $M_\infty = 0.84$, and $Re_\infty = 18.2 \times 10^6$ under various angles of attack. The detailed comparison of surface pressure distributions at the 65% spanwise section is shown in Fig. 8 for three angles of attack. The computed results are in very good agreement with the data [18], noticing the accurate capturing of the shock locations. Solutions at other spanwise locations also give similar level of agreement with the data.

The convergence histories are presented in Fig. 9 for three different angles of attack. They show a continuing decrease in 800 steps (600 fine-grid steps) by about four orders of magnitude from the largest values, at nearly the same rates even though the flow features have varied considerably.

The particle traces of two angles of attack, $\alpha = 3.06$ and 5.06, at different wingspans are given in Fig. 10, showing little spanwise excursion, except at the wing tip for the $\alpha = 3.06^o$ case, but appreciable three-dimensional effect for higher $\alpha = 5.06^o$

Turbulent flows over a wingbody configuration were calculated. The geometry is shown in Fig. 11, where the sting is included in the calculation. The computation domain was gridded using the chimera overset grid technique and the entire grid composed of seven grids. Figure 12 depicts the pressure coefficients at various spanwise locations on the wing. The computed results are in excellent agreement with the measured data of [19]; this is also true along the body lines.

Finally, Fig. 13 displays a well-behaved convergence history, reducing the residual error by more than five (5) orders of magnitude in 800 steps.

Figure 14 illustrates the effects of discretization accuracy on surface pressure predictions for the

cavitation number K $=2(p_\infty - p_v)/\rho_\infty U_\infty^2 = 0.8$. As shown, the pressure response, using the first order and second order accurate discretizations, agree very well with the data, except near the suction peak and stagnation point, where the second-order prediction is in closer accord with the experimental data.

Figure 15 illustrates the effect of lowering the cavitation number on the flow response. As K decreases, the pressure in the expansion region drops to the vapor pressure, resulting in the generation of a vapor phase and the growth of a cavitation bubble. Pressure recovery further downstream leads to the collapse of the cavity in a "wake" region. The structure of the wake region is strongly influenced by both the thermodynamic model and the velocity field, which in itself is influenced by the turbulence model.

Next we come to discuss the effect of grid generation towards accuracy and effeciency of CFD simulations.

3   DRAGON Grid

For a practical three-dimensional geometry, the time spent in generating a grid represents a serious bottleneck in the entire CFD analysis cycle, taking up to 80% of the total CFD analysis time, as detailed in [20,21] in which the breakdown of the duration of each task is recorded. See for example, Fig. 16. Hence, grid generation is an area where significant payoff can be realized. Furthermore, high quality grids for encompassing viscous regions are essential to yielding an accurate and efficient solution.

Overset and unstructured grid methods schemes currently are two mainstream approaches for dealing with complex geometry.

The overset grid method can yield structured grids with good quality, such as orthogonality and smoothness, and can easily control grid spacing. However, the nonconservative interpolations in the overlapped region can give rise to a spurious solution, especially through regions of sharp gradients.

The unstructured grid method also possesses the flexibility to generate grids around complex geometries. However, the unstructured grid method has been shown to be memory and computation intensive [22]. Also, it is known that prismatic meshes are necessary to accurately resolve viscous layers around bodies, implying the need for constructing structured-like grids in order to resolve the viscous layers.

The DRAGON grid method [23-25] will result in structured grids in the major portion of the computation domain and only small regions filled with unstructured grids. It has three important advantages: (1) preserving strengths of the overset grid, (2) eliminating difficulties encountered in the overset scheme, and (3) enabling grid communication in a fully conservative and consistent manner. Consequently, the DRAGON grid method can deliver a high quality grid for a complex multi-components geometry in an efficient and robust manner.

In [23], the DRAGON grid method was first proposed and demonstrated for 2D problems. It adapted the thinking the overset grid method. However, it is more general and robust than the overset grid method since it does not require overlapping of grids and it completely avoids the issues about orphan points and bad quality points, which usually are the most time consuming part of the overset method. Figure 17 shows the connection between the overset and DRAGON grids. In the overlapped region of the overset grid, a hole is created using the PEGSUS code [26] and subsequently replaced with triangular meshes in the DRAGON grid.

To demonstrate the capability of the DRAGON grid code, we consider a typical film-cooled turbine vane, which includes the vane, coolant plena, and 33 holes inside of the vane. Figure 18 depicts the resultant DRAGON grid, where the connecting regions between the 33 holes and the flow domain are filled with unstructured grids. It gives a deep insight into this DRAGON grid by means of cutting through the grid, where attention has been paid to the leading edge region. The 33 individual structured grids for the holes have been created without trying to

topologically join them to the grids representing the external flow domain. In this regard, the DRAGON grid scheme could be considered as a more flexible and easier approach.

3.1 Results and discussion

First, we consider a supersonic flow of Mach 3 through a convergent channel, where the top and front side walls are each bent by a wedge angle of 10 degrees, thus creating two wedge shocks of equal strength and subsequent interaction between them. A strip of unstructured-meshed region is placed in the mid-section of the channel (not shown). The two wedge shocks intersect and generate a corner shock region manifested by the slip lines emanating from the triple point. As seen in Fig. 19, this region progressively becomes larger as the wedge shocks sweep toward the opposite walls. Eventually these two wedge shocks reflect and interact with the flow previously generated by the corner shocks, making the flowfield even more complicated.

The result on a single structured grid is also included for comparison. We see that both sets of results are essentially the same, except in the core region characterized by the slip lines.

Now, we give the results of a flow over turbine stator vanes [27]. Figure 20 shows the DRAGON grid, which consists of a background H-type grid, an O-type viscous grid around the vane, and an unstructured grid region between them. The static pressure distributions of the present DRAGON grid solution are plotted in Fig. 21 and they are in very good agreement with the data of [27] measured at three spanwise locations, 13.3%, 50%, and 86.6% respectively.

4 Concluding Remarks

With the introduction of the numerical speed of sound in the AUSM$^+$flux scheme, it now yields accurate results at low Mach number and efficient convergence at a rate (nearly) independent of Mach number and angle of attack. Interestingly, the convergence rate is even enhanced at transonic speeds with the numerical speed of sound.

We have presented the extension of the DRAGON grid method into three-dimensional space. This method preserves the advantageous features of both the structured and unstructured grids, while eliminating or minimizing their respective shortcomings. As a result, it is amenable to the quick creation of quality viscous grids for various individual components with complex shapes found in an engineering system. The DRAGON grid generation can realize the time saving from months to days.

Furthermore, the flow solutions confirm conservation of fluxes through the interfaces of structured-unstructured regions, and the results are in very good agreement with the measured data, thus demonstrating the reliability of the method.

5 References

1. M.-S. Liou and C. J. Steffen, *J. Comput. Phys.* **107**, 23 (1993).

2. M.-S. Liou, NASA TM 106524 (1994); also *J. Comput. Phys.* **129**, 364 (1996).

3. Y. Wada and M.-S. Liou, *SIAM J.Sci. Comput.* **18**, 633 (1997).

4. M.-S. Liou and J. R. Edwards, AIAA Paper 99-3268-CP, 1999.

5. J. R. Edwards and M.-S. Liou, *AIAA J.* **36**, 1610 (1998).

6. J. R. Edwards, Franklin and M.-S. Liou, AIAA 99-3327-CP, 1999.

7. R. Beam and R. Warming, *AIAA J.* **16**, 393 (1978).

8. A. Jameson and E. Turkel, *Math. Comput.* **37**, 385-397 (1981).

9. A. Brandt, *Lecture Notes in Mathematics* **960** 220 (1982).

10. J. M. Weiss and W. A. Smith, AIAA Paper 94-2209, 1994.

11. J. L. Steger and R. W. Warming, *J. Comput. Phys.* **40**, 263-293 (1981).

12. B. van Leer, *Lecture Notes in Physics* **170**, 507 (1982).

13. P. L. Roe, *J. Comput. Phys.* **43**, 357–372 (1981).

14. S. Osher and F. Solomon, *Math Comput.* **38**, 339–374 (1982).

15. M.-S. Liou, *J. Comput. Phys* **160** 623 (1997).

16. D. Darracq, S. Champagneux, and A. Corjon, AIAA Paper 98-2411, 1998.

17. D. Gartling, *International J. Numerical Methods in Fluids* **11**, 953 (1990).

18. V. Schmitt and F. Charpin, Appendix B1, AGARD-AR-138, 1984.

19. D. A. Treadgold, A. F. Jones, and K. H. Wilson, Appendix B4, AGARD-AR-138, 1984.

20. R. Taghavi, "Automatic, parallel and fault tolerant mesh generation from CAD on Cray research supercomputers," Technical report, Cray User Group Conference, Tours, France, 1994.

21. S. E. Rogers et al., AIAA Paper 2000-4216-CP, 2000.

22. F. Ghaffari: AIAA Paper 94-0163, 1994.

23. M.-S. Liou, K.-H. Kao: NASA TM 106709, 1994.

24. Y. Zheng, M.-S. Liou and K. C. Civinskas, NASA TM 1999-209458, 1999.

25. M.-S. Liou and Y. Zheng, to appear in *Frontiers of Computational Fluid Dynamics – 2000*, D. A. Caughey, M. M. Hafez (eds.), World Scientific Publishing Company, Singapore, 2000.

26. N. E. Suhs, R. W. Tramel, "PEGSUS 4.0 user's manual", AEDC-TR-91-8, 1991.

27. L. J. Goldman, R. G. Seasholtz, NASA Technical Paper 2018, 1982.
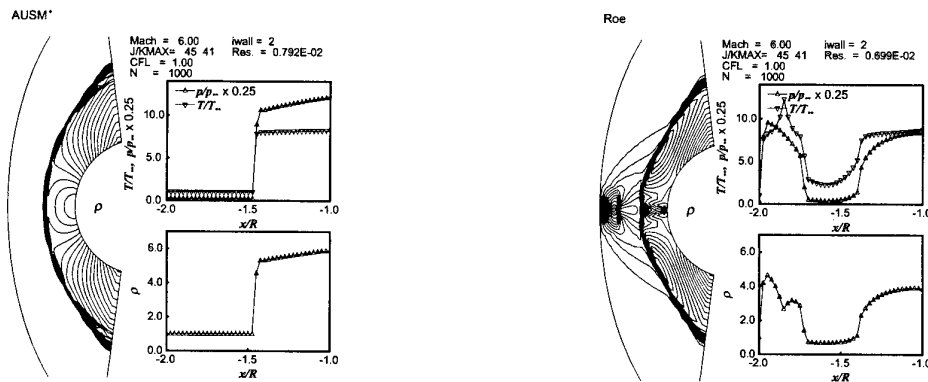
Fig. 1 Supersonic ($M_\infty = 6$) blunt body problem; profiles along the stagnation streamline using $AUSM^+$(L) and Roe's (R) schemes respectively.
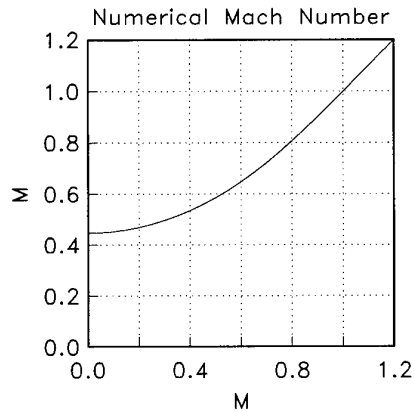
Fig. 2 Numerical Mach number vs Mach number
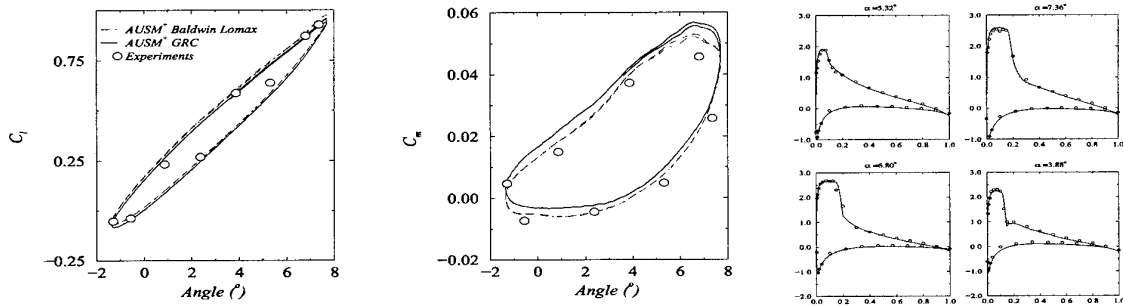
Fig. 3 Comparison of C_l and C_m for the NACA 0012 airfoil,using the GRC and B-L turbulence models. And comparison of C_p at four pitching angles, from [16].
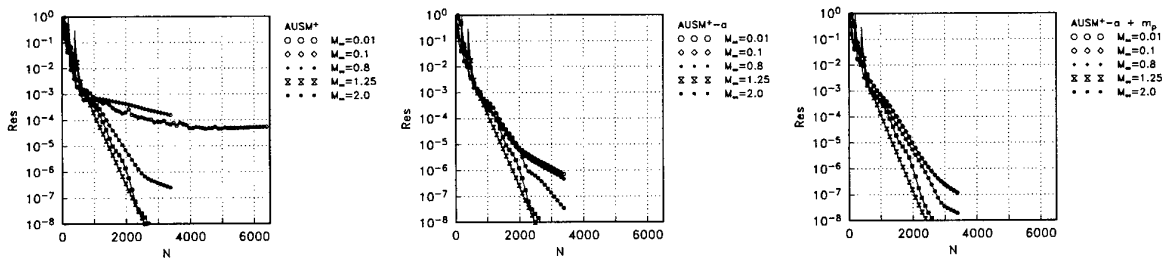

Fig. 4 Convergence history for the shuttle external tank problem: (Left) AUSM$^+$, (Middle) AUSM$^+$-a, (Right)AUSM$^+$-ap.
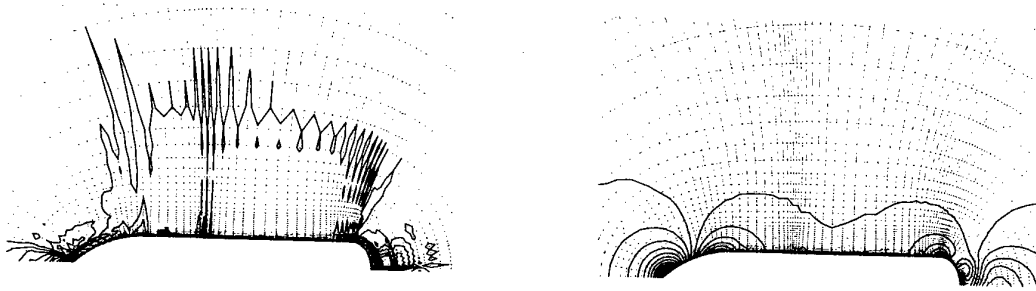
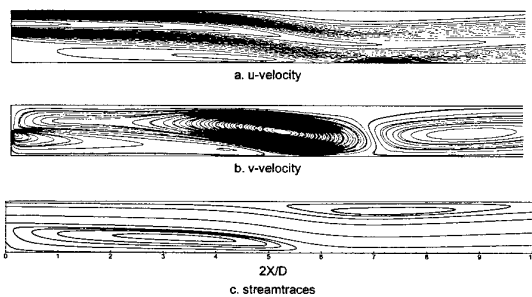Fig. 5 Pressure contours for the shuttle external tank problem obtained at N=6400 time steps for $M_\infty = 0.01$, using the standard AUSM$^+$(L) and AUSM$^+$–a (R).

Fig. 6 Structure of backward-facing step flowfield (Re = 800).
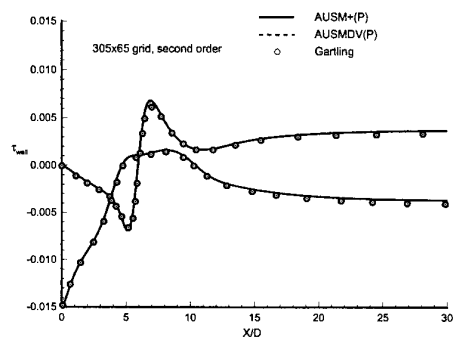
Fig. 7 Wall shear stress comparisons: backward-facing step flowfield (Re = 800).
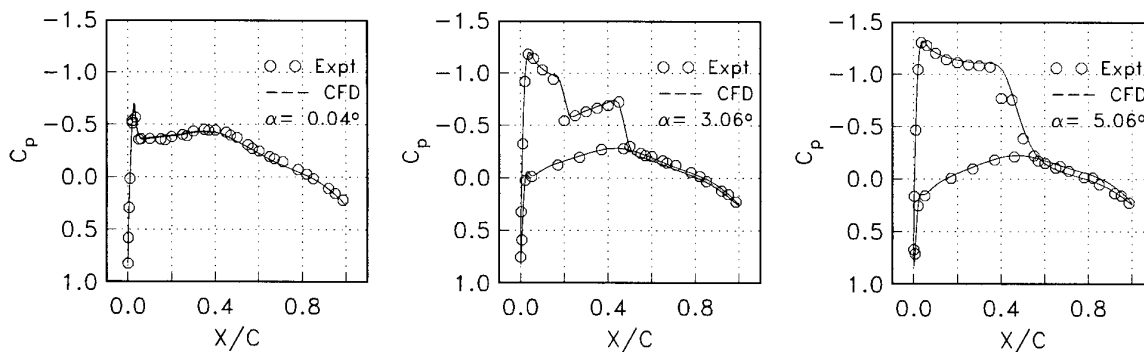
Fig. 8 Pressure distribution at the spanwise section, 65% of the ONERA M6 wing, for various angles of attack, $M_\infty = 0.84, Re_\infty = 18.2 \times 10^6$.
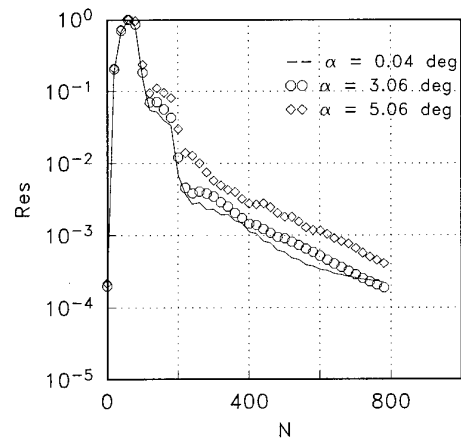
Fig. 9 Convergence history for the ONERA M6 wing problem at three angles of attack, $M_\infty = 0.84, Re_\infty = 18.2 \times 10^6$.

Fig. 10 Particle traces for the ONERA M6 wing problem at $M_\infty = 0.84, Re_\infty = 18.2 \times 10^6$., and Left: $\alpha = 3.06^o$, Right: $\alpha = 5.06^o$.
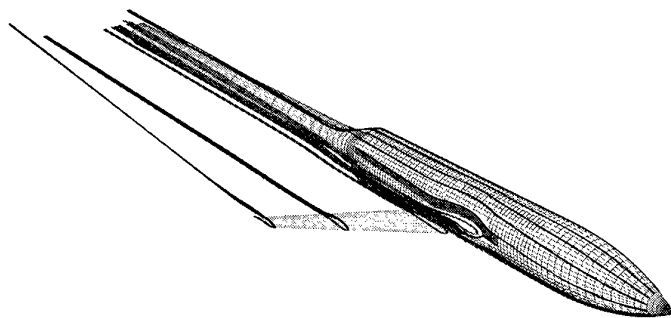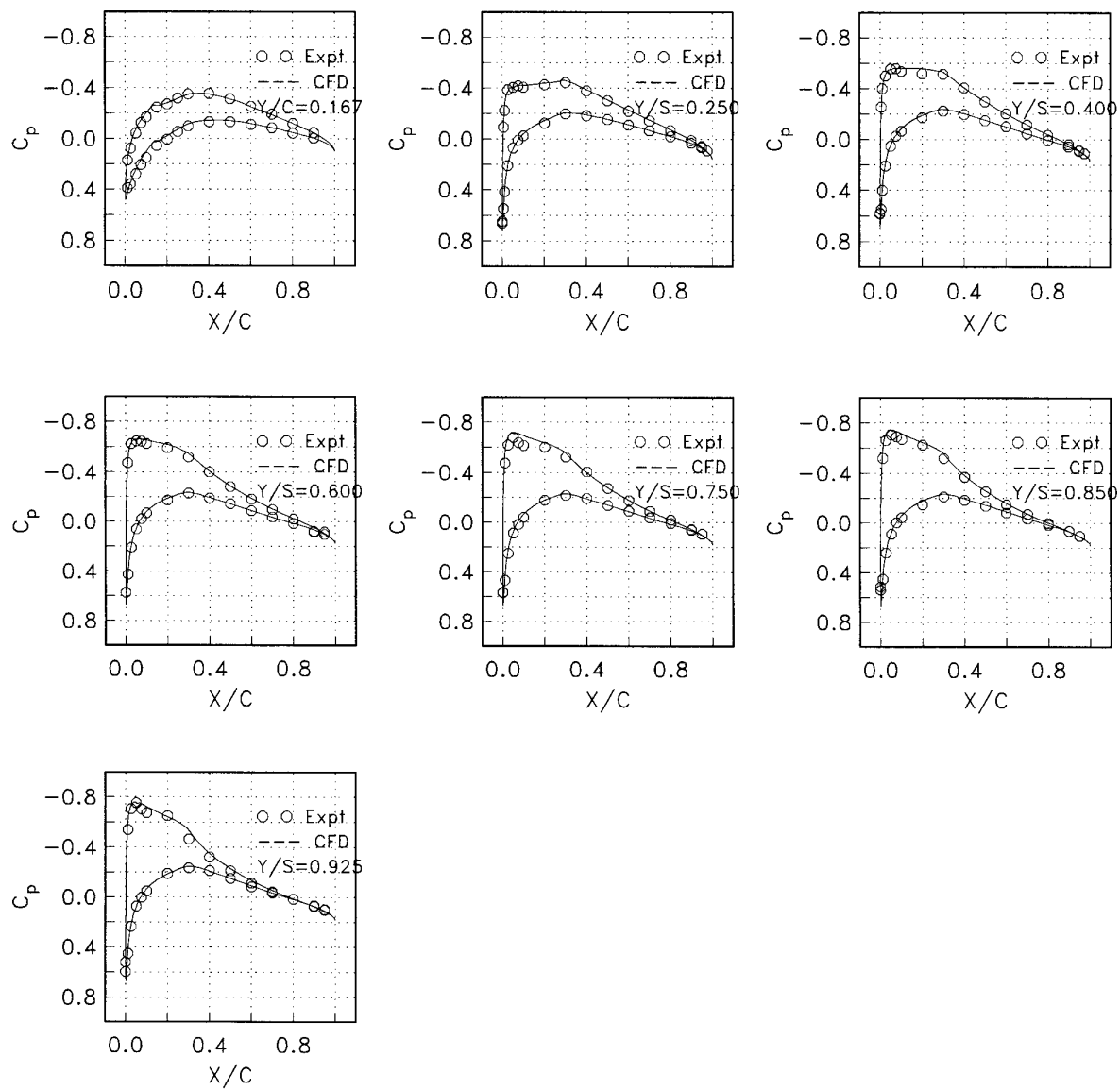

Fig. 11 Particle traces around the body and wing.

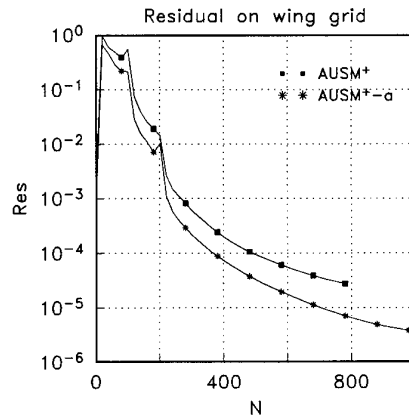Fig. 12 Pressure distribution at various sections of the wing, $M_\infty = 0.8, \alpha = 2^o, Re_\infty = 0.167 \times 10^6$.

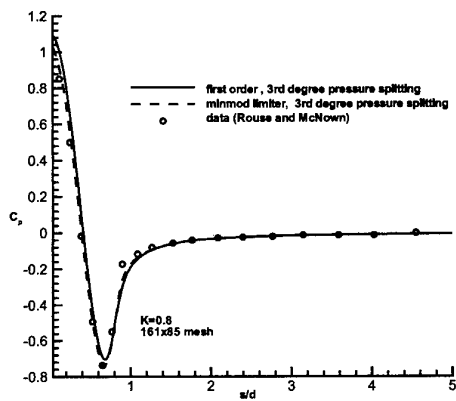Fig. 13 Convergence history for the wingbody problem.

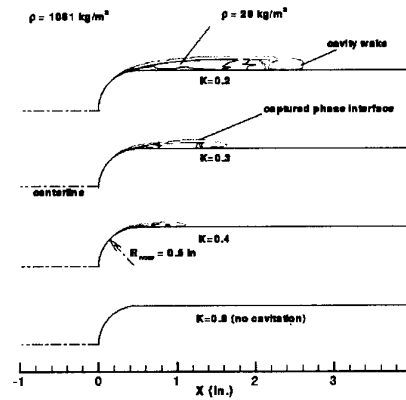Fig. 14 Surface pressure distributions: K=0.8.

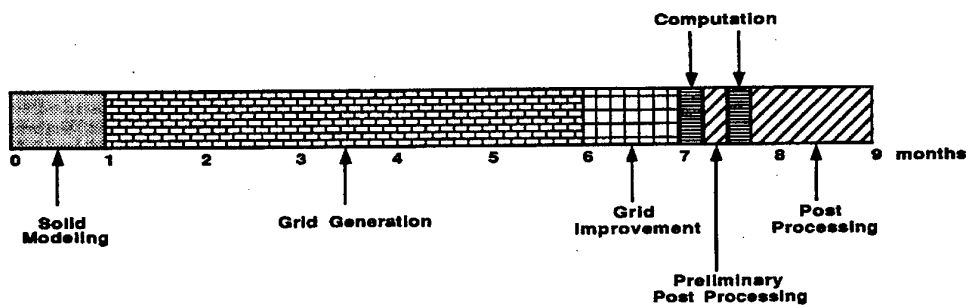Fig. 15 Density contours: liquid water flow over hemisphere/cylinder.

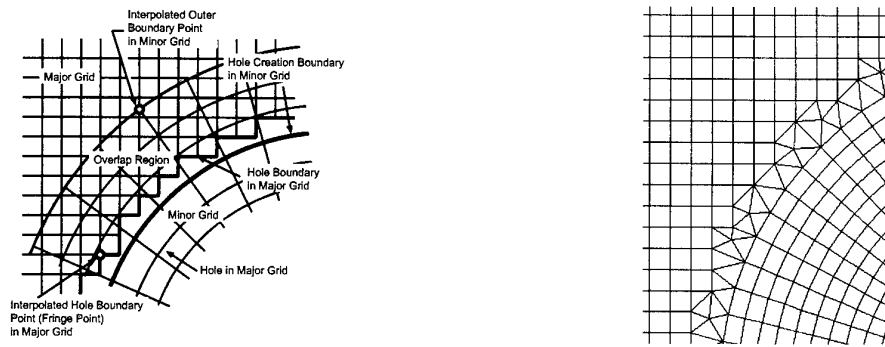Fig. 16 Duration of each task in a large scale CFD project.

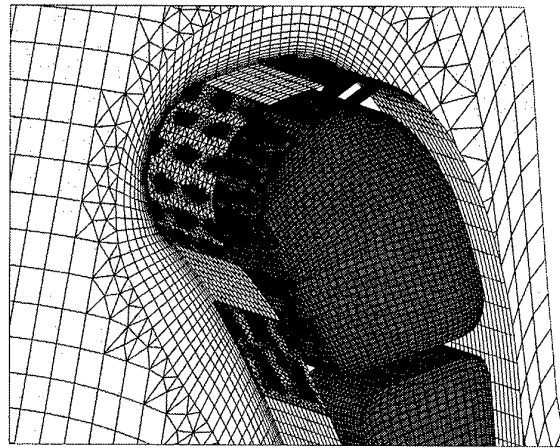Fig. 17 Comparison of the Chimera grid (Left) and the DRAGON grid (Right).

Fig. 18 Cut-through view of the DRAGON grid in the leading edge region of the film-cooled turbine vane.
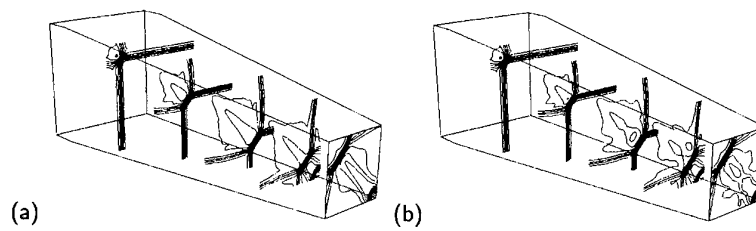

Fig. 19 Mach number distribution of the flow at various stations: (a) Single grid; (b) DRAGON grid.
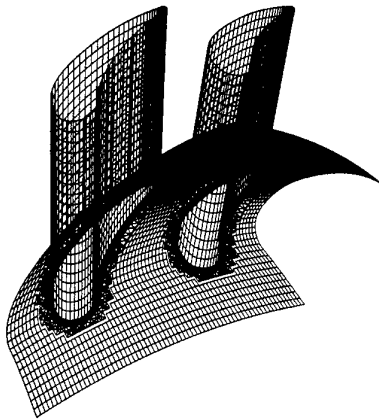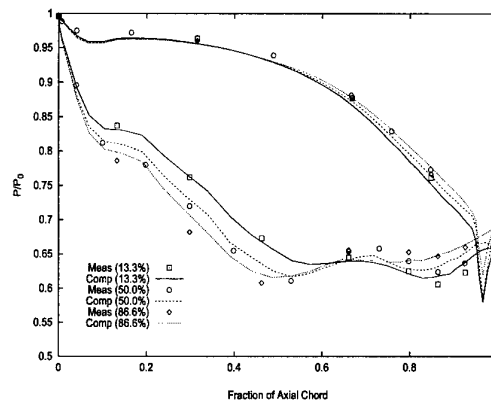
Fig. 20 DRAGON grid of the annular turbine cascade.

Fig. 21 Computed and measured static pressure distributions at 13.3%, 50% and 86.6% of span from hub.

2E1 AEROELASTIC ANALYSIS OF ACTIVE TWIST HELICOPTER ROTOR BLADES

SangJoon Shin* and Carlos E. S. Cesnik**

Active Materials and Structures Laboratory, Massachusetts Institute of Technology
Cambridge, Massachusetts, 02139-4307, U.S.A.

Key Words: Helicopters, V/STOL

ABSTRACT

Vibration reduction can be achieved in helicopter rotors by redistributing the vibratory aerodynamic loads on each blade individually. This can be realized by actively modifying the twist distribution along the blade radius. This paper presents the aeroelastic framework developed to design integrally twisted active helicopter blades. The effects of the active material embedded in the structure are carried throughout all the steps of analysis. An active twist rotor (ATR) blade was designed and manufactured in order to investigate the issues of the current concept. It uses embedded active fiber composites as the means to achieve the twist deformation. Using the developed active aeroelastic model, numerical results are compared to non-rotating and rotating experimental frequency response data. Correlation between the model and experiments is very good. The model presented here can be used as a design tool for future active aeroelastic tailored rotor systems.

1. INTRODUCTION

Helicopter vibration is a phenomenon mainly induced by the instantaneous asymmetry of the aerodynamic loads acting on the blade at different azimuth locations, and such asymmetry becomes more and more severe as the helicopter flight speed increases. Quite complicated aerodynamic environments are exhibited by the individual rotor blades in helicopter during forward flight. There have been conventional (passive) methodologies in the helicopter community to reduce such vibration. However, during the last two decades, active methods to alleviate helicopter vibration based on the idea of directly modifying unsteady aerodynamic loads acting upon the rotor blades have been studied and may be broadly classified as higher harmonic control (HHC) and individual blade control (IBC).[1] Several outstanding results were obtained in terms of vibration reduction performance, and it includes analytical studies searching for an optimal control scheme, wind tunnel tests with either small or full-scaled model, and flight tests. However, these concepts based on employing additional hydraulic actuators installed on either non-rotating (beneath swashplate) or rotating frames (between pitch links) were not entered into full-scale development yet because of severe fatigue introduced at the actuator components and complexity of the systems.

Recently there were several attempts to take advantage of active materials for individual blade control[2] since those materials can bring systems advantages in terms of weight and power consumption when compared with traditional hydraulic systems. Two main distinct concepts have been under development for the active material application:

rotor blade flap actuation, and integral blade twist actuation.[3] The rotor blade flap actuation concept has been studied in various ways and that is beyond the scope of the present paper. The integral actuation concept,[4-5] on the other hand, presents itself as an aggressive alternative with several potential benefits. Besides providing redundancy in operation, the integral concept does not increase the profile drag of the blade unlike discrete flap concepts. Moreover, the actuators once embedded in the composite construction become part of the load bearing structure, making the active blade a truly integrated multifunctional structure that allows for effective construction, assembly, and maintenance of future low vibration and low noise rotor blades.

A research program between NASA Langley/Army Research Laboratory and MIT has been established to investigate the specific issues related to the modeling and design of Active Twist Rotor (ATR) systems, evaluate their effectiveness for IBC in forward flight, and the impact on vibration and noise reduction. As part of the ATR study, extensive wind tunnel test will support the proposed concept and will provide a first-of-a-kind experimental data for validation of the concept and the developed active blade modeling framework. The tests are conducted using a 2.74-m diameter 4-bladed fully-articulated aeroelastically scaled wind tunnel model designed for testing in the heavy gas environment of the NASA Langley Transonic Dynamics Tunnel (TDT). The Aeroelastic Rotor Experimental System (ARES), shown in the TDT in Fig. 1, is used to test the ATR model. The TDT utilizes a heavy gas test medium with a speed of sound approximately one half that of sea level standard air. This, as well as the TDT's variable density test capability, permits full scale rotor tip Mach numbers, Froude numbers, and Lock numbers to be matched simultaneously at model scale.
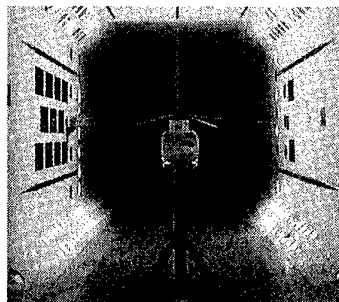

Figure 1. ARES testbed in TDT with the ATR blade.

This paper discusses the theoretical framework developed to analyze ATR blades, and its correlation with preliminary tests, both on the bench and in hover.

2. THEORETICAL MODEL

For analyzing helicopter blades with embedded strain actuators, a framework is needed such that the effects of the active material embedded in the structure are carried out throughout all the steps of the analysis. A new analytic formulation was created for active rotor blade modeling that is able to model realistic blade cross section like the one needed for the ATR concept. As described below, an asymptotical analysis takes the electromechanical three-dimensional problem and reduces it into a set of two analyses: a linear analysis over the cross section and a nonlinear analysis of the resulting beam reference line.

2.1. Cross-Section Analysis

The new asymptotical formulation to analyze multi-cell composite beams incorporating embedded piezoelectric plies distributed throughout the blade was developed and presented in detail in Ref. 9. While restricted to thin-walled beams, it yields closed form solutions of the displacement field (which is derived and *not* assumed), and stiffness and actuation constants. The availability of correct closed form expressions is essential to determine design paradigms on this new type of blade, mainly concerning to the tradeoffs between torsional stiffness and twist actuation. These stiffness and actuation constants will then be used in a beam finite element discretization of the blade reference line. The beam constitutive relation relating beam generalized forces (axial force, twist, and two bending moments, respectively) with beam generalized strains (axial strain, twist curvature, and two bending curvatures) and corresponding generalized actuation forces (function of the geometry, material distribution, and applied electric field) is obtained in the following form:

$$\begin{Bmatrix} F_1 \\ M_1 \\ M_2 \\ M_3 \end{Bmatrix} = \begin{bmatrix} K_{11} & K_{12} & K_{13} & K_{14} \\ K_{12} & K_{22} & K_{23} & K_{24} \\ K_{13} & K_{23} & K_{33} & K_{34} \\ K_{14} & K_{24} & K_{34} & K_{44} \end{bmatrix} \begin{Bmatrix} \gamma_{11} \\ \kappa_1 \\ \kappa_2 \\ \kappa_3 \end{Bmatrix} - \begin{Bmatrix} F_1^{(a)} \\ M_1^{(a)} \\ M_2^{(a)} \\ M_3^{(a)} \end{Bmatrix} \quad (1)$$

where $[K]$ is the stiffness matrix function of geometry and material distribution at the rotor cross section. From this formulation, all K_{ij} and the generalized actuation forces are given by closed form expressions,[6] or for a more general geometry by finite element analysis.[7]

2.2. Global Beam and Aerodynamics Analysis

The geometrically exact beam equations follow from the asymptotical analysis and include the distributed actuation. As direct extension of Ref. 8, the original nonlinear formulation allows for small strain and finite rotations, and is cast into a mixed variational intrinsic form. The embedded actuation effects come in the new constitutive relation that modifies the 1-D finite element formulation. Its implementation was performed on the aeroelastic hover solution described in Ref. 9. The solution of the 1-D beam analysis provides blade displacement and generalized stress fields due to external loading and piezoelectric actuation, which are of interest in the analysis of static and dynamic deformations and aeroelastic stability.

Based on a thin airfoil theory, the external aerodynamic loads acting on the rotor blade surface are formulated in rotating conditions (either in hover or forward flight). Since the aerodynamic model used in this formulation contains the induced velocity terms explicitly, it is necessary to solve them simultaneously. In this analysis, finite-state dynamic inflow equations based on Peters and He[10] is adopted. In its derivation, new state-variables are generated to describe the inflow velocity at discrete spanwise locations by dynamic equilibrium equations between inflow quantities and pressure imposed on the rotor blades. These equations usually involve the structural variables and their time derivatives, such as displacements and rotations and, therefore, they need to be solved concomitantly with the structural equilibrium equations.

2.3. Solution of Aeroelastic System

The structural equilibrium equations from the blade analysis can be grouped into structural (F_S) and aerodynamic terms (F_L) as follows:

$$F_S(X, \dot{X}, V) - F_L(X, Y, \dot{X}) = 0 \quad (2)$$

where X is the vector of structural variables, Y the inflow variables, and V is the vector of magnitudes of the electrical field distribution shape. Similarly, the inflow dynamics can be represented by separation into pressure (F_P) and inflow (F_I) components:

$$-F_P(X, Y) + F_I(Y, \dot{Y}) = 0 \quad (3)$$

The solution of interest for the coupled set of equations above can be derived based on small perturbation from steady-state equilibrium:

$$\begin{Bmatrix} X \\ Y \end{Bmatrix} = \begin{Bmatrix} \overline{X} \\ \overline{Y} \end{Bmatrix} + \begin{Bmatrix} \check{X}(t) \\ \check{Y}(t) \end{Bmatrix} \quad (4)$$

For the solution of steady-state equilibrium, one needs to solve a set of nonlinear equations of both Eqs. (2) and (3):

$$\begin{cases} F_S(\overline{X}, 0, \overline{V}) - F_L(\overline{X}, \overline{Y}, 0) = 0 \\ -F_P(\overline{X}, \overline{Y}) + F_I(\overline{Y}, 0) = 0 \end{cases} \quad (5)$$

The steady-state equilibrium solution can be found very efficiently using Newton-Raphson method.

In order to investigate the dynamic response of the blade with respect to voltage applied to the embedded anisotropic strain actuator, a state-space representation is required after the steady-state solution is obtained. By perturbing Eqs. (2) and (3) using Eq. (4) about the calculated steady state, one gets

$$\begin{bmatrix} \dfrac{\partial F_S}{\partial X} - \dfrac{\partial F_L}{\partial X} & -\dfrac{\partial F_L}{\partial Y} \\ -\dfrac{\partial F_P}{\partial X} & \dfrac{\partial F_I}{\partial Y} - \dfrac{\partial F_P}{\partial Y} \end{bmatrix}_{\substack{X=\overline{X} \\ Y=\overline{Y}}} \begin{Bmatrix} \check{X} \\ \check{Y} \end{Bmatrix} + $$

$$\begin{bmatrix} \dfrac{\partial F_S}{\partial \dot{X}} - \dfrac{\partial F_L}{\partial \dot{X}} & 0 \\ 0 & \dfrac{\partial F_I}{\partial \dot{Y}} \end{bmatrix}_{\substack{X=\overline{X} \\ Y=\overline{Y}}} \begin{Bmatrix} \dot{\check{X}} \\ \dot{\check{Y}} \end{Bmatrix} + \quad (6)$$

$$\begin{bmatrix} \dfrac{\partial F_S}{\partial V} & 0 \\ 0 & 0 \end{bmatrix}_{\substack{X=\overline{X} \\ Y=\overline{Y}}} \{V\} = \begin{Bmatrix} 0 \\ 0 \end{Bmatrix}$$

from which the transient solution can be found. Since the aerodynamics is expressed as coupled through the blades,

the system equations must be transformed to multi-blade coordinates resulting in a form of multi-harmonic series. In the present hover analysis, only the collective components of those need to be considered.

Eq. (6) is a state-space representation, and can be written in the following general form:

$$\begin{cases} EX = A\dot{X} + BV \\ y = CX + DV \end{cases} \quad (7)$$

where y is the output vector of sensors embedded along the blade (strain gauge bridges configured for torsion or bending strain measurements). Frequency response function of the blade can be calculated using the following Laplace transform:

$$\frac{\overline{y}(s)}{\overline{V}(s)} = C(Es - A)^{-1}B + D \quad (8)$$

Note that the coefficient matrix E is usually singular due to the mixed formulation of the beam model.

3. BENCH TEST STUDIES

Using the developed framework, an ATR prototype blade was designed and manufactured successfully.[11] Before investigating the ATR vibration reduction during forward flight, a correlation was attempted regarding the adequacy of the present modeling methodology. This is accomplished based on both bench and hover experiments, which are described in detail here.

The non-rotating dynamic characteristics of the blade can be evaluated from the frequency response of an applied sinusoidal excitation to the AFC actuators. Fig. 2 shows the result of laser displacement sensor (for tip twist angle) readings and the theoretical prediction as function of the actuation frequency. As one can see, the first torsional mode is clearly identified at approximately 85 Hz, and this result matches well with model prediction. The peaks at the torsional natural frequency in the model prediction are found quite higher (tend to infinite) than those in the bench test results since no damping is included in the structural model. This already indicates that some structural damping should be added to the model. Once the aerodynamics is included in the problem, its damping will bring the peak to finite amplitude. While the strain results could be obtained at high excitation voltages, the dynamic tip twist was measured at low voltages due to the limitation on the range of the laser sensors. At 400 V_{pp}, the peak-to-peak tip twist response of the blade is approximately 3.5°.
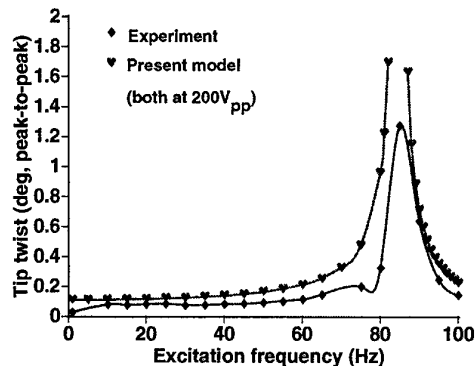

Figure 2. Tip twist response of the ATR prototype blade on the bench.

Such an increased dynamic response around the first

torsional natural frequency is expected to affect the twist response over the frequency range of interest when the blade is rotating. It makes the frequency response quite flat after 1P (11.5 Hz), compensating for the inherent degradation authority of the piezoelectric material with frequency. Therefore, the theoretical model presented herewith shows very good correlation with experimental test on the frequency response for both tip twist actuation and torsional deformation of the active blade.

4. HOVER TEST STUDIES

The ATR prototype blade was used with three other similar passive blades for hover testing as a four-bladed fully-articulated rotor system inside the NASA Langley TDT[12] (shown in Fig. 1). The test conditions include harmonic sine dwell actuation in either normal air or heavy gas medium environment. The rotational speed was varied (full 688 rpm and 10% below that), as well as the collective pitch setting (0°, 4° and 8°). During the hover tests, a total of 26 data channels were monitored and stored to investigate the aeroelastic characteristics of both the overall rotor system and the individual blade. These signals include 6-component rotor system balance loads, strain gauges embedded in the active blade, pitch link loads, etc.

From the theoretical model developed in this study, the frequency response of the ATR prototype blade can be computed for the hover condition. As a sample result, Fig. 3 shows the internal torsional moment at 31% blade radial station and its comparison with the experimental data for the case of heavy gas environment, 688 rpm, 2,000 V_{pp} excitation, and varying collective pitch settings (0°, 4°, 8°). As one can see from both magnitude and phase of the torsion gage readings, the actuation authority is insensitive to the blade static loading (represented by the different collective settings). Also, the first torsion resonance frequency appears at about 70 Hz (6.3 P), lower than the bench result (85 Hz), which is associated with the pitch link flexibility, the aerodynamic damping effects, and the effective change on the total length of the blade (due to its mounting on the hub). Even though the analytical model overpredicts magnitude of the blade deformation in the low frequency actuation regime, the correlation is fairly good. Moreover, the analytical prediction clearly confirms the previous experimental findings that the actuation authority is insensitive to the blade static loading.
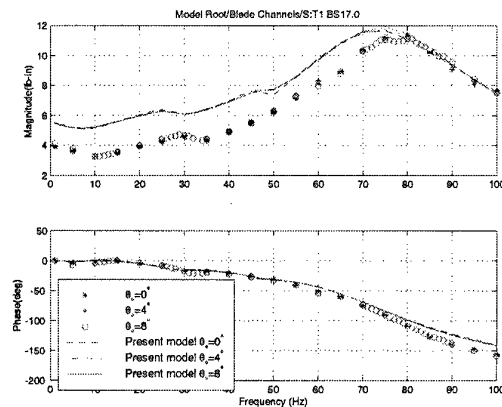

Figure 3. Torsional moment at 31% blade radius of the ATR prototype blade in hover (688 rpm, heavy gas, 0.00472 slug/ft³ density, 2,000 V_{pp} actuation).

Frequency response sensitivity with respect to rotor rotational speed and test medium density also shows that the actuation authority is insensitive to such perturbation except one at the torsional resonance frequency due to the change in the aerodynamic damping with medium density. The theoretical model predicts those trends very well, and again overpredicts the magnitude of the torsional moment.

To estimate the potential capability of vibration reduction using the current ATR blade concept, CAMRAD II[12] is used in forward flight condition. Its model employs an equivalent torque couple to represent the twist actuation generated by the actuators. The present cross-sectional analysis provides the active moment to be used in that analysis. Once the CAMRAD II model is calibrated, similar correlation with the present model for this experimental data can be verified.[12] Fig. 4 shows the 4P vertical hub shear force that the ATR system is predicted to be subjected at a given forward flight condition as function of the phase of the applied actuation. Without actuation, the projected 4P vertical force is approximately 6 lb. The four-active bladed system under 2,000 V_{pp} actuation (equivalent to an actuation ratio of 0.5 in Fig. 12) is expected to reduce the 4P vibration of about 60% to 80% at $\mu=0.30$, $C_T/\sigma=0.075$ and $C_x/\sigma=-0.0046$.
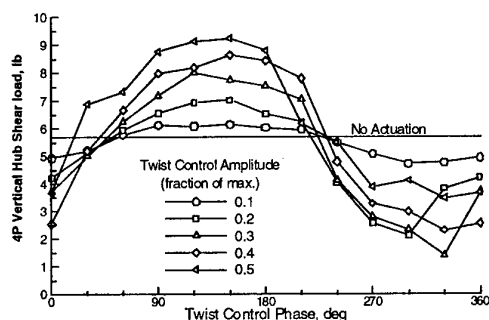

Figure 4. Variation of thrust induced by twist actuation at ATR system in forward flight ($\mu=0.30$, $C_T/\sigma=0.075$, $C_D/\sigma=-0.0046$).

5. CONCLUSIONS

This paper presented an analytical framework, and the corresponding correlation with bench and hover test results for an active rotor blade concept. The active rotor blade was designed to reduce rotor vibratory loads by piezoelectrically controlled twisting on the individual blades. A study of the frequency response of an active blade was conducted for both non-rotating and hover conditions. Correlation between the developed model and the ATR experimental data was very good. Both analytical and experimental results show that the twist actuation authority of the ATR blade is independent of the collective setting up to approximately 10P, and the only dependence on rpm and altitude show near the torsional resonance frequency due to its dependency on the aerodynamic damping. For all the aeroelastic results, the phase correlation of the vibratory twist moment was excellent. The model, however, generally overpredicts the magnitude of the moment due to the lack of structural damping. The discrepancies at low frequency are between 1% and 50% (in few frequency locations) which are associated with uncertainties on the active material properties, hub dynamic properties, and the unmodeled led-lag damper. Future tests and simulations will be extended to forward

flight condition for a full validation of the concept. Finally, based on a calibrated model, estimation of 4P vertical hub shear force at $\mu=0.30$ shows potential for 60% to 80% vibratory load reduction. The presented modeling, bench and hover test results on this prototype blade set the foundation for future development of the ATR concept for IBC in forward flight.

REFERENCES

1. Shaw, J., Albion, N., Hanker, E. J. and Teal, R. S., "Higher Harmonic Control: Wind Tunnel Demonstration of Fully Effective Vibratory Hub Force Suppression," Journal of the American Helicopter Society, 31-1, pp.14—25, 1989

2. Friedmann, P. P., "The Promise of Adaptive Materials for Alleviating Aeroelastic Problems and Some Concerns," Proceedings of Innovation in Rotorcraft Technology, Royal Aeronautical Society, London, United Kingdom, June 24—25, 1997.

3. Giurgiutiu, V., "Recent Advances in Smart-Material Rotor Control Actuation," Proceeding of the 41st AIAA/ASME/ASCE/AHS/ASC Structures, Structural Dynamics, and Materials Conference, Atlanta, Georgia, April 4—6, 2000, AIAA Paper No. 2000-1709.

4. Chen, P. and Chopra, I., "Hover Testing of Smart Rotor with Induced-Strain Actuation of Blade Twist," AIAA Journal, 35-1, pp. 6—16, 1997.

5. Rodgers, J. P. and Hagood, N. W., "Development of an Integral Twist-Actuated Rotor Blade for Individual Blade Control," AMSL Report #98-6, Active Materials and Structures Laboratory, Massachusetts Institute of Technology, October 1998.

6. Cesnik, C. E. S. and Shin, S. J., "On the Modeling of Active Helicopter Blades," International Journal of Solids and Structures, in press, 2000.

7. Cesnik, C. E. S. and Ortega-Morales, M., "Active Beam Cross-Sectional Modeling," SPIE's 7th International Symposium on Smart Structures and Materials, Newport Beach, California, March 5—9, pp. 3984—62, 2000.

8. Hodges, D. H., "A Mixed Variational Formulation Based on Exact Intrinsic Equations for Dynamics of Moving Beams," International Journal of Solids and Structures, 26-11, pp. 1253—1273, 1990.

9. Shang, X. and Hodges, D. H., "Aeroelastic Stability of Composite Rotor Blades in Hover," Proceedings of the 36th AIAA/ASME/AHS Structures, Structural Dynamics, and Materials Conference, New Orleans, Louisiana, April 10—12, 1995.

10. Peters, D. A. and He, C. J., "A Closed Form Unsteady Aerodynamic Theory for Lifting Rotor in Hover and Forward Flight," Proceedings of the American Helicopter Society 43rd Annual Forum, St. Louis, Missouri, May, 1989.

11. Cesnik, C. E. S., Shin, S.-J., Wilkie, W. K., Wilbur, M. L. and Mirick, P. H., "Modeling, Design, and Testing of the NASA/Army/MIT Active Twist Rotor Prototype Blade," Proceedings of American Helicopter Society 55th Annual Forum, Montreal, Canada, May 25—27, 1999.

12. Wilbur, M. L., Yeager Jr., W. T., Wilkie, W. K., Cesnik, C. E. S., and Shin, S. J., "Hover Testing of the NASA/Army/MIT Active Twist Rotor Prototype Blade," American Helicopter Society 56th Annual Forum, Virginia Beach, Virginia, May 2—4, 2000.

2E2 Development and Current Status of MH2000 Helicopter

Takashi Kobayashi* and Kiyoshi Sakura**

Nagoya Aerospace Systems, Mitsubishi Heavy Industries, Ltd.

10, Oye-cho, Minato-ku, Nagoya, 455-8515, JAPAN

Abstract

The development of the MH2000 commercial helicopter, which had been dreamed of for a long time, was started in April 1995.   This is the first purely Japanese-made commercial helicopter. The paper presents the outline of the MH2000 development emphasizing its unique features for a short-term development.   In addition to the short development period, MHI developed both the aircraft and its engine at the same time, which is the first case in the industry.   To achieve the unique aspects of MH2000 development, we take some new approaches in design and manufacturing stages.   Mitsubishi Heavy Industries (MHI) conducted a significant reduction of development period and development cost in order to minimize the risk of development with quick response to the market trends. Currently three production types are delivered to the domestic market, and further improvement is being planned in MHI for possible expansion of the commercial helicopter in the twenty-first century.

Introduction

It had long been the dream of MHI to develop commercial helicopters.   For this purpose, element technologies have been accumulated in fundamental studies, while trial components have been manufactured to establish original technical basis.   In addition, as a result of market research, along with promotion of operational deregulation and construction of heliports, it is expected that the demand in the Japanese domestic market will expand as the problems of noise, safety, ride quality and price are solved to establish operational advantages.

Element technologies have advanced to the level just before verification of an actual helicopter, and new technologies for solving the problems have been developed.   Development of the RP1 prototype was started in July 1992 in order to avoid the risk of direct full development.

Throughout the manufacture of this RP1 prototype and ground tests and flight tests, the basic technologies for development of the helicopter and new techniques for realizing sales points have been proved.   The technical background has been established, and methods of developing at lower cost and in a shorter time have been verified.

On the basis of these achievements, the development of the first commercial helicopter, the MH2000, was started in April 1995.

Outline of MH2000

The MH2000 is the first purely Japanese-made commercial helicopter (**Fig.1**). In addition, all of the most important dynamic
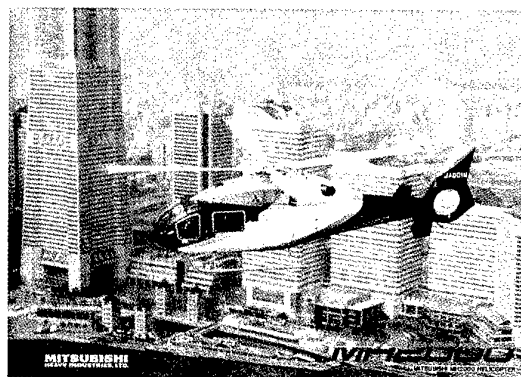

Fig. 1   MH2000 Helicopter

---

*   Deputy-director, Civil Aircraft Engineering Department
**   Manager, Civil Aircraft Engineering Department

components of the helicopter, namely, the rotor, engine, and transmission have been exclusively manufactured by MHI, and no such helicopter has been ever built in the world. . For the MH2000 development, based on the former RP1 experience, MHI decided to build those components by itself. This means that the company emphasized on entire development of helicopter system to learn integration technique.

The MH2000 is a middle-size multipurpose helicopter with two turbo shaft engines (**Fig.2**). Its maximum take-off weight is 4,500kg, its maximum speed is 150kt (280 km/h) and flight time is 4 Hr at the maximum case. The basic configuration with some major components is shown in **Fig.3**.

Development of MH2000 was started in April 1995 (**Fig.4**), and an application for the type certificate was submitted to the Civil Aviation Bureau, Ministry of Transport, on April 18. A preliminary T/C (Type Certification) board was held on May 10, and the type certification program was officially started. After the inspections and preflight T/C board on July 25-26, 1996, the maiden flight was successfully performed on July 29. The interim T/C board was held on March 27-28 and May 22-23, 1997, the final T/C board was held on June 11, and the type certificate was issued on June 26, 1997. During the certification program period, various and a number of flight tests are conducted with tow prototype helicopters. The total amount of flight was about 300 flights and 500 flight hours. At the point of the T/C approval, MH2000 was opened to the public and sales activities started.

The engine, MG5-110, was simultaneously developed at Nagoya Guidance & Propulsion Systems, and its type approval was issued on June 9, 1997, in accordance with the Basic T/C of the aircraft.

On the other hand, immediately after the Basic T/C is approved, an additional type certification program was started so as to improve the operation capabilities, using the two flight test helicopters. The type certificate amendment was issued on January 12, 1998. The airworthiness certificate (A/W) was issued for the second aircraft on January 13, 1998.

While the Amendment T/C work was running, a design program for the production MH2000 has already started in the middle of 1997. Some additional procedures for certification including another flight tests are performed using both prototype and production-type aircraft through 1998 until middle of 1999, before the production T/C was approved in September 1999. MHI had manufactured three production helicopter and the first one was delivered on October 1, 1999. In 2000, MHI has begun to manufacture the succeeding lot of MH2000 and, on the other hand, is conducting sales promotion.

As described above, MHI conducted a significant reduction of development period comparing with a traditional aircraft development. As a result of the short-term process, its development cost was minimized so as to correspond to the market trends, which minimized the risk of development at the same time.

For the first step of the business, the Japanese type certificate was obtained within the shortest period of time. The possible next step for the overseas market would be taken after well satisfactory results in the domestic market were confirmed and, from an engineering point of view, design feedback from customers has been done.

Technical Features of MH2000

MHI has introduced various new technologies in MH2000 to achieve superior capabilities as a helicopter of the twenty-first century.

Major technical features include the following.
(1) Reduction of External Noise
   - Newly designed main rotor blade with low noise and low vibration characteristics
   - Two mode RPM operation with FADEC (Full Authority Digital Electronic Control) engine control
(2) Comfortable cabin environment
   - Spacious cabin
   - Low noise and vibration level
(3) Safety features
   - Twin engine and crashworthy design
   - Map Display System (MDS) with GPS
   - Automatic Flight Control System (AFCS)
(4) Superior performance
   - Flight speed
   - Range
(5) Operating economy
   - Low price helicopter with low cost design
   - Reduced Direct Operational Cost (DOC)

In the MH2000 design, MHI has been seeking not only the high performance as a helicopter but also familiarity with human, e.g. silence and safety.

In the design and T/C work, a lot of tests, including component tests and flight tests, had been conducted to collect data and verify the performance of the helicopter shown above. Currently MHI continues engineering flight tests with the prototype MH2000, and those results have been successively applied to production aircraft to improve its capabilities.

Future Plan of MH2000

Helicopter is considered one of the best fit transportation media for the Japanese local situation. Approximately 1000 commercial helicopters are in service in Japan to date and this number is almost a half of the total Japanese general aviation. Therefore, MHI expects considerable expansion of market demands for helicopters if the appropriate hardware and the framework of society are provided.

With the recognition of this situation, MHI plans to continue the commercial helicopter business with enhancing the performance of the MH2000.

Major enhancements are investigated in the following subjects.
- More comfortable cabin : low vibration and noise
- More silent external noise
- High quality cabin interior
- Enhanced autopilot (AFCS)
- IFR (Instrument Flight Rules) operation
- High flight performance : higher cruise speed
- External equipments : camera, hoist, etc.
- Much easier maintenance

Realizing such advanced features, the MH2000 can be used for more versatile use such as EMS, rescue, broadcasting and offshore not only in a domestic area but also an international field.

The large cabin and cargo room of the MH2000 can carry various equipments which are required for helicopter missions, such as medical service, rescue and broadcasting. Because it is remarkably silent in the cabin, operators can manipulate those equipments easily with each crew communicating. Installation of optional equipments affects aircraft weight and cabin space and may cause deterioration of the flight performance. However, in the case of the MH2000, optional equipments scarcely reduce the performance as the helicopter originally has great cabin volume.

In this point of view, the MH2000 holds potential for future modifications and optional configurations as a multipurpose helicopter. MHI plans to further improve the MH2000 taking advantages of the enhancements and the potential described here.

Conclusions

(1) Mitsubishi Heavy Industries, Ltd. (MHI) has started the development of the MH2000 helicopter in order to extend its business in the Japanese commercial helicopter market.

(2) As a development of an entirely new commercial helicopter, MHI introduced the short-term process in design and manufacture fields and some unique technical features are applied to the helicopter.

(3) By the acquisition of a type certificate (basic, amendment and production) and an airworthiness certificate, the MH2000 began to fly in skies of Japan as a commercial helicopter. This was the first step for the commercial production of the MH2000.

(4) The production design was promoted in parallel with type certification work. MHI had manufactured three helicopters as the first lot of production MH2000 to date, which had been delivered for the customers.

(5) It is further planned to promote the production project while enhancing the performance of the MH2000 in various aspects so that the helicopter can be operated for versatile use.

References

(1) Toda, N., Harada, T., and Sato, A., "Rapid Prototype Development of the Mitsubishi RP1 Helicopter", American Helicopter Society 55th Annual Forum, Montreal, Canada, May 1999.

(2) Toda, N., "Review of MHI Helicopter Development", Heli Japan 98, Gifu, Japan, April 1998.

(3) Toda, N., Kobayashi, T. et al., " Application of MH2000 Commercial Helicopter", MHI Technical Review Vol.36, No.2, June 1999.

(4) Sakura, K., Kobayashi, T., "Development of MH2000, New Commercial Helicopter", American Helicopter Society 56th Annual Forum, Virginia Beach, Virginia, May 2000.
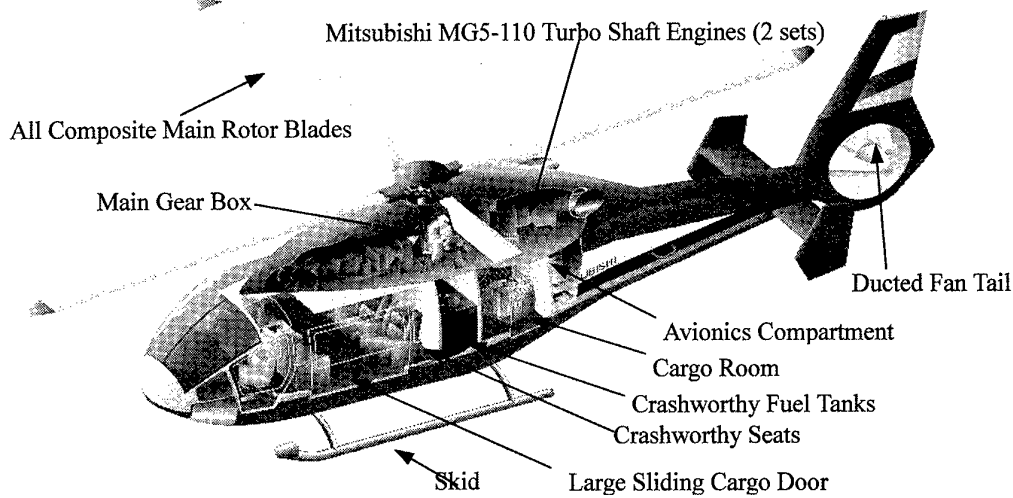
Mitsubishi MG5-110 Turbo Shaft Engines (2 sets)

All Composite Main Rotor Blades

Main Gear Box

Ducted Fan Tail

Avionics Compartment

Cargo Room

Crashworthy Fuel Tanks

Crashworthy Seats

Skid

Large Sliding Cargo Door

Fig. 2   MH2000 Configurations

Fig. 3   MH2000 3 View Drawing

φ12.20m

2.10m

3.12m

4.30m

3.10m

3.80m

12.20m

14.00m

5.38°

	1995	1996	1997	1998	1999

APR   MAR

G/A ▽

Design

Manufacture

Basic T/C

Maiden Flight ▽ (JUL)

Gound Test

Flight Test

T/C approval ▽ (JUN)

A/W (#2) ▽ (JAN)

Design

Flight Test

Design

Amendment T/C

Production T/C

1st Delivery ▽ (OCT)

Production T/C ▽ (SEP)

Manufacture

Flight Test

T/C: Type Certificate
A/W: Airworthiness
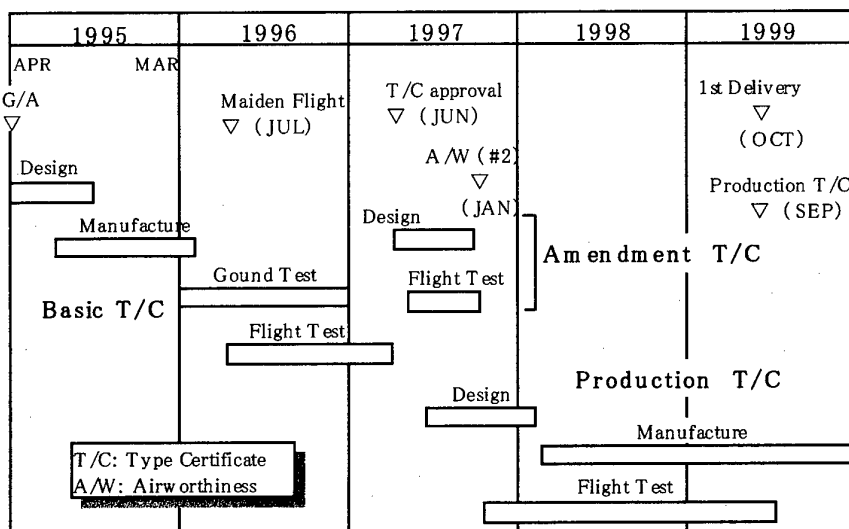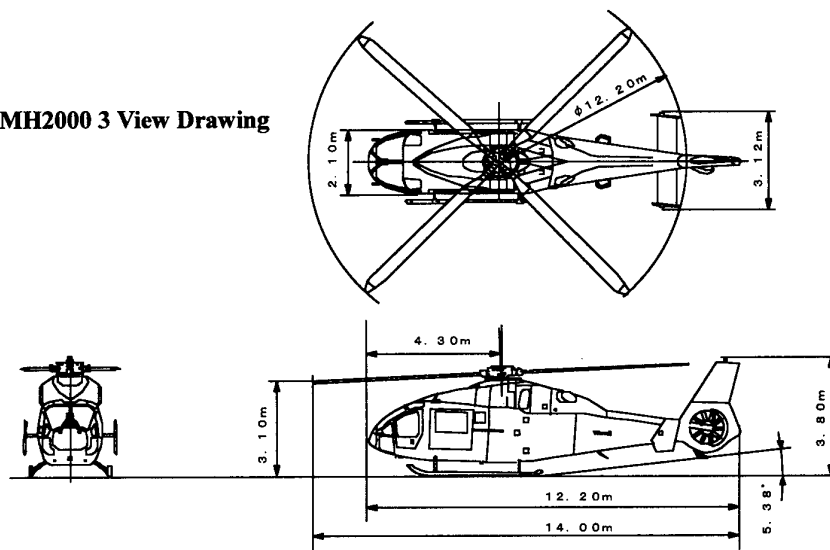
Fig. 4   MH2000 Development Schedule

2E3　Large Scale UAV System Operation Concept

Junichiro Sumita

Churyo Engineering Co.

Key words ; UAV, Autonomous, Remote Control

ABSTRACT

Future UAV's will fly safely among the manned aircraft in the general open air space, with the "autonomous" flight control. A high-reliably built autonomous and fault tolerant system requires extremely complex and expensive configuration, which is adverse for prevailing the UAV.

It is proposed in this paper that Remotely Piloted Operation for those UAV's can still be a solution to reduce the system complexity, getting free from many inconveniences caused from having the ground facilities.

The concept to conform autonomous control laws and several ideas to improve the remotely piloted operation are suggested. Top leveled sequence control over Flight Management System in hierarchy in control laws of the aircraft is a key factor, in which an expert type of autonomous control logic is described. The pilot guidance display system in landing phase is another key for a successful remote pilot system. The deflection control of the stick and pedals in the cockpit is also useful in landing controls. Moreover, a virtual cockpit system with high reality is to have a significant contribution.

The fault tolerant and modular design concept are described necessary to minimize the system complexity and maintainability.

1. Introduction

In not so far future, we might have large scale UAV systems such as Unmanned Freighter System, by which we could get overnight delivery service in every corner in the world. The freighter could fly in Mach 5 ~ 6 by hypersonic vehicles in 2020 time frame, according to NASA. [1] From the operational point of view, the UAV are expected to be safe and reliable in flight as same as or more than the conventional manned aircraft, especially because it would fly in the general air space, sharing with the manned aircraft. The safety requirement for UAV is almost same even in the case of small UAV, as long as it shares the flying space with ordinary vehicles.

Although the history of UAV have been long since WW1, encountering many times of ups-and-downs, the significance of the role with practical operability has been recently growing and accepted in general public, and it seems to establish a firm foundation of a new genre of the aircraft, by having many successful reconnaissance vehicles in the area conflicts of these days. [2] Even a concept of combat UAV would be realized in near future. [3]

In civil area, it is also expanding the application, such as in observation platforms of border, traffic, volcano, weather, etc. and spraying fertilizer on farmland, and so forth. NASA has been also paying great efforts to build high altitude observation platforms by UAV in its ERAST program. [4]

Almost all of the current UAV's are controlled by the remotely piloted way with rather simple flight control system operated in the restricted area or time or roles. [5] A simple structure in the configuration of the flight control system is for pursuing low life-cycle costs. It is considered that the safety of the UAV is kept by confining them to a limited range by elaborated operational procedures with the flight termination mode in control laws, and by other safety laws of the system.

Japan has an experience to develop and operate QF-104, full scale drone which is modified from F-104, under a remotely piloted control. The system had only 10^{-5} level of reliability, but kept the operational safety by keeping it under good maintenance conditions and aerodynamic flight termination mode as a design. Although it used normal runway of the air base, it was important for it to be operated under an isolated situation. [6]

Since to have a remote control causes many nuisances for the UAV operation, which is aiming to be free from human hands, the partial autonomous operation is now realized in several UAV examples in the USA. [5] This also means that the autonomous control technology is not so matured enough to control the vehicle throughout the flight.

Most of the civil applications of UAV in future, including Unmanned Freighter, are expected to be operated in General Air Space, coexisting with the manned vehicle. We are required to build highly reliable and safe vehicle system to win the public credibility.

2. Problem Area in Civil Use of UAV

The general air space flying with the manned aircraft, which is sought to be operated for the UAV in near future, requires that the UAV should be safe, and have no hazardous aspects in the operation. It

is apparent that we would be required to ensure the operational safety through the system integrity.

We do not have the standard figure of requirements for the system reliability of the UAV, as a regulation. But it is easily estimated that we are to be required to have the same or higher reliability level than that of ordinary manned vehicles. The 10^{-9} level of flight control system plus Human Pilot are the current combination of the manned vehicles for the extremely critical phenomena, according to the FAR Part 25. This means that 10^{-12}, for example, or higher would be a requirement for the UAV as the system reliability, or much higher redundancy requirement for the system might also be suggested from the points satisfying the public asking for the highly safe operation of the system.

As the redundancy of the system increases, the system complexity increases exponentially, and it becomes more expensive.

As for the small scale of the Civil UAV, there might be a room to have a restricted operation to keep a high level of safety requirements. Therefore, the problem is sole to the large scale UAV for civil applications which will absorb the growing mission requirements in wide varieties.

Under the above situation, the remote control can still be a solution to cope with to realize the future UAV by minimizing the system complexity. Nonetheless Remote Control has many inconveniences, such as in needing tremendous amount of pilot training, and facilities of ground cockpit, etc. This causes so much trouble that Japan has lost the enthusiasm to plan the following new UAV programs next to QF-104. Thus the main system of UAV is also going to and should go to a complete "autonomous" control, including the automatic landing, so as to meet with workload saving and reliable operations without human hands. However, the autonomous control technology is still in immature.

Furthermore, the digital interface with the current ATC system should be established to match with the advanced autonomous system.

3. System Configuration of the Large Scale UAV

Consequently, the most effective system of the large scale UAV should have an autonomous control with a remotely piloted operation as a back-up.

The Large Scale UAV's require more highly reliable systems than in Manned Vehicle. It is considered to be proper that $4 \sim 5$ redundancies are applied in the design for the fully autonomous configuration of the UAV system, being in line with the would-be requirement.

However, if we could add a remotely piloted route

in the control of the aircraft as a back up, the triplex redundancies for the system should be adequate. This means the remote control can contribute to reduce the system complexity to $1/1.3 \sim 1/3$ [7], which could compensate for demerits in increasing several pieces of equipment for the remote control.

In this case we can refer to the same requirement as in FAR ; The system of 10^{-9} plus human pilot in the ground can be equivalent to manned vehicles. Moreover, human pilot in the loop is to be a key factor to be able to give the reliability to the public.

10^{-9} is astonishingly difficult level to achieve successfully. The fault tolerant concept, which make the most of the functional alternatives, should be applied to the design of the aircraft and the flight control system to minimize the redundancy, and the actual number of parts. Beginning from skewed sensors of Rate-Gyro and G-Meter, Multi-Microprocessers, Smart Actuators, Redundant Data Bus, etc., the aircraft system configuration with alternate control surfaces conforms basic ideas for the fault tolerant design. Furthermore, the modular hardware design concept is proposed for the system, as well as Avionics Systems, to keep high reliability with high maintainability, by using the commercial parts on-the-shelf.
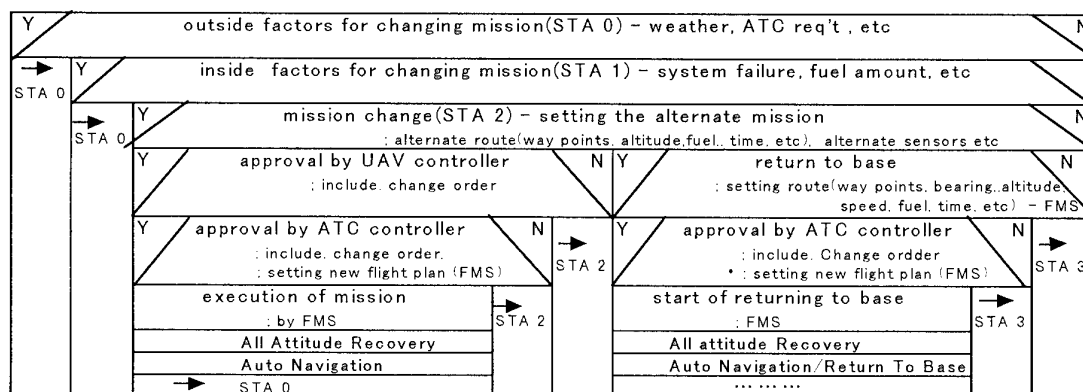
4. Autonomous Control of the UAV

The recent trend in controlling the UAV described above is to apply the autonomous control law. This is a right direction to pursue the merits of the UAV which is featured by the name of "unmanned" and to save workloads in their operation as much as possible. This should be expanded to include the landing phase.

It is also recognized that this is not yet to be matured enough to leave the vehicle to the control to full extent, for the artificial brain to generate the control to be able to cope with the unexpected situation is still under developing phase.

The autonomous control laws at the current stage can be conformed by having the top hierarchy autonomous sequence logic to control the existing systems of FMS, Auto-pilot and Flight Controls, [8] which also should have clear-cut hierarchy structures, and receive the pilot access in only one level. We know the ways and procedures to operate the vehicle successfully under the current Air Traffic Control. The expert system to express those knowledge into auto-sequences can be a semi-artificial brain for an adequate autonomous logic in control. One example of top leveled sequences by Chapin chart is shown at Table 1. [8] This shows that there are no new concepts and procedures to be newly verified. We can say accordingly that the autonomous technology by an expert type of auto-sequence is already on our hands.

Table 1　　　　　　　Top Level Chapin Chart - Autonomous Mission Change

Y						
outside factors for changing mission(STA 0) - weather, ATC req't , etc						N

STA 0

Y	inside factors for changing mission(STA 1) - system failure, fuel amount, etc	N

STA 0

Y	mission change(STA 2) - setting the alternate mission	N
	; alternate route(way points, altitude,fuel., time. etc), alternate sensors etc	

Y	approval by UAV controller	N	Y	return to base	N
	; include. change order			; setting route(way points, bearing,,altitude speed, fuel, time, etc) - FMS	

Y	approval by ATC controller	N	→ STA 2	Y	approval by ATC controller	N	→ STA 3
	; include. change order. ; setting new flight plan (FMS)				; include. Change ordder • : setting new flight plan (FMS)		

execution of mission		→ STA 2	start of returning to base		→ STA 3
; by FMS			; FMS		
All Attitude Recovery			All attitude Recovery		
Auto Navigation			Auto Navigation/Return To Base		
→ STA 0			… … …		

5 . Improvements in Remote Control

The radio wave control is above cited as a most effective way to conform the UAV system, which is a very common and sole method for the current UAV system configuration. Although this is vulnerable to the jamming in the war plane, we can have ways nothing to do it for civil use.

It is extremely important that we can generate the innovative ground system, by which we can eliminate nuisances due to the application of the way of remote control.

1) Ground Cockpit Improvements

Most of the UAV applications in USA have a joy stick in a console-type of operator devices to control the vehicle. And the operator is not necessarily to be qualified as a pilot.

QF-104 had a cockpit of a stick and pedals, similar to F-104, and F-104 pilots for the aircraft operation. This is one of factors, by which the project was successful without having an accident throughout its operational phase .

Basing on the experiences , the further improvements about the ground cockpit are suggested to be applied as follows.

a) Cockpit with High Virtual Reality

The ground cockpit is to have the high degree of reality in controls as in the manned aircraft, and should have a stick or wheel (can be a side-stick) and pedals as control devices, and similar instrument panels to the actual cockpit, to ease the pilot controls as much as possible.

And the controller should be qualified as a pilot who can actually fly under ATC in the general air space.

b) Visual Cues as in Dome-typed Simulator

The visual reality for the pilot is also so important that the dome type screen for the projectors should be necessary, where we can have the wide front view over 180 . This

requires three sets of cameras on board, but only front view camera is to have high resolution, with also high resolution picture of only central part of front screen of the dome. The concept is shown in Fig.1.

c) Sound Cues

The sounds of up-and-down of gears and flaps and engine operation etc. can be promoters for the cockpit reality . The simulation of body reactions in aircraft movement is not necessarily required from the cost effective point of view.
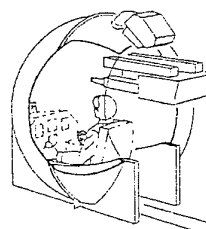

Fig.1　Dome Type Ground Cockpit

2) Visual Symbols System for Pilots Guidance

The proper flight path can be generated from GPS data and actual air data sensors on board. The deviation from the proper-to-be glide path and the actual aircraft position, expressed by speed vector type, can give the pilot the adequate landing maneuver control tools. The concept for the symbols display over-laid on the pilot front TV screen monitors the front view of the UAV is shown in Fig. 2 .

In the case of QF-104, we utilized the vectoring capability of the tracking antenna of the system, and had a guidance symbols for proper landing path, which was so mandatory for the aircraft control.

3) Control Laws in Ground Proximity

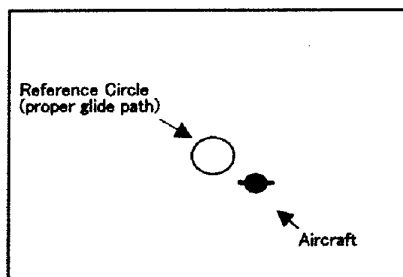In the remote control, much bigger time lag is

Fig. 2 Pilot Guidance Symbols System
(Head Up Display)

inevitable, comparing to the ordinary aircraft. This causes the difficulty in UAV control especially in the flight phase at the vicinity to the ground, owing to the impacts from varied side winds and gusts of the circumstances.

It was reported that the stick and pedal deflection control with the attitude or the heading hold of Auto Pilot function was very contributing for a stable pilot control in landing phase in the QF-104. Consequently, similar control laws seem to be required in general to perform maneuvers in high handling quality.

The concept in the QF-104 is shown in Fig.3.

6. Conclusions

The UAV that fly in General Air Space with the manned aircraft in future should have highly reliable system, which is required to meet with FAR PART 25. The remote control can play a role for reducing the system complexity. It is described that 10^{-3} level of reliability in the autonomous flight control system with a remotely piloted control as a backup is appropriate for the related UAV.

The design concept for the related system configuration should be Fault Tolerant and a modular conformed to reduce the system complexity to a reasonable size, to be capable for a good maintenance, and acquire the public credibility.

As the autonomous control of all the phase of flight is a prerequisite for the future UAV, the more complete expert type of auto-sequences control laws should be generated and verified in the flight.

Furthermore the proper digital interfaces with the ATC should be required to get more complete un-man oriented operations.

There is a concept that we can suppress a superficial figure of reliability, if we limited the operation of the UAV to a restricted area. This kind of discussion is proper and adequate to have a small and cheap version of the UAV. Although the system complexity is reduced by the lowered reliability requirement in this case, the back-up system can also contribute for further reduction of complexity.

To have Remote Control capability is important.

Japan will have many UAV applications. Some experimental vehicles in UAV are actually planned, under the autonomous operational concept. The author would like to recommend to give them a remote control route in control as a back-up.

References

1) "NASA Commercial Technology Policy" May 1996
2) "UAV on the Hills : A report on UAV−Related Activity on Capitol Hill" Association for Unmanned Vehicle Systems, 1997
3) D.A.Deets " Operational Concepts for Uninhabited Tactical Aircraft" NASA/TM−206549, 1998
4) NASA FACTS SHEET "ERAST Project", www.dfrc.nasa.gov
5) J.H.Del Frate,G.B.Cosentino "Recent Flight Test Experience with Uninhabited Aerial Vehicles at the NASA Dryden Flight Research Center" NASA/TM−206546, 1998
6) Jun Sumita "General Description on QF-104" Symposium AUVS, 1992
7) S.S.Osder " Chronology Overview of Past Avionic Flight Control System Reliability in Military & Commercial Operation" AGARD−AG−224, 1978
8) Jun Sumita " Autonomous Flight Control Study in UAV" JSASS 31st annual meeting, pp.138−141, 2000
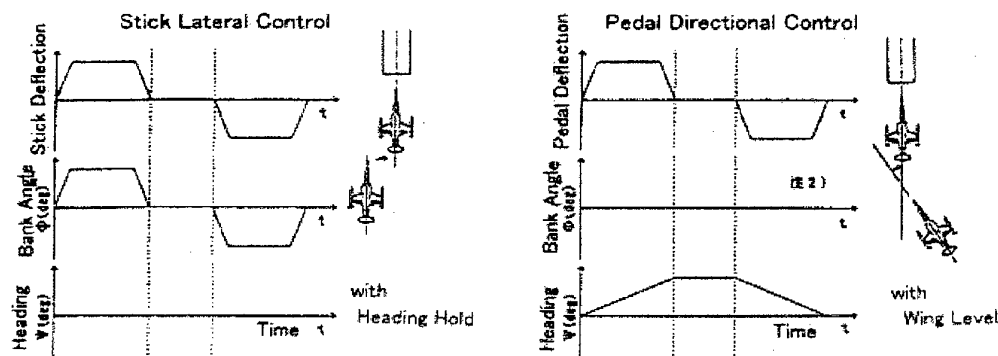
Fig. 3 Ground Proximity Control Law

2E4 Optimization of Flapping Wing Motion

Keiichi Ito* and Shinji Suzuki**

*University of Tokyo, Dept. of Aeronautics and Astronautics, 7-3-1Hongo, Bunkyoku, Tokyo

**University of Tokyo, Dept. of Aeronautics and Astronautics, 7-3-1Hongo, Bunkyoku, Tokyo

Key Words: Aerodynamics, Unsteady Flow

Abstract

This is a preliminary investigation for creating a design tool for flapping wings for Micro Air Vehicles. MAV is a small-scale aircraft (no more than 15cm in any dimension), which is aimed to be used as a surveillance device. A Vortex Lattice Method is employed to model a finite-span flapping wing. The flapping wing model investigated in this paper is a rigid rectangular-planform plate with two degrees of freedom, i.e. pitching and heaving. An optimization is performed to find out an optimum coupling between pitching and heaving for maximum thrust and minimum power.

Nomenclature

A_{ij}, B_{ij} = influence coefficient to the control point

$\tilde{A}_{ij}, \tilde{B}_{ij}$ = influence coefficient to the quarter chord

AR = aspect ratio

c = wing chord

ea = elastic axis (center of pitch) location

h = panel vertical distance

L = lift as in wind tunnel coordinate

D = drag as in wind tunnel coordinate

t = time

U = free-stream velocity

q =pitch rate

S = wing area

$\vec{V}$ = velocity vector

x, y, z   = wing coordinates with y along elastic axis

x_i = x-coordinate of control point

Γ = vortex or circulation

Γ_b = bound vortex

Γ_w = wake vortex

θ = pitch angle

ρ = air density

ϕ = potential function

Introduction

Recently, flapping wing flight has attracted considerable attention due to the DARPA's (Defense Advanced Research Program Agency of the U.S.) initiative to promote research on Micro Air Vehicles (MAVs). In the past years, there has been a fairly good number of research concerning the mechanics and aerodynamics of flapping wing. However, few literatures are available on designing an optimal flapping wing. Computational tools to design a flapping wing with desired performance are needed. This paper will present preliminary efforts towards such objectives. Here, Vortex Lattice Method was employed to model the aerodynamic force exerted to a rigid flapping wing. The coupling of heaving and pitching motion were optimized using a Genetic Algorithms code developed by Houck et al. Inertial forces due to the mass and geometry of the wing are not considered in this paper.

Vortex Lattice Method

The VLM represents the wing as a planar surface on which a grid of vortex lattices is superimposed. The velocities induced by each vortex lattice at a specified control point are calculated using the law of Biot-Savart. A summation is performed for all control points on the wing to produce a set of linear algebraic equations for the vortex strengths that satisfy the condition of no flow through the wing, i.e. the tangential condition (at the control points). A few

---

*Graduate Student, Department of Aeronautics and Astronautics

**Professor, Department of Aeronautics and Astronautics

governing equations are in order. For an irrotational flow, the velocity may be expressed in terms of potential function

$$\vec{V} = \nabla \phi \qquad (1)$$

In incompressible flow, the continuity equation is

$$\nabla \cdot \vec{V} = 0 \qquad (2)$$

Thus,

$$\nabla^2 \phi = 0 \qquad (3)$$

Another condition that has to be satisfied by the solution is Kevin's theorem, namely, that there is no net change in the circulation in the field at any time step, or

$$\frac{d\Gamma}{dt} = 0 \qquad (4)$$

In this research, the model, which satisfies these four equations, consists of panels having a constant bound vortex in each quarter chord of a rectangular cell. A control point is located in each cell at the three-quarter point of centerline. As stated previously, if the incident air velocity to the control points are known, a linear algebraic system of equation can be set up to solve for the unknown bound vortex strengths at every time step. The vortex strengths Γ s determined from the past time steps are shed behind the wing to form the wake. In the present model, one panel is used chordwise to represent the bound vortices and the wake is planar, and constrained in the same plane as that of the wing as shown in Fig. 1. The wing is a rigid rectangular-planform plate with two degrees of freedom, i.e. pitching with respect to y-axis and heaving along z-axis. The simplicity of the model works in favor of the optimization process discussed in the next section. The bound vortex strengths Γ_b s are determined from the following equation.

$$-U\sin\theta - qx_i + \frac{\partial h_i}{\partial t}\cos\theta =$$

$$\left[A_{ij}\right]\begin{bmatrix}\Gamma_{b_1}\\ \vdots \\ \vdots \\ \Gamma_{b_n}\end{bmatrix} + \left[B_{ij}\right]\begin{bmatrix}\Gamma_{w_1}\\ \vdots \\ \vdots \\ \Gamma_{w_m}\end{bmatrix} \qquad (5)$$

Once Γ s are determined, the pressure difference can be determined using unsteady Bernoulli equation as derived by Katz. Then, lift and induced drag can be calculated from the following equations.

$$L = \rho U \sum_{k=1}^{n}\Gamma_{b_k}\Delta y + c\frac{d}{dt}\left(\sum_{k=1}^{n}\Gamma_{b_k}\right)\Delta y \qquad (6)$$

$$D = L\tan\theta + \frac{\rho\left(\sum_{k=1}^{n}W_k\Gamma_{b_k}\right)\Delta y}{\cos\theta} \qquad (7)$$

where

$$\begin{bmatrix}W_1\\ \vdots \\ \vdots \\ W_n\end{bmatrix} = \left[\tilde{A}_{ij}\right]\begin{bmatrix}\Gamma_{b_1}\\ \vdots \\ \vdots \\ \Gamma_{b_n}\end{bmatrix} + \left[\tilde{B}_{ij}\right]\begin{bmatrix}\Gamma_{w_1}\\ \vdots \\ \vdots \\ \Gamma_{w_m}\end{bmatrix} \qquad (8)$$

$$+U\sin\theta + qx_i - \frac{\partial h_i}{\partial t}\cos\theta$$

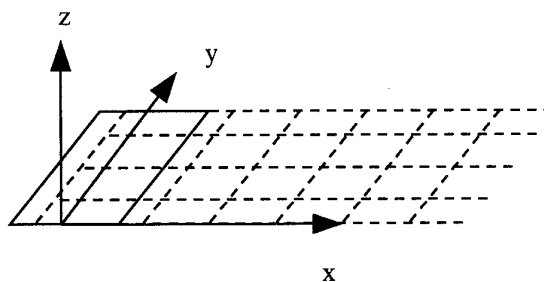When D is negative, it means the flapping is producing thrust.

Fig. 1

Power is computed from the following equation

$$P = L\dot{h} + M_p\dot{\theta} \qquad (9)$$

where M_p is pitching moment about ea.

Genetic Algorithms

In obtaining some of the results in next section, Genetic Algorithms was employed as an optimization tool. It was preferred among other optimization methods due to the ease of implementation to the problem at hand. One of the advantages of GA is that it does not require derivative information. Since the aerodynamic forces are calculated using vortex-lattice method, this feature was particularly convenient. GAs search the solution space of a function through the use of simulated evolution, i.e. the survival of the fittest strategy (C. Houck et al.) The basic idea is as follows. First, populate the solution space with individuals with different combinations of genes (or variables), i.e. chromosomes. Thus, for example, if we want to maximize y as in the following equation

$$y = f(x_1, x_2, x_3) \qquad (7)$$

x_1, x_2, and x_3 can be thought of as genes whereas a row vector $[x_1, x_2, x_3]$ as a chromosome or individual. A population consists of numerous instances of this vector. Then, give better chance of survival to the more fit individual from the population and pass the characteristics of the fit individual to the next generation (or search the state-space neighborhood of these individuals) through an operation called cross over (usually, two new individual is created out of two parents). Mutation is employed to avoid premature convergence. Successive application of the process enables to find the optimal solution. In the current study, decimal base floating-point representation of genes was used (as opposed to binary base representation of genes commonly observed in the literature).

Results

Numerical computation of thrust and power was performed based on the simple model described previously. The following values were used in the calculation unless specified otherwise.

ea = 0.25

h = chord length
S = 0.075 m^2
AR = 3
U = 1 m/s
ρ = 1 kg/m^3

Fig. 2 shows the thrust at various flapping frequencies with elastic axis, or center of pitch, at 40% of chord. The estimated weight of MAV, which is about 0.05 N (Shyy et al.), is also shown in the figure. Fig. 3 shows the thrust with respect to the phase difference between heaving and pitching. Fanning forward means that at maximum h the wing is pitching up and at minimum h it is pitching down. Fanning backward means that at maximum h the wing is pitching down and at minimum h it is pitching up. At phase difference of +90 deg., the wing has zero pitch at either max. h and min. h but pitches down in down stroke and pitches up in up stroke. At phase difference of –90 deg., the wing has zero pitch at either max. h and min. h but pitches up in down stroke and pitches down in up stroke. Two cases are shown: one with elastic axis at quarter chord and the other at 40% chord. In Fig. 4, GA was used to determine the phase difference for maximum thrust for given flapping frequency elastic axis was fixed at quarter chord. The phase difference is shown in Radians. The result is consistent with that of Azuma. Fig. 5 shows the efficiency with respect to flapping frequency. Efficiency is defined as the ratio between thrust coefficient and power coefficient, i.e. C_T/C_P. Fig. 6 gives the phase difference for maximum efficiency for given flapping frequency. Again, in obtaining Fig. 5 and 6, GA was used. In all cases where GA was employed, they converged in less than 7 generation with a population of 100. In calculating power, the apparent mass effect was also considered. In Fig. 6, the plot computed without the apparent mass effect were consistent with the analytical result obtained by Azuma.
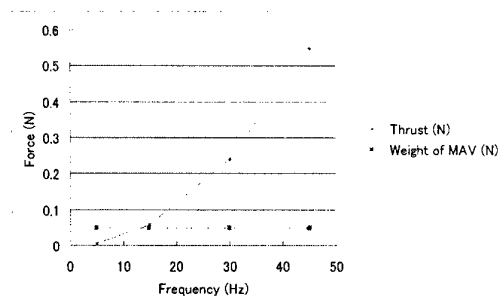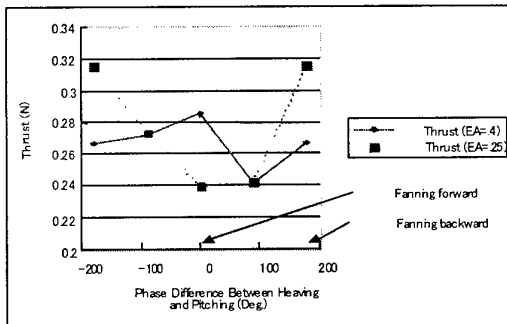
Fig. 2 Thrust at various frequencies
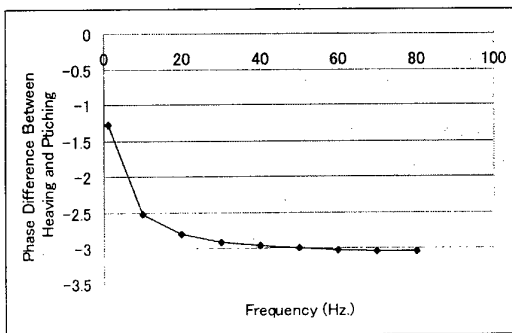

Fig. 3 Thrust and elastic axis location

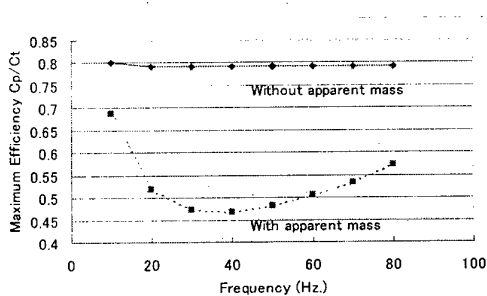
Fig. 4 Phase difference for maximum thrust

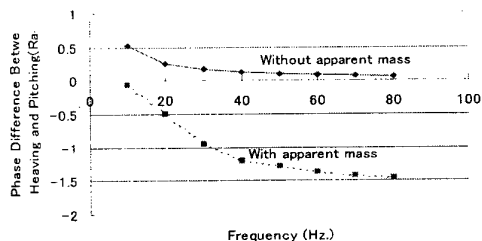Fig. 5 Maximum efficiency at various frequencies

Fig. 6 Phase difference for maximum efficiency

Conclusions

The results show the possibility of using simple aerodynamic model and optimization algorithms to design a flapping wing. In this paper, only the coupling of heaving and pitching were considered. Convergent optimal solutions were obtained with respect to flapping frequencies. A more sophisticated model can be developed to optimize not only the flapping but also the planform shape, inertia and elastic properties.

References

1. Azuma, A., "The Biokinetics of Flying and Swimming," Springer-Verlag, pp. 100 – 109.

2. Bisplinghoff, R. L., Ashley, H., and Halfman, R. L., "Aeroelasticity," Addison-Wesley, pp. 260 – 261, 274, 285, 393 – 394, 1955.

3. Haupt, R. L., and Haupt, S. E., "Practical Genetic Algorithms," John Wiley & Sons, pp. 1 – 64, 1998.

4. Houck, C. R., Joines A. J., and Kay, M. G., "A Genetic Algorithm for Function Optimization: A Matlab Implementation," Manual for GAOT (Genetic Algorithms Optimization Toolbox), North Calorina State University.

5. Winfield, J. F., "A Three Dimensional Unsteady Aerodynamic Model with Application to Flapping-Wing Propulsion," Master Thesis, U. of Toronto, pp. 1 – 75, 1990

6. Katz, J., "Method for Calculating Wing Loading During Maneuvering Flight along a Three-Dimensional Curved Path," J. Aircraft, Vol. 16, November 1979, pp. 739 – 741.

7. Levin, D., and Katz, J., "Vortex-Lattice Method for the Calculation of the Nonsteady Separated Flow over Delta Wings," J. Aircraft, Vol. 18, December 1981, pp. 1032 – 1037.

8. Shyy, W., Berg, M., and Ljungqvist, D., "Flapping and Flexible Wings for Biological and Micro Air Vehicles," Prog. Aero. Sci., Vol. 35, 1999, pp. 455 – 505.

9. Vest, M. S., and Katz, J., "Unsteady Aerodynamic Model of Flapping Wings," AIAA J. Vol. 34, July 1996, pp. 1435 – 1440.

2E5 ACOUSTIC BEHAVIOUR OF CAVITIES DUE TO FLUID-STRUCTURE INTERACTION PROBLEMS

L. J . Pedroso[1] and M.V. G. de Morais [2]
Universidade de Brasília - Faculdade de Tecnologia
Departamento de Engenharia Civil - Cx. Postal 04492
70.919-970 - Brasília - DF – BRAZIL
lineu@unb.br or pedroso@struc.polymtl.ca

Key Words: Dynamic, Acustic, Fluid-Structure Interaction, Finite Element Method

ABSTRACT

This paper presents a symmetric variational formulation for the calculation of dynamic problems regarding a fluid-structure interaction. The discretization of the problem is obtained through the method of finite elements as applied to the functionals of a solid, a fluid and an interface. This paper also makes a comparison between the coupled and uncoupled dynamic behaviours for a given test and its verification through analytical solutions.

1. INTRODUCTION

The interaction between the fluid and the structure greatly affects the structural response and can be found in many engineering applications, such as nuclear reactors, offshore platforms, ships, turbines, barrages, etc. It is crucial that its effects be taken into account.

The validation of the formulation in this paper has been developed by various authors [1], and it includes a Lagrangian description for the solid and an Eulerian description for the fluid. Other sorts of formulation are to be found in the specialised literature [2,3,4,5,6], and they consider only the hydrostatic pressures or the velocity potential as variables for the fluid, and the nodal displacements for the solid. Other authors [7,8,9], however, have used Lagrangian formulations for the nodal displacements of the solid and the fluid.

This paper will only analyse inviscid and irrotational fluids, which are limited by pre-determined domains and have slight displacements. The variables involved are a displacement X_s, a pressure p and a potential Π (similar to a displacement potential for fluid), which is also useful for symmetrizing the problem.

The dynamic behaviour of systems in frequency domain of free vibrations for simple problems is studied, always making comparison with analytical results and results provided the literature. Problems such as ill conditioning of matrixes have been pinpointed and solved, and the results obtained have proved to be in accordance with the values predicted.

2. THEORICAL FORMULATION

Considering a structure with linear and homogeneous elastic behaviour within a domain V_s and an inviscid and irrotational fluid within a domain V_f. And, Σ is the surface comprising V_s and V_f, where the fluid-structure interaction takes place. The slight displacements made by the structure are determined by the degree of freedom of displacement $X_s(x,y,t)$. The fluid description is obtained

through the following variables of pressure: P and Π.

2.1 FUNCTIONAL ($\Im$) OF FLUID ($\Im_f$) – STRUCTURE ($\Im_s$) COUPLED SYSTEM

Using a variational analysis of a dynamic problem, the functional $\Im$ of the coupled system must be determined in such a way that the first variation of $\Im$ regarding an arbitrary increase of X_s and p lead to equilibrium equations. In order to achieve that, the functional $\Im$ is obtained through the association of $\Im_s$ and $\Im_f$ so that there is a coincidence with the coupling term. And, with a view to obtaining the classical expression $\Im' = \Im_1 - \omega^2 \Im_2$, a supplementary (or dual) variable $\pi = -p/\omega^2$ is associated to the pressure variable, thus leading to the final functional $\Im'$ related to fluid-structure system [10,11,12]:

$$\Im' = \frac{1}{2} \int_{V_s} \overline{\overline{\sigma}} \otimes \overline{\overline{\epsilon}}\,dv + \frac{1}{2} \int_{V_f} \frac{1}{\rho_f c^2} p^2 \,dv$$

$$-\omega^2 \left[\frac{1}{2} \int_{V_s} \rho_s (x_s)^2 \,dv - \frac{1}{2} \int_{V_f} \frac{1}{\rho_f} (\mathrm{grad}\pi)^2 \,dv \right. \quad (1)$$

$$\left. - \int_{V_f} \frac{1}{\rho_f c^2} p\pi\,dv - \int_{\Sigma} \pi x_s \cdot n d\Sigma \right]$$

The first two terms represent the strain energy of the structure and of the fluid (compressibility). The third term represents the kinetic energy contained in the structure. The three remaining terms represent the kinetic energy of the fluid (the complexity of the inertial term associated to the fluid is due to the fact that the dual variables p and π are employed to determine it).

2.2 FINITE ELEMENT DISCRETIZATION

We discretize the variational indicated expressions through a standard isoparametric interpolation function for X_s-P-Π variables,

$$x_s \cong x_{s,h} = \sum_{i=1}^{n} h_i x_{s,i};$$

$$p \cong p_h = \sum_{i=1}^{n} h'_i p_i; \ \pi \cong \pi_h = \sum_{i=1}^{n} h''_i \pi_i \quad (2)$$

where h_i, h'_i, h''_i are the various shape functions involving solid and fluid variables, and n is the number of element nodes.

By using the linear elastic element 2D of plane stress state (PSS) in order to discretize the solid domain, we

---

obtain the most general configuration of the problem,

$$X_{s,h} = H\vec{X}_{s,h} \qquad (3)$$

where, u, v, w are displacement functions of solid element for directions x, y and z, respectively; u_i, v_i, w_i represent the nodal displacements of solid element in node i for corresponding directions; h_i is the interpolation function for node i; [H_u H_v H_w] are the shape functions associated to all element nodes regarding the subscript displacement, and H is the shape function matrix for an element with n nodes; $\vec{X}_{s,h}^T = [u_1 \ v_1 \ w_1 \ u_2 \ v_2 \ w_2... \ u_n \ u_n \ u_n]$ is the nodal displacement vector for an element containing n nodes. Similarly, for the elements of the fluid, we have,

$$p_h = h'\vec{P}_h \ e \ \pi_h = h''\vec{\Pi}_h \qquad (4)$$

where p_h and π_h correspond to approximated functions of pressure and the variable π of fluid domain; p_i and π_i are nodal values of pressure and π variable of the fluid in node i; h_i' and h_i'' represent the interpolation function of pressure and of variable π in node i.

2.3 FIRST VARIATION OF THE FUNCTIONAL

By replacing the polynomial approximations in each term of functional (1), it is possible to compose the discretized functional of the fluid-structure problem:

$$\begin{aligned}
\mathfrak{I}'_h &= \frac{1}{2} X_{s,h}^T \cdot \int_{V_s} B^T D B dv \cdot X_{s,h} \\
&+ \frac{1}{2} \frac{1}{\rho_f c^2} P_h^T \cdot \int_{V_f} h^T h dv \cdot P_h \\
&- \omega^2 \left[\frac{\rho_s}{2} X_{s,h}^T \cdot \int_{V_s} H^T H dv \cdot X_{s,h} \right] \qquad (5) \\
&- \frac{1}{2} \frac{1}{\rho_f} \Pi_h^T \cdot \int_{V_f} \nabla h^T \cdot \nabla h dv \cdot \Pi_h \\
&- \frac{1}{\rho_f c^2} P_h^T \cdot \int_{V_f} h^T h dv \cdot \Pi_h \\
&- X_{s,h}^T \cdot \int_{\Sigma} H^T (\vec{n} \cdot h) d\Sigma \cdot \Pi_h
\end{aligned}$$

By minimising the approximated functional (5) regarding $X_{s,h}$, P_h and Π_h, we have the matrix expression for fluid-structure interaction (FSI) problems,

$$\left[\begin{bmatrix} K_{xx} & 0 & 0 \\ 0 & K_{pp} & 0 \\ 0 & 0 & 0 \end{bmatrix} \right.$$

$$\left. -\omega^2 \begin{bmatrix} M_{xx} & 0 & -M_{x\pi} \\ 0 & 0 & -K_{p\pi} \\ -M_{x\pi}^T & -K_{p\pi}^T & -M_{\pi\pi} \end{bmatrix} \right] \cdot \left\{ \begin{matrix} X_{s,h} \\ P_h \\ \Pi_h \end{matrix} \right\} = 0 \qquad (6)$$

where K_{xx} and M_{xx} are the stiffness and structure mass matrixes, K_{pp} is the compressibility matrix of the fluid ("stiffness matrix"); $M_{\pi\pi}$ describes the inertial effects of the fluid, and M_{xx}. and $K_{p\pi}$ correspond to the coupling matrixes X_s-Π and P-Π, respectively.

Matrix system (6) shall provide the natural modes for

fluid-structure coupling. The soluction in the time domaine will be easily obtained

3.NUMERICAL RESULTS

This set of problems [11] include a stiffness cavity with a movable boundary (a stiffness plate) which is discretized through linear triangular finite elements (LTFE) in a plane stress state (PSS) on an elastic support (springs), and the fluid is also discretized by LTFE

Case 1A - Square Open Cavity with a Piston (Fig. 1)

The coupled and uncoupled analytical solutions of the problem are [10,11], respectively,

$$\omega = \pi c \left(\frac{n_x^2}{L_x^2} + \frac{n_y^2}{4L_y^2} \right)^{\frac{1}{2}}, n_x = 0,1,2,\cdots; n_y = 1,3,5,$$

$$\& \qquad \lambda^2 \left(\mu + \frac{1}{\lambda} tg\lambda \right) = \alpha \qquad (7)$$

where $\mu = m_s/m_f =$ ratio between the piston mass and the fluid mass; $\alpha = (KL)/(\rho_f c^2 \cdot S) =$ ratio between the spring stiffness and the fluid volume stiffness; $\lambda = (\omega \cdot L)/c =$ ratio between the cavity length and the wave length for a given natural frequency.

The analytical and numerical results, in terms of the frequencies, are shown in table 1

Uncoupled Modes				
		ω - rad/s		
	Mode	Num.	Ref.[3]	Theoric.
Piston	-	14.32	15.19	14.32
Fluid	1 - 10	2359.36	2359.35	2356.19
	2 - 11	5360.29	5317.50	5268.58
	3 - 20	7154.72	7154.55	7068.58
	4 - 21	8748.01	8719.01	8495.38
	5 - 12	10060.19	9968.31	9714.84
Coupled Modes				
		ω - rad/s		
	Mode	Num.	Ref.[3]	Theoric.
Fluid Piston	1	7.62	7,59	8,04
	2	3597.83	3597,82	3586,65
	3	5288.32	5316,83	5268,58
	4	7873.30	7873,08	7758,90
	5	8614.61	8717,87	8495,38

Table 1 - Frequencies Results of Case 1A
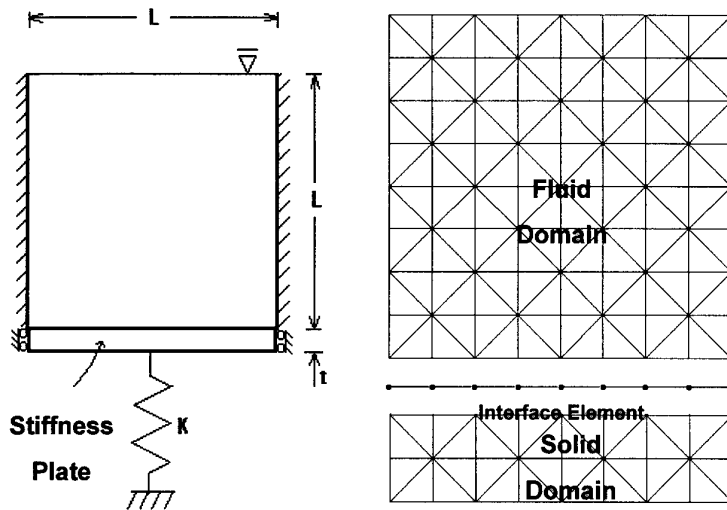
Problem's Data:

Geometric Characteristics:

$L_x = L_y = L = 1m; t = 0.05m$

Fluid Characteristics:

$\rho_f = 1000 \text{ kg/m}^3; c = 1500 \text{ m/s}$

Solid Characteristics:

$E = 2.10 \cdot 10^{11} \text{ N/m}^2; \nu = 0.3$

$\rho_s = 7800 \text{ kg/m}^3$

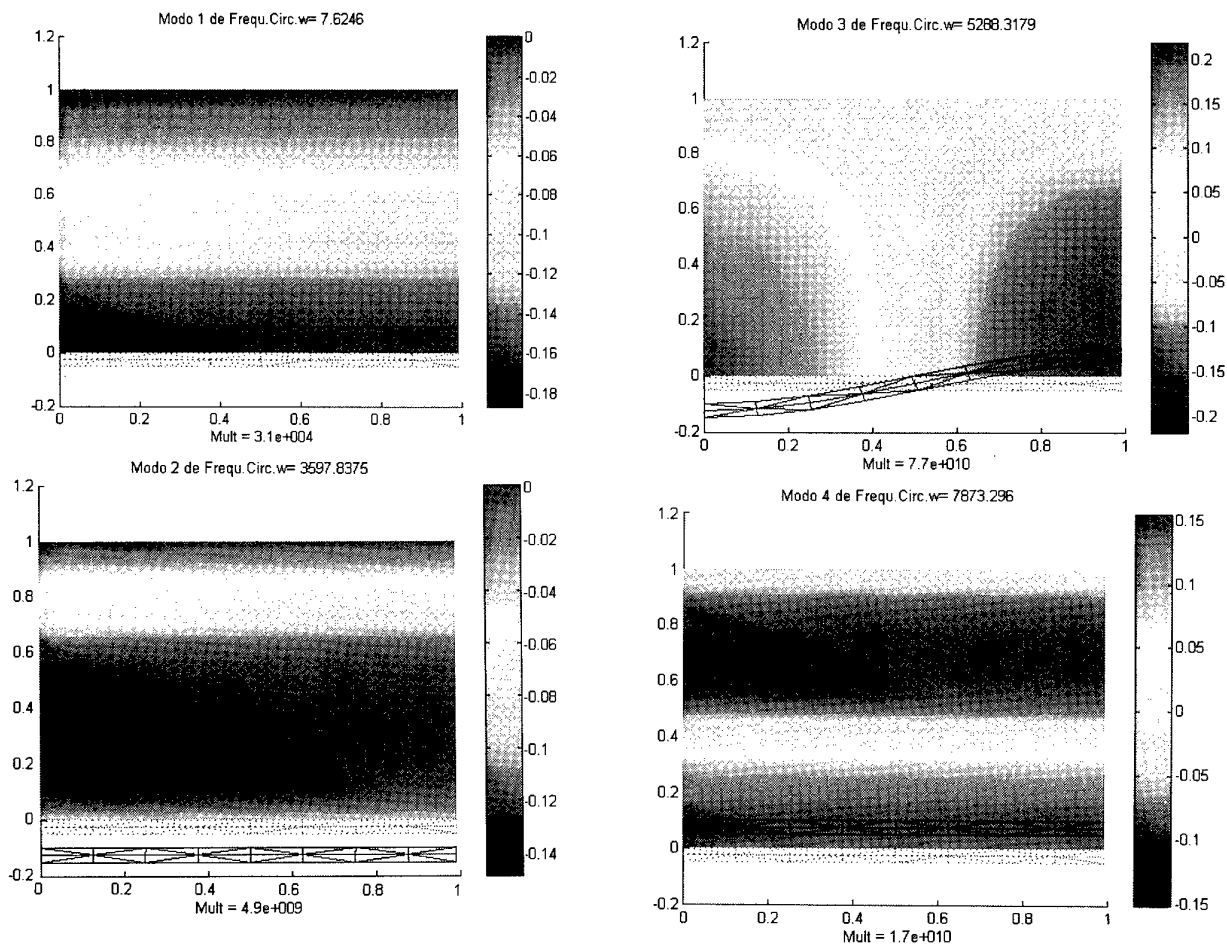Figure 1 - Scheme of Case 1A and Finite Element Mesh of Problem.

Figure 2a- Coupled Vibrations Modes of Case 1A :
(a) 1st and (2) 2nd modes

Figure 2b- Coupled Vibrations Modes of Case 1A :
(c) 3rd and (d) 4th modes

By analysing the modes and frequencies in the system, we can realise that the first coupled frequency derives from the additional mass effect, this frequency being given approximately by $\omega^2 = K/(m_s + m_f)$. This is an indication that for low frequencies the compressibility effect can be neglected. It is also possible to notice that there is an uncoupling of the transversal modes, which is due to the unidirectional translation displacements of the piston as a stiff body.

Case 1B - Square Cavity with a Double Piston

The cavity mentioned above is employed again, with two plates in opposite ends. The coupled solution [10] (phase and phase opposition) are, respectively,

$$\lambda^2 \left[\mu - \frac{1}{\lambda} \left(\frac{1}{\tan \lambda} - \frac{1}{\text{sen} \lambda} \right) \right] = \alpha,$$

$$\lambda^2 \left[\mu - \frac{1}{\lambda} \left(\frac{1}{\tan \lambda} + \frac{1}{\text{sen} \lambda} \right) \right] = \alpha \qquad (8)$$

The coupled analytical solution is applied to the longitudinal modes, while the transversal modes are identical to the uncoupled solution (look like the Eq.(7a). These results are displayed in Table 2.

Coupled Modes				
	ω - rad/s			
	Mode	Numerical	Ref.[3]	Theoric.
Fluido - Plate	1	9.48	10,06	9,48
	2	2821.61	2821,72	2816,31
	3	4735.56	4737,14	4712,39
	4	6409.07	6409,20	6346,84
	5	6771.16	6776,79	6664,32

Table 2 - Frequencies Results of Case 1B.

The remarks above about the coupling effect can also be fully applied in this case. A coupling can only be found in those cases where the transversal mode component corresponds to zero. The existence of two mobile plates enables the fluid column to have a certain mobility, thus generating a mode (phase) of additional mass, whose frequency is $\omega_1^2 = 2\pi K/(2m_s + m_f/2)$.

4.CONCLUSIONS
The solution of the problem as a whole is extremely simplified due to the use of symmetrical matrixes. A classical algorithm (QZ method) has been employed to solve eigenvalue problems. One of the problems was a difficulty in reaching an accordance with analytical solution due to numerical errors caused by the ill-conditioning of matrixes.

The results obtained have been excellent as compared to analytical calculations. The minor discrepancies were partly due to discretization and ill-conditioning of eigenvalue problem.

The results obtained through the comparison between the coupling and uncoupling cases show how important the influence of the solid-fluid interaction was on the main frequencies in the system and modal shapes.

6. REFERENCES
1. Morand, H. and Ohayon, R. "Substructure variational analysis of the vibrations of coupled fluid-structure systems - FE results," *Int.J.num.Meth.Engng.*, Vol.14, 1979, pp.741-755.
2. Olson, L.G. and Bathe, R.J. "Analysis of fluid-structure interactions. A direct symmetric coupled formulation based on the fluid velocity potencial," *Computers & Structures*, Vol.21, 1985, pp.21-32.
3. Barbosa, A.N., "Uma formulação potencial simétrica para o cálculo estático e dinâmico de problemas de interação fluido-estrutura," *Thesis of Msc, UnB-FT/EnC, E.D.M. 008A/98*, Brasil, 1998.
4. Barbosa, A.N. and Pedroso, L.J., "A study for fluid-structure interaction based on the displacements and fluid potential respectively in solid and fluid domain," *4° WCCM*, CD-ROM, Argentina, 1997.
5. Zienkiewicz, O.C. and Newton, R.E. - "Coupled vibrations of a structure submerged in a compressible fluid," *Symp.Finite Element Techn.*, 1969, Stuttgart.
6. Zienkwiecz, O.C. and Bettess, P. "Fluid-structure dynamic interaction and wave forces, an introduction to numerical treatment," *Int.J.num.Meth.Engng.*, Vol.13, 1978, pp.1-16.
7. Bleytschko, T.B. and Kennedy, J.M. "A fluid-structure finite element method for the analysis of reactor safety problems," *Nucl.Eng.Des.*, Vol 38, 1976, pp.71-81.
8. Wilson, E.L. and Khalvati, M. "Finite elements for dynamic analysis of fluid-solid systems," *Int.J.numMeth.Engng.*, Vol.19, 1983, pp.1657-1668.
9. Hamdi, M.A and Ousset, Y. "A displacement method for the analysis of vibrations of coupled fluid-structure systems," *Int.J.num.Meth.Eng.* Vol.13, 1978, pp.139-150.
10. Gibert, R.J., *Vibration des Structures - Interactions avec les Fluides - Sources d'Excitation Aléatoires*, Edition Eyrolles, Paris, 1988.
11. Morais, M.V.G. de – Modelizações numérica pelo MEF em problemas de interação fluido-estrutura. *Thesis of Msc - UnB-FT/EnC*, E.DM 008A/00, junho (2000).
12. Morais, M.V.G.de e Pedroso, L.J. – A numerical approach for study on acoustic behaviour of cavities and ducts, CFD2K -*8th Canadian Annual Conf of the CFD*; june/2000,Montréal-Ca

2E6   ANALYTICAL STUDY OF NOISE EFFECT ON BIFURCATION CHARACTERISTICS OF TRANSONIC FLUTTER OBSERVED IN WIND TUNNEL TESTS

Hiroshi Matsushita[*], Lasse Engbo Christiansen[**], Tue Lehn-Schiøler[**], and Péter Gránásy[***]

[*] National Aerospace Laboratory, 16-13-1 Ohsawa, Mitaka-shi, Tokyo 181-0015, Japan
[**] Technical University of Denmark, Building 309, 2800 Kgs. Lyngby, Denmark
[***] GE Hungary Ltd., 1340 Budapest, Vací ut 77, Hungary

Key Words: Aeroelasticity, Wings and Airfoil Sections, Unsteady Flows

ABSTRACT

Several nonlinear characteristics in transonic flutter of a high aspect ratio wing have been observed through a series of wind tunnel tests carried out at the transonic wind tunnel of National Aerospace Laboratory. The nonlinear dynamic analysis of the test data shows that almost all flutter behave as large amplitude limit cycle oscillation (LCO) as a subcritical Hopf bifurcation. We had a few cases in which flutter of a small amplitude LCO seemed to happen and was stabilized in such a manner as a supercritical Hopf bifurcation. We found out the possibility that a noise may produce a similar response as a supercritical Hopf bifurcation even with a nonlinear system that has only a subcritical-type Hopf bifurcation. This paper discusses, by numerical analysis of a normal model, these noise effects on bifurcation phenomena in transonic flutter.

1. INTRODUCTION

In transonic regions, air flow often separates due to shock waves moving on the wing surface, and in most cases flutter takes the form of limit cycle oscillation (LCO)[1-3]. The first author and his group have carried out a series of flutter tests in the transonic wind tunnel for a high aspect ratio wing aiming at getting better understanding of the transonic LCO flutter. In collaboration with the fourth author, various kinds of bifurcation have been found for a wide range of dynamic pressures such as a subcritical Hopf bifurcation involving an unstable limit cycle[4-6]. The present authors have proposed a two-degrees-of-freedom, finite dimensional nonlinear model having fourth order nonlinear terms, which can explain the fundamental nonlinear phenomena observed in the wind tunnel tests[7].

In the wind tunnel tests, most of the flutter that occurred was associated with a subcritical-type Hopf bifurcation, but we have found indications of a supercritical-type Hopf bifurcation in a certain case. The Danish group led by Prof. Mosekilde has pointed out the possibility that noise could produce a similar phenomenon as a supercritical Hopf bifurcation even in the nonlinear dynamic system having only a subcritical-type Hopf bifurcation[8,9]. In the following chapters, several nonlinear phenomena found in the wind tunnel test are first reviewed and noise effect problems are discussed.

---

* Director for Special Research
** Graduate student, Department of Physics
***Technical manager

2. EXPERIMENTAL OBSERVATION OF BIFURCATON IN TRANSONIC FLUTTER

Figure 1 shows a wind tunnel model of a high aspect ratio wing. It has a leading edge and a trailing edge control surfaces. They are used for active flutter control research[10]. Basically the wing has a supercritical section except at an inflated middle part where the wing section is symmetrical and two sets of electric motors are installed. For LCO investigation in the wind tunnel tests, a leading edge control surface is used as a source of excitation and wing response is recorded by four accelerometers and seven pairs of strain gages fixed at a wing spar. Each pair of strain gages measures the bending and torsion components of the strain.
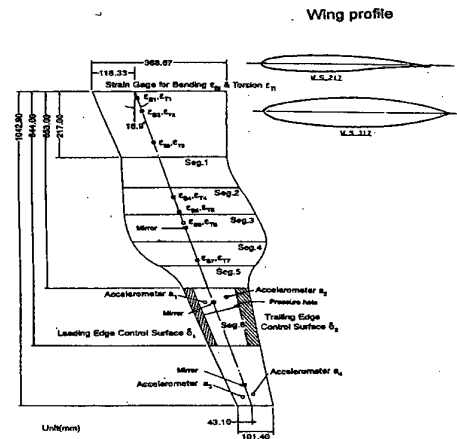

Fig. 1 High aspect ratio wing model

In the wind tunnel tests at the transonic wind tunnel of the National Aerospace Laboratory, it turned out that this wing behaves a typical transonic flutter. The wing has transonic dip phenomena and every flutter has the form of LCO. In each flutter, when the tunnel pressure is increased, the wing jumps up to LCO as shown at the top chart in Fig. 2. Successive investigation cleared that, even at lower dynamic pressure than the specific pressure, the wing can be brought into LCO state if it's excited above certain energy level. The LCO thus attained eventually is stabilized if the tunnel pressure is further decreased as shown in Fig. 3, where, after removing a leading edge control surface excitation and attaining LCO (middle chart), decreasing the tunnel pressure (bottom chart) stabilizes the wing (top chart).

The results of nonlinear dynamics analysis of these tests are summarized in Fig. 4, which shows the LCO amplitude against dynamic pressure. The stability
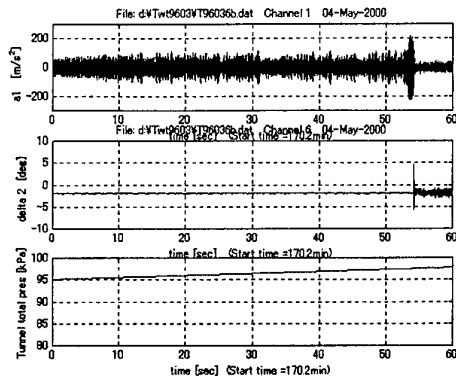
Fig. 2 Time history going to nominal flutter
during increasing wind tunnel pressure
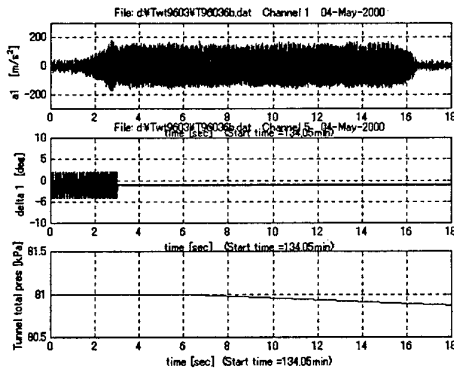
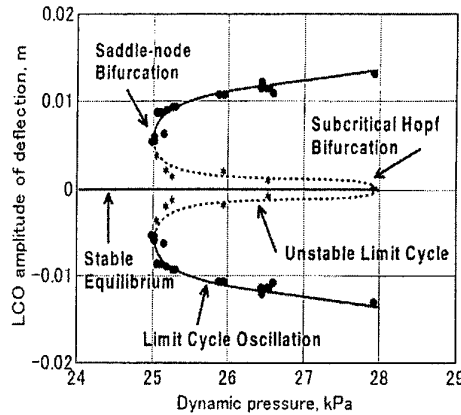Fig. 3 Quasi-steady decrease of the dynamic
pressure at the saddle node bifurcation

Fig. 4 Bifurcation diagram obtained
by the wind tunnel tests
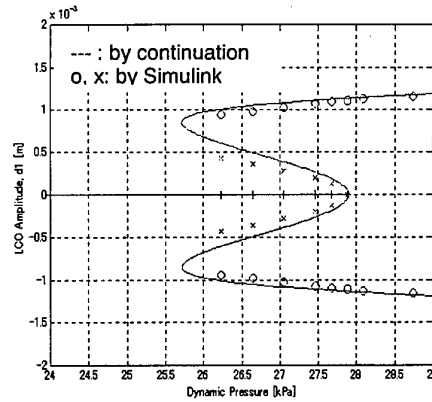
Fig. 5 Bifurcation diagram of 2-DOF
nonlinear equation (1)

boundary, or unstable limit cycle, defined by the crosses has some uncertainty, and the stable region under the boundary is rather narrow. Every possible source of disturbance may decrease the stability region; such as turbulence in the wind tunnel flow, flow separation occurring at the wing, etc.

3. NONLINEAR MATHEMATICAL MODEL

The first author *et al.* have developed a nonlinear math model in the form of a two-degrees-of-freedom, finite state nonlinear differential equation[7]. Introducing the fourth order nonlinearity in q_i, $i = 1,2$ to the generalized damping term, they have obtained the following sixth order nonlinear differential equation.

$$\dot{x} = \tilde{A}x; \quad x = [q, \dot{q}, z]^T \in R^6 \qquad (1)$$

where the system matrix is,

$$\tilde{A} = \{a_{ij}\} = \begin{bmatrix} 0 & I & 0 \\ -(M-A_0)^{-1}(K-A_2) & -(M-A_0)^{-1}(C-\tilde{A}_1) & -(M-A_0)^{-1} \\ B_a & 0 & -\Lambda \end{bmatrix} \in R^{6\times6} \qquad (2)$$

Here, the diagonal components of the aerodynamic part in block (2, 2) in Eq. (2), a_{33a} and a_{44a} are modified to be

nonlinear terms which have the form $(1 + \beta_1 q_1^2 + \gamma_1 q_1^4)a_{33}$ and $(1 + \beta_2 q_2^2 + \gamma_2 q_2^4)a_{44a}$, respectively.

In order to make comparison with the test results, an output equation that relates the state variables in Eq. (1) with the output variables measured in the wind tunnel tests is necessary. Since two sets of measured and derived variables, acceleration a_1, a_2, velocity v_1, v_2 and deflection d_1, d_2 at two positions on the wing are enough for comparison, the output equation takes the form

$$y = Cx; y = [a_1, a_2, v_1, v_2, d_1, d_2]^T \in R^6 \qquad (3)$$

The set of equations (1) and (3) comprises the nonlinear 2DOF math model for transonic flutter.

Figure 5 displays the simulation results in term of the deflection at the accelerometer #1. The coefficients in the math model are set as $\beta_1 = \beta_2 = 0.5$, $\gamma_1 = \gamma_2 = -0.2$. The solid line in the figure was obtained by Continuation Method[8], while the symbols were obtained by Simulink. Two results are coincident except with a small difference at the unstable limit cycle branch. Fig. 5 has a good correspondence with the test results in Fig. 4.

4. NOISE EFFECT ON BIFURCATION

In a few cases, we observed a different type of flutter. It occurred during an active flutter suppression experiment. At slightly higher speed than nominal flutter with the control loop engaged, when the system was disengaged flutter of small amplitude LCO occurred. While decreasing the wind tunnel dynamic pressure, the amplitude was decreasing in such a manner as shown in Fig. 6. At first the amplitude was decreasing linearly, but at certain point, about 250 sec point in the figure, the amplitude stopped to decrease but kept constant against decreasing the dynamic pressure. This phenomenon seemed to be explained as a supercritical Hopf bifurcation. During the last test, various attempts to reproduce this small amplitude LCO was made, however, none of them were successful. In order to investigate the noise effect, we have added white noise to both a normal form of a Hopf-bifurcation and the 2DOF model. The way we applied noise to the system is described in Ref. 8.
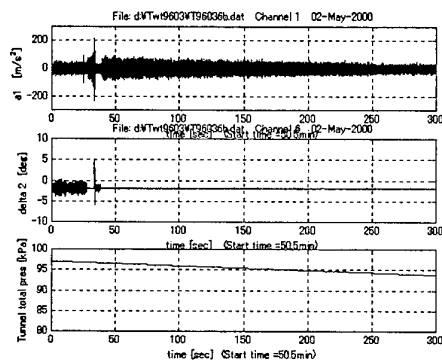
Fig. 6 Supercritical-type Hopf bifurcation as the dynamic pressure decreasing

The normal form has basically the same structure as the 2DOF model of Eq. (2) in that it has fourth order coefficients at the damping terms as follows,

$$\dot{x} = \lambda x - \omega y + \alpha x\left(x^2 + y^2\right) + \beta x\left(x^4 + y^4\right)$$
$$\dot{y} = \omega x - \lambda y + \alpha y\left(x^2 + y^2\right) + \beta y\left(x^4 + y^4\right)$$
(4)

The Hopf bifurcation is subcritical when α is chosen to be negative as shown in Fig. 8.
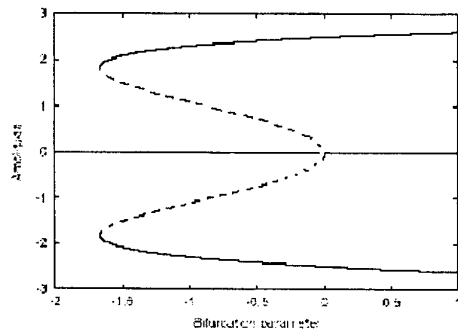

Fig. 7 Bifurcation diagram for the normal form of a Hopf bifurcation, Eq. (4)

In the region between the Hopf bifurcation point and the saddle-node bifurcation (Fig. 7), applying noise to the system revealed different things depending on the amplitude of the noise. Starting at the stable focus (equilibrium) and applying a small amplitude noise, the solution stayed, as expected, near the focus (Fig. 8 (a)). Increasing the noise level led to a jump to LCO, i.e., the noise excites the wing above the unstable limit cycle, and the solution is 'caught' on the stable limit cycle. In-
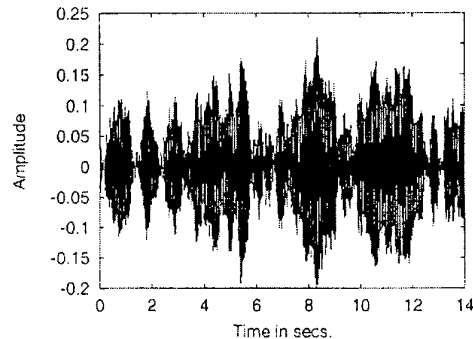
(a) Low noise makes the solution staying near the stable focus
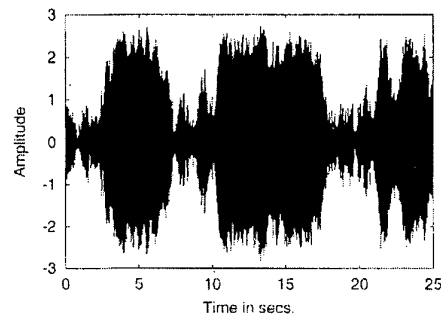
(b) High level of noise pushes the solution back and forth between LCO and the focus

Fig. 8 Different noise effect depending on the noise level

creasing the noise level even further, the system jumps back and forth between focus and the stable limit cycle, the noise level is enough to 'push' the system from the oscillation past the unstable limit cycle. An example can be seen in Fig. 8 (b), this has never been seen in the experiments and indicates that the noise in the real system is not this high.

Applying a low level noise to the normal form below the Hopf bifurcation produces something that looks like a small amplitude limit cycle as the amplitude of the noise is increased as shown in Fig. 9. When the bifurcation parameter is decreased the amplitude of the noise also decreases until it reaches a stable level. The shape of this is approximately the same as the one found experimentally (Fig. 6). Therefore, we now believe that the wing does not undergo a supercritical bifurcation.

We executed the same analysis to 2DOF model of Eq. (1), and a reproduction of a flutter case can be seen in Fig. 10. The noise level is set so that it corresponds with the amplitude of the large oscillation in the same way as in the experiments. In the simulation, the ve-
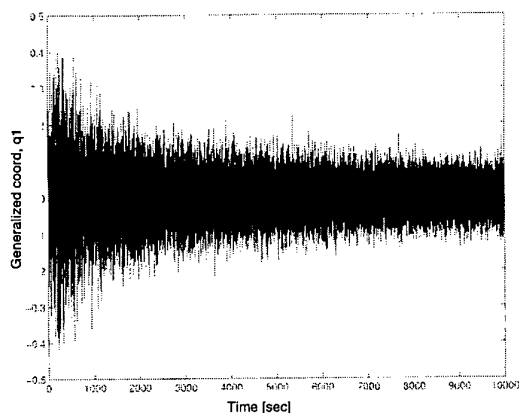
Fig. 9 Numerical simulation of the phantom supercritical bifurcation

locity is slowly increased while noise is applied to the system. The coordinates on the y-axis are, in the numerical case, the first generalized coordinate q_1, and in the experimental case, the acceleration of the wing. Considering the eigenvalues moving perpendicularly to the imaginary axis and crossing it, we believe that it should be possible to see "the phantom supercritical bifurcation" in this model. However, we have not been able to find it, possibly because the change in amplitude is not as large as in the normal form.

The noise applied in our investigations has been white noise, however. This might not be in accordance with the experiments especially because the shockwave oscillates on the surface of the wing. Further analysis is needed to determine how the noise composition should be.
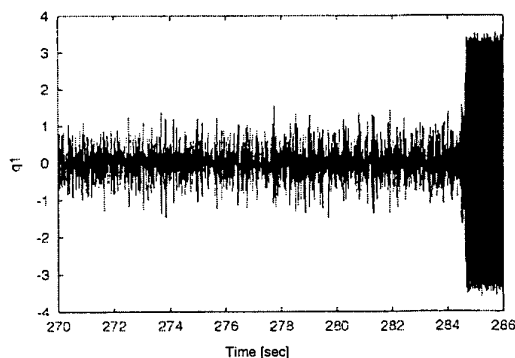

Fig. 10 Numerical simulation of subcritical Hopf bifurcation

5. CONCLUSIONS

Flutter of a high aspect ratio wing in transonic region observed in a series of wind tunnel tests behaves mostly as a large amplitude LCO that happens as a subcritical Hopf bifurcation. In few cases flutter of a small amplitude LCO seemed happen and was stabilized gradually as a supercritical Hopf bifurcation, but it can be explained as a noise effect on a system of a subcritical bifurcation as follows.

Noise existing in the system greatly affects the nature of bifurcation diagram; adding noise produces a temporal behavior similar to what a supercritical bifurcation would produce. Though noise will make it difficult to make a clear distinction between a subcritical and a supercritical Hopf bifurcation, the system may have only a subcritical bifurcation.

REFERENCES

1. Cunningham, A. M., Jr., "Practical Problem: Airplanes," Chapter 3, *Unsteady Transonic Aerodynamics*, Nixon, D., ed., Progress in Astronautics and Aeronautics, 120, AIAA, pp. 75-132, 1989.
2. Dowell, E. H., "Nonlinear Aeroelasticity," *Flight-Vehicle Materials, Structures and Dynamics*, 5, Part II, Chapter 4, ASME, pp. 213 – 239, 1993.
3. Schewe, G. and Deyhle, H., "Experiments on Transonic Flutter of a Two-Dimensional Supercritical Wing with Emphasis on the Non-Linear Effects," Proceedings of the Royal Aeronautical Society Conference on "UNSTEADY AERODYNAMICS", 1996.
4. Gránásy, P., Matsushita, H., and Saitoh, K., "Nonlinear Analysis of Transonic Flutter," Proceedings of the 10th International Sessions in Aircraft Symposium, JSASS, PP. 66-69, 1996.
5. Gránásy, P., Matsushita, H., and Saitoh, K., "Nonlinear Aeroelastic Phenomena at Transonic Region," Proceedings of CEAS International Forum on Aeroelasticity and Structural Dynamics 1997, Vol. III, Rome, pp. 379-385, 1997.
6. Matsushita, H., Saitoh, K., and Gránásy, P., "Nonlinear Characteristics of Transonic Flutter of a High Aspect Ratio Wing," Proceedings of 21st ICAS, Melbourne, pp. 1-7, 1998.
7. Matsushita, H., Saitoh, K., and Gránásy, "Two Degrees-of-Freedom Nonlinear Math Model with Fourth Order Nonlinear Aerodynamics for Transonic Limit Cycle Flutter," Proceedings of the International Forum on Aeroelasticity and Structural Dynamics 1999, June 1999.
8. Lasse Engbo Christiansen and Tue Lehn-Schiøler, "Stochastic Modeling of Transonic Flutter," Department of Physics, The Technical University of Denmark, Denmark, 2000.
9. Matsushita, H., Gránásy, p., Christiansen, L. E., Lehn-Schiøler, T., and Mosekilde, E., "Investigation of Nonlinear Phenomena in Transonic Flutter - wind Tunnel Tests and Nonlinear Dynamics Analysis," Proceedings of 3rd International Conference on Non-Linear Problems in Aviation and Aerospace, 2000, to appear.
11. Saitoh, K. Baldelli, D. H. Matsushita, H., and Hashidate, M., "Robust Controller Design and Its Experimental Validation for Active Transonic Flutter Suppression," Proceedings of CEAS International Forum on Aeroelasticity and Structural Dynamics 1997, Vol. II, Rome, pp. 393-399, 1997.

2E7   TWO-DIMENSIONAL ACTIVE FLUTTER SUPPRESSION IN THE TRANSONIC REGIME

Takanori DEGAKI* and Shinji SUZUKI**

University of Tokyo, 7-3-1 Hongo, Bunkyo-ku, Tokyo 113-8656, Japan
University of Tokyo, 7-3-1 Hongo, Bunkyo-ku, Tokyo 113-8656, Japan

ABSTRACT

This paper describes two-dimensional active flutter suppression to cope with the transonic dip. The airfoil has plunge and pitch degrees of freedom. The control surfaces are leading and trailing edges. The aerodynamic forces acting on the airfoil are calculated by solving Euler's equations using computational fluid dynamics. The control laws are sliding mode control, linear quadratic regulator and linear quadratic gaussian with loop transfer recovery. The simplified transonic aerodynamic models for designing the controllers are identified from random inputs and computed outputs. At a specific altitude, flutter arises between Mach number of 0.7 and 0.88 corresponding to the transonic dip. Each controller makes the airfoil to be stable all through the Mach number of flutter occurrence. The sliding mode controller gives higher flutter speed than the other controllers. These characteristics indicate that sliding mode control is useful for active flutter suppression in the transonic flight.

1. INTRODUCTION

An aircraft cruising at supersonic speed has aeroelastically the severest point in the transonic regime, in which the transonic dip appears and the flutter speed remarkably drops. Beyond the Mach number of the transonic dip, flutter does not arise. Although the supersonic aircraft passes through the transonic regime instantly, its structural design must be targeted for the transonic regime. An alternative idea against the transonic flutter is an active control that is effective only in the while of passing through the transonic dip.

When we consider the active flutter suppression at the transonic speed, two questions must be considered: derive a transonic aerodynamic model for controller design; validate the control performance. For the first question, adaptive control and robust control are suggested. For the second question, experiments and computational fluid dynamics (CFD) are studied. The active flutter suppression at a Mach number in the transonic regime was carried out using H∞ controller[1, 2] or optimal regulator with Kalman estimator.[3] A digital adaptive controller was introduced for active flutter suppression undergoing time varying flight conditions.[4] It was indicated that the parameter estimator possibly failed to follow the aeroelastic system change depending on the flight paths. Another adaptive control application for the transonic flutter suppression was carried out, in which CFD-based aerodynamic loads were used.[5] The adaptive controller was a good candidate for suppression of the transonic flutter associated with strong shocks.

We suggest sliding mode control (SMC)[6] as a potential solution for the active transonic flutter suppression through the dip. SMC has a feature that if the model errors are satisfied matching condition, the dynamics of the system on sliding surface is the same as that of the model. Since the aeroelastic system with leading and trailing edge control surfaces satisfies the matching condition, SMC can be expected to suppress the transonic flutter despite aerodynamic model errors or aerodynamic characteristics change depending on Mach numbers. This indicates that SMC that is designed for a certain Mach number can be used through the Mach numbers in the transonic dip.

In this study, we calculate the flutter speed of the airfoil NACA 64A006 in Mach number of 0.6 to 0.9. Considering a flight path at a constant altitude, we determine the Mach numbers, at which flutter occurs. Although the airfoil oscillates divergently between those Mach numbers, SMC effectively suppress the flutter. We next confirm that SMC increase the flutter speed at all Mach numbers investigated. Compared to linear quadratic regulator (LQR) or linear quadratic gaussian with loop transfer recovery (LQG/LTR), in which identified unsteady aerodynamic model is incorporated, SMC remarkably increases the flutter speed.

2. EQUATIONS OF MOTION

The two-dimensional wing section used in this study is shown in Fig. 1. This airfoil is supported by two springs, i.e., bending spring and torsional spring. Those two springs mean the bending and torsional stiffness of a real three-dimensional wing. The plunge displacement h is positive downward and the pitch angle $\acute{a}$ is positive head up. The control surfaces for flutter suppression are the leading and trailing edges. Both are positive downward.

The governing equations of the airfoil is

$$\begin{bmatrix} 1 & x_\alpha \\ x_\alpha & r_\alpha^2 \end{bmatrix}\begin{Bmatrix} \xi'' \\ \alpha'' \end{Bmatrix} + \frac{1}{\overline{U}^2}\begin{bmatrix} (\omega_h/\omega_\alpha)^2 & 0 \\ 0 & r_\alpha^2 \end{bmatrix}\begin{Bmatrix} \xi \\ \alpha \end{Bmatrix} = \frac{1}{\pi\mu}\begin{bmatrix} -1 & 0 \\ 0 & 2 \end{bmatrix}\begin{Bmatrix} C_l \\ C_m \end{Bmatrix} \quad (1)$$

where the prime indicates the derivative with respect to nondimensional time $\acute{o}$. The lift and moment coefficients are calculated by solving Euler's equation using CFD. Deriving Eq. (1), we assume that a) the dynamics of leading and trailing edges are neglected, i.e., the flaps perfectly track the reference inputs, b) reaction torque due to moving edges has no influence on the wing itself and c) the static moment and the moment of inertia of the wing section do not change before and after the edge deflection.

* Graduate Student, Department of aeronautics and Astronautics
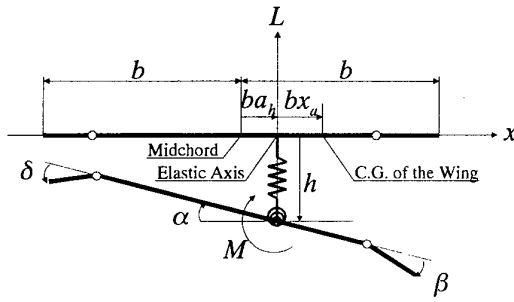** Professor, Department of aeronautics and Astronautics

Fig. 1 Two-dimensional wing section with leading and trailing edges. It is restrained from bending and torsional motion by two springs acting a distance ba aft of midchord. Lift and pitching moment about the elastic axis are

3. CONTROLLER DESIGN

Since the controller needs to work effectively through the transonic dip, it has to be robust against the aerodynamic change with the Mach numbers. In this study, we try and compare three control laws, SMC, LQR and LQG/LTR. Before designing a controller based on the Eq. (1), we must consider an aerodynamic model that define the relation between aerodynamic forces, C_l and C_m, and attitude of the airfoil, $\hat{i}$ and $\acute{a}$. Targeting the transonic regime, however, we are hopeless to find the aerodynamic model physically. An alternative approach is identification.

Now that SMC and LQR need full states feedback, the aerodynamic model has to be represented using algebraic linear combination of states like quasi-steady aerodynamic model:

$$C_l = C_{l\alpha}\left(\alpha + \xi'\right) + C_{l\beta}\beta + C_{l\delta}\delta$$
$$C_m = C_{m\alpha}\left(\alpha + \xi'\right) + C_{m\beta}\beta + C_{m\delta}\delta \tag{2}$$

where aerodynamic derivatives are constant and not dependent on the frequency.

On the contrary, LQG/LTR is used for the system with output feedback. Therefore the aerodynamic model is not limited to quasi-steady but can be dealt with unsteady. The unsteady aerodynamics, if it is linear, is represented using matrix transfer function:

$$\begin{Bmatrix} C_l \\ C_m \end{Bmatrix} = \begin{bmatrix} C_{l\xi}(s) & C_{l\alpha}(s) & C_{l\beta}(s) & C_{l\delta}(s) \\ C_{m\xi}(s) & C_{m\alpha}(s) & C_{m\beta}(s) & C_{m\delta}(s) \end{bmatrix} \begin{Bmatrix} \xi \\ \alpha \\ \beta \\ \delta \end{Bmatrix} \tag{3}$$

where aerodynamic derivatives are functions of Laplace variable s. Unlike the quasi-steady aerodynamics of Eqs. (2), Eqs. (3) are linear differential equations and the aerodynamic forces are dynamically related to the attitude of the airfoil.

Whichever we choose among Eqs. (2)-(3), the aerodynamic derivatives must be identified. In Eqs. (2), the derivatives are easy to be obtained using steady calculation of CFD. In Eqs. (3), they are more difficult because we explicitly identify the transfer functions as functions of s. In this study, we apply prediction error method to an output error model[7] of each aerodynamic force. The procedure, which is to find $C_{l\acute{a}}$, is as follows: (1) move the pitch angle $\acute{a}$ randomly; (2) calculate the fluctuation of the lift coefficient C_l; (3) from the time

histories of $\acute{a}$ and C_l, obtain the lift slope $C_{l\acute{a}}$, which is a discrete transfer function, as to minimize the one step prediction error of C_l; 4) transform the discrete transfer function to continuous transfer function. The other aerodynamic derivatives in Eq. (3) are also obtained with the same procedure.

If once the aerodynamic model is identified, we can prepare the aeroelastic model and design a controller. The controller is expected to suppress the flutter through the transonic dip. This indicates that the controller must work effectively even though the aerodynamic characteristics depending on the Mach number is far from that used for the controller design.

SMC can deal with such a problem. It is a kind of variable structure controls and has a remarkable feature that the dynamics on the sliding surface is unchanged regardless of the model errors as far as the matching condition is satisfied. The aeroelastic problem of this study can be directly applied to SMC formulation. The aeroelastic problem of Eqs. (1) incorpolated with Eqs. (2) is transformed into state space form as

$$x' = Ax + Bu \tag{4}$$

where $x = \begin{bmatrix} \xi & \alpha & \xi' & \alpha' \end{bmatrix}^T$ and $u = \begin{bmatrix} \beta & \delta \end{bmatrix}^T$. The criterion for determining a sliding surface is minimizing

$$J = \int_{t_s}^{\infty}\left(xQx^T\right)dt \tag{5}$$

on the sliding surface. From Eq. (5), the equations of the sliding surfaces are determined as

$$Sx = 0. \tag{6}$$

The control inputs are

$$u = -SAx - kSx/\|Sx\| \tag{7}$$

where k must be determined considering the difference of actual dynamics and nominal model.

Another candidate for the active transonic flutter problem is LQR. Although it is not robust controller or cannot explicitly incorporate model errors into the controller design, it can be applied to the system with much model errors because it has enormous stability margin due to the circle condition. For the state space equation of (4), the objective function

$$J = \int_{0}^{\infty}\left(xQx^T + uRu^T\right)dt \tag{8}$$
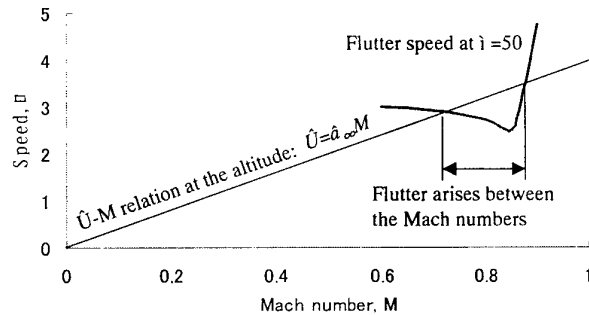

Fig. 2 Flutter speed at $\hat{i}$=50 around the transonic regime. Above the curve of flutter speed, flutter arises. When we assume a flight altitude and decide the speed of sound, we can draw the line of $\hat{U}$-M relation. If the line intersects the curve of the flutter speed, then flutter arises between the Mach numbers at which $\hat{U}$-M line exceeds the flutter speed curve.

is to be minimized. The control inputs are obtained as

$$u = -Kx \quad (9)$$

where K is control gain.

Both SMC and LQR need full state feedback. That restricts the applicable aerodynamic model to quasi-steady aerodynamics. Unlike this, LQG/LTR can be applied to the system of output feedback. For the state space equations

$$x' = Ax + Bu + Gw$$
$$y = Cx + v \quad (10)$$

the control inputs are

$$u = -F\hat{x}$$
$$\hat{x}' = A\hat{x} + Bu + K(y - C\hat{x}) \quad (11)$$

The loop transfer function of Eqs. (10)·(11)

$$F(sI - A + BF + KC)^{-1} KC(sI - A)^{-1} B \quad (12)$$

does not correspond to that of full state feedback

$$F(sI - A)^{-1} B. \quad (13)$$

This is the reason that the robustness of LQG deteriorates. LQG/LTR improves that shortcoming. If we assume that the disturbance is added to the inputs, $G=B$, and its intensity approaches infinity, the loop transfer function of Eq. (12) approaches Eq. (13). This indicates that the controller with Kalman filter has the same robustness as that with full state observation.

4. SIMULATION

The airfoil using in this study is NACA 64A006. The properties are $a_h=-0.2$, $r_a=0.5$, $x_a=0.2$ and $\dot{u}_h/\dot{u}_a=0.3$. The hinge axes of the leading and trailing edges are located at 20% and 75% of the chord, respectively. Before starting the simulation of flutter control, we carefully compare our CFD results with other studies[8 9] and validate our computational code. We choose the design point of the controller as $M=0.85$, $i=50$ and $\hat{U}=3.4$. Using CFD, the aerodynamic coefficients of the steady flow at $M=0.85$ are obtained as $C_{l\dot{a}}=14.4$, $C_{l\dot{a}}=8.90$, $C_{l\dot{a}}=-0.0148$, $C_{m\dot{a}}=1.53$, $C_{m\dot{a}}=-0.355$ and $C_{m\dot{a}}=-0.279$.

The flutter speed around the transonic region is determined using U-g method[10] as shown in Fig. 2. In this region, the flutter speed varies remarkably and is accompanied with transonic dip. Assuming $\hat{U}=4M$ in Fig. 2, we can find that flutter arises between $M=0.7$ and 0.88. The corresponding speed is between $\hat{U}=2.8$ and 3.52. Some examples of the airfoil motions are shown in Fig. 3. The airfoil motion in the transonic dip is divergent after only a few cycles.

To suppress the transonic flutter shown in Fig. 3, SMC is firstly designed. The criterion of Eq. (5) is decided as time integral of total energy (kinetic energy and potential energy). When the SMC is applied to the flutter
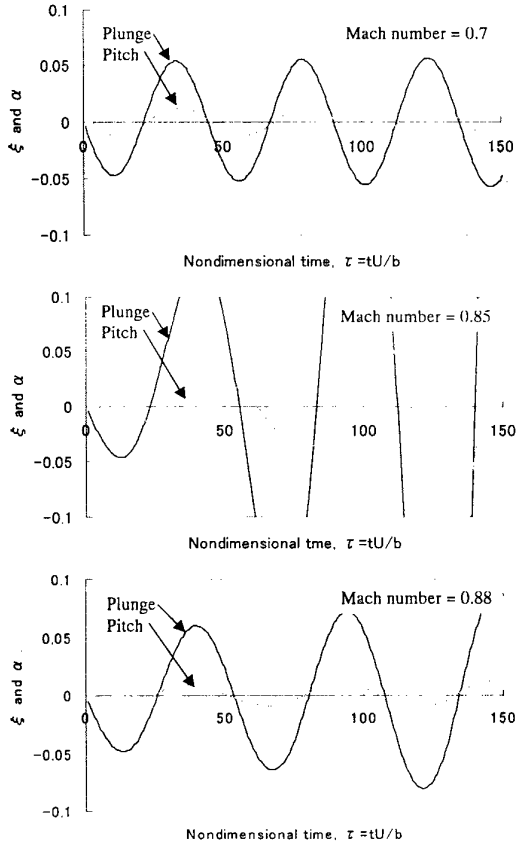

Fig. 3 Time histories of plunge displacement and pitch angle at three Mach numbers in the transonic dip: $M=0.7$ (beginning of the dip), 0.85 (the deepest point in the dip and also design point of the controller) and 0.88 (end of the dip). The initial condition is $i=-0.01/\hat{U}$.
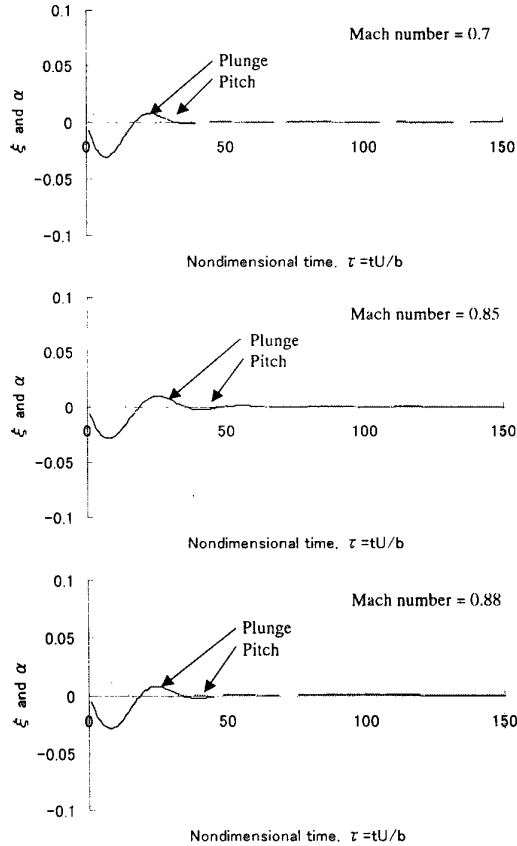
Fig. 4 Time histories of plunge displacement and pitch angle using SMC. The initial condition is $i=-0.01/\hat{U}$.

of Fig. 3, the airfoil motion becomes stable as shown in Fig. 4. Although the SMC is designed based on M=0.85 and $\hat{U}$=3.4, it works effectively for flutter of other Mach numbers in the transonic dip. The flutter speed of SMC used airfoil is also investigated. Applying the SMC, we can augment the flutter speed as $\hat{U}$=20 or more. That speed, which depends on Mach numbers, is the upper bound of SMC application. Beyond the speed, the SMC fails to suppress the flutter. There also exists the lower bound of SMC application as in Fig. 5. Below the speed of the lower bound, the SMC destabilizes the airfoil that is stable without control. The region of the speed in which the SMC can be applied is between the upper and lower bound in Fig. 5.

LQR and LQG/LTR can also suppress the transonic flutter, whose control performance is almost same as that of SMC. Tuning to show the same control performance, we investigate the flutter speed with LQR or LQG/LTR application as in Fig. 6-7, respectively. Their flutter speed, upper bound in Fig. 6-7, is certainly augmented using LQR or LQG/LTR, but their degrees of the augmentation are far little than using SMC. Since we identified the unsteady aerodynamic model and used it in LQG/LTR design, we expected that LQG/LTR must show better performance than LQR. In reality, the flutter speed of LQG/LTR is lower than that of LQR. This is because the robustness of LQG/LTR is deteriorated using an observer. The LTR method used in LQG/LTR design recovers only the loop transfer function broken at input point. Therefore the loop transfer function broken at the output point cannot be recovered.

5. CONCLUSIONS

We demonstrated using CFD the possibility of active control for the transonic flutter, in which the transonic dip appeared. Each controller, SMC, LQR and LQG/LTR, successfully suppressed the transonic flutter at any Mach numbers through the transonic dip. In those three controllers, SMC augmented the flutter speed most. Although unsteady aerodynamics was identified and incorporated, LQG/LTR showed lower flutter speed than SMC due to the robustness deterioration.

Fig. 5 Flutter speed with SMC application. Between the speed of upper and lower bound, SMC stabilize the oscillation. The flutter speed without control is also shown.
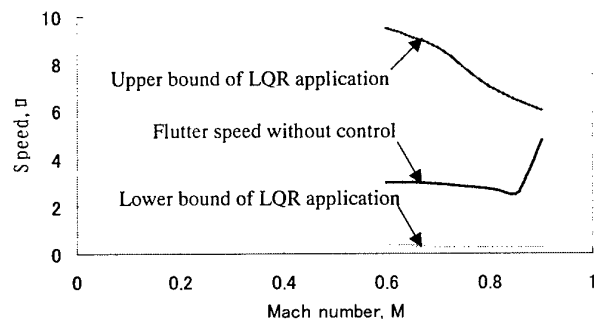

Fig. 6 Flutter speed with LQR application. Between the speed of upper and lower bound, LQR stabilize the ocsillation. The flutter speed without control is also shown.
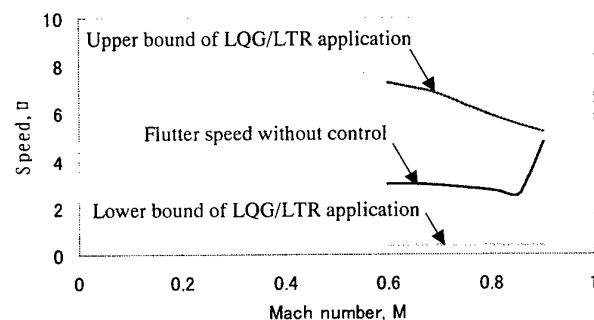

Fig. 7 Flutter speed with LQG/LTR application. Between the speed of upper and lower bound, LQG/LTR stabilize the oscillation. The flutter speed without control is also shown.

REFERENCES

1 Baldelli, D., Ohta, H., Matsushita, H., Hashidate, M. and Saitoh, K., "Flutter margin augmentation systhesis using normalized coprime factors approach," Journal of Guidance, Control, and Dynamics, 18-4, pp. 802-811, 1995.

2 Fujimori, A., Matsushita, A., Saitoh, K. and Ando, Y., "Model modification of a high-aspect-ratio aeroelastic wing and active flutter suppression," Proceedings The 37th Aircraft Symposium, 1C2, pp. 81-84, 1999 (in Japanese).

3 Matsushita, H., Saitoh, K. and Granasy, P., "Research on active control of aeroelastic systems at national aerospace laboratory in Japan," International Journal of Intelligent Mechatronics, 3-1, pp. 34-51, 1998.

4 Pak, C., Friedmann, P. and Livne, E., "Digital adaptive flutter suppression and simulation using approximate transonic aerodynamics," Journal of Vibration and Control, 1-4, pp. 363-388, 1995.

5 Friedmann, P,. Guillot, D. and Presente, E., "Adaptive control of aeroelastic instabilities in transonic flow and its scaling," Journal of Guidance, Control, and Dynamics, 20-6, pp. 1190-1199, 1997.

6 Nonami, K. and Tian, H., "Sliding mode control," Corona Publishing, 1996 (in Japanese).

7 Ljung, L. and Glad, T., "Modelling of Dynamic Systems," Prentice Hall, 1994.

8 Yang, T.Y., Guruswamy, P., Striz, A.G. and Olsen, J.J., "Flutter Analysis of a NACA 64A006 Airfoil in Small Disturbance Transonic Flow," Journal of Aircraft, 17-4, pp. 225-232, 1980.

9 Yang, T.Y. and Chen, C., "Transonic flutter and response analyses of two 3-degree-of-freedom airfoil," Journal of Aircraft, 19-10, pp. 875-884, 1982.

10 Washizu, K., "Aeroelasticity," Kyoritu Publishing, 1969 (in Japanese).

$2\mathrm{E}8$ Flutter Simulation of a Transonic Wing

Takaaki Sato, Shigeru Obayashi and Kazuhiro Nakahashi
Tohoku University
Department of Aeronautics and Space Engineering,
Sendai 980-8579-01, Japan
Email: sato@ad.mech.tohoku.ac.jp, :obayashi@ieee.org

Key Word: Unsteady Flows

Abstract

Flutter simulation of a transonic wing has been presented using a moving grid system. At first, a Navier-Stokes code has been validated by comparing computed solutions with experimental data for the oscillatory motion of rectangular wing. Then, flutter simulation of a high-aspect-ratio swept back wing has been presented. Aeroelastic responses are computed using the modal analysis based on the finite-element method. The computed flutter boundaries are obtained and compared with NAL (National Aerospace Laboratory) flutter tunnel test.

Introduction

To advance the safety of aircraft, the capability to predict unsteady loads such as maneuver loads and gust loads on the aircraft will be needed with greater accuracy. Because of the high cost and risk involved, however, it is not practical to conduct a large number of aeroelastic wind-tunnel tests. By complementing such expensive experiments with computational methods, the overall cost of the development of an aircraft can be considerably reduced.

To estimate unsteady loads, the rigid body assumption of the aircraft may not be good enough. The aircraft should be treated as a flexible body. Several studies have been reported by coupling CFD analysis with Computational Structural Dynamics. For example, Guruswamy developed a Naveir-Stokes code for aeroelaststic simulations [1][2]. Then to reduce the computational time, Byun and Guruswamy developed a parallel version of the code[3]. The flutter calculations based on a parallel, multiblock, multigrid flow solver by Liu, et al[4]. Kheirandish et al. also presented flutter simulation[5]. However, these codes are not in public domain, and the access to such codes is limited. Also, they concentrated on calculating the flutter boundary. There are not many reports estimating maneuver loads or gust loads.

Our final goal is to simulate various unsteady aeroelastic phenomena. In this paper, the computational aeroelastic method is developed and validated with experiment as a milestone.

To verify the present code at first, unsteady flows over rectangular wing undergoing prescribed oscillatory motions[6] are computed. The unsteady code solves the Navier-Stokes equations using the moving grid systems. Then, flutter simulation of a high-aspect-ratio swept back wing is presented. Structural responses are loosely coupled with CFD analysis. The modal data is generated by the finite-element method[5].

Numerical Algorithms

The thin-layer Navier-Stokes equations used in this study can be written in conservation-law form in a generalized body-conforming curvilinear coordinate system for three dimensions as follows:

$$\partial_\tau \hat{\mathbf{Q}} + \partial_\xi \hat{\mathbf{E}} + \partial_\eta \hat{\mathbf{F}} + \partial_\zeta \hat{\mathbf{G}} = \frac{1}{\mathbf{R}_e}\partial_\zeta \hat{\mathbf{G}}^V \tag{1}$$

where $\tau = t$, $\xi = \xi(t,x,y,z)$, $\eta = \eta(t,x,y,z)$, and $\zeta = \zeta(t,x,y,z)$. The turbulent viscosity is evaluated by the Baldwin-Lomax algebraic eddy-viscosity model.

The governing structural equations of motion of a flexible wing are using the Rayleigh-Ritz method[6]. In this method, the resulting aeroelastic displacements at any time are expressed as a function of a finite set of assumed modes.

It is assumed that the deformed shape of the wing can be represented by a set of discrete displacement vector $\{\mathbf{d}\}$ can be expressed as

$$\{\mathbf{d}\} = [\varphi]\{\mathbf{q}\} \tag{2}$$

where $[\varphi]$ is the modal matrix and $\{\mathbf{q}\}$ is the generalized displacements vector. The matrix form of the structural equations of motion is

$$[\mathbf{M}]\{\ddot{\mathbf{d}}\} + [\mathbf{C}]\{\dot{\mathbf{d}}\} + [\mathbf{K}]\{\mathbf{d}\} = \{\mathbf{F}\} \tag{3}$$

where $[\mathbf{M}]$, $[\mathbf{C}]$, and $[\mathbf{K}]$ are modal mass, damping, and stiffness matrices, respectively. Each matrices and modal data are generated from a finite-element analysis. $\{\mathbf{F}\}$ is aerodynamic force vector and it is obtained from integrating aerodynamic forces acting on the wing surface.

The structural equation of motion (3) is solved by a numerical integration technique based on the Runge-Kutta sheme. Using the resulting displacements, all computational grids are moved using the grids generation system described in the following section. Then the flow field is calculated on the new grid and the resulting aerodynamic forces are integrated again. Iterating this cycle, aeroelastic simulation is performed.

Grids Deformation Systems

The present CFD grid uses the C-H grid topology. The C-H grid is deformed every time based on the wing deformation as follows.

1) Obtain a camber surface of the initial configuration of wing.
2) Integrate the structural equation of motion and obtain the generalized displacement for each mode.
3) Deform the camber surface using the generalized displacements. Interpolate the surface with a spline curve in the chordwise direction and with a liner interpolation in the spanwise direction.
4) Add wing thickness to the deformed camber surface and determine the new wing surface grid points.
5) Generate the new computational grid based on the new surface configuration algebraically.

Results

Oscillating Rectangular Wing

To verify the present code, unsteady flows over rectangular wing undergoing prescribed oscillatory motions are computed. It has NACA64A010 airfoil section and an aspect ratio of 4. The unsteady data are given when a rigid wing is oscillating in the pitching motion, $a(t) = a_m - \overline{a} \sin(\omega t)$ about the axis at $x/c = 0.5$,

Rectangular wing

$M_\infty = 0.8$ Computations
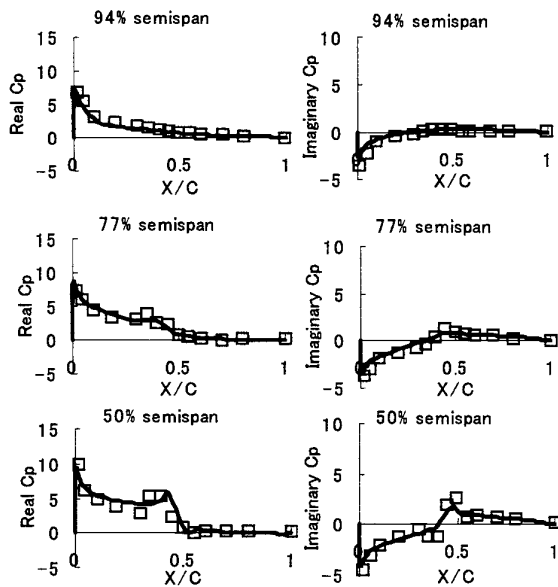$a_m = 0°$, $\overline{a} = 1°$ □   Experiments
$k = 0.27$ ——

Fig. 1 Comparison of computed upper surface unsteady pressures with experiment over the rectangular wing.

where c is the chord length and ω is the pitching frequency in radian per second. The flow is computed at $M_\infty = 0.8$ with a mean angle of attack $a_m = 0$ deg, a pitch amplitude $\overline{a} = 1$ deg, and a reduced frequency $k = 0.27$ ($k = \omega c / U_\infty$). Unsteady computations are started from the corresponding steady-state solution.

Figure 1 shows the comparison of real and imaginary parts of the first Fourier component between the computed and measured unsteady upper surface pressure coefficients of the wing at various spanwise locations with a time step size of 3600 steps/cycle. The results show a good agreement with experimental data[6] and the inboard shock wave motion is captured clealy. Throughout the test case presented here, the accuracy of the present unsteady code is confirmed favorably.

Flutter Simulation

Aeroelastic-response analyses are conducted for a high-aspect-ratio swept back wing shown in Fig 2. This configuration is based on the preliminary design of the YXX transport project and a computational model is taken from the NAL (National Aerospace Laboratory) flutter tunnel model with 1/45 of a full scale aircraft. Aspect ratio, taper ratio and thickness-to-chord are 10, 0.324 and 16%, respectively. It has supercritical airfoil section made of metal spar and urethane panel[5].

The wing is modeled by the plate. Figure 3 shows the mode shapes and frequencies of the first six normal modes for the wing. Using the normal modal data shown in Fig. 3, aeroelastic responses were computed by integrating the flow equation and the aeroelastic equation.

The flow conditions are $M_\infty = 0.70$, $R_e = 2.4 \times 10^6$, angle of attack $a = 2$ deg and several dynamic pressure are picked up around the flutter boundary obtained by the NAL flutter tunnel test. Aeroelastic computations are started from corresponding steady state solutions of the rigid wing.
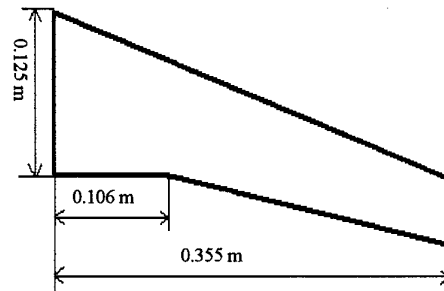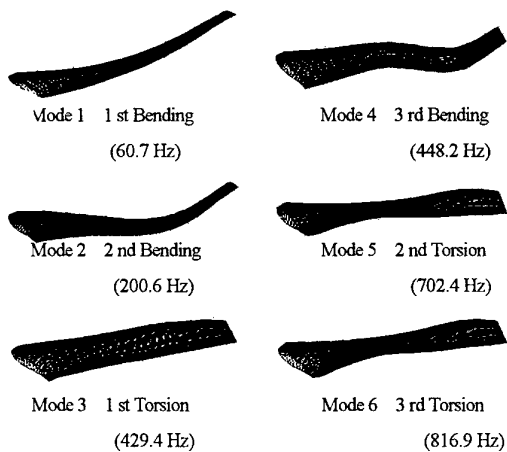

Fig. 2 YXX wing planform

Mode 1   1 st Bending
(60.7 Hz)

Mode 4   3 rd Bending
(448.2 Hz)

Mode 2   2 nd Bending
(200.6 Hz)

Mode 5   2 nd Torsion
(702.4 Hz)

Mode 3   1 st Torsion
(429.4 Hz)

Mode 6   3 rd Torsion
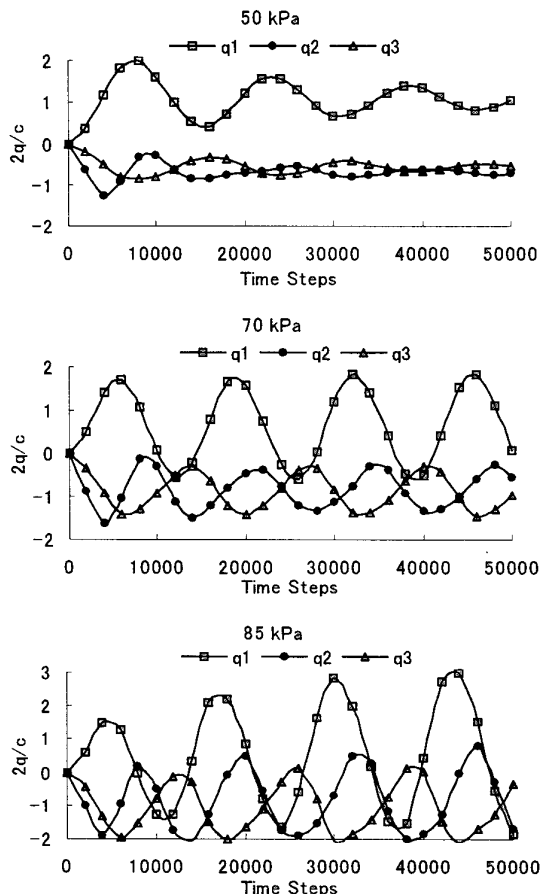(816.9 Hz)

Fig. 3 Mode shapes and frequencies

Fig. 4 The time history of generalized displacements of the fist three modes at the dynamic pressure 50kPa, 70kPa and 85kPa.

Figure 4 shows the time history of generalized displacements of the fist three modes at the dynamic pressures 50kPa, 70kPa and 85kPa. When the dynamic pressure is 50kPa, each generalized displacement decays with time, indicating that the aeroelastic system is stable at this condition. At higher dynamic pressures, the system becomes less and less stable until the displacements diverge as shown at 85kPa. When the dynamic pressure is 70kPa, all generalized displacements neither converge nor diverge. This is considered at the flutter boundary and it agrees well with the NAL flutter tunnel test.

Figure 5 shows time histories of actual displacements and aerodynamic forces at three spanwise locations at 70kPa. It shows that when the wing bends up, C_L reduces due to the wing twist. Aerodynamaic coefficients vary periodically along with the wing deformation at the flutter boundary.

Figure 6 shows the Mach contours of at 95% semi span at 70kPa during the oscillation. As the deformation becomes larger, the flow separates from the leading edge.
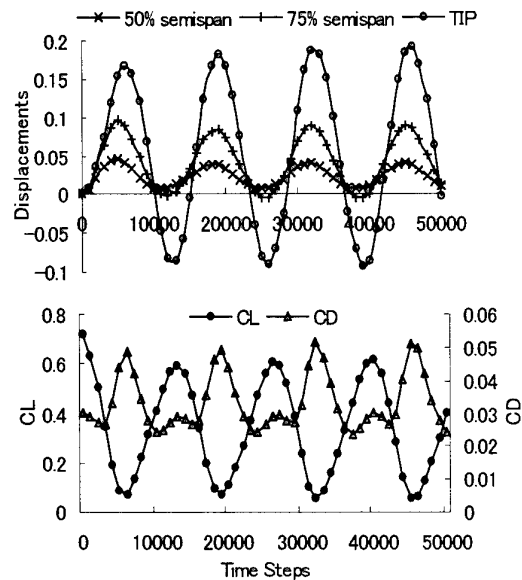

Fig. 5 Time histories of displacements, C_L and C_D at 70kPa.

Conclusions

Flutter Simulation of a transonic wing was performed associated with a moving grid system. At first, unsteady flows over rectangular wing undergoing prescribed oscillatory motions are computed. The results show good agreements with experimental data.

Then, flutter simulation of a high-aspect-ratio swept back wing is presented. Structural responses are computed using the modal analysis based on the finite-element method. The computed flutter boundary agrees well with the NAL flutter tunnel test.
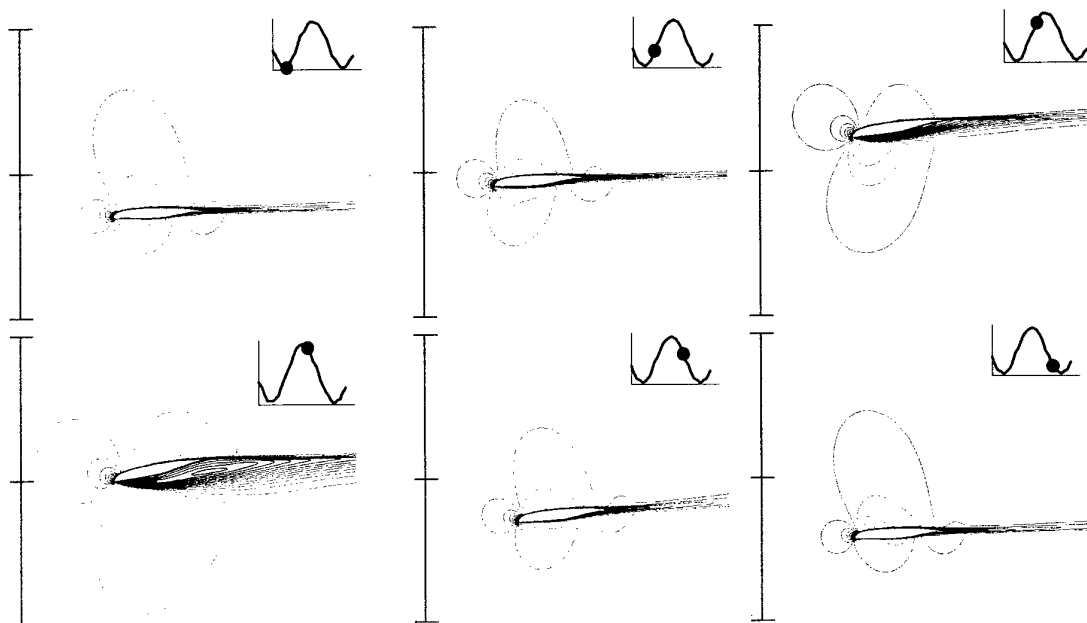
Fig. 6 The Mach contours of at 95% semi span at 70kPa during the oscillation.

References

[1] G. P. Guruswamy, "Integrated Approach Coupling of Structures and Fluids," AIAA Jornal, Vol. 27, No. 6, 1989, pp. 788-793.

[2] G. P. Guruswamy, "Unsteady Aerodynamic and Aeroelastic Calculations for Wings Using Euler Equations," AIAA Jornal, Vol. 28, No. 3, 1990, pp. 461-469.

[3] C. Byun and G. P. Guruswamy, "Aeroelastic Computations on Wing-Body-Control Configurations on Parallel Computing," AIAA Paper 96-1389, April, 1996.

[4] F. Liu, J. Cai, Yhu, A. S. F. Wong, and H. M. Tsai, "Calculation of Wing Flutter by a Coupled CFD-CSD Method," AIAA Paper 2000-0907, January, 2000.

[5] H. R. Kheirandish, G. Beppu and J. Nakamichii, "Numerical Flutter Simulation of a High-Aspect-Ratio Swept-Back Wing Based on the Navier-Stokes Equations," Journal of the Japan Society for Aeronautical and Space Sciences, Vol 45, No. 525, Oct. 1997 (in Japanese).

[6] S. Obayashi, G. P. Guruswamy and P. M. Goorjian, "Streamwise Upwind Algorithm for Computing Unsteady Transonic Flows Past Oscillating Wings," AIAA Jornal, Vol. 29, No. 10, 1991, pp. 1668-1677.

[7] E. H. Dowell, "A Modern Course in Aeroelasticity," Kluwer Academic Publishers, Dordrecht, 1995.

2E9   ADVANCING FRONT SURFACE TRIANGULATION BASED ON CAD DATA

Yasushi ITO[*] and Kazuhiro NAKAHASHI[**]
Tohoku University, Aoba-yama 01, Sendai 980-8579, JAPAN

Key Words: Aircraft, Fluid Dynamics

ABSTRACT
This paper presents an approach to generate unstructured surface meshes for CAD (Computer-Aided Design) surface models, which may have intersections, with minimum user interventions. The basic method employed here is to apply the advancing front method directly on the CAD surfaces. The key point of this approach is to use geometric features, such as ridges and corner curves of a given geometry, as the initial fronts for the advancing front method. By use of the geometric features, the original configuration is precisely preserved and the surface meshing procedure is significantly simplified. The capability of the method is demonstrated for models of an airplane piggybacked on a rocket booster and an insect.

1. INTRODUCTION
Computational Fluid Dynamics (CFD) has demonstrated its effectiveness for many different types of geometries and field regimes. However, grid generation has been continuously recognized as a bottleneck in the CFD process. This difficulty arises mainly from two significant factors: the definition of the boundaries of the domain to be meshed, and the grid generation itself.

One of the ways to settle the former problem is to link the grid generator closely to CAD. CAD software has a lot of output formats. The stereolithography (STL) format, which has become the *de facto* standard in rapid prototyping [1], is employed in the present approach as background grids for the surface meshing because of its simplicity.

Other file formats that represent the model as a set of polygons —DXF (Drawing Interchange Format) [2], 3DS (3D Studio file) and PLOT3D file for the structured surface grid for example— can be also easily converted to the STL format. However, the DXF and 3DS files often have intersecting surfaces. It is necessary to remove the intersections before the surface meshing process.

The quality and the local grid density of a surface mesh directly affect to the solution accuracies in CFD problems, especially for the aerodynamic evaluation of airplanes. This suggests that surface grid generation methods must have a strong controllability of the grid density on condition that the original geometry is preserved as much as possible. User interventions, therefore, are still required for the surface grid generation. On the contrary to the automation, this demand is essential for the surface meshing in order to obtain the best result within limited computational resources.

Surface grid generators are anticipated to be user-friendly. The conventional ones, however, are not always so. The main reason originates in the employment of a so-called mapping method, where a 3D surface must be decomposed into a collection of surface patches. This procedure often requires hundreds of hours of manipulation for the generation of the surface patches to obtain a satisfying surface grid. This surface decomposition is not essential to generate high quality surface meshes, and should be avoided to reduce work load.

Here an efficient and effective surface triangulation method has been developed [3]. The method is based on the direct advancing front method [4] for the surface meshing. One of the advantages of this approach is that it dose not require the division of the surface into a lot of patches. Furthermore, the initial fronts are useful to determine the local grid densities by distributing the grid points of user-specified number on them. The initial fronts are setup efficiently by the automatic reconstruction process of geometric features. This initial front setup based on the geometric features assures the accurate representation of the CAD model and minimizes the user interventions.

In this paper, we discuss a surface grid generation method in which the user interventions are minimized while the controllability of the grid is enhanced by utilizing the GUI (Graphical User Interface). The method is applied to several airplane configurations and a hornet model, which has interacting surfaces, to demonstrate the capability.

2. SURFACE GRID GENERATION METHOD
A flowchart of the surface grid generation procedure is shown in Fig. 1.

In the first step, CAD data files are read. The STL file format is used as the input. Other file formats that represent the model as a set of polygons can be also easily converted to the STL format.

In the second step, the CAD surface is automatically corrected in order to use it as a background grid for the surface meshing. The surface data prepared in STL often has ill-conditioned facets: overlapping facets, gaps [5], highly

---

[*] Graduate student, Department of Aeronautics and Space Engineering

[**] Professor, Department of Aeronautics and Space Engineering

stretched facets [3] and so on. Overlapping facets and gaps prevent the accurate surface definition and highly stretched facets will interrupt the surface meshing because their normal vectors are not calculated precisely. By identifying the commonly appeared ill-conditioned facets, most of them can be fixed automatically. Other types of objectionable facets will be easily found and revised on GUI environment if necessary.

In the third step, the geometric features (ridges) are automatically reconstructed. Grid points are distributed on these curves to form initial fronts for the advancing front method. Source lines and points may be added to control local grid density and to represent the model more accurately. Sample ridges are shown in Fig. 2b.

In the fourth step, the advancing front method is applied directly on the CAD-defined background grid. The positions of new nodes are temporarily calculated with linear interpolation because of the robustness. After the triangulation, a second-order correction algorithm [6], for the exact surface recovery, is applied to the new nodes.

In the fifth step, the computational boundaries are defined so as to generate the volume grid. The outer boundary generation is simplified by preparing several templates for the outer-boundaries.
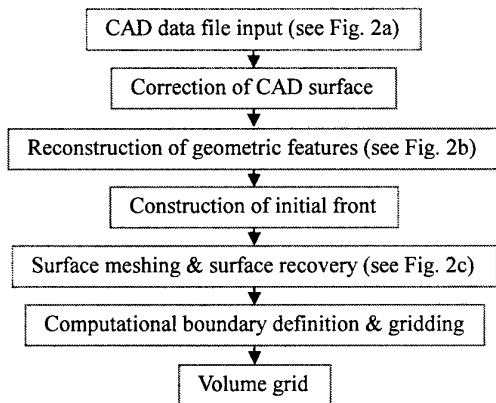
3. APPLICATIONS
3.1 NAL experimental airplane model

Figure 3 shows a semi-span model of a NAL (National Aerospace Laboratory of Japan) experimental supersonic airplane piggybacked on a solid rocket booster that will be launched to altitude of 15,000 meters in 2002 [7]. Several derivative models were prepared by CATIA in order to evaluate the differences of the aerodynamic effects caused by the projections such as connections between the airplane and the booster, and fairings on the booster. The intensity of shock waves that are generated from the projections depends on their existences and positions, and directly affects the flight characteristic particularly in transonic flow regions [8]. Figure 4 shows a surface mesh for the original model. The mesh has 116,414 nodes and 232,824 faces. It takes about 3 hours to generate the mesh for each model, and most of it is spent on the mouse operation such as adding ridges and specifying division parameters at each ridge.

A volume grid was generated by a Delaunay method [9]. It has 672,489 nodes and 3,656,818 tetrahedra. Euler calculations were performed and computed results at a freestream Mach number of 1.6 and an angle of attack of zero are shown in Fig. 5.

Fig. 3   NAL experimental airplane model and detected ridges

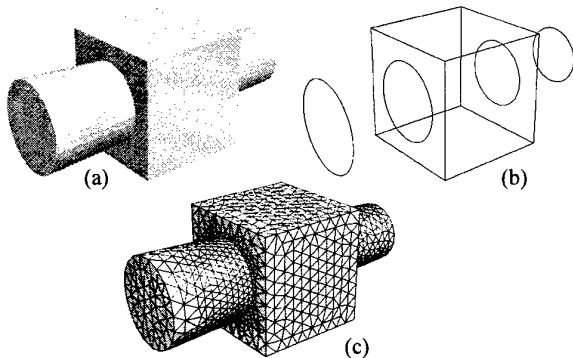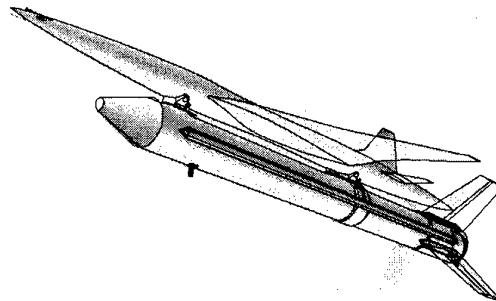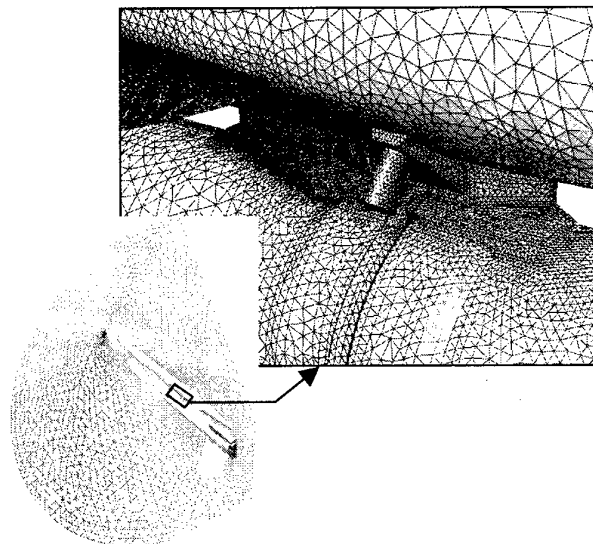Fig. 1   Flowchart of grid generation

Fig. 2   Example of surface meshing: (a) CAD geometry; (b) detected ridges; (c) surface mesh

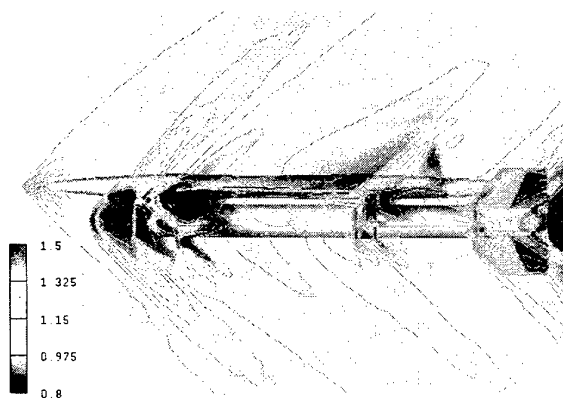Fig. 4   Surface mesh of NAL experimental airplane model

Fig. 5   Euler calculation for NAL experimental airplane model (M_∞ = 1.6, α = 0.0): pressure distribution on the symmetry plane

3.2 Hornet model

Figure 6 shows a hornet configuration. The configuration data was prepared as a DXF file. This format was developed by AutoDesk to allow CAD data to be interchanged between different applications. The DXF file generally represents a configuration as a collection of parts and each part is made of polygons. It is easy to subdivide polygons into triangular faces, but the interacting faces among each part have to be eliminated.

Two approaches can be considered: a) surface meshing for each part and re-triangulation near the intersections and b) conversion of intersecting surfaces into a single surface, which is used as a background grid for the surface meshing. The former is described in [10] and [11]. This approach is effective for simple geometries such as spheres, cylinders and cubes. For complex geometries, however, this approach has limitations because it is difficult to adjust sizes of triangles of each part near the intersections.

The intersecting faces are therefore eliminated beforehand in order to define a background grid for the surface meshing as a single surface. This operation is carried out automatically in the following way. Figure 7 shows an application for two cubes.

(a)   For each part, make a tight-fitting oriented bounding box as shown in Fig. 8, and search the intersecting boxes [12] in order to reduce the computing time. If the boxes intersect, the base parts are considered to intersect.

(b)   Select intersecting two parts. For each edge of one of the parts, search the crisscrossing triangular faces of the other part, and calculate the intersecting points, such as black points in Fig. 7a.

(c)   Remove nodes that are inside the object, such as a white point in Fig. 7a.

(d)   Add edges of intersection and nodes on both ends of them, which are calculated in (b).

(e)   Divide polygons, which made of divided original edges and newly created edges in (d), into triangles.

(f)   Remove highly stretched faces if necessary.

In addition, some node movement is required in this case because the defined surface is very rough particularly at the legs. If the model is given as a solid model, CAD systems can output the water-proof STL data as was the case for the NAL experimental supersonic airplane model shown in the previous section.

The surface grid generation method was applied to the revised surface. After the reconstruction of geometric features, several ridges were added particularly at the legs because the defined surface is rough and coarse as mentioned above (see Fig. 6). Surface triangulation was then performed as shown in Fig. 9. The generated surface mesh has 66,824 nodes and 132,626 faces. The required CPU time on Pentium III (600 MHz) PC is about 3 minutes for the surface grid generation process in this case. The total required time for the surface mesh was about one day. Most of these works is to eliminate interacting faces that are contained in DXF files and to move nodes. If the model is given by a CAD solid model, this modification becomes trivial.

A half sphere was selected for the computational outer boundary shape. The volume grid was generated in the same way with the previous section, and has 741,728 nodes and 4,183,735 tetrahedra. Incompressible Navier-Stokes calculations were performed, and Fig. 10 shows the computed results at a Reynolds number of 10^4. The wing was fixed in the zero dihedral angle.
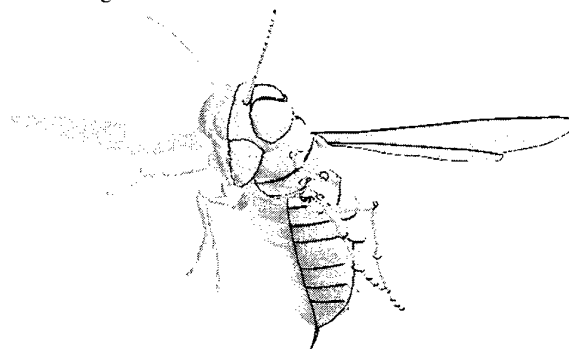

Fig. 6   Hornet model and ridges (black lines)
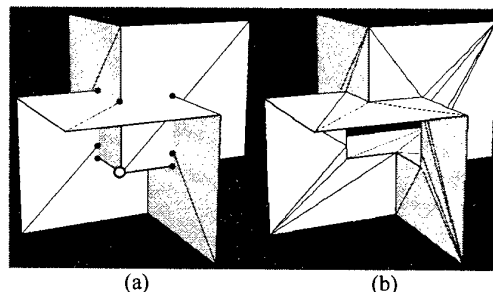

(a)   (b)

Fig. 7   Boolean union: (a) two cubes that interact each other; (b) after removing the interaction
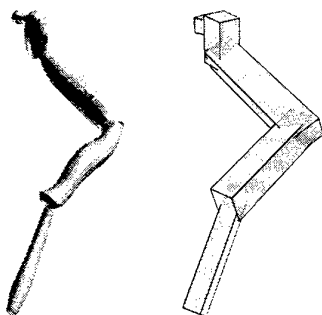
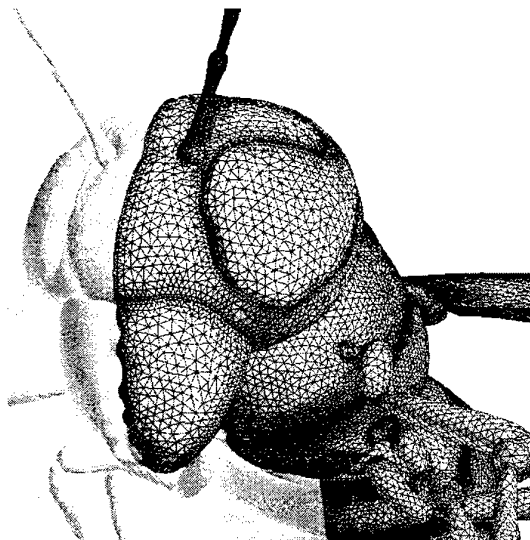Fig. 8   Tight-fitting oriented bounding boxes for the front leg
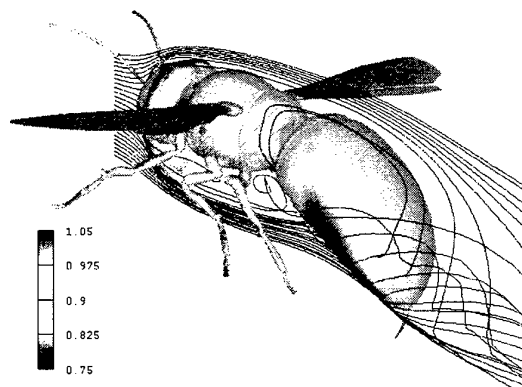

Fig. 9   Surface mesh of the hornet

Fig. 10   Incompressible Navier-Stokes calculation for the hornet ($Re = 10^4$, $\alpha = 0.0$)

4. CONCLUSIONS

A surface triangulation method using CAD data was presented. The automatic reconstruction process of geometric features assures the accurate representation of the CAD model. The initial front setup based on the geometric features minimizes the user interventions. The method was applied to models of the NAL experimental airplane and a hornet. The time needed for surface grid generation was significantly reduced.

The ability to generate surface meshes over interacting surfaces was also demonstrated.

ACKNOWLEDGEMENTS

REFERENCES

[1] *Stereolithography Interface Specification*, 3D Systems, Inc., CA, 1989.

[2] *AutoCAD Reference Manual*, AutoDesk, Inc., CA, 1990.

[3] Ito, Y. and Nakahashi, K., "Direct Surface Triangulation Using Stereolithography (STL) Data," AIAA Paper 2000-0924, 2000.

[4] Nakahashi, K. and Sharov, D., "Direct Surface Triangulation Using the Advancing Front Method," AIAA Paper 95-1686-CP, 1995, pp.442-451.

[5] Leong, K. F., Chua, C. K. and Ng, Y. M., "Study of stereolithography file errors and repair. Part 1. Generic solution," *International Journal of Advanced Manufacturing Technology*, Vol. 12, No. 6, 1996, pp. 407-414.

[6] Löhner, R., "Regridding Surface Triangulation," *Journal of Computational Physics*, Vol. 126, No. 1, 1996, pp.1-10.

[7] Iwamiya, T., "NAL SST Project and Aerodynamic Design of Experimental Aircraft," Proc. of the 4th ECCOMAS Computational Fluid Dynamics Conference, Athens, John Wiley & Sons Ltd., Chichester, 1998, pp.580-585.

[8] Fujita, T., Ito, Y., Nakahashi, K., and Iwamiya, T., "Effect of Small Components on the Aerodynamic Coefficients of NAL Experimental Supersonic Airplane in Ascent," Paper to be presented at the JSASS 14th Int. Sessions in the 38th Aircraft Symposium, 2000.

[9] Sharov, D. and Nakahashi, K., "A Boundary Recovery Algorithm for Delaunay Tetrahedral Meshing," Proc. of the 5th Int. Conf. on Numerical Grid Generation in Computational Field Simulations, 1996, pp.229-238.

[10] Lo, S. H., "Automatic Mesh Generation over Intersecting Surfaces," *International Journal for Numerical Methods in Engineering*, Vol. 38, 1995, pp. 943-954.

[11] Shostko, A. A., Löhner, R. and Sandberg, W. C., "Surface Triangulation over Intersecting Geometries," *International Journal for Numerical Methods in Engineering*, Vol. 44, 1999, pp. 1359-1376.

[12] Gottschalk, S., Lin, M. C. and Manocha, D., "OBB-Tree: A Hierarchical Structure for Rapid Interference Detection," Proc. of SIGGRAPH '96, Computer Graphics, Annual Conference Series, 1996, pp. 171-180.

2E10 NUMERICAL SIMULATION OF A DUAL-COMBUSTIOR SCRAMJET FLOW-FIELD

Xu Shengli*   Yue Pentao**
(a University of Science and Technology of China, Hefei 230026, P.R.China)
***Hirotoshi Kubota
(b The University of Tokyo, Tokyo, Japan)

Key Words: supersonic flow, supersonic combustion, scramjet,
shock tunnel, numerical simulation

ABSTRACT

The internal flow-field of a dual-combustor scramjet, without fuel injection and combustion, was studied in this paper. The experiment was carried out in a reflected shock tunnel, and schlieren photographs were obtained. Upwind TVD scheme was used to solve three-dimensional, complete Navier–Stokes equations by multi-domain method for the test nozzle and scramjet. Also, several geometrical parameters were varied to show their effects on scramjet flow field. For a typical case, i. e. $h_p= 12.93mm$, the computed shock waves are similar to those in photographs, and static pressures along the lower median wall are also in agreement with experimental results. The flows in the inlet, supersonic combustor and aft nozzle are relatively simpler, but rather complex in the subsonic combustor. Along the lower wall, the separated flow, started from expansion wall surface, evolves into a contact surface till to the subsonic combustor entrance. By reducing h_p, shifting the splitter upwards and rotating it clockwise, the recirculation zone moves upstream along the lower wall till to the inlet, and contact surface is raised up. In most cases, contact surfaces along the lower wall are seriously distorted. Overflow will occur at subsonic combustor entrance. Then, the flow is choked in scramjet duct.

INTRODUCTION

Kerosene fueled scramjet is a preferable propulsion power for M=6~8 aerodynamic vehicles[1][2][3], such as missiles[4]. The advantages for kerosene are higher volumetric heat release and jet penetration. The disadvantages are unsatisfactory combustibility and long ignition delay. Also, there exists breakup and atomization for kerosene jet. The results show that dual-combustor is a good way to alleviate such difficulties. Dual-combustor scramjet is composed of two combustors. One duct is a subsonic combustor as an igniter, the other is a supersonic one. Most kerosene burns in the subsonic combustor. Exhausted gas with rich and active radicals from the subsonic combustor, ignites stoichiometric fuel air mixture in supersonic combustor. In the 1970's, Billig studied dual-combustor scramjet, i. e. SCRAM-MOD1. SCRAM-MOD2 for missiles[4][5]. A different one was studied by UTRC which three subsonic combustors are installed evenly in the same cross-section[6]. Without fuel injection and combustion, the cold flow field of a dual–combustor scramjet was studied experimentally by NASA Langley Research Center[7]. The static pressure distribution was measured along lower and upper median walls. In summary, the concerned works are usually conducted in conventional tunnels. Due to the problem of wind tunnel unstart, the size of model scramjet is very limited. It is difficult to visualize the scramjet internal flow field because of interference of external flow around the test model. In this paper, a highly integrated duct with inlet, dual-combustor and aft nozzle was designed, and was connected directly to nozzle as a test section in a shock tunnel. In experiment, the emphasis was on schlieren visualization to internal flow field. Then, the computed waves denoted by pressure contours are also presented for a comparison with those in schlieren images. The numerical investigation was conducted to show the transition mechanism from supersonic to subsonic flow in the subsonic combustor. The purpose are to know (1) shock waves appearing in flow field.(2) interaction of inflow at combustors inlet. (3) effects of geometrical parameters, such as nozzle throat height h_p, translation distance and rotation angle of the splitter.

1.   TEST RIG AND EXPERIMENTAL RESULTS.

A highly integrated duct with dual-combustors is shown in Fig.1. In convenience for flow visualization, the side -walls can be interchanged. The side-walls may be glass windows or metal covers with transducer ports. The numerical boundary is the same as that for digitally manufacturing contour.

The experiment was done in a reflected shock tunnel. The inlet of this integrated duct is directly connected to a nozzle with designed Mach number 3.15. The nozzle exit is 40 mm×70mm in height and width. Fig.2 gives a schlieren image for flow field in inlet and dual-combustor.
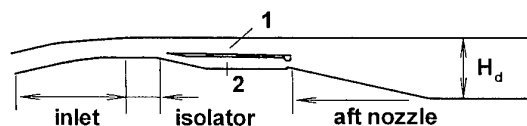

Fig.1 Schematic of dual-combustor scramjet
1,supersonic combustor; 2,subsonic combustor

Fig.2 Schlieren photograph of inlet and dual combustors (h_p=12.93mm)

* Associate Professor.   Depart of Mechanics and Mechanical Engineering
** Ph D Student,   Depart of Mechanics and Mechanical Engineering
*** Professor,   Department of Aeronautics and Astronautics

2. GOVERNING EQUATIONS AND NUMERICAL SCHEMES

2. 1 Governing Equations

In Cartesian system, the fully Navier-Stokes equation is as follows

$$\frac{\partial U}{\partial t} + \frac{\partial E}{\partial x} + \frac{\partial F}{\partial y} + \frac{\partial G}{\partial z} = \frac{\partial E_v}{\partial x} + \frac{\partial F_v}{\partial y} + \frac{\partial G_v}{\partial z} \qquad (1)$$

Where U is a conservative variable vector. E, F, G, are convective and E_v, F_v, G_v are viscous vectors. In a curvilinear system, Eq.(1) is rewritten as

$$\frac{\partial \hat{U}}{\partial \tau} + \frac{\partial \hat{E}}{\partial \xi} + \frac{\partial \hat{F}}{\partial \eta} + \frac{\partial \hat{G}}{\partial \zeta} = \frac{\partial \hat{E}_v}{\partial \xi} + \frac{\partial \hat{F}_v}{\partial \eta} + \frac{\partial \hat{G}_v}{\partial \zeta} \qquad (2)$$

Where $\tau = t$, $\xi = \xi(x,y,z)$, $\eta = \eta(x,y,z)$, $\zeta = \zeta(x,y,z)$, $\hat{U} = J^{-1} \cdot U$, $\hat{E} = J^{-1} \cdot (\xi_x E + \xi_y F + \xi_z G)$,

$\hat{F} = J^{-1} \cdot (\eta_x E + \eta_y F + \eta_z G)$, $\hat{G} = J^{-1} \cdot (\zeta_x E + \zeta_y F + \zeta_z G)$, J is the Jacobian matrix. Only laminar flow is considered in this paper.

2. 2 Numerical scheme

Upwind TVD scheme is used to discretize convective terms, and central difference scheme for viscous term. The discretized equation (2) is in form of

$$\hat{U}_{i,j,k}^{n+1} = \hat{U}_{i,j,k}^n - \frac{\Delta\tau}{2\Delta\xi}[(\hat{E}_{i+1,j,k}^n - \hat{E}_{i-1,j,k}^n) + (\hat{F}_{i,j+1,k}^n - \hat{F}_{i,j-1,k}^n) + (\hat{G}_{i,j,k+1}^n - \hat{G}_{i,j,k-1}^n)$$
$$- (\hat{E}_{v,i+1,j,k}^n - \hat{E}_{v,i-1,j,k}^n) - (\hat{F}_{v,i,j+1,k}^n - \hat{F}_{v,i,j-1,k}^n) - (\hat{G}_{v,i,j,k+1}^n - \hat{G}_{v,i,j,k-1}^n)$$
$$+ (R_{i+1,j,k}^n \Phi_{i+1,j,k}^n - R_{i-1,j,k}^n \Phi_{i-1,j,k}^n) + (R_{i,j+1,k}^n \Phi_{i,j+1,k}^n - R_{i,j-1,k}^n \Phi_{i,j-1,k}^n)$$
$$+ (R_{i,j,k+1/2}^n \Phi_{i,j,k+1/2}^n - R_{i,j,k-1/2}^n \Phi_{i,j,k-1/2}^n)]$$

Where R is right eigen vector of Jacobian matix. The expression for Φ can be found in Ref.[8].

2. 3 Auxiliary Conditions

The total pressure and total temperature are determined by equilibrium contact surface theory in a reflected shock tunnel. The method of multi-domain is used in the computation. At the block interfaces, a special data match is assigned. The computation of nozzle is from its throat.

Initial conditions: The initial values for the nozzle is given by theory of one dimensional isentropic flow. The variables at nozzle exit are specified as inflow parameters for the integrated duct.

Boundary conditions: Initially, variables at nozzle throat are determined by one dimensional isentropic relations from total pressure and total temperature. Along the walls, the non-slip conditions are specified for velocity, zero pressure and temperature gradient are imposed. The variables at duct exit are extrapolated linearly.

3. RESULTS AND DISCUSSION

3. 1 Grid generation

Computational grids are shown in Fig.3. The grids for nozzle and combustors are initially generated by algebraic method, then, modified by solving Laplace equation. Finally, a linear extrapolation was used to get clustered grid along walls. The grids for nozzle and integrated duct are $101 \times 51 \times 20$, $231 \times 70 \times 20$, respectively. Only a symmetrical domain in z direction is considered.
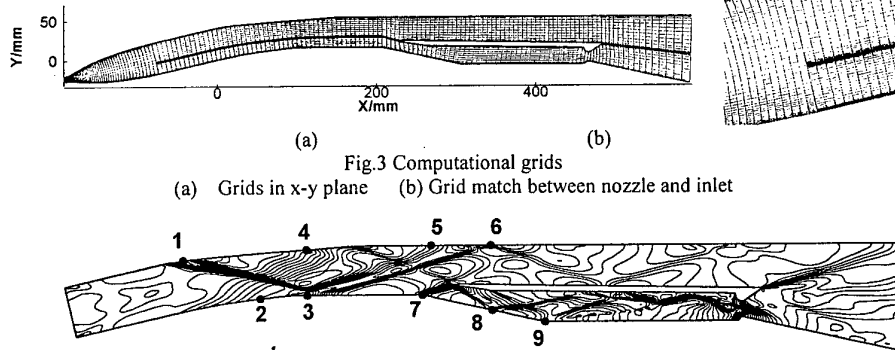

(a) (b)

Fig.3 Computational grids
(a) Grids in x-y plane (b) Grid match between nozzle and inlet
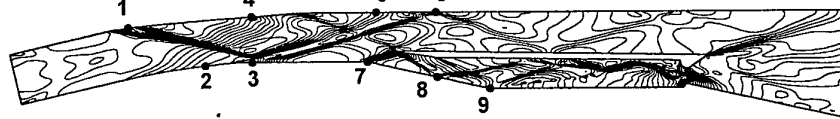
Fig.4 Pressure contours at symmetrical plane of inlet, dual-combustor and aft nozzle scramjet

3. 2 Computation of nozzle flowfield

The nozzle flowfield was numerically studied to avoid giving boundary layer at scramjet inlet. The results show that the flow at nozzle exit is quite uniform, and computed average exit Mach number is 3.20. In consequent computation, the value of variables at center of nozzle exit is chosen as reference parameters for equation non-dimensionalization. The computed static pressure and temperature are $1.469 \times 10^4 Pa$ and $7.698 \times 10^5 Pa$, respectively.

3. 3 Computation of internal flow field of dual combustors

In Fig.4, the pressure contours are presented at median plane, z=0.5w. At point 1, the compression waves are generated, then, a weak shock is formed downstream. At point 3, a recirculation zone is generated. The weak shock reflects at the recirculation zone. A reflected shock and expansion waves are also formed. At point 5, expansion waves are absorbed. A re-reflected shock is generated at point 6, and its strength is further reduced until it reaches to the supersonic duct exit. At point 4, expansion waves go through the weak shock and reflect as compression waves, which are absorbed near the sharp corner of splitter. At point 7, expansion waves are generated and denote the local flow is supersonic. These expansion waves are reflected as

compression waves at splitter wall. At point 9, an oblique shock is generated. Because the flow is choked at subsonic combustor throat, complicated pressure waves are formed in subsonic combustor. The shock waves denote that local flow in the subsonic combustor is intrinsically supersonic. A further comparison indicates that the computed shock is in good agreement with that in schlieren image(Fig.3). Because of the flow's impact on the splitter, the shock position doesn't coincide with experimental result precisely. At point 2, as shown in Fig.5, the flow is separated, and a contact surface is evolved downstream till to subsonic duct inlet. By contrast to Fig.2 and Fig.4, the velocity field in Fig.5 helps to determine the contact surface. It is noted that a small separated region is formed close to upper wall, but it disappears quickly downstream because of wall compression.

(a)   z=0.5W

(b)   z=0.34W
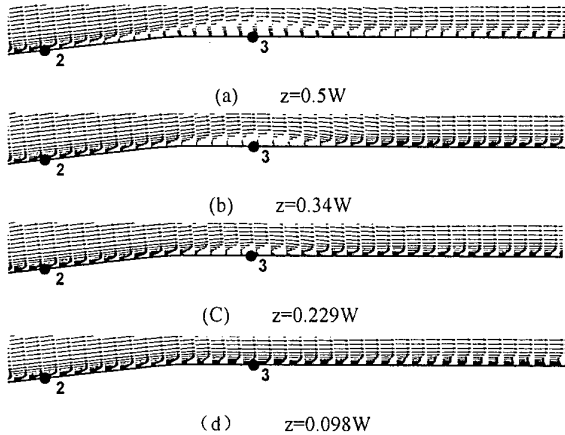

(C)   z=0.229W

(d)   z=0.098W

Fig.5 Velocity distribution of separated zones along z direction

Fig.6 presents the distribution of static pressure and its experimental value along the low median wall. Where p_t is the static pressure in Ref.[7]. Although the inflow Mach number is the same, but the total pressures of inflow are 1.29Mpa in Ref.[7] and 0.77Mpa in this paper, corresponding to static pressures 0.028Mpa and 0.015Mpa, respectively. After transformation, the computed static pressures are in qualitative agreement with experimental ones. Because the size of the integrated duct in this

paper is larger than that in Ref.[7],therefore, the shock position is different. In Fig.6, at x/H=6, the higher experimental value denotes the shock appears earlier than that in this paper.
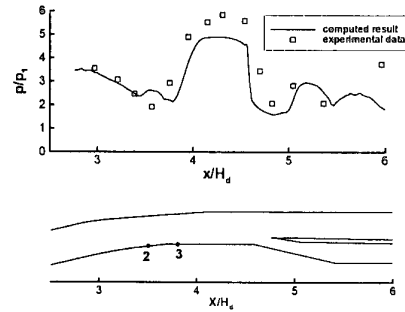

Fig.6 Pressure distribution along scramjet low median wall

In following sections, several geometrical parameters are numerically tested to show their effects on the flowfield.

3.4   Nozzle throat height h_p

In subsonic combustor, it is important to know how supersonic flow is decelerated into subsonic. In this section, splitter is positioned certainly during the computation, but throat height is reduced continuously. Fig.7 shows the velocity field in the subsonic combustor. In Fig.7(a), h_p=14.00mm, the recirculation zones are small. They locate upstream of subsonic combustor throat and close to walls. Obviously, the supersonic flow dominates in subsonic combustor. In Fig.7(b), h_p=10.0mm, the separated flow region is expanded and pushed upstream. Supersonic and subsonic flows share the flow field equally. In Fig.7(c), h_p=5.93mm, the separated flow is further pushed upstream. In subsonic combustor, the flow is fully subsonic, and supersonic flow is decelerated into subsonic by going through these recirculation regions. In scramjet inlet, the contact surface is raised but not distorted. In the region between contact surface and low wall surface, the flow becomes subsonic. In Fig.7, it can be found that flow in aft nozzle becomes uniformly as h_p is reduced.

(a) h_p=14.00mm

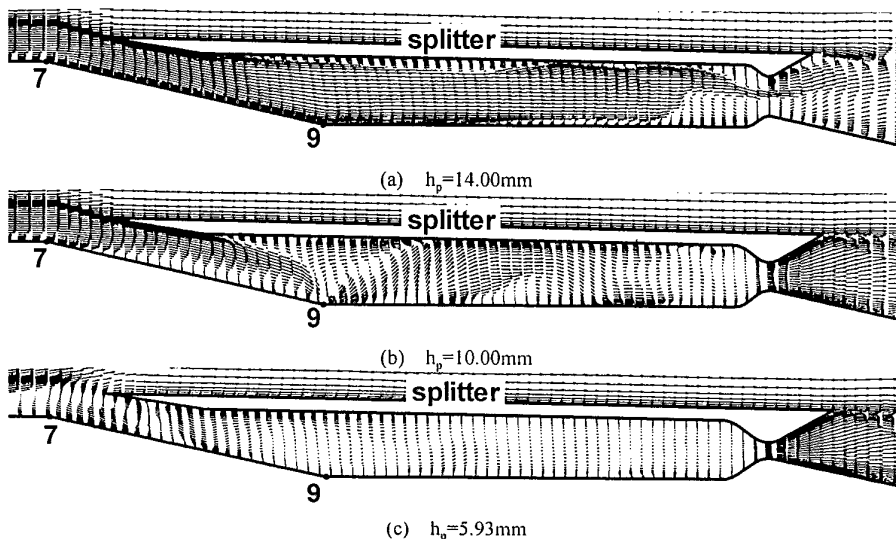(b) h_p=10.00mm

(c) h_p=5.93mm

Fig.7 Velocity field in subsonic combustor with different h

In summary, the supersonic flow is decelerated into subsonic through recirculation regions in the subsonic combustor. By reducing h_p, the separated flow is extended and pushed

upstream, till it reaches the inlet section. Then, subsonic flow is formed and contact surface is raised. In some cases, the contact surface covers the subsonic combustor entrance, and it is

distorted seriously.

Fig.8 gives the distribution of pressure contours. As h_p is reduced, it is obvious that the pressure waves in the subsonic combustor becomes more complicated, and the oblique shock in aft nozzle becomes stronger. In Fig.8(c), the subsonic duct is congested, and inflow of the supersonic duct is seriously affected.

In Fig.8, If h_p is larger than its critical value, flow in supersonic combustor and inlet section is almost unaffected by varying h_p. But if h_p is less than its critical value, flow in supersonic combustor is affected and the entire subsonic combustor is congested. For different h_p, the flow states can be summarized in Table 1.
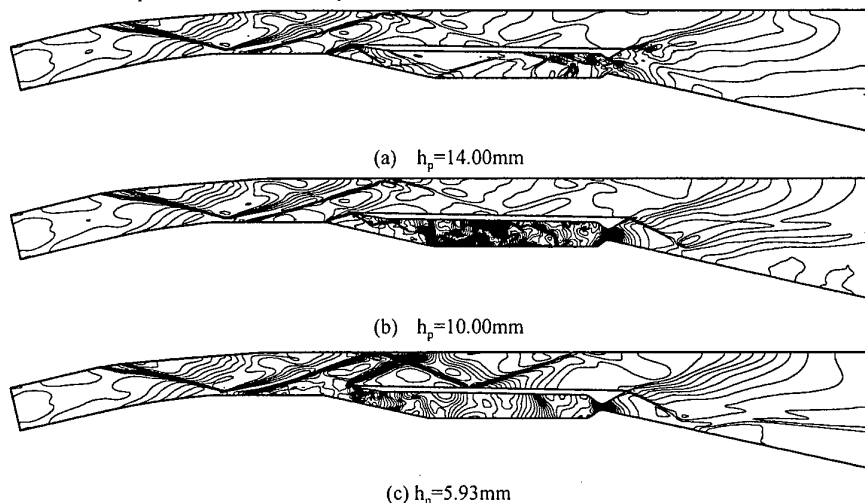

(a) h_p=14.00mm

(b) h_p=10.00mm

(c) h_p=5.93mm
Fig.8 Pressure contours with different h_p

Table 1 Flow states for different h_p

h_p(mm)	14	10	5.95
subsonic combustor	supersonic dominated	subsonic and supersonic occupied equally	fully subsonic
combustors entrance	unaffected	unaffected	congested

3. 5 Rotation of splitter

When the splitter is rotated 3 degree clockwise, Fig.9

presents the velocity field. In Fig.9(a), a recirculation region is formed near the sharp point of splitter. It is obvious that the integrated duct is congested. The contact surface is raised and distorted. The inverse subsonic flow appears in the region between contact surface and the lower wall surface. The flow in subsonic combustor is completely subsonic and an overflow is also demonstrated. Fig.9(b) gives the distribution of pressure contours. The pressure contours become disordered, especially at the subsonic combustor and isolator section because of the interactions between shock waves and separated flow. In the supersonic combustor, it is clear that flow is still supersonic but inflow is affected greatly.

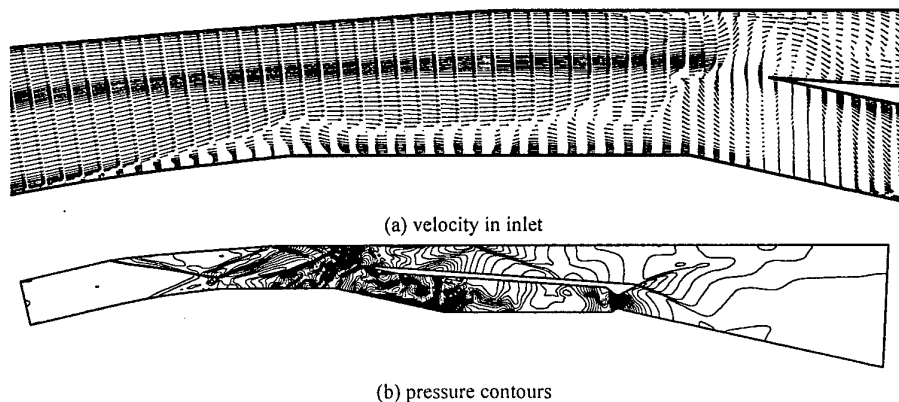(a) velocity in inlet

(b) pressure contours
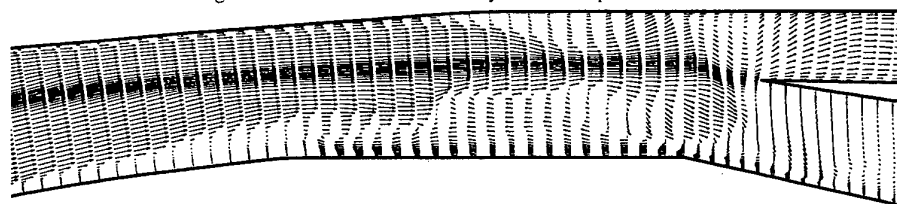Fig.9 Pressure contours and velocity field with splitter rotation

Fig.10 Velocity field with splitter shifted upwards

3. 6 Vertical translation of splitter

In this subsection, the splitter is translated 12mm upwards but h_p keeps unchanged. Fig.10 gives the velocity field at scramjet inlet. In Fig.10, several large separated zones are formed in the duct, and contact surface is distorted seriously. The results indicate that flow in subsonic combustor is completely subsonic and gas Mach number is rather low, but flow in the supersonic combustor is still supersonic. The entire duct is congested greatly and no obvious shock wave appears. Flow conditions in subsonic combustor and isolator are summarized as in table 2.

Table 2 Flow conditions at different splitter positions.

splitter position	translated 12mm upwards	rotated 3 deg clockwise
subsonic combustor	fully subsonic	subsonic dominated
combustors entrance	congested	congested seriously

4. CONCLUSION

1. Numerical simulations and experimental studies were conducted on cold flow field of a dual-combustor scramjet. Several geometrical parameters were investigated in this paper. For typical experimental conditions, the computed shocks are in agreement with those in schlieren photographs.

2. Compression, expansion waves and weak shock waves appear in scramjet inlet. The results indicate that the inlet design is successful because total pressure loss is small while flow is deflected. Close to the lower wall, a contact surface is evolved from recirculation zone till it reaches the subsonic combustor entrance. Flow is supersonic at both sides of the contact surface. The flow in aft-nozzle and in supersonic combustor is less complicated than that in subsonic combustor.

3. If the splitter is positioned constantly, by reducing h_p, the supersonic flow region is decreased but subsonic flow increased. The separated flow is pushed upstream. The supersonic flow is decelerated into subsonic by going through recirculation zones.

4. The mechanism of scramjet congestion was investigated in this paper. If the inflow keeps unchanged. By decreasing h_p, translating splitter upwards and rotating splitter clockwise, correspond to increasing mass flow rate of the subsonic combustor. Then, the recirculation region is pushed upstream and goes into the inlet section along the lower wall. The contact surface is raised, and covers the subsonic combustor entrance. In some cases, the contact surface is distorted seriously and boundary layer is separated. Then, an overflow appears and flow in the integrated duct is congested.

REFERENCE

[1] Liu Ling, Liu Jinghua, et al. Supersonic combustion and Scramjet. Xi'an: Northwest Polytechnic University press, 1991 (in Chinese)

[2] Waltrup P J. Liquid fueled supersonic combustion ramjets: A research prospective of the past, present and future. AIAA Paper 86-0518, 1986

[3] Vinogradov V A, Kobigsky S A, Petrov M D. Experimental investigation of kerosene fuel combustion in supersonic flow. J Propulsion and Power, 1995, 11(1): 130

[4] Billig F S, Waltrup P J, Stockbridge R D. The integral-rocket, dual combustion ramjet: A new propulsion concept. J Spacecraft and Rockets, 1980, 17(5): 499

[5] Billig F S. SCRAM—A supersonic combustion ramjet missile. J of propulsion and power, 1995, 11(1): 1139

[6] Kay I W, Peschke W J, Guile R N. Hydrocarbon fueled scramjet combustor investigation. AIAA Paper 90-2337, 1990

[7] Andrews E H, Trexler C A, Emami S. Tests of a fixed-geometry Inlet-combustor configuration hydrocarbon-fueled, dual-mode scramjet. AIAA Paper 94-2817, 1994

[8] Yee H C, Klopeer G H, Montagne J L. High-Resolution Shock-capturing schemes for inviscid and Viscous Hypersonic Flows. J. Comput. Phys, 1990, 88 (1): 31

2E11 Effect of Small Components on the Aerodynamic Coefficients of NAL Experimental Supersonic Airplane in Ascent

Takeshi FUJITA[1], Yasushi ITO[1], Kazuhiro NAKAHASHI[2] and Toshiyuki IWAMIYA[3]

Dept. of Aeronautics and Space engineering, Tohoku University, Sendai 980-8579-01, Japan
National Aerospace Laboratory, 6-13-1 Osawa, Mitaka 181-0015, Japan

Key Word: Aircraft, aerodynamics

ABSTRACT

Aerodynamic coefficients of the NAL experimental airplane piggybacked on a solid rocket booster in ascent are numerically evaluated by solving the Euler equations on unstructured tetrahedral grids. The airplane and the rocket booster have various small parts on them, such as a Pitot tube on the airplane, pipe covers and connecting fringes on the rocket booster. The effect of these small parts on the aerodynamic coefficients of the piggyback configuration during the transonic to supersonic accent fright is investigated in detail. The computed results show good agreements with wind tunnel results in lift and drag coefficients for the supersonic flow regime. In the transonic regime, it is shown that the small parts attached on the rocket booster generate shock waves on the lower surface of the airplane, resulting significant changes in the pressure distribution on the wing. The results indicate that the detail representation of the original geometry is very important for accurate evaluation of the transonic lift coefficients. A combination of CAD-based modeling and the efficient surface meshing scheme allows the quick modification of the configurations to identify the effects of each small component.

1. INTRODUCTION

The CAD outputs of an experimental supersonic airplane and a rocket booster are shown in Fig. 1. The fuselage length of the airplane is 11.5 m, and the span is 4.718 m. The models were defined by CATIA at the National Aerospace Laboratory of Japan. Detailed parts, such as a Pitot tube on the airplane, pipe covers and connecting fringes on the rocket booster, are represented exactly in the CAD models, as shown Fig. 1. In order to compute flows around such a complex configuration, a seamless procedure from the CAD output to the surface meshing is required for the precise surface reconstruction of the original CAD-defined model in the computational space. Here the CATIA is used to build the models and to modify them in order them to fit to the CFD. The CAD is also used to remove some small parts on the rocket booster for the investigation of their effect to the aerodynamic coefficients.

The experimental airplane and the rocket booster were defined independently by CAD. Then, they were superposed as shown in Fig. 1. Before the output, two regions of the configuration were modified on CATIA; 1) static pressure holes in Pitot tube ahead of airplane, 2) very little gaps at the connecting fringes between the airplane and the rocket booster. These holes and gaps sometimes cause difficulties in generating the grids and in the flow computations. Since they are so small that their influence on the flow field will be negligible.

To generate a surface grid, the stereolithography (STL) data was generated by CATIA. The STL data format is designed for the rapid prototyping and represents a surface via a set of triangular faces. This file contains only pure geometric information of the model so that it is easily manipulated.

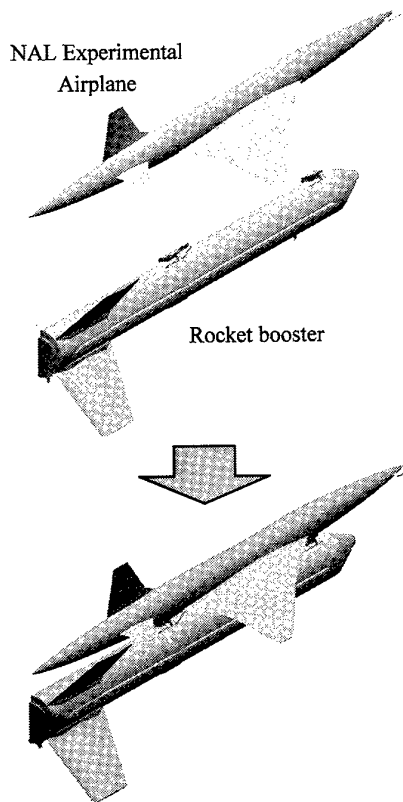NAL Experimental Airplane

Rocket booster

Fig. 1 Superposition of two CAD models

[1] Graduate student, Department of Aeronautics and Space Engineering
[2] Professor, Department of Aeronautics and Space Engineering
[3] National Aerospace Laboratory

The Edge Editor, a surface meshing software developed at Tohoku University [2], was used to generate the surface grid with STL data of NAL experimental airplane. The flowchart of the surface grid generation procedure is shown in Fig. 2. After reading the geometry data, some pre-processing is performed before the surface meshing. This procedure constructs information of geometrical feature lines as shown in Fig. 3 as well as a background grid for surface meshing. Then, using the feature lines as the initial fronts, the advancing front algorithm is applied to the background grid. For the volume grid generation, the method also generates outer and symmetrical boundary grids as well. The volume grid is generated by Delaunay tetrahedral meshing [3]. Finally, this volume grid contained 658,532 node points and 3,570,327 tetrahedral elements.
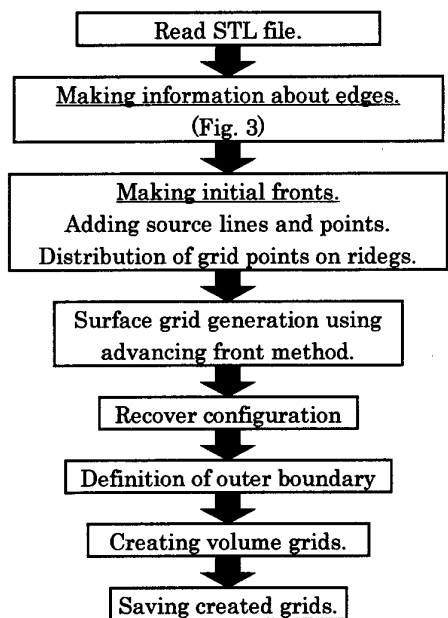

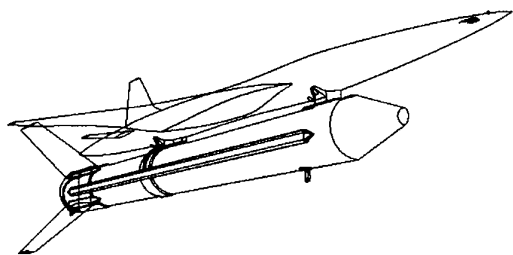Fig. 2 Flowchart of surface grid generation

Fig. 3 Reconstruction of geometric features

2. RESULT

The Euler equations were calculated using the unstructured grid solver [4]. The computed pressure distribution of this airplane with the rocket booster as well as the pressure contours on symmetrical boundary is shown in Fig. 4. The free stream Mach number is 1.05 and an angle of attack is zero. Computed pressure distribution at M_∞=2.0 are shown in Fig. 5. The Pitot tube ahead of the experimental airplane and the connecting fringes between airplane and rocket booster create shock waves. These shock waves influence on the pressure distributions on the airplane body and the rocket booster. The shock wave that generated at the node of booster reflects on the lower surface of the airplane.
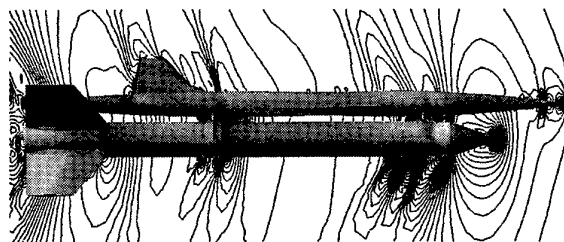

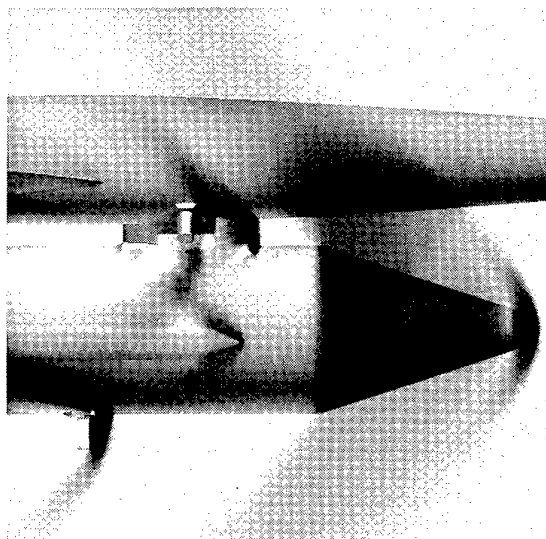Fig. 4 Computed pressure contours at M_∞= 1.05

Fig. 5 Computed pressure distribution at M_∞=2.0

In Fig. 6, the computed lift coefficients (C_L) are compared with the result of wind tunnel tests, obtained at the National Aerospace Laboratory of Japan. At Mach number 0.9 and 1.05, there are about 10% differences between the experimental and the computed results. This discrepancy is mainly due to the inability of the Euler computation for the shock-boundary layer interactions. The Navier-Stokes computation is necessary for the transonic regime. In the supersonic regime, the differences between the experiment and computation are less than 6%. The computed results show good agreements with wind tunnel results even with the inviscid flow assumptions. To check the grid dependency, the result obtained by a fine grid, which contains 1,016,074 node points, was also shown in the figure. There is not much difference between two grids, one contains 0.66 millions nodes and another has 1.02 millions nodes so that the grid of 0.66 million nodes is mostly fine enough to accurately simulate this flow field.
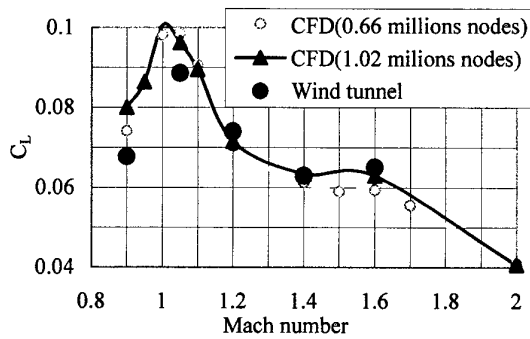
Fig. 6 Lift coefficients of wind tunnel test and CFD

In order to investigate the influences of the Pitot tube and the connecting fringes, a clean configuration where the small components were removed was prepared by CAD. The computed pressure contours of the clean configuration, corresponding to Fig. 4 of the fully detailed configuration, are shown in Fig. 7. The free stream Mach number is 1.05 and an angle of attack is zero. By comparing the computed pressure contours of Fig. 7 for the clean configuration with those shown in Fig. 4 for the detailed configuration, it is apparent that the shock wave formations are quite different in two results.
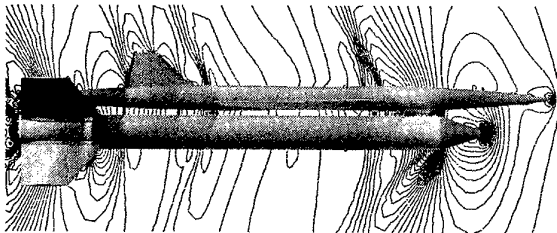

Fig. 7 Computed pressure contours of smooth

configuration at M_∞=1.05,α=0deg

The lift coefficients (C_L) and the drag coefficients (C_D) of the clean configuration were also compared with the detail configuration, as shown in Fig. 8 and Fig. 9. The difference of the lift coefficients between two results is about 50% in the transonic flow regime. Although the removed parts in the clean configuration are very small compared with the fuselages and the wings, but its effects on the lift coefficient is quite large. This reason is that a shock wave is generated upstream of rear connecting fringe and it significantly alters the pressure distribution on lower surface of main wing. Actually, Fig. 10 clearly shows a shock wave at lower surface of the main wing of the detail configuration. Pressure coefficient distributions which compares the detail configuration with the clean one around the main wing at section ① and ② are shown in Fig. 11. Pressure distribution is substantially changed by the shock wave occurred at the lower surface by the projections. This causes great difference of C_L in Fig. 8.
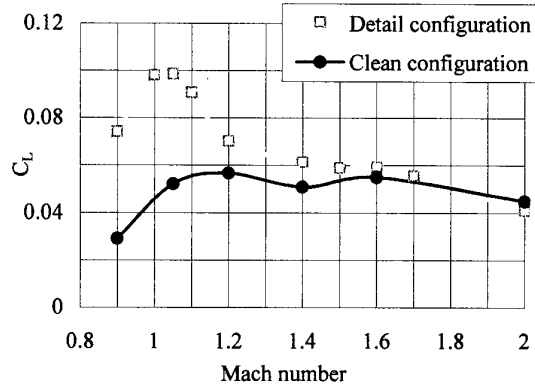

Fig. 8 Lift coefficient both detail and clean configurations

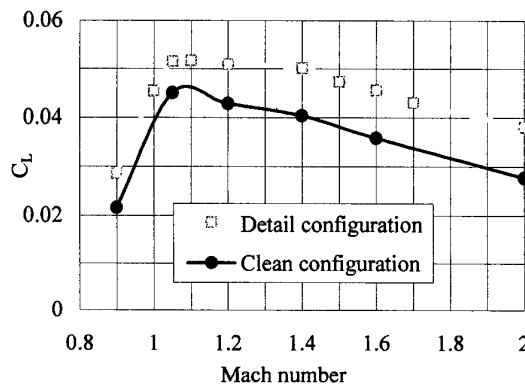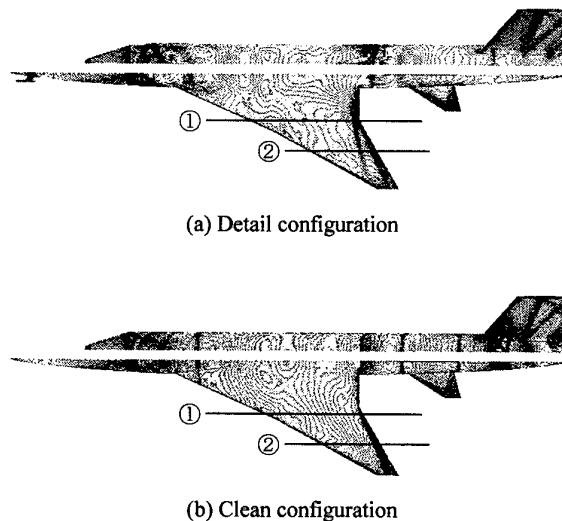
Fig. 9 Drag coefficient both detail and clean configurations

(a) Detail configuration

(b) Clean configuration

Fig. 10 Pressure contours on lower surface of experimental airplane and upper surface of booster at
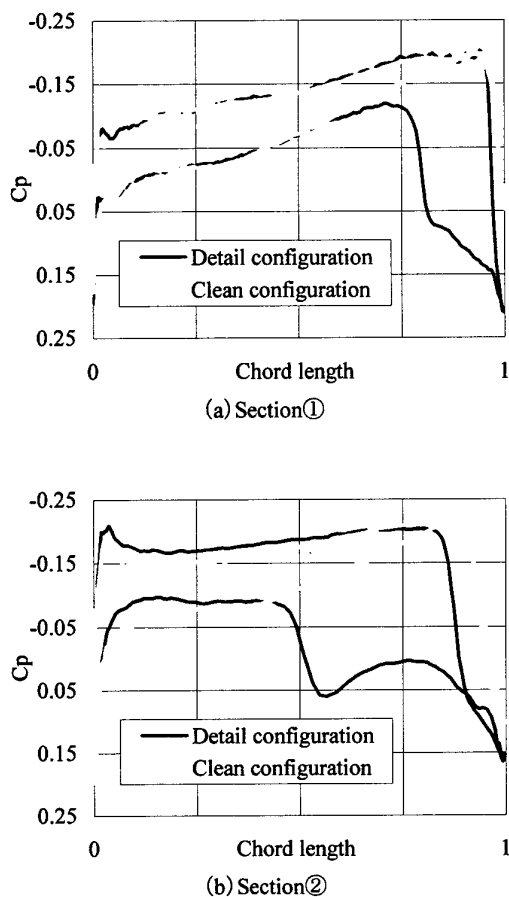
M_∞= **1.05**

(a) Section①

(b) Section②

Fig. 11 Cp distribution at main wing at M_∞=1.05

REFERENCE

[1] Iwamiya, T., "NAL SST Project and Aerodynamic Design of Experimental Aircraft," to be published in Proceedings of the 4th ECCOMAS Computational Fluid Dynamics Conference, Athens, John Wiley & Sons Ltd., Chichester, 1998, pp.580-585.

[2] Ito, Y., Nakahashi, K., "Direct Surface Triangulation Using Stereolithography (STL) Data," AIAA Paper 2000-0924, 2000

[3] Sharov, D. and Nakahashi, K., "A Boundary Recovery Algorithm for Delaunay Tetrahedral Meshing," 5th Int. Conf. On Numerical Grid Generation in Computational Field Simulation, 1996, pp.229-238.

[4] Sharov, D. and Nakahashi, K. "Reordering of Hybrid Unstructured Grids for Lower-Upper Symmetric Gauss-Seidel Computations", AIAA Journal, Vol.36, No.3, pp.484-486, 1998.

3. CONCLUSION

Aerodynamic coefficients of the NAL experimental airplane piggybacked on a solid rocket booster in ascent were numerically evaluated by solving the Euler equations, and compared with the wind tunnel results. The configuration was defined by CATIA, and the surface grid was generated directory on the CATIA defined surface using the STL output. The computed results show good agreements with wind tunnel results in lift and drag coefficients for the supersonic flow regime. The clean configuration, where small attachments were removed, was also calculated to investigate the effects of those small parts on the aerodynamic performance. The computed results showed significant change in the transonic lift coefficients. Small parts attached at the rocket booster generate shock waves on the lower surface of the airplane, resulting significant changes in pressure distribution on the wing. A combination of CAD-based modeling and the efficient surface meshing scheme allows the quick modification of the configurations to identify the effects of each small components.

2E12 AUTOMATED TARGET PRESSURE SPECIFICATION FOR INVERSE DESIGN METHOD OF AN AIRFOIL

Tjoetjoek Eko Pambagjo[*], Kazuhiro Nakahashi[**], Shigeru Obayashi[***]

Tohoku University, Sendai 980-8579-01, Japan

Key word : Wings and Airfoil Sections

ABSTRACT

This paper presents the process of target pressure specification for airfoil design with utilizing the Takanashi inverse design method. The target pressure distribution is constructed by using an empirical estimation approach. It is done automatically based on geometrical and flow constraint. To obtain better results in achieving the constraints, the target pressure distribution is modified iteratively during the design cycle.

The combination of the automated target pressure specification and Takanashi's inverse design method works successfully to design a thick airfoil in transonic flow.

1. Introduction

The problem of airfoil design has been existed since man started thinking about 'flying' until the present time. The design starts with required aerodynamic performances such as lift, drag and pitching moment at a certain flow condition. The airfoil design problem is solved by applying the direct method or the inverse method. In the direct method the airfoil design engineer work directly on the airfoil geometry. The geometry is modified and calculated and/or tested to obtain the aerodynamics performance. The process is repeated until the desired results are obtained.

Inverse design method has been used widely in many different areas. One area that extensively utilizes the inverse design method is the airfoil design. Several inverse design methods are available. The main problem of utilizing the inverse design method to design an airfoil is the construction of the target pressure distribution. Not only the target pressure should be achievable but the target should also include some geometric constraint such as thickness and leading edge radius.

In the inverse approach the solution process begins with designing a target pressure distribution based on the required aerodynamic performances. Figure 1 shows the general illustration of the inverse design process. One of the existing inverse algorithms is developed by Takanashi [1], which uses integrated transonic small perturbation equation to find the geometry correction corresponding to the difference between the target pressure distribution and the estimated pressure distribution of a given airfoil. The resulting equation is the mathematical model of the relation between the aerodynamic geometry and pressure distribution.

In general the inverse design process consist of two processes, which are independent to each other. One is the analysis process, which consists of grid generation and flow calculation, and the other is the design process itself. The flow simulation is the direct design in essence and any flow simulation can be utilized. With this arrangement the existing flow analysis can be utilized. When a new more powerful flow analysis becomes available then only the flow analysis part needs to be upgraded. It is also possibility to utilize wind tunnel as the flow analysis. The design part consists of the solution of the inverse problem and the smoothing algorithms as required.

The pressure difference between the initial and the target forms an input of the inversely formulated transonic small perturbation equation. The solution of the equation provides the geometry correction Δz , which is used to modify the initial geometry to form a new geometry. The flow solution of the new shape may be obtained by applying the Navier-Stokes equations. If the design requirements are not satisfied, the design cycle is repeated with the new geometry as the new initial geometry. The process is repeated until the pressure different is converged to certain criteria.
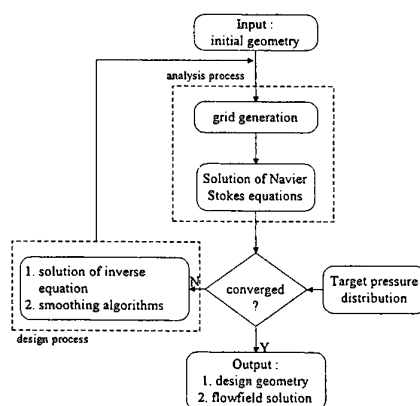
Figure 1. Schematic diagram of the inverse design process

The most common problem of utilizing the inverse design method as a design tool is the specification of the target pressure. The generation of the target pressure distribution is based on the required aerodynamic performance. However other discipline in aircraft design may pose additional requirements that are usually translated into geometry constraints such as the maximum thickness or local thickness.

In this paper the constrained target pressure specification described in reference [2] is applied to Takanashi's inverse design. Only for the maximum thickness is considered here. An airfoil of 18% thickness to chord will be designed by using this technique. Such thick airfoil is needed in Blended Wing Body (BWB) airplane design. The BWB configuration requires thick airfoil in the inboard wing where the passenger's cabin is located.

[*] Graduate Student, Department of Aeronautics and Space Engineering
[**] Professor, Department of Aeronautics and Space Engineering
[***] Associate Professor, Department of Aeronautics and Space Engineering

2. Target pressure generation

The target pressure can be generated to realize the required aerodynamic performance such as lift, drag and pitching moment. Here the lift and pitching moment coefficient can be estimated by simply integrating the pressure distribution. On other hand drag cannot be estimated precisely by a direct integration of the pressure distribution. At the present time only wave drag will be considered and it will be discussed briefly later in this section. The requirements from other discipline are usually converted into thickness requirements. An example is a thickness requirement for structural strength or a space requirement to carry enough fuel.

To translate the geometric constraint into pressure distribution, a method has been developed by Campbell [2]. To manipulate the pressure distribution during the design process, the pressure distribution is divided into several regions bounded by several control points. The location of the control points and their pressure levels are obtained by using two approaches, *empirical estimation approach* and *control point fitting approach*. To obtain better results in achieving the constraints, the target pressure distribution is modified iteratively during the design cycle.

Empirical Estimation Approach

The empirical estimation approach is used to design the initial target pressure distribution based on empirically derived equations with a global flow condition and geometric constraints as independent variables. Here the pressure distribution on each surface is divided in several region bounded by seven control points as shown in figure 2. The detail pressure distribution between the control points can be generated by analytical function. To reduce any slope discontinuity the pressure distribution near the control points are smoothed.
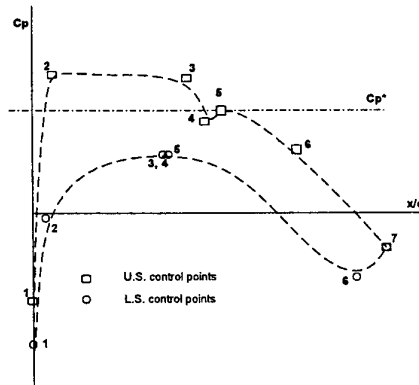

Figure 2. Control points to be used to generate target pressure

The method to estimate the location of the control points is summarized below.

Point 1

$$\left(x_1\right)_{lower} = 0.01\left(c_L + 4c_m\right)\sqrt{1 - M_\infty^2} \tag{1}$$

$$\left(C_{p,1}\right)_{lower} = C_{p,o} \approx 1 + 0.27 M_\infty^2 \tag{2}$$

$$\left(x_1\right)_{upper} = 0$$

$$\left(C_{p,1}\right)_{upper} = C_{p,o} - \left(c_L + 4c_m\right)\frac{0.015}{r_{le}} \tag{3}$$

When the control point locations of the lower and upper surface do not coincide, a straight line is used to connect those two points.

Point 2 and 3

The chordwise locations of point 2 are used to achieve the required leading edge radius constraints. The initial locations are defined by the following equations:

$$\left(x_2\right)_{upper} = 0.5t/c \tag{4}$$

$$\left(x_2\right)_{lower} = \left(x_2\right)_{upper} - 0.02 \tag{5}$$

For the same pressure level, blunter airfoil can be achieved by shifting the control point farther forward.

The initial level pressure of point 2 and 3 are obtained based on lift and thickness requirement

$$C_{p,2} \text{ or } C_{p,3} = C_{p,t} \pm C_{p,l} \tag{6}$$

where $C_{p,t}$ is the contribution from a thickness requirement given by:

$$C_{p,t} = \frac{At/c}{\sqrt{1 - M_\infty^2}} \quad \text{, where } A \text{ is set to } -3.3 \tag{7}$$

and the contribution from a lift requirement $C_{p,l}$ is given by:

$$C_{p,l} = -0.5c_L \tag{8}$$

In equation (6), the positive and negative sign are used for upper and lower surface respectively.

The third control point on each surface initially is located at $x=0.4$. However when shock is presence this point is moved to

$$x_3 = M_\infty^2 \tag{9}$$

The pressure coefficient at point 3 is obtained based on drag constraint, which is the wave drag. The wave drag can be estimated by using the relation

$$c_{D,w} = A_1\left(M_1 - 1\right)^4 \tag{10}$$

where the coefficient A_1 is given by:

$$A_1 = \frac{0.04}{\left(t/c\right)^{1.5}}$$

Based on the wave drag constraint, the maximum allowable shock Mach number (M_1) can be determined by using equation (10) and then it is converted to the minimum allowable pressure coefficient imposed at point 3.

Point 4 and 5

For a subcritical flow point 4 is coincident with point 3. For

supercritical flow the pressure coefficient is computed by using Rankine-Hugoniot equation. Base on the observation of of the results of the Navier-Stokes solver [3] used in this study, the chordwise location of point 4 is set at

$$x_4 = 1.045 M_\infty^2$$

The chordwise location of point 5 is located at $0.01c$ aft of point 4. The pressure coefficient is computed using equation (6) with the restriction that the value cannot be more negative than the sonic pressure coefficient.

Point 6 and 7

Control point 7 is located at the trailing edge with the pressure coefficient is set at

$$C_{p,7} = 2t/c$$

The control point 6 are obtained with different method depend on the pitching moment requirement. The chordwise location for both upper and lower surface are initially located at x=0.9. If the required c_m is less than –0.1 then the upper surface point is moved to midway between point 5 and point 7. The pressure coefficient is obtained by using equation (6). The thickness part is given by the relation :

$$C_{p,t,6} = C_{p,t} + \left(C_{p,7} - C_{p,t}\right)\frac{\bar{x}_6 - x_5}{\left(x_7 - x_5\right)^{0.7}}$$

where $\bar{x}_6$ is the average of the locations of the upper and lower control points, $C_{p,t}$ is the value from equation (7). The lift component at point 6 is obtained by the following equation :

$$C_{p,l,6} = C_{p,l}\frac{x_7 - \bar{x}_6}{x_7 - x_5}$$

where $C_{p,l}$ is obtained from equation (8).

This target pressure distribution may not meet the entire requirement. For example the required pitching moment coefficient may not be satisfied since this parameter is not used to determine the pressure level. Furthermore the lift coefficient may not meet the requirement. In Such case the pressure level at point 2 and 6 should be adjusted to meet the constraints.

Control Point Fitting Approach

An alternative approach to generate the target pressure is the control point fitting approach. This method is especially useful when the objective is to modify the existing airfoil to meet the constraint. In this method the control point position are obtained based on the pressure distribution of the original airfoil.

Control point 1 corresponding to the leading edge of the airfoil or to the stagnation point if it does not occur at the leading edge. Control point 2 corresponding to the end of the initial rapid acceleration defined as the point where $dC_p/dx \geq -10$ or where $x \geq 0.1$ whichever comes first. Control point 3 and 4 are arbitrarily located at x=0.3 unless shock is detected. When shock is detected the location of point 3 is moved to the beginning of adverse pressure gradient and point 4 is moved to the first point with subsonic local Mach

number. The shock wave is considered to be present when $dC_p/dx \geq 5$ in region of supersonic flow. Control point 5 is set at x=0.4 or at the analysis point past point 4, whichever further aft. Control point 6 is located at x=0.85.

The pressure coefficients at the control points are initially taken from the corresponding location of the original pressure distribution. These values are then moved to meet the constraint. The estimation of the new values uses the same method as in the empirical technique. The detail target pressure is specified by simply retaining the shape of the original airfoil distribution.

Although in most cases the initial control points can be generated automatically, in some cases manual adjustments may still be required. In addition the initial pressure distribution may need to be adjusted before it is used in the control point fitting approach. For example point 6 of the lower surface may need to be shifted to coincide with the maximum cove pressure on a supercritical airfoil.

Automated Target pressure specification

In order to meet the constraint more closely during the design process the target pressure distribution is modified based on the intermediate result as suggested in reference 2. Figure 3 shows the schematic diagram of this process. The pressure distribution is modified automatically, for example every 5 design cycle.

This method modified the pressure level as in the empirical estimation approach. The main different is that when modifying the target pressure, perturbation form of the equations is used instead of absolute relationships developed for target pressure generation. For example, the relationship between maximum airfoil thickness and the average pressure level at control point given in equation (7) becomes :

$$\Delta C_p = \frac{A\left(\Delta t/c\right)}{\sqrt{1 - M_\infty^2}}$$

where $\Delta t/c$ is the different between the desired thickness ratio and the current thickness ratio.
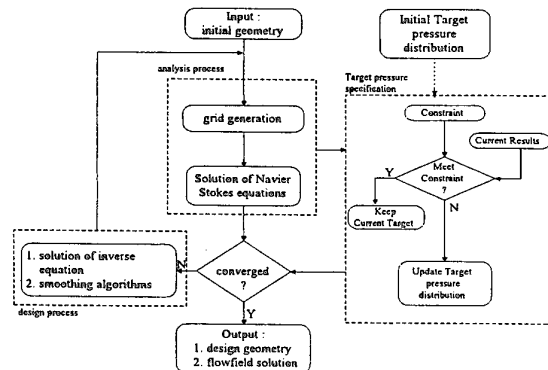

Figure 3. Schematic inverse design process with automated target pressure specification

3. Design Results

The goal of this study is to investigate the use of the target

pressure specification method described in above section to design a thick airfoil. The final target is to design an airfoil with thickness ratio of 18%. In this paper two cases are presented, the first is the design of a 12% thickness airfoil and the second is that of 18% thickness airfoil.

The flowfield solution is obtained by using the Navier-Stokes equations. The Navier-Stokes equations were solved using a C type mesh contains 161x93 grid points. The boundary layer on the airfoil was assumed to be fully turbulent and the Baldwin-Lomax turbulence model was used. The Navier-Stokes solver [3] adopted the LU-SGS method for the time integration and the right hand side was solved by 3rd order upwind scheme.

Case 1

The objective is to design an airfoil with a maximum thickness ratio of 12%. The aerodynamic constraints include a lift coefficient of 0.6, a pitching moment coefficient greater than –0.15 and wave drag coefficient less than 0.0005. The flow condition is at a free stream Mach number of 0.75, an angle of attack at 0 deg., and a Reynolds number of 10x10⁶.

The initial target pressure distribution is generated by utilizing the empirical estimation approach. After the design location of the shock wave is captured during the iteration, the control point fitting approach is employed. At this stage the target pressure is regenerated based on the intermediate pressure distribution. After the control points are obtained then the shape of the pressure distribution is used to regenerate the target pressure distribution between the control points.

From this stage after every five cycle the target pressure is modified to obtain a closer match to the constraints. The design result is a maximum thickness ratio of 12%, a lift coefficient of 0.6, a total drag coefficient of 0.0127 and a pitching moment coefficient of –0.1455. These results satisfy the specified constraints successfully.

Figure 4 shows the design result. The final target pressure is achieved except in the shock wave area.
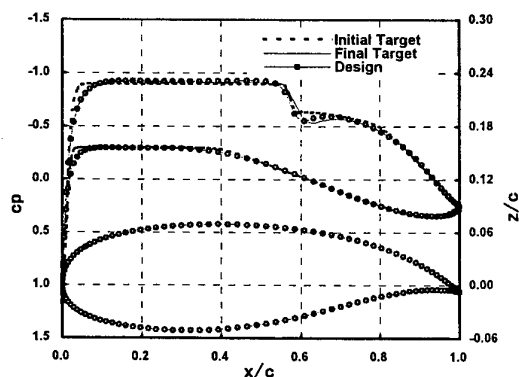

Figure 4. Design Airfoil shape and corresponding pressure distribution for case 1

Case 2

The objective of case 2 is to design a thicker airfoil. The desired maximum thickness ratio is 18% with aerodynamic constraints include a lift coefficient of 0.4, a pitching moment coefficient greater than –0.11. The flow condition is set at a free stream Mach number of 0.74, an angle of attack at 0 deg., and a Reynolds number of 10x10⁶. NACA 0012 is used as the initial geometry.

In this case the initial target pressure distribution is specified by utilizing the control point fitting approach. The initial airfoil is taken from NASA supercritical airfoil [4], NASA SC(2)-0518. Although this airfoil originally has a blunt trailing edge, for the brevity the airfoil is modified to have a sharp trailing edge. At the flow condition its aerodynamic properties are a lift coefficient of 0.38, a total drag coefficient of 0.0191 and a pitching moment coefficient of –0.1134.

After the target shock wave location is captured, the process is continued by utilizing the automated target generation. At the final design, the properties of design airfoil are a lift coefficient of 0.401, a total drag coefficient of 0.0148 and a pitching moment coefficient of –0.1089. The maximum thickness ratio is 18%. These properties indeed meet with both the flow and geometric constraints.

Figure 5 shows the design result. The design airfoil has more thickness in the aft portion and in leading edge area. Although in general the target pressure is achieved there is still small discrepancy in the shock area.
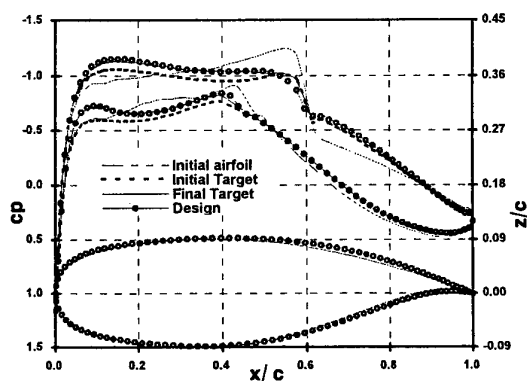

Figure 5. Designed Airfoil shape and corresponding pressure distribution for case 2

4. Conclusion

The target pressure specification method presented in reference [2] forms a very useful tool both to design an initial target pressure and to modify the existing one. The combination of the automated target pressure specification and Takanashi's inverse design method works successfully to design a thick airfoil in transonic flow. The drawback of the present approach is the slow convergence in supercritical flow. It requires more design iterations to capture the target shock location.

References

[1]. Susumu Takanashi, 'Iterative Three-Dimensional Transonic Wing Design Using Integral Equations', Journal of Aircraft, Vol. 22, No. 8, August 1985, pp. 655-660.

[2]. Richard L. Campbell, 'An Approach to Constrained Aerodynamic Design with Application to Airfoils', NASA TP-3260, November 1992.

[3]. Shigeru Obayashi and Guru P. Guruswamy, 'Convergence Acceleration of an Aeroelastic Navier-Stokes Solver', AIAA Paper 94-2268, 1994.

[4]. Charles D. Harris, 'NASA Supercritical Airfoil, *A Matrix of Family-Related Airfoils*, NASA TP-2969, March 1990.

2E13 Simulation of Wing Tip Vortices Using Vorticity Confinement on Unstructured Grid

Mitsuhiro MURAYAMA[*], Kazuhiro NAKAHASHI[**], and Shigeru OBAYASHI[***]

Tohoku University, Aoba 01, Sendai 980-8579, JAPAN

Key Words: Aircraft, Fluid Dynamics

ABSTRACT

This paper discusses the Vorticity Confinement method coupled with adaptive grid refinement method around vortex core on unstructured grid. The resulting method is applied to the numerical simulations of a wing tip vortex around a stationary NACA0012 wing to evaluate the capability of the present method. It has been shown that the adaptive refinement method and the vorticity confinement can keep the vorticity away from the numerical diffusion. The results obtained in this study show the possibility of accurate simulations of vortical flows by using unstructured grids and the vorticity confinement although the method has some problems about the dependency of the confinement parameter.

1. INTRODUCTION

Following recent development of CFD, demand for the accurate numerical simulations of flows at off-designed conditions with separations and vortices is growing. Analysis of such flow fields is very important in engineering. For example, the BVI (Blade-Vortex Interaction) problems and vibratory loading problems due to vortices impingement on helicopter rotor and aircraft fuselages must be solved for the improvement of the performance and safety. To deal with the congestion at airports accompanied with the rapid growth of the aviation, the strength of the wing-tip vortices during the take-off and landing must be estimated precisely.

However, the accuracy of CFD about the vortical flows is still not good enough. Although the grid near the body surface is very fine for the resolution of the boundary layer in the Navier-Stokes computations, the grid becomes rapidly coarser as it becomes far away from the body surface. There, the vortices are highly diffused due to the discretization. One way to minimize numerical dissipation of the vortices is to employ a highly dense grid. However, accurate numerical simulations of flows around 3-D complex bodies with large-scale separations and vortices are difficult within the realistic number of grid points. Instead, the adaptive grid method may be a promising approach to reduce the discretization error. We proposed an effective and efficient adaptive grid refinement method for the improvement of grid resolution around a vortex center using the vortex center identification method. The resulting method was applied to the flows around a delta wing and showed significant improvements of resolution of the leading-edge separation vortices [1]. However, further improvements will be needed to model the vortex rather than to refine the grid.

"Vorticity Confinement" has been proposed to reduce the diffusive property of the vortical flow simulations [2-4]. In the method, the source term added to the Navier-Stokes equations works as it convects the discretization error back into the vortex center and thus confine the vortex. The method is applied to incompressible flows, for example, flows around helicopter rotors with fuselage, and shows reasonable improvements [3]. However, the method is still needed to be tuned for the confinement parameter at a particular grid. In addition, Vorticity Confinement has been used on Cartesian grids or structured surface conforming grids, not on unstructured grids. Unstructured grids will be more suitable for the numerical simulation around 3-D highly complex bodies.

The objective of this paper is to develop the Vorticity Confinement method coupled with the unstructured grid method. The resulting method is applied to the numerical simulations of a wing tip vortex around a stationary NACA0012 wing to evaluate the capability of the present method.

2. VORTICITY CONFINEMENT

The general formulation of the Vorticity Confinement for unsteady incompressible flows can be expressed as follows [2]:

$$\nabla \cdot \vec{q} = 0 \tag{1}$$

$$\partial_t \vec{q} = -(\vec{q} \cdot \nabla)\vec{q} + \nabla(p/\rho) + \mu \nabla^2 \vec{q} - \varepsilon \vec{s} \tag{2}$$

where $\vec{q}$ is the velocity vector, p pressure, ρ density. ε is a numerical coefficient which controls the size of the convecting vortical regions. The simple expression of the Confinement term is

$$\vec{s} = \hat{n} \times \vec{\omega} \tag{3}$$

$$\hat{n} = \nabla\eta / |\nabla\eta| \tag{4}$$

where

$$\vec{\omega} = \nabla \times \vec{q} \tag{5}$$

$$\eta = |\vec{\omega}| \tag{6}$$

$\vec{\omega}$ is the vorticity vector.

Recently, this Vorticity Confinement method has been extended to compressible flows. In such attempts, there is a way to consider the Confinement as a body force which may be added to the integral momentum equation. The rate of the work done by the force is then added to the energy conservation law [4]. The integral conservation laws for mass, momentum and energy with Confinement term may be written as

$$\frac{\partial}{\partial t} \int_\Omega \mathbf{Q} dV + \oint_{\partial\Omega} (\mathbf{F(Q)} - \mathbf{G(Q)}) \cdot \mathbf{n} dS = \int_\Omega \mathbf{S} dV \tag{7}$$

where $\mathbf{Q} = [\rho, \rho u, \rho v, \rho w, e]^T$ is the vector of conservative variables; ρ is the density; u, v, w are the velocity components in the x, y, z directions; and e is the total energy. The vectors $\mathbf{F(Q)}$ and $\mathbf{G(Q)}$ represent the inviscid and viscous flux vectors and $\mathbf{n}$ is the outward normal of $\partial\Omega$ which is the boundary of the control volume Ω. $\mathbf{S}$ is the confinement term and can be written as

$$\mathbf{S} = \begin{pmatrix} 0 \\ \rho \mathbf{f}_b \cdot \hat{i} \\ \rho \mathbf{f}_b \cdot \hat{j} \\ \rho \mathbf{f}_b \cdot \hat{k} \\ \rho \mathbf{f}_b \cdot \mathbf{V} \end{pmatrix} \tag{8}$$

where $\mathbf{f}_b$ is a body force per unit mass. Now, this body force

[*] Graduate student, Department of Aeronautics and Space Engineering
[**] Professor, Department of Aeronautics and Space Engineering
[***] Associate Professor, Institute of Fluid Science

for the Confinement of the compressible flows is defined as

$$\mathbf{f}_b = -\varepsilon \hat{n} \times \vec{\omega} \tag{9}$$

where ε is a Confinement parameter and $\hat{n}$ is defined in Eq. (4).

Although Vorticity Confinement is extended to model a boundary layer, the confinement is limited to the wake regions here. The hybrid unstructured grid comprised of tetrahedral, prisms, and pyramids generated by the method described in Ref. [5] is used to compute the boundary layer near the body surface accurately and efficiently and the confinement is limited to the wake regions. The prismatic semi-structured grid is generated around viscous boundary surfaces and covers viscous regions while the tetrahedral grid covers the rest of the computational domain. Pyramid grid is used for the junction at prismatic and tetrahedral grids.

3. FLOW SOLVER

The equations (7) are solved by a finite volume cell-vertex scheme, where the control volume Ω_i at mesh i is a non-overlapped dual cell. With this control volume boundary, Eq. (7) can be written in an algebraic form as follows,

$$\frac{\partial \mathbf{Q}_i}{\partial t} = -\frac{1}{V_i}[\sum_{j(i)} \Delta S_{ij} \mathbf{h}(\mathbf{Q}_{ij}^+, \mathbf{Q}_{ij}^-, \mathbf{n}_{ij}) - \sum_{j(i)} \Delta S_{ij} \mathbf{G}(\mathbf{Q}_{ij}, \mathbf{n}_{ij})] + \mathbf{S}_i \tag{10}$$

where ΔS_{ij} is a segment area of the control volume boundary associated with the edge connecting points i and j. The term $\mathbf{h}$ is an inviscid numerical flux vector normal to the control volume boundary, and $\mathbf{Q}_{ij}^{\pm}$ are values on both sides of the control volume boundary. The subscript of summation, $j(i)$, refers to all node points connected to node i.

The Harten-Lax-van Leer-Einfeldt-Wada (HLLEW) Riemann solver [6] is used for the numerical flux computations. Second-order spatial accuracy is realized by a liner reconstruction of the primitive variables $\mathbf{q} = [\rho, u, v, w, p]^T$ inside the control volume, viz.,

$$\mathbf{q}(x, y, z) = \mathbf{q}_i + \Psi_i \nabla \mathbf{q}_i \cdot (\mathbf{r} - \mathbf{r}_i) \tag{11}$$

where $\mathbf{r}$ is a vector pointing to point (x, y, z); and i is the node number. The gradients associated with the control volume centroids are volume-averaged gradients computed using the value in the surrounding grid cells. A limiter, Ψ, is used to make the scheme monotone. Here Venkatakrishnan's limiter [7] is used because of its superior convergence properties.

To compute viscous stress and the heat flux terms in $\mathbf{G(Q)}$, spatial derivatives of the primitive variables at each control volume face are evaluated directly at the edges.

A one-equation turbulence model by Goldberg-Ramakrishnan (G-R)[8] was implemented to treat turbulent flows. This model does not involve wall distance explicitly so that it is of great benefit to unstructured grid method.

The lower-upper-symmetric Gauss-Seidel (LU-SGS) implicit method, originally developed for structured grid is applied in order to compute the high Reynolds number flows efficiently. The LU-SGS method on unstructured grid can be derived by splitting node points $j(i)$ into two groups, $j \in L(i)$, and $j \in U(i)$ for the first summation in LHS of Eq. (10). With $\Delta \mathbf{Q} = \Delta \mathbf{Q}^{n+1} - \Delta \mathbf{Q}^n$, the final form of the LU-SGS method for the unstructured grid becomes the following two sweeps:
Forward sweep:

$$\Delta \mathbf{Q}^* = \mathbf{D}^{-1}[\mathbf{R}_i - 0.5 \sum_{j \in L(i)} \Delta S_{ij}(\Delta \mathbf{h}_j^* - \rho_A \Delta \mathbf{Q}_j^*)] \tag{12a}$$

Backward sweep:

$$\Delta \mathbf{Q}_i = \Delta \mathbf{Q}_i^* - 0.5 \mathbf{D}^{-1} \sum_{j \in U(i)} \Delta S_{ij}(\Delta \mathbf{h}_j - \rho_A \Delta \mathbf{Q}_j) \tag{12b}$$

where $\Delta \mathbf{h} = \mathbf{h(Q + \Delta Q) - h(Q)}$, and

$$\mathbf{D} = (\frac{V_i}{\Delta t} + 0.5 \sum_{j(i)} \Delta S_{ij} \rho_A)\mathbf{I}, \tag{13}$$

$$\mathbf{R}_i = -\sum_{j(i)} \Delta S_{ij} \mathbf{h}_{ij}^* + \sum_{j(i)} \Delta S_{ij} \mathbf{G}_{ij}^n \tag{14}$$

The term $\mathbf{D}$ is diagonalized by the Jameson-Turkel approximation [9] of the Jacobian as $\mathbf{A}^{\pm} = 0.5(\mathbf{A} \pm \rho_\mathbf{A}\mathbf{I})$, where ρ_A is a spectral radius of Jacobian $\mathbf{A}$.

The lower/upper splitting of Eq. (12) for the unstructured grid is done by a grid reordering technique [10] that was developed to improve the convergence and the vectorization.

4. RESULTS

The geometry used in the present study is a NACA0012 rectangular wing of aspect ratio of 3. The axial direction coincides with the wing chord direction. The outer boundary is a sphere whose radius is 15-root chord length. Solutions were obtained at a freestream Mach number, $M_\infty = 0.12$. The Reynolds number based on the root chord is 0.9×10^6 at angle of attack of $10.0°$.

First, computation was performed on the grid shown in Fig. 1. The total number of the grid points is 614,095. Computed vorticity contours are shown in Fig. 2. In this case, the wing tip vortex disappeared rapidly because the grid away from the body surface becomes coarser.

Then the grid shown in Fig. 3, which has approximately homogeneous grid density in the wake region, was constructed by the division of the original grid. The total number of the grid points is 701,037. The vorticity contours obtained on this grid was shown in Fig. 4. Compared with the results on the initial coarse grid, the vorticity remains in some degree. However, the vortex is still diffused.

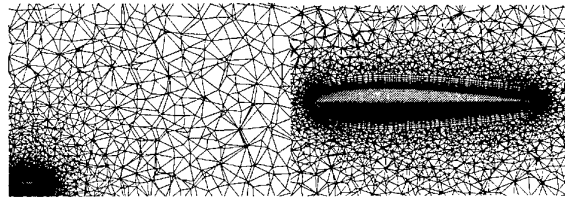(a) Wake region   (b) Close-up view
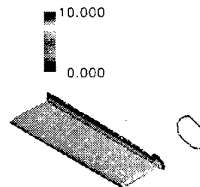Fig. 1. Computational grid at 95% semi-span (Coarse grid)

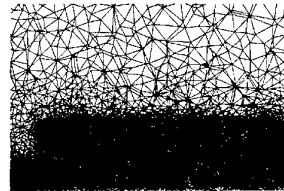Fig. 2. Vorticity contours at the coarse grid

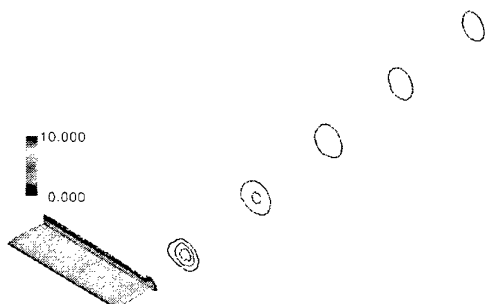Fig. 3. Computational grid at 95% semi-span (Fine grid)

Fig. 4. Vorticity contours at the fine grid

Adaptive grid refinement method using the vortex center for the concentration of the grid points around the vortex core to decrease the diffusion of the vorticity is applied to the fine grid. The grid is refined twice and the resulting number of grid points is 815,262. The results are shown in Figs. 5-7. The results show the improvement about the vorticity magnitude by the adaptive grid refinement. More grid refinement may improve the results, but from the limitation of the computational resources, the physical model to keep the vortices from diffusion may be required.
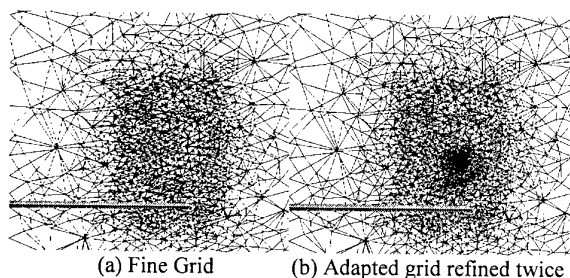

(a) Fine Grid   (b) Adapted grid refined twice
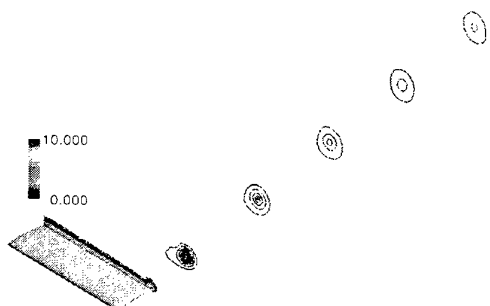Fig. 5. Cut views of the grid at x/c=5.0

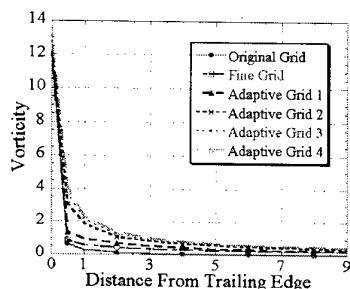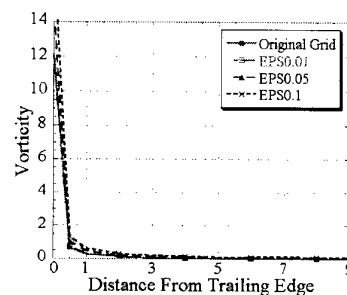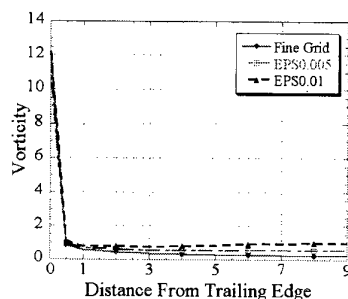Fig. 6. Vorticity contours at the adaptive grid refined twice

Fig. 7. The variation of the maximum vorticity magnitude around vortex center

Finally, the results using vorticity confinement are shown in

Fig. 8. The vorticity contours with vorticity confinement on the coarse grid are shown in Fig. 9. In the case of the coarse grid, the wing tip vortex highly diffused in spite of the vorticity confinement although a minor improvement can be seen over the initial result. While, the results on fine grid shown in Fig. 10 show more improvement although the overall level of the vorticity magnitude is still low. However, larger values of the confinement parameter ε lead to extra effects as shown in Fig. 10. Then the results on the adapted grid refined twice are shown in Fig. 11. It is apparent that the vorticity was confined and the method successfully decreased the numerical diffusion of the vorticity by the coupling of the adaptive grid refinement method and the vorticity confinement. The vorticity contours on a cut view at x/c=5 are shown in Fig. 12. In these figures, it can be seen that the vortex core position is not affected by the confinement and the vorticity is concentrated to the vortex core. However, the effect highly depends on the value of the confinement constant coefficient, ε and grid density. Moderate ε improves the results, while the large ε works extra correction. From these results, it can be seen that optimal ε which is different by the place and grid may be required.

(a) Coarse grid

(b) Fine grid
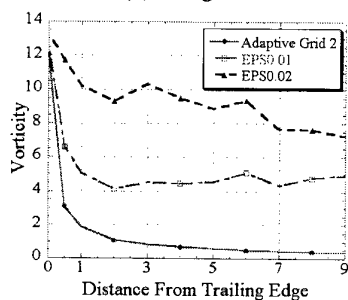
(c) Adapted grid refined twice
Fig. 8. The variation of the maximum vorticity magnitude around vortex center with vorticity confinement
(EPS : vorticity confinement parameter ε)

ε =0.1

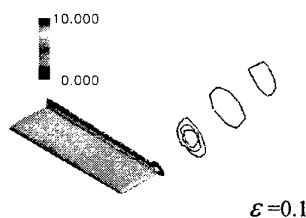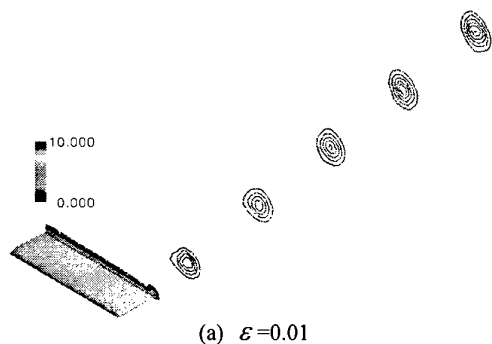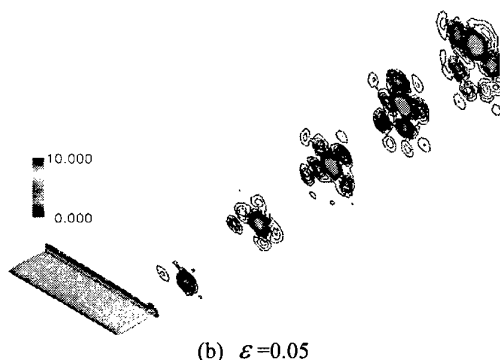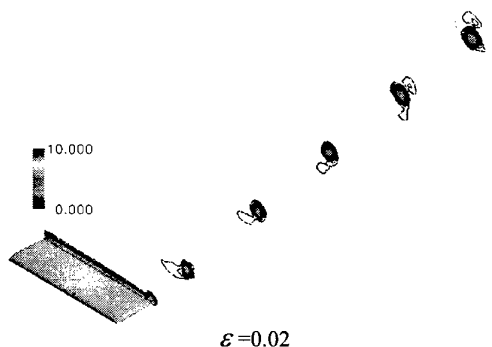Fig. 9. Vorticity contours at the coarse grid with vorticity
confinement

(a) ε =0.01

(b) ε =0.05

Fig. 10. Vorticity contours at the fine grid with vorticity
confinement

ε =0.02

Fig. 11. Vorticity contours at the adaptive grid refined twice with
vorticity confinement

(a) Without confinement　(b) With confinement ε =0.02

Fig. 12. Vorticity contours in the cross flow plane at x/c=5.0 of
the adaptive grid refined twice

5. CONCLUSION

The Vorticity Confinement method coupled with adaptive grid refinement method around vortex core was applied to the numerical simulations of the wing tip vortices on the unstructured grid. It has been shown that the adaptive refinement method and the vorticity confinement can keep the vorticity away from the numerical diffusion. The results obtained in this study show the possibility of accurate simulations of vortical flows by using unstructured grids and the vorticity confinement. However, the results highly depend on the value of the confinement constant coefficient, ε. Further study will be needed for the vortex confinement.

REFERENCE

[1] Murayama, M., Nakahashi, K., and Sawada, K., "Numerical Simulation of Vortex Breakdown Using Adaptive Grid Refinement with Vortex-Center Identification," AIAA Paper 2000-0806, 2000.

[2] Steinhoff, J. and Underhill, D., "Modification of the Euler Equations for "Vorticity Confinement": Application to the computation of interacting vortex rings," *Physics of Fluids*, Vol. 6, 1994, pp.2738-2744.

[3] Steinhoff, J., Yonghu, W., and Lesong, W., "Efficient Computation of Separating High Reynolds Number Incompressible Flows Using Vorticity Confinement," AIAA Paper 99-3316, 1999.

[4] Hu, G. and Grossman, B., "A Numerical Method for Vortex Confinement in Compressible Flow," AIAA Paper 2000-0281, 2000.

[5] Sharov, D. and Nakahashi, K., "Hybrid Prismatic/Tetrahedral Grid Generation for Viscous Flow Applications," *AIAA J.*, Vol. 36, No.2, pp.157-162, 1998.

[6] Obayashi, S. and Guruswamy, G. P., "Convergence Acceleration of an Aeroelastic Navier-Stokes Solver," AIAA Paper 94-2268, 1994.

[7] Venkatakrishnan, V., "On the Accuracy of Limiters and Convergence to Steady State Solutions," AIAA Paper 93-0880, 1993.

[8] Goldberg, U. C. and Ramakrishnan, S. V., "A Pointwise Version of Baldwin-Barth Turbulence Model," *Comp. Fluid Dyn.*, Vol. 1, 1993, pp.321-338.

[9] Jameson, A. and Turkel, E., "Implicit Schemes and LU Decompositions," *Mathematics of Computation*, Vol. 37, No. 156, 1981, pp.385-397.

[10] Sharov, D. and Nakahashi, K., "Reordering of 3-D Hybrid Unstructured Grids for Lower-Upper Symmetric Gauss-Seidel Computations," *AIAA J.* Vol. 36, No. 3, 1998, pp.484-486.

2E14   VORTICAL FLOWS PAST CAMBERED FLYING DISKS

Yuichiro Goto[†], Riho Hiramoto[‡], Hiroshi Higuchi[*] and Ingo Meisel[§]

Institute of Fluid Science

Tohoku University

Sendai, Japan

Key Words: Fluid Dynamics, Aerodynamics, Boundary Layers

ABSTRACT

Experimental investigations on the vortical flows past spin-stabilized cambered flying disks are carried out in a low-speed wind tunnel. Using flow visualization techniques, detailed flow characteristics depicting the trailing vortices, boundary layer separation and wake structure are obtained. Effects of disk geometry, attack angle and disk rotation on trailing vortices are studied. Results indicate that the effect of rotation on the vortex wake is negligible at high angles of attack, but the effect of the rotation and disk geometry can be observed as a downwash enhancement at low lifting condition. In particular, the rotation influences boundary layer transition and separation on smooth upper surface. Trailing vortex formation and wake unsteadiness are found to depend on the edge and other cross sectional geometry.

1. INTRODUCTION

A disk flying at a moderate angle of attack may be regarded as a conventional wing with a small aspect ratio. While its lift slope is lower than with a higher aspect ratio wing, a disk-wing can produce a monotonically increasing lift coefficient at extremely high angle of attack. An aircraft with a circular wing was developed in the past, as in the XF5U or more recently for "Micro Air Vehicles." However, not enough information is available as to the boundary layer behavior, wake structure or trailing-vortex formation process.

Other applications of a flying disk are related to sports aerodynamics and are accompanied by spin stabilization. Ganslen[1] obtained lift and drag coefficients for the discus. Soong[2] and Frohlich[3] analyzed the flight trajectories by integrating the translational and rotational equations of motions with given aerodynamic data on the lift and drag.

Cambered disks have been popular as a commercial product. There have been some smoke flow visualization studies at low speeds[4,5] and force measurements[6]

on a recreational flying disk. While the lift measurements did not show clear effect of the disk rotation, the low speed smoke visualization indicated asymmetric tip vortices with disk rotation. Present authors have initiated experimental work to survey the flowfield over and behind the flying disk. In their previous work recently presented[7], it is shown that the rotation suppresses trailing boundary layer separation over a disk model at low angles of attack, by keeping laminar boundary layer on receding side and triggering early transition on advancing side, and both flows lead to increasing downwash. In this study, a more detailed investigation on the flow field, particularly focusing on effect of various disk geometries, is carried out. Our goal is to clarify the mechanism of lift generation and formation of the trailing vortices from spinning surface as well as the resultant curved trajectory of rotating flying disk from a point of view of flight dynamics. The present study may help provide interpretation regarding this commonly seen flying object. Furthermore, this basic study aims to provide insight into possible engineering applications to practical flight vehicles.

2. EXPERIMENT

Commercially available flying disks and a flat disk were used in the experiment. The cross sections of the models are shown in Fig. 1. Unlike a discus used for athletic competitions, these recreational disks are cambered with a rim for finger grip. The diameter of the disks, free stream velocity and Reynolds numbers based on the diameter are also indicated. The flat disk model used for comparison (Fig. 5(e)) is 5 mm thick and the edge is rounded with 2.5 mm radius.

The models are mounted at the center on a thin rod. A DC motor at the base provides the desired rotational speed in either direction. The non-dimensional rotation speed Ω is the ratio of the edge velocity normalized by the free stream velocity. Clockwise rotation viewed from the top is defined as the positive Ω. The open test sections are used where the width of the octagonal nozzle exit measures 0.81 m. Most of the measurements are made with the free stream velocity 8 m/s. The nominal test speed and disk angle of attack are selected based on

---

(a) Model A (D=0.210m, , Re=1.1x10⁵)

(b) Model B (D=0.210m, Re=1.1x10⁵)

(c) Model C (D=0.248m, Re=1.3x10⁵)

(d) Model D (D=0.242m, Re=1.3x10⁵)

(e) Flat disk (D=0.120m, Re=8.0x10⁴)
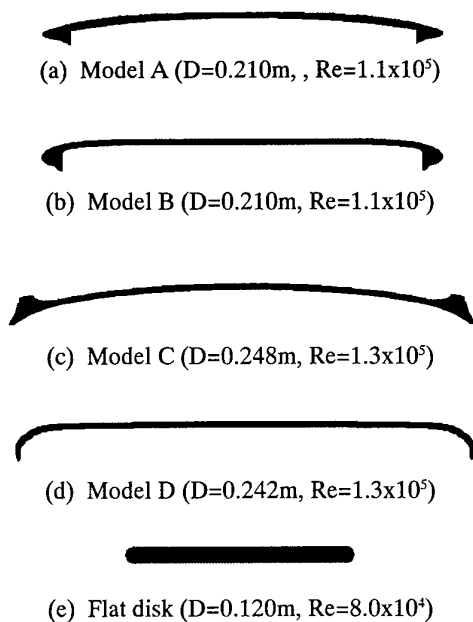
Fig. 1 Cross sections of the flying disks
(a-d) U=8.0m/s, (e) U=10.0m/s

(a) Model A

(b) Model B

(c) Model C

Fig. 2 Top views, $\alpha=15°$, $\Omega=0.8$

(a) x/D=1.0   (b) x/D=5.4

Fig. 3 Vortex roll-up (model A), $\alpha=15°$, $\Omega=0.8$

throw tests and ease of experimentation.

Flow visualizations are conducted with a smoke wire technique illuminated by a laser sheet. The flow motions are recorded on a SONY TRV-900 3CCD digital camcorder. Cartesian coordinate system is employed, where the origin is located at the top center of the disk with x-axis in the free stream direction, y and z in the vertical and z in the transverse directions, respectively.

3. RESULTS AND DISCUSSION

The overall flow fields past models A, B and C at the angle of attack, $\alpha=15°$ and the non-dimensional rotation speed, $\Omega=0.8$ are shown in Fig. 2 (a), (b) and (c), respectively. Further results including PIV measurements on model A have been reported in detail in Ref. 7. Smoke wire is placed horizontally upstream of the model. The height of the wire was adjusted so that smoke lines reach the stagnation point at the leading edge in each case during the present experiment.

Model C has a sharp lip on the upper surface, causing the shear layer to separate over the upper surface. In Fig. 2(c), smoke lines showing inside edges of vortex paths seem to remain more in the free stream direction compared to those over model A and B (see Fig. 2(a) and (b).) In case of model C, trailing vortices appear to be less influenced by the rotating disk surface due to separation at the leading edge (see Fig. 1(c)). In Fig. 2(b), periodic structure in the wake, either with shear layer instability or vortex shedding, can be seen starting from just behind of the trailing edge between paths of the trailing vortices. The periodic structure behind this model was seen better with rotation rather than without (not shown). This may be due to the more blunt, rounded

trailing edge. The wake of the model D was substantially more irregular than other cases. The difference in the wake appearance behind different models is yet to be clarified. Furthermore, one must take into account the phenomenon within the circular cavity on pressure side or just appearance of smoke due to small change of smoke paths by the rotation as observed in previous work[7].

Figures 3 show the rolled-up vortex pair behind model A at downstream stations (x/D=1.0 and 5.4) illuminated by a laser sheet normal to the flow. Length scales are taken arbitrarily in the figures. A difference in brightness between two vortex cores in Fig. 3(b) is caused by small change of smoke path due to rotation instead of asymmetry of vortex strength itself[7].
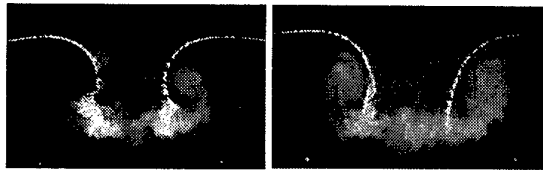
(a) Model B   (b) Model C

Fig. 4 Vortex roll-up, $\alpha=15°$, $\Omega=0.8$, x/D=1.0

Figures 4 show the rolled-up vortex pair behind models B and C at x/D=1.0. The trailing vortices and horizontal wake shear layer as well as arched dotted smoke lines behind model C are different from those behind model A (Fig. 3(a)) and model B (Fig. 4(a).) For example, the trailing vortices are further apart, and less interaction with the wake shear layer is seen. The arched smoke lines in Fig. 4(b) reach the shear layer almost vertically consistent with the sharp boundary between trailing vortices and the flow behind the trailing edge in Fig. 2(c). Further downstream (not shown), difference of vortex wakes among the models became smaller. (To be exact, comparison should have been made keeping the lift coefficient constant, rather than the geometric angles of attack.) No asymmetry of vortex wake due to the rotation was recognized in the conditions.

As reported earlier on the model A[7], the effect of disk rotation at high angle of attack is found to be small for other models, and the effect of modified boundary layer on the trailing vortices is also expected to be stronger at more moderate attack angle. Therefore, the angle of attack is set to $\alpha=0°$. Visualizations in earlier works[4,5] were also carried out at $\alpha=0°$. Figure 5 shows a top view of model A with $\alpha=0°$ and with rotation. Comparison with that without rotation (not shown) revealed that the flow appears to separate from the upper surface near the trailing edge without rotation, but separation is suppressed with rotation. The behavior of the boundary layer is further investigated. As seen in the streamwise cross section in Fig. 6(a), the boundary layer remains laminar without rotation and separates near the trailing edge. On the advancing side, in Fig. 6(b), the boundary layer goes through transition and the separation is suppressed. On the other hand, boundary layer on the receding side in Fig. 6(c) is laminar and yet remains attached up to the trailing edge. Due to the suppression of the separation, flow follows the disk surface and the downwash is increased. Asymmetric transition of the flow is caused by the different velocity gradient between the advancing and receding sides. The effect of the rotation is shown in Figs. 7 and 8. Because of the unsteady shear layer, end view images are ensemble-averaged in order to make trend obvious in Figs. 7. Asymmetry due to the rotation is not observed from the figures.

Figure 9 shows top view of model B with $\alpha=0°$ under rotation. In the figure, smoke is more concentrated on the receding side and diffused on the advancing side. The effect of rotation influencing on asymmetry is observed in Figs. 10. A lump of smoke near the center
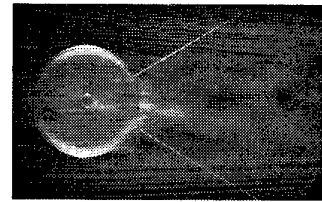
Fig. 5 Top view (model A), $\alpha=0°$, $\Omega=0.8$

(a) Without rotation
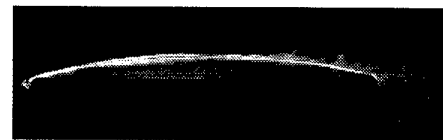
(b) Advancing side

(c) Receding side

Fig. 6 Boundary layer (model A); cross sectional side views, $\alpha=0°$, z/D=0.33
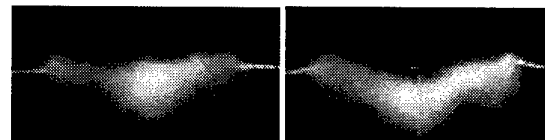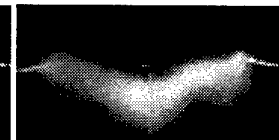
(a) $\Omega=0$ (b) $\Omega=0.8$

Fig. 7 Averaged end views (model A), $\alpha=0°$, x/D=1.0
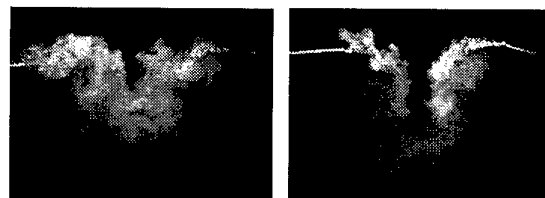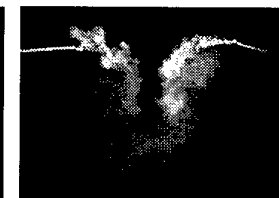
(a) $\Omega=0$ (b) $\Omega =0.8$

Fig. 8 End views (model A), $\alpha=0°$, x/D=5.4

region of the shear layer deflects slightly toward advancing side. The effect of the rotation is also seen further downstream as shown in Fig. 11 though the flow are both nearly symmetric.

Figure 12 shows top view of model C with $\alpha=0°$ and with rotation. In the figure, added circulation in the horizontal plane is recognizable, i.e. the flow on the receding side (upper side in the figure) deflects toward

Fig. 9 Top view (model B), α=0°, Ω=0.8

(a) Ω=0.8   (b) Ω=-0.8

Fig. 10 Averaged end views (model B), α=0°,
x/D=1.0

(a) Ω=0   (b) Ω=0.8

Fig. 11 End views (model B), α=0°, x/D=5.7

Fig. 12 Top view (model C), α=0°, Ω=0.8

(a) x/D=1.0   (b) x/D=4.8

Fig. 13 End views (model C), α=0°, Ω=0.8

(a) Model D: α=5°, Ω=0.8,   (b) Model E: Re=8.0x10⁴,
x/D=1.0   α=10°, Ω=0.75, x/D=1.5

Fig. 14 End views behind model D and E

4. CONCLUSION

Detailed flow visualization study was conducted to clarify the effect of geometries and rotation of flying disks. Various regions of the flow field such as the boundary layer above the rotating disk, the wake trailing vortex roll-up and surface flow were investigated and some mechanisms of enhancement of trailing vortices were discussed.

REFERENCES

[1]Ganslen, R. V., "Aerodynamic and Mechanical Forces in Discus Flight," The Athletic Journal, 44, 1964.
[2]Soong, T.-C., "The Dynamics of Discus Throw," J. App. Mech. Pp. 531-536, 1976.
[3]Frohlich, C., "Aerodynamic Effects on Discus Flight," Am. J. Phys., Vol. 49, No. 12, pp. 1125-1132, 1981.
[4]Nakamura, Y. and Fukamachi, N., "Visualization of the Flow past a Frisbee," Fluid Dyn, Res., Vol. 7, pp. 31-35, 1976.
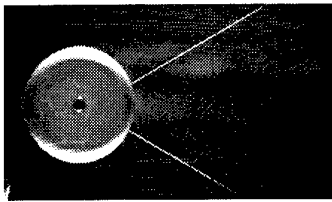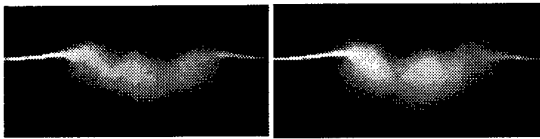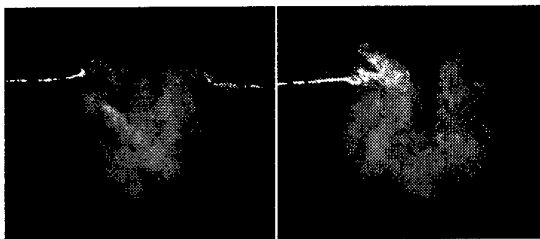[5]Asai, M. and Yamamoto, M., "Frisbee-The Flow about a Frisbee," J. Japan Soc. Fluid Mech., Vol. 17, No. 1, 1998 (in Japanese).
[6]Yasuda, K., "Flight- and Aerodynamic Characteristics of a Flying Disk," J. Soc. Aero. Space Sci., Vol. 47, No. 547, pp. 16-22. 1999 (in Japanese).
[7]Higuchi, H., Goto, Y., Hiramoto, R. and Meisel, I., "Rotating Flying Disks and Formation of Trailing Vortices," AIAA Paper 2000-4001, Applied Aerodynamics Conference, June 2000.
[8]Meisel, I., "Struktur der Umstromung einer angestellten Scheibe," Diplomarbeit, Universitat Karlsruhe, 2000

advancing side, as in so-called Magnus effect. Figures 13 show the end views at x/D=1.0 and 4.8. In spite of the effect of the rotation mentioned above, no other signs of asymmetry are observed in the wake. The smoke pattern showing downwash in Fig. 13(b) is similar to those of the other models with rotation (see Fig. 8(b) and Fig. 11(b)). In the throw tests, the flight behavior of the disk model C was found to be stable and somewhat insensitive to the throw conditions, likely due to fixed separation lines independent of the boundary layer flow.

Model D is perhaps of most popular design. Figure 14(a) shows the flow behind model D with moderate attack angle, α=5° and with rotation. The position of the shear layer on the receding side seems lower than that on the advancing side with rotation, but ensemble averaged image (not shown) did not reveal any difference of positions of trailing vortices.

Figure 14(b) shows end view of flat disk model at α=10° with rotation. No effect of rotation is observed from the visualizations. The topology of the flow on the flat disk model without rotation[8] was investigated in detail using oil dots flow method on a highly polished disk surface. The results will be discussed at conference.

As for the flight dynamics of the rotating cambered disk, important factors would be the moments due to possible asymmetric lift distribution and gyroscopic effect induced by the forward center of pressure. A numerical simulation of the flow around flying disk has been initiated.
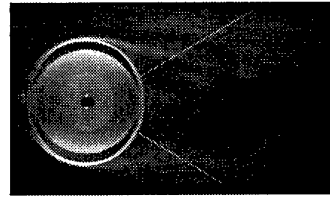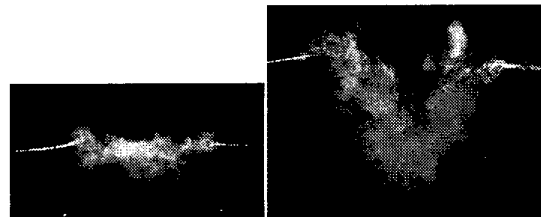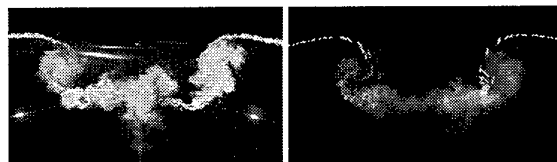
IL3 A MULTIDISCIPLINARY OPTIMIZATION METHOD FOR DESIGNING BOUNDARY LAYER INGESTING INLETS

David L. Rodriguez*

Dept. of Aero./Astro., Stanford University, Stanford, CA

Key Words:Aerodynamics, Boundary Layers

1. Abstract

The Blended-Wing-Body is a conceptual aircraft design with rear-mounted, over-wing engines. Two types of installations have been considered for this aircraft: partially buried engines with boundary layer ingesting inlets and the more conventional podded engines with pylons. For both designs, the tight coupling between the aircraft aerodynamics and the propulsion system poses a difficult design integration problem. This paper presents a design method that approaches the problem using multidisciplinary optimization. A Navier-Stokes flow solver, an engine analysis method, and a nonlinear optimizer are combined into a design tool that correctly addresses the tight coupling of the problem. Results from optimization runs on the podded installation are presented.

2. List of Symbols

α	aircraft angle of attack
C_D	drag coefficient
C_L	lift coefficient
C_M	pitching moment coefficient
η_r	inlet pressure recovery
$\dot{m}$	air flow rate
$\dot{m}_a$	required engine air flow rate
$\dot{m}_a^*$	predicted engine air flow rate
$\dot{m}_f$	fuel burn rate
$\dot{m}_{ff}$	air flow rate through fan-face
P_t	total pressure
P_{t_∞}	freestream total pressure
T	required engine thrust
X	geometric design variables

3. Background

Boundary layer ingestion (BLI) by a propulsion system is a design concept that can improve propulsive efficiency. Ingesting the low momentum flow in the boundary layer reduces the ram drag. This concept is currently being considered for the Blended-Wing-Body (BWB), a large passenger transport configuration (Figure 1) currently being developed by Boeing, NASA, and several universities including Stanford. The BWB airframe and propulsion system are more tightly coupled than the same systems on a conventional aircraft. Hence, conventional design methods are unable to properly integrate these systems and fail to fully exploit the advantages of BLI. This lack of an effective propulsion integration method has been the primary motivation for a current

---

* Research Assistant, Aircraft Aerodynamics and Design Group, Member AIAA.
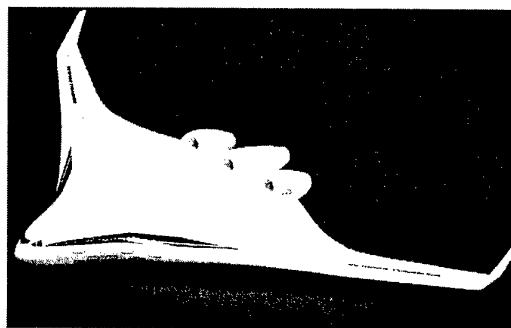
Figure 1: BWB conceptual design.

research project at Stanford. Aerodynamic and propulsion system analysis methods are coupled with a nonlinear optimizer creating a more effective tool for designing an inlet/airframe configuration that incorporates the BLI concept.

Podding the engines and installing then on over-wing pylons is the other type of installation being considered for the BWB design. For comparison and to determine the benefits (if any) of BLI, the design tool can be applied to the podded engine design as well. The problem is essentially the same since the coupling between the aerodynamic and propulsion systems still exists. The podded engine design also presents a less complex test for the inlet design tool due to the lack of separated flow usually present in a boundary layer ingesting inlet.

4. Method

The method described here has already been presented in References 1 and 2. However, for completeness the method is again described in this section. Note that although the motivation for the development of this inlet design method are the BLI inlets on the BWB, this method can be effectively applied to a more conventional podded engine design. The examples presented in the results section are in fact on a podded nacelle design.

A BLI inlet exhibits a strong coupling between the airframe aerodynamics and the propulsion system. The more low-momentum flow the inlet ingests, the lower the aerodynamic drag on the airframe and the lower the thrust requirement on the propulsion system. On the other hand, ingesting this boundary layer flow also reduces the inlet pressure recovery which reduces propulsive efficiency. An effective design method must be able to address this trade-off between aerodynamic and propulsive efficiencies and hence must be multidisciplinary in approach. The design method developed for this work addresses this coupling by integrating three basic tools: an aerodynamics analysis method, a propulsion system simulator, and a nonlinear optimizer. Brief descriptions of these tools and the integration techniques follow.

The aerodynamics method currently being used is an advanced Navier-Stokes method. CFL3D[3] is a cell-centered, finite volume code developed at NASA-Langley. It uses a third-order, upwind-biased spatial discretization for the convective and pressure terms

and a central-difference scheme for the shear stress and heat transfer terms. An implicit scheme is used for time-advancement. The code is extremely versatile with its large selection of turbulence models and ability to handle multiblock, patched, embedded, and overlapping grids. This versatility along with its popularity and validated accuracy were the primary reasons for selecting this code for the design tool. The turbulence model that was used for all computations discussed in this paper is the one-equation Spalart-Allmaras[4] model. This model was chosen for its simplicity and its applicability to the multiblock grids necessary to analyze a complex configuration such as the BWB with nacelles installed. For the inlet design tool, CFL3D provides predictions of aerodynamic forces (lift, drag, and moment) along with the necessary fan face properties (predicted air flow rate and inlet pressure recovery).

The propulsion system simulator is an engine analysis code developed at NASA-Lewis. The NEPP[5] code allows for 1D, steady-state, thermodynamic analysis of gas turbine engines. The design specifications of each engine component (such as the fan, turbine, burner, and inlet) are specified by the user allowing design and off-design analyses of the engine. The NEPP code was chosen for its speed, ability to handle off-design conditions, and wide usage in industry and government research. For the inlet design tool, the engine simulator takes the required thrust and inlet pressure recovery provided by the aerodynamics analysis and computes the fuel burn rate and the required inlet air flow rate.

The BWB engines studied in this work are advanced ducted propellers (ADP). While the bypass ratio (BPR) of the engine has not been finalized, the range of bypass ratios being studied is wide; BPR's as large as 22 have been considered. However, for the work presented here, the bypass ratio (and actually the whole engine design) was held constant at 12. Varying the engine design would require including weight in the optimization problem and weight must be assumed constant for the method of this paper to produce reasonable results.

NPSOL[6] is a gradient-based, constrained, nonlinear optimizer developed at Stanford University. An advanced quasi-Newton algorithm is implemented where each major iteration involves the solution of a quadratic subproblem based on the current objective function value, gradient, and Hessian approximation. Constraints can be linear or nonlinear. The NPSOL optimizer was chosen for its robust ability to handle nonlinear problems.

These three tools have been integrated into a multidisciplinary design tool. The basic architecture of this design tool is depicted in Figure 2. Taking computed information from the aerodynamics and propulsion analyses, the optimizer uses a set

of user-specified design variables to minimize an objective function. For all the work discussed in this paper, this objective function is the engine fuel burn rate. The set of design variables usually includes geometric variables to modify the inlet/airframe shape, the angle of attack to control the total lift of the airframe, and an inlet back pressure level to ensure air flow compatibility between the engine analysis and the flow solver.

This air flow compatibility between the engine analysis and the flow solver is critical to the design methodology. The inlet air flow rate predicted by the flow solver must be the same as the required air flow rate that is computed by the engine analysis to make the problem consistent. This compatibility constraint can be satisfied by using the predicted air flow rate as a design variable. The flow solver can use this predicted air flow rate as an input and modify the corresponding boundary condition to attain this rate. As it minimizes the objective function, the optimizer modifies the value of the predicted air flow rate to ensure that it is equal to the required air flow rate computed by the engine analysis code. However, in practice the design variable used for this compatibility constraint is not the predicted air flow rate but rather a back pressure level.

The boundary condition used in the flow solver to control the air flow rate through the inlet is the standard "engine-outflow" type. At the boundary, the static pressure is specified and the values of the other flow variables are extrapolated from inside the flowfield. In order to obtain a specific flow rate, this back pressure must be determined iteratively which is extremely inefficient computationally. By using the back pressure value itself as the design variable, this iterative process is eliminated and the optimizer has direct control of the boundary condition. As before, the back pressure is modified to ensure the air flow compatibility constraint is satisfied as the objective function is minimized.

As shown in Figure 2, the design variables are passed from the optimizer to the flow solver. After modifying the inlet/airframe shape and the computational grid accordingly, the flow solver computes values for required aircraft thrust and inlet pressure recovery. These values are passed to the engine simulator where the fuel burn rate and required air flow rate are computed. These values are then in turn passed back to the optimizer. The lift and moment coefficients along with the predicted air flow rate are also passed back to the optimizer. The optimizer uses these computed values to determine a new set of design variables by trying to minimize the objective function and satisfy the constraints. The process repeats until an optimal solution is found.

Several nonlinear constraints are necessary to complete the problem. First of all, the lift of the aircraft is constrained be equal to the cruise lift coefficient. To trim the aircraft, a pitching moment constraint must also be introduced. As discussed earlier, the air flow compatibility constraint is necessary. Geometric constraints on the wing and nacelle (such as those necessary due to the aircraft structural design) manifest themselves as a set of linear constraints on the geometric design variables used in the problem.

Force Computation

Normally the force computation process with a CFD method is straightforward: integrate the pressure and skin friction forces on all solid walls. However, for the case with an engine, the correct method is not so clear. Accurately analyzing the flow within the engine is obviously not an option due to its complexity and therefore the engine must modeled. The typical way of modeling the engine is to introduce a flow exit-plane in the inlet and a flow
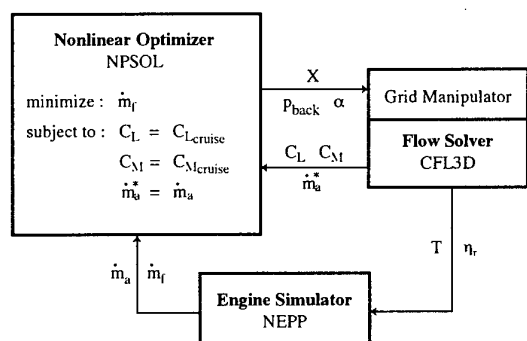
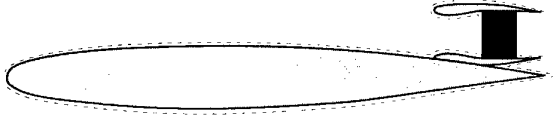Figure 2: Inlet design tool architecture.

Figure 3: Control volume used to compute forces on an airframe/inlet configuration.

entrance-plane at the engine exhaust region. This engine modeling is represented in Figure 3. Special boundary conditions are applied at the engine entrance and exit to control the properties of the flow through these planes. Computing forces on this configuration is not straightforward due to the fact that some flow exits the computational domain at the fan face and some flow enters at the engine exit plane; but it is still possible. Consider the control volume shown in Figure 3 which includes all the solid surfaces and the engine fan-face and exhaust planes. To compute the total force acting on this control volume, the pressure, shear forces, *and* momentum flux at the control volume boundaries must be integrated. Note that the momentum flux through the solid walls is zero and the shear forces (which are parallel to the control volume boundary) on the fan-face and engine exhaust planes are negligible.

For steady, unaccelerated cruise flight, the integration of these forces on this control volume should be zero. However, in the inlet design method, the engine simulator must be supplied with a gross thrust to balance the drag and thrust in the design problem. To compute the gross thrust of the engine using the CFD method, the force due to the flow entering the computational domain at the engine exit plane must be determined. This means the momentum flux and pressure must be integrated on this boundary face. Since the total force integration is zero, the force acting on all solid surfaces and the fan face is equal (except in sign) to the gross thrust and is the total drag (including any ram drag) of the aircraft. Therefore, the gross thrust requirement of the engine can also be computed by integrating the pressure and skin friction on all solid surfaces and the pressure and momentum on the fan-face.

Computation of Fan-face Total Pressure Recovery

The method of computing pressure recovery is an issue of much debate. The propulsion analysis method requires a single value that represents the total pressure losses at the fan face. Since the total pressure can vary over the fan-face area, the only solution is some sort of integrated quantity. When the total pressure distribution is not constant over the fan face, the correct integration scheme is not obvious. Many methods exist including area integration, mass flow integration, momentum integration, and even various forms of energy integration. All these methods can give very different results for a fan face with a widely varying total pressure distribution, like that found in a BLI inlet for example. The method chosen for this inlet design method is based on the work by Livesey[7]. This integration method computes pressure recovery by assuming a constant entropy flux and weighting the integration appropriately:

$$\eta_r = \frac{1}{P_{t_\infty}} \exp\left(\frac{1}{\dot{m}_{ff}} \int_{\text{fan face}} \left(\ln P_t \right) d\dot{m} \right) \quad (1)$$

Note that momentum is *not* conserved with this method. While other methods which do conserve momentum exist, these methods either do not conserve other important properties (such

Figure 4: Three-view of baseline podded BWB design.

as mass flow rate) or involve some sort of conservative mixing process which reduces the total energy of the flow. While it is still unclear whether the method of Equation 1 is the correct method (if there even *is* a correct method), Livesey provides some argument for selecting this method. This integrated quantity is therefore the value of pressure recovery that is sent to the engine simulator in the inlet design method. Note that the issue of a widely varying total pressure distribution is not as much of a problem for the podded nacelle case since the air ingested is predominantly uniform. However, the integration method of Equation 1 is included in the method so that future BLI inlet optimization work can be performed.

5. The Design Problem

Ultimately, the inlet design method will be applied to both the podded nacelle and BLI inlet designs of the BWB. At the time of publication of this paper, only the podded design problem was successfully completed. The BLI inlet design is underway but no results are available. The results from the podded nacelle design are presented here showing that the inlet design method is also applicable to a more conventional type of inlet design.

Configuration Definition

As detailed in Reference 8, the original BWB design had BLI inlets. However to determine the true advantages of the BLI installation, a podded installation must also be studied as a baseline for comparison. Using the baseline wing of Reference 8, a podded configuration was identified. The inlet design method was then applied to this configuration. Since no flow separation is present in the inlets of the podded design, this provided a less challenging test problem for the method before the more challenging BLI inlet design is attempted.

The baseline podded configuration is shown in Figure 4 in 3-view format. The pylons were designed to have a reasonable thickness and are symmetric. The engines are canted at 5° angle of attack from the wing reference plane and have no cant in the yaw direction. The thickness and in particular the radius of curvature of the inlets were selected using conventional design methods.

Some views of the computational grid used for the optimization work on this configuration are given in Figure 5. The computational grid was created by removing a block of a baseline wing grid and inserting nacelle grids. The interfaces between the wing and nacelle grids are not point-match and therefore the patching algorithm included in CFL3D was used for boundary conditions. The total number of points in this grid is just over
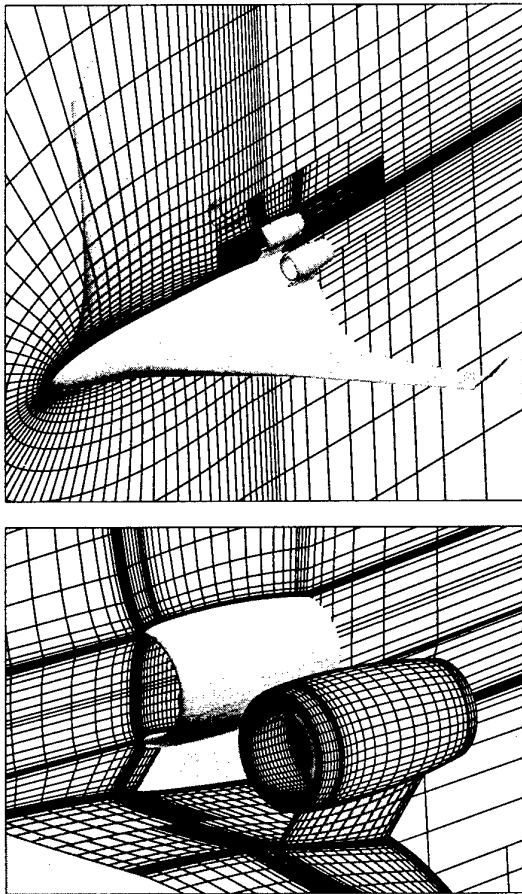
Figure 5: Views of computational grid used for BWB podded inlet installation.

Variable	Type	Location
1	angle of attack	entire aircraft
2	inlet back pressure	centerline engine fan-face
3	inlet back pressure	outboard engine(s) fan-face
4	linear wing twist	outboard wing section
5	inlet length	centerline nacelle
6-7	inlet/nacelle camber	centerline nacelle
8	pylon height	centerline nacelle/pylon
9	nacelle pitch	centerline nacelle
10	inlet length	outboard nacelle
11-14	inlet/nacelle camber	outboard nacelle
15	pylon height	outboard nacelle/pylon
16	nacelle pitch	outboard nacelle
17	nacelle yaw	outboard nacelle/pylon
18	pylon camber	outboard pylon

Table I: Design variables used in podded BWB optimization.

476,000. Obviously this is a very coarse grid for such a complex configuration. But to keep computation times reasonably low, optimization was performed on this grid.

Objective Function and Constraints

The objective function for this optimization case is the fuel-burn rate. This objective will allow the inlet design method to optimally integrate the propulsion system and the airframe inasmuch as the design variables will permit. The aircraft weight is assumed constant. The lift and air flow compatibility constraints are necessarily enforced in this problem. Of course, in this case, there are two air flow compatibility constraints since there are two engines. Also included in this case is a constraint which makes certain the pitching moment does not become lower than -0.17, based on the pitching moment of the baseline wing alone design. Ideally this pitching moment should be 0.0 meaning the aircraft is properly trimmed. However, the baseline wing design used in this example has a high node-down pitching moment which could not be corrected without major redesign work. Therefore instead of trimming the aircraft which would result in a large drag penalty, the pitching moment constraint makes certain the pitching moment does not get any worse in the inlet integration process. Also, constraints on the nacelle thickness and inlet leading edge radius were not necessary since no thickness design variables were included in this problem.

Design Variables

Ideally, a large number of design variables (~30-50) would be used to optimize complex geometry like the podded BWB. However, to make computation times manageable in a research atmosphere, only 18 were selected and are listed in Table I. The angle of attack and inlet back pressure variables are necessary to help enforce the lift and air flow compatibility constraints. A wing twist variable (washout) was also added to help enforce the pitching moment constraint. The variable adds a linear twist variation to the outboard section of the wing which is effective in controlling the pitching moment of a swept wing. Only the outboard wing twist is affected so that the cabin section is not warped.

The remaining variables control the shape and orientation of the nacelles themselves. These include the inlet length, inlet camber (which controls the inlet area distribution and outer shape of the nacelle), the nacelle pitch and yaw, the pylon height, and the pylon camber. Note that no thickness variables were included. Since the baseline nacelles were designed to have the minimum thickness and inlet lip radius, thickness variables were deemed mostly ineffective for this case. This may not be entirely true since thickness variables would allow for the control of inlet area distribution and the outer nacelle contours, which are important for controlling the shock strength and location on the nacelle outer surface. However, computation time limits forced the

omission of these variables.

To demonstrate the geometric changes induced by the geometric design variables (4-18), each variable was perturbed separately and the resulting geometries shown in Figure 6. The perturbations are slightly exaggerated for clarity. The inlet length variables simply scale the nacelle length. It simply moves the inlet leading edge forward or backward and stretches or compresses the nacelle surface accordingly. The camber variables are based on cosine functions that range over a specified circumferential angle. The magnitude of the perturbation peaks at the center of the range and fades to zero at the edges of the range. The pylon height variable scales the pylon so that the sweep of the pylon remains constant. The nacelle pitch and yaw variables pivot the entire nacelle around a specified point. The pylon camber variable applies a sine function to the camber of the outboard pylon.

Results and Discussion

Two cases were completed on the BWB podded design. The first case, which included only the first three design variables, was completed to provide a true baseline value and to analyze the cruise performance of the baseline geometry. The second case includes all the variables and provides the optimal configuration shape (limited by the design space spanned by the design variables). These two cases are presented here and compared.

Analysis of Baseline Podded BWB Design

Only the first three design variables (angle of attack and two back pressures) are included in this case. Likewise, only the lift and air flow compatibility constraints are included in this problem. This optimization is performed to determine the performance of the baseline podded BWB configuration at cruise conditions which will provide a baseline for comparison once the optimization with all design variables is completed. The constraints were satisfied very quickly (3 design steps). More results from this baseline run are presented in the comparison figures in the next section. The performance of this baseline configuration is summarized in Table II.

Optimization of Podded Baseline BWB Design

The 18 design variables of Table I were used to minimize the fuel-burn rate of the baseline podded BWB configuration subject to the lift, moment, and air flow compatibility constraints. The final results are compared to the baseline results of Section in Table II. The optimization history is given in Figure 9. With the 18 design variables, the inlet design method was able to reduce the fuel-burn rate by almost 10%. This performance improvement was entirely due to the reduction in drag of over 23 counts since the pressure recovery of both inlets actually increased.

A comparison of the baseline and optimized geometries is given in Figure 7. The major difference is the height of the centerline pylon. The optimizer has moved the nacelles as far apart as possible with the selected design variables to relieve the shocks that form in the channel. The reduction of shock strength is better illustrated the pressure contour plots in Figure 8. The channel between nacelles is clearly a major source of drag and therefore the optimizer did what it could to improve the flowfield in this region. Since the spanwise location of the nacelles was held fixed due to engine-out performance constraints, the best the optimizer could do was raise the centerline nacelle as high as possible and still not violate the moment constraint. The centerline nacelle was raised higher than the outboard nacelles because then only one pylon's wetted area would increase where if the outboard nacelles were raised higher, two pylons' wetted areas
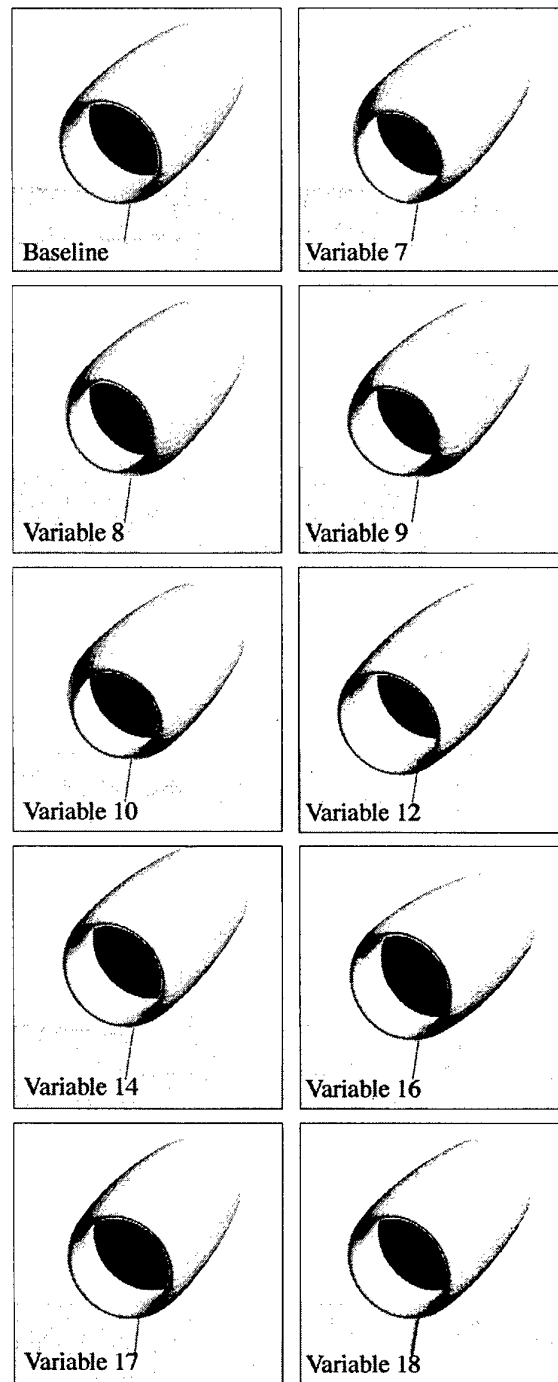
Figure 6: Effects of perturbed design variables on podded BWB geometry.

would increase. Of course, the structural weight of the pylon may be the true limiting factor in the pylon height, but since structural analysis was included in the method at this point, the pylon weight penalty was not addressed.

The pressure contours (Figure 8) also show that the pressure gradients in the vicinity of the inlets have been reduced. The nacelle yaw, pitch, and inlet camber have been tailored to allow the flow to be ingested cleanly and therefore with minimal drag

penalties. The yaw of the outboard nacelles has also been increased to further alleviate the shock strengths in the channel. This could cause problems in the engine-out flight condition
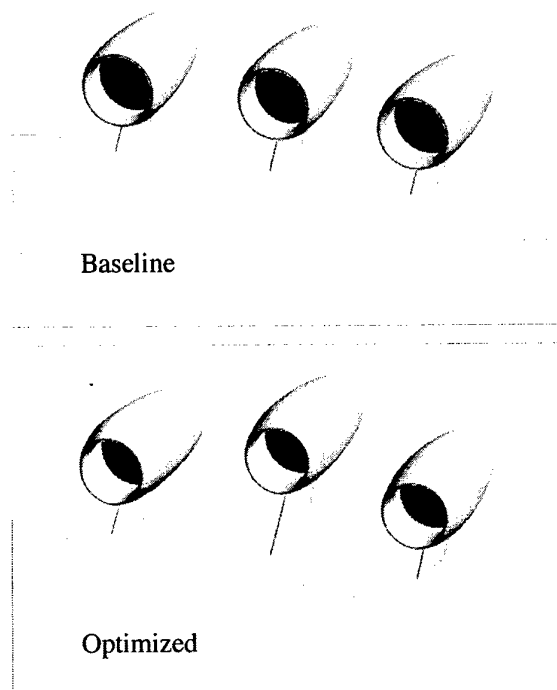
Figure 7: Comparison of baseline and optimized podded BWB configurations.
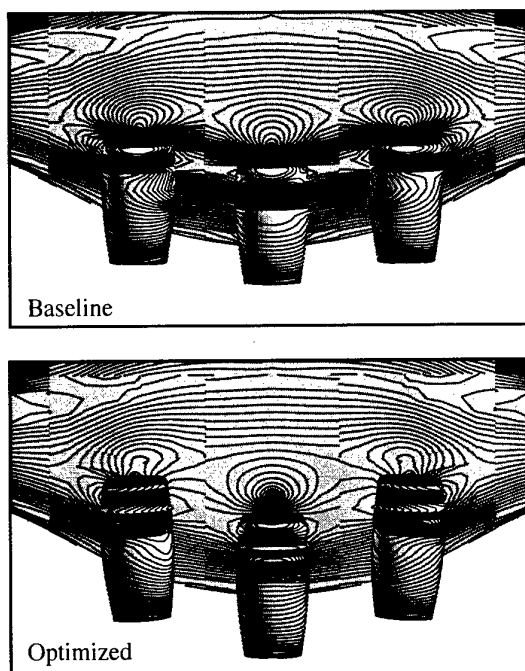
Figure 8: Pressure contours on the baseline and optimized podded BWB configurations.

Performance Parameter	Baseline	Optimized
Fuel Burn Rate (lb/hr)	32467	29336
Lift Coefficient	0.5000	0.5000
Pitching Moment Coefficient	-0.1676	-0.1700
Drag Coefficient	0.03074	0.02842
Centerline Engine Mass Flow Error	0.0000	0.0000
Centerline Engine Inlet Pressure Recovery	0.9963	0.9920
Outboard Engine Mass Flow Error	0.0000	0.0000
Outboard Engine Inlet Pressure Recovery	0.9957	0.9926

Table II: Performance comparison of baseline and optimized podded BWB configuration.

since the moment are of the outboard nacelle has been increased. Further design work may have to include a yaw constraint to address this.

6. Conclusions

An inlet design method has been developed by integrating a Navier-Stokes flow solver, an engine simulator, and a nonlinear optimizer. This multidisciplinary design method correctly addresses the coupling between the propulsion system and the airframe. The method was applied to a podded nacelle BWB configuration but is also appropriate for a BLI inlet design. The method proved to be effective for the podded case in improving the design by significantly reducing the selected objective function and still satisfying all necessary constraints. The complex variable method for computing the necessary gradients proved to be very successful and efficient for practical use. The method has successfully identified the baseline spacing between the nacelles is a major source of drag.

7. Future Work

The next step is to apply this method to a BLI configuration like that shown in Figure 1. This should prove to be a more challenging problem because of the almost certain presence of separation in the inlets. However, if successful, the method should reduce this separation since it is a source of poor pressure recovery and drag. One other constraint which must be included in the BLI case is a distortion constraint. Engine companies require that inlets provide at most a specified level of distortion and BLI inlets are notorious for violating this limit. By including distortion as a constraint in the optimization problem, the inlet design method should be able to reduce if not eliminate the violation of this distortion limit.

8. Acknowledgments

9. References

1. Rodriguez, D.L. and Kroo, I.M., "A 2D Multidisciplinary Design Method for Boundary Layer Ingesting Inlets," AIAA 99-0838, 1999.
2. Rodriguez, D.L., "A 3D Multidisciplinary Design Method for Boundary Layer Ingesting Inlets," AIAA 2000-0424, 2000.
3. Rumsey, C., Sanetrik, M., Biedron, R., Melson, N., and Parlette, E., "Efficiency and Accuracy of Time-Accurate Turbulent Navier-Stokes Computations," *Computers & Fluids*, Vol. 25, No. 2, pp. 217-236, 1996.
4. Spalart, P. and Allmaras, S., "A One-Equation Turbulence Model for Aerodynamic Flows," AIAA 92-0439, 1992.
5. Klann, J. and Snyder, C., *NEPP Programmer's Manual*, NASA TM 106575, 1994.
6. Gill, P.E., Murray, W., Saunders, M.A., Wright, M.H., "User's Guide For NPSOL 5.0: A Fortran Package for Nonlinear Programming," TR SOL 94, Stanford University, 1994.
7. Livesey, J.L., "Flow Property Averaging Methods for Compressible Internal Flows," AIAA 82-0135, 1982.
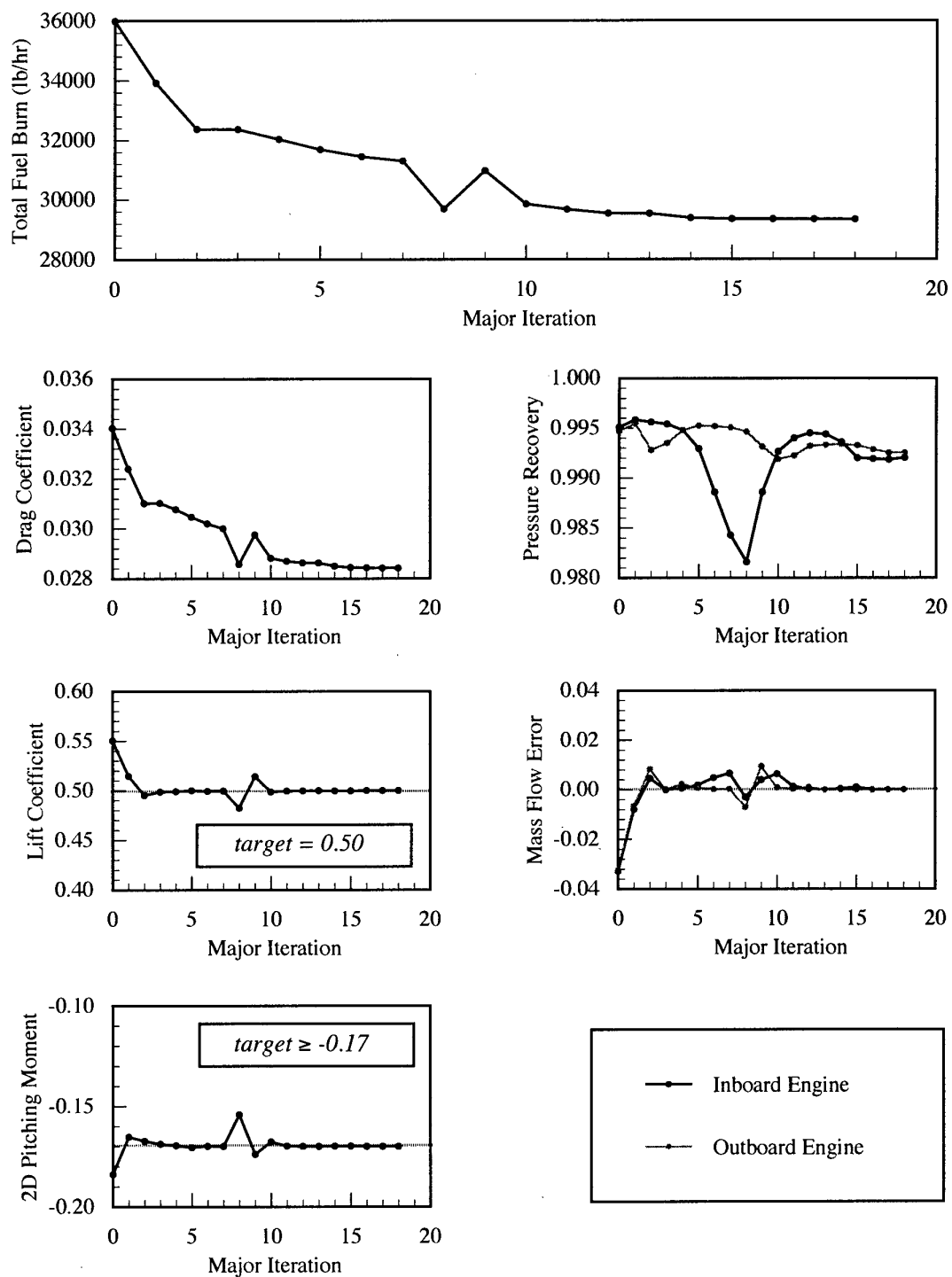8. McDonnell Douglas Aerospace, "Blended-Wing-Body Configuration Control Document (CCD-2)," January 1996.

Figure 9: Optimization history of 18 design variable podded BWB run.

3E2　Deployment of a Beam in Plane Motion of a Body

Sang-Won Kim* and Ji-Hwan Kim**

Seoul National University
Shinrim-Dong, Gwanak-Ku, Seoul, 151-742, Korea

Key Words　:　Deployment

Abstract

Present work deals with a study on the deployment of a cantilever beam with translation and rotational motions, which is restricted in a plane. The equations of motion are derived with respect to non-Cartesian coordinate system. In the formulation of equations, geometrically non-linear effect and shear deformations are included. An assumed mode method is applied, and numerical convergence characteristics are studied, also. Types of motion are classified as 'slow' or 'fast' deployment and rotation of beam. In addition, the effect of translational motion of a body is studied, and the dynamic characteristics for the behavior of the beam are investigated.

Introduction

Spacecraft or satellites are composed of various flexible sub-structures to be deployed in space. In addition, new type of materials has been developed to allow the weight reduction, and the large deformation should be included in modeling and analysis of the structures. It is exemplified as antenna, stabilizing boom, solar array, large truss-type structures, and so on. Flexible space structures can be modeled by the beams, plates and shells. Especially, large space structures can be analyzed as the combination of beams, and they should be considered that the large deformation including the effect of rigid-body motions due to translation and rotation of the body. Simo and Vu Quoc[1,2] considered the geometrically non-linear effect in the formulation of equations for beam undergoing large overall motions. These works were performed by Kane and Ryan[3], Haering et al.[4,5]. They considered large overall motion of support with the centrifugal effect as well as the translational motion. Ryan[6] proposed to extend previous research works for the satellite in three-dimensional space without any restriction for the motion of main body.

Research works for the dynamic analysis of beam with varying length can be summarized as follows. Tabarrok et al. [7] tried to obtain an analytical solution for the deflection of axially moving beam with a constant speed. Downer and Park [8] suggested a finite element model for the analysis of beam in deployment. In this work, dynamics of axially moving highly flexible beam were deeply investigated. The number of finite elements nodes remained fixed, and the finite element length was allowed to vary. Yuh and Young [9] considered a rotational motion of axially moving beam. Assumed mode method was used to obtain the numerical results, and the results were compared with the experimental data. Yüksel and Gürgoze [10], Gürgoze and Yüksel [11] investigated the rotational motion of

the robot arm, and tried to model the robot arm as the axially moving beam. In addition, deflection of the robot arm was studied with the inclusion of concentrated mass at the tip. It was also studied that the effect of axially moving velocity of the beam. Stylianou and Tabarrok[12,13] solved an axially moving beam problem by using the finite element method in which the elements were functions of time. Fung et al.[14] derived the governing equations and boundary conditions for an axially moving beam with a tip mass. It was indicated that rigid-body motion and flexible vibration were non-linearly coupled. On the other hand, Huang et al. [15] studied the dynamic stability of a cantilever beam attached to a translational / rotational base in two dimensional space.

In the present study, the deployment of beam is to be analyzed. The main body is assumed to have a perfect rigidity, and the beam can be moved in a plane with translation and rotation. In addition, the beam is assumed to include the stretching effect as well as the geometrically non-linear effect. Non-Cartesian curvilinear coordinate systems are used in the formulation of the equations of motion. An assumed mode method is used in the numerical analysis, and convergence study for the results are performed for typical examples.

Equations of Motion
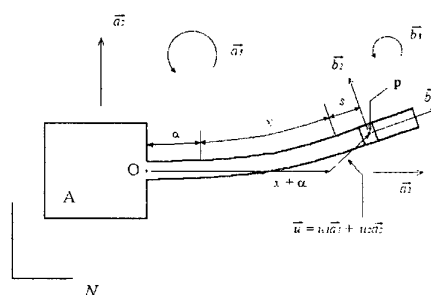
Fig. 1 Deployment of a Beam in 2 - Dimensional Space

Fig. 1 shows a schematic diagram for a deployment of flexible beam from a rigid body A. The beam is defined in the Newtonian reference frame N, and unit vectors a_1 and a_2 are attached to a body A. In the present study, non-Cartesian coordinate x is used to indicate the location of the material point, and s denotes the arc-length of stretch of the material

* Research Assistant, School of Mechanical and Aerospace Engineering
** Associate Professor, School of Mechanical and Aerospace Engineering

point at x. We will consider the geometrically non-linear effects as well as shear deformations. Unit vectors $\mathbf{a}_1$ and $\mathbf{a}_2$ are defined at the arbitrary point of the beam. Additionally, α denotes the deployment of beam, $\mathbf{u}_1$ and $\mathbf{u}_2$ indicate the orthogonal component in the direction of $\mathbf{a}_1$ and $\mathbf{a}_2$. For the convenience in the formulation of the equations of motion for the deployment, the cross sectional geometric properties are assumed to be symmetry with respect to width b of the beam.

Inertial velocity of the point o, and angular velocity of A in N is given by,

$$^{N}\mathbf{v}^{O} = v_1\mathbf{a}_1 + v_2\mathbf{a}_2 \qquad (1\text{-}a)$$

and

$$^{N}\boldsymbol{\omega}^{O} = \omega\mathbf{a}_3 \qquad (1\text{-}b)$$

Position vector P^{op} of beam under the deployment is,

$$\mathbf{P}^{op} = (x + \alpha + u_1)\mathbf{a}_1 + u_2\mathbf{a}_2 \qquad (2)$$

For the geometric relation between the arc-length of stretch s and Cartesian variable x with the deployment α can be written as[16],

$$x + s + \alpha = \int_{-\alpha}^{x}[(1+u_{1,\sigma})^2 + u_{2,\sigma}^2]^{\frac{1}{2}}d\sigma \qquad (3)$$

where $(\ )_{,\alpha}$ denotes the partial derivertive with respect to α.

Applying the binomial expansion of the integrand of Eqn 4, then

$$s = u_1 + \frac{1}{2}\int_{-\alpha}^{x}u_{2,\sigma}^2\,d\sigma + \text{H.O.T} \qquad (4)$$

where H.O.T. denotes the higher-order terms which is to be omitted.

Differentiate Eqn 4 with respect to t,

$$\dot{s} = \dot{u}_1 + \int_{-\alpha}^{x}u_{2,\sigma}\,\dot{u}_{2,\sigma}\,d\sigma \qquad (5)$$

Now we express the equations of motion in terms of generalized active force(F_i) and generalized inertia force(F_i^*) as follows[17].

$$F_i + F_i^* = 0 \quad (i = 1,\dots,n) \qquad (6)$$

where n denotes the number of degrees of freedom.

Generalized active force(F_i) can be written in terms of the potential energy U,

$$F_i = -\partial U/\partial q_i \quad (i = 1,\dots n) \qquad (7)$$

where q_i denotes the generalized coordinates.

In this work, we will investigate the dynamic behavior of beam with varying length α and with the translation and rotational motion as in Fig.1. The potential energy U of the beam can be expressed as,

$$U = \frac{1}{2}\int_{-\alpha}^{L}\frac{P^2}{EA}dx + \frac{1}{2}\int_{-\alpha}^{L}\frac{M^2}{EI}dx + \frac{1}{2}\int_{-\alpha}^{L}\frac{KV^2}{GA}dx \qquad (8)$$

where P, M and V denote an axial force in the direction of s, bending moment and a shear force at an arbitrary point x. In addition, L, E, G, A and K denote the initial length, Young's elastic constant, shear modulus, cross-sectional area of the beam and shear correction factor, respectively.

In Eqn 8, P, M and V can be expressed in terms of s, u_2 and θ_1 as can be found in Ref.[3].

Generalized inertia force(F_i^*) can be expressed as,

$$F_i^* = \int_{-\alpha}^{L}{}^{N}\mathbf{v}_i^{P} \cdot {}^{N}\mathbf{a}^{P}\rho dx - \int_{-\alpha}^{L}{}^{N}\boldsymbol{\omega}_i^{dB} \cdot ({}^{N}\mathbf{a}^{dB} + {}^{N}\boldsymbol{\omega}^{dB} \times {}^{N}\boldsymbol{\omega}^{dB})I_3 dx \qquad (9)$$

where I_3, ρ and dB denote the moment of inertia, mass per unit length and cross-section of the beam.

We choose a set of functions to represent the modes for the cantilever beam with deployment as in Ref.[10,11],

$$s(x,t) = \sum_{j=1}^{\mu}\Phi_{1j}(x,t)q_j(t) \qquad (10\text{-}a)$$

$$u_2(x,t) = \sum_{j=1}^{\mu}\Phi_{2j}(x,t)q_j(t) \qquad (10\text{-}b)$$

$$\theta_1(x,t) = \sum_{j=1}^{\mu}\Phi_{3j}(x,t)q_j(t) \qquad (10\text{-}c)$$

where $\Phi_{ij}(x, t)$ $(i=1,2,3;j=1,\dots,\mu)$ denotes the mode shapes of the beam.

We can obtain the approximate equations of motion by applying these assumed modes in the Eqn 6,

$$\mathbf{M}\ddot{\mathbf{q}} + \mathbf{G}\dot{\mathbf{q}} + \mathbf{K}\mathbf{q} = \mathbf{F} \qquad (11)$$

where $\mathbf{M}$, $\mathbf{G}$ and $\mathbf{K}$ represent mass matrix, gyroscopic matrix and stiffness matrix. Vectors $\mathbf{q}$ and $\mathbf{F}$ denote displacements and force vectors, respectively.

Numerical Results and Discussions

As a numerical example, we consider the deployment of isotropic beam with rectangular cross-section. Material properties are chosen as in reference [10,11]:

$L = 1.4\ m$, $I_3 = 1.563 \times 10^{13}\ m^4$, $A = 0.00075m^2$, $K = 0.8509$, $E = 7 \times 10^{10}\ N/m^2$, $\rho = 2700 kg/m^3$, $G = 2.6 \times 10^{10}N/m^2$

Translation and rotational motion of rigid body A with a deployment of a beam is assumed to be given by Eqn 12.a - 12.d as in reference [10,11].

$$\alpha(t) = \alpha_0 + \alpha_t\phi(t) \qquad (12.a)$$

$$\omega(t) = \omega_0 + \omega_t\phi(t) \qquad (12.b)$$

$$v_1(t) = v_{10} + v_{1t}\phi(t) \qquad (12.c)$$

$$v_2(t) = v_{20} + v_{2t}\phi(t) \qquad (12.d)$$

where $\phi(t)$ means $[t-(T/2\pi)\sin(2\pi t/T)]/T$ and $0 <t< T$. Eqn 12.a defines the deployment α ,and Eqn 12.b shows the rotational motion of beam. Eqn 12.c and 12.d indicate the $\mathbf{a}_1$ and $\mathbf{a}_2$ component of velocity, respectively.

Runge-Kutta method of analysis is applied to solve the Eqn 11. We choose a time interval 0 to 0.5 seconds, and divide it into a sufficiently small step to achieve converged numerical results. Table 1 shows the numerical data for the beam with deployment and rotational motion. In addition, we assume that v_{10} and v_{20} are equal to 0, but v_{1t} and v_{2t} are equal to π. Case Da shows the relatively slow speed of deployment as compared with the case Db. And, the case Ra has the relatively slow speed of rotation with respect to Rb.

Table 1 Motions

Motion	Case	α_0(m)	α_t(m)	ω_0(rad/s)	ω_t(rad/s)
Deployment	Da	0.7	0.35	0	0
	Db	0.7	0.7	0	0
Rotation	Ra	0	0	0	$\pi/4$
	Rb	0	0	0	π

We consider the cases with the combination of deployments (Da or Db) with rotation of a beam (Ra or Rb). Initial condition for the tip deflection of beam is chosen as 0.01 m. Fig.2 shows tip deflection of beam as a result of deployment Da with simultaneous motion of rotation Ra without the translational motion of a body. Results indicate that the tip deflection and the period of vibration is increased due to the deployment of the beam.
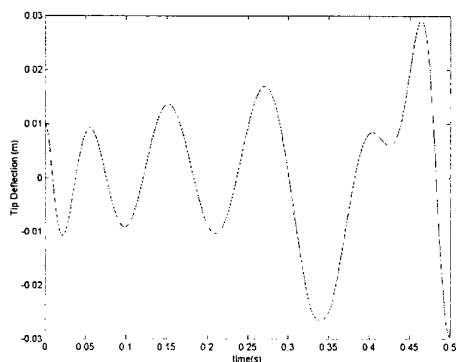
Fig.2 Deflection of Beam without Translational Motion
(Da and Ra)

Fig.3 shows tip deflection of beam as it is moved with the velocity π under the motion Da and Ra. For the translational motion of a body given as π, the tip deflection has no significant difference as compared with Fig.2.

Now, we study the relatively fast deployment and slow rotation of a beam. In Table 1,these are Db and Ra case. Fig.4 shows the tip deflection of beam without translational motion of a main body, and is almost equal to Fig.5 for the tip deflection with the translational motion of a body.

Fig.6 considers the results for the relatively fast deployment and three cases of rotations. In this analysis, translational motion of the main body is included also. Coriolis centrifugal force effect is increased due to the increase in the speed of rotation, and the un-symmetry of the response are shown to be appeared.

Fig.3 Deflection of Beam with Translational Motion
(Da and Ra)

Fig.4 Deflection of Beam without Translational Motion
(Db and Ra)
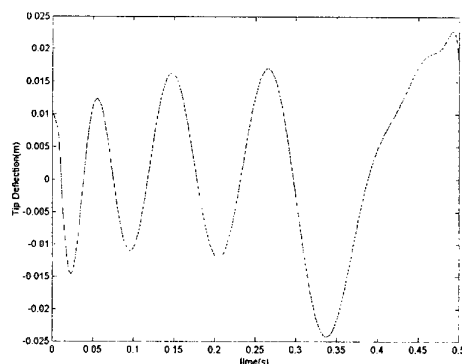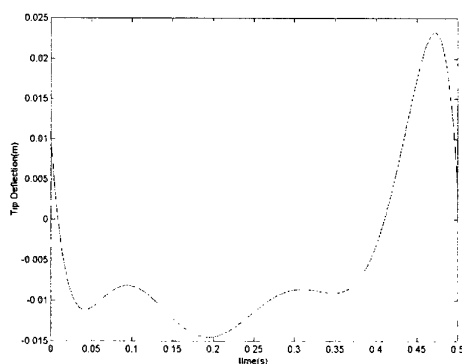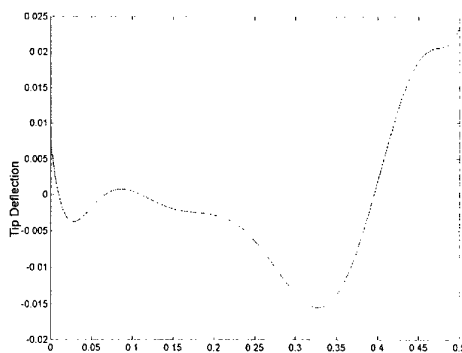
Fig.5 Deflection of Beam with Translational Motion
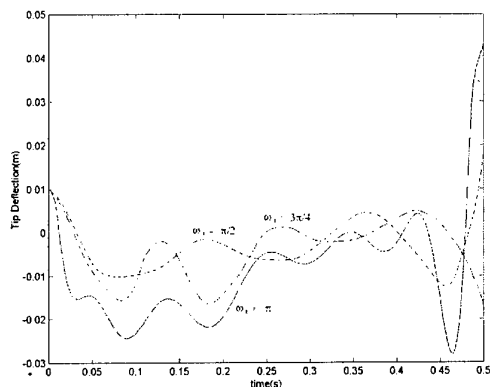(Db and Ra)

Fig.6 Deflection of Beam with Translational Motion
(Db and Rb)

Conclusions

In this study, we use the non-Cartesian coordinate system to describe the dynamics of beam. Translational motion of the main body is included or not, and the deployment with rotational motion of a beam is studied, in detail. The results can be summarized as follows. Coriolis centrifugal force effect due to the rotational motion of a beam results in the increase of the un-symmetry of the vibration pattern.

Acknowledgement

References

1. Simo ,J.C. and Vu-Quoc, L. "The Role of Non-linear Theories in Transient Dynamic Analysis of Flexible Structures," Journal of Sound and Vibration, Vol.119, No.3 , pp.487-508, 1987.

2. Simo, J.C. and Vu Quoc,L. "On the Dynamics in Space of Rods Undergoing Large Motion – A Geometrically Exact Approach," Computer Method in Applied Mechanics and Engineering, Vol.66, No.2, pp.125-161, 1988.

3. Kane, T.R. and Ryan ,R.R. ,"Dynamics of Cantilever Beam Attached to a Moving Base," Journal of Guidance, Vol.10, No.2, pp.139-151, 1987.

4. Haering, W.J., Ryan, R.R. and Scott, R.A., "New Formulation for Flexible Beams Undergoing Large Overall Plane Motion", Journal of Guidance, Control, and Dynamics," Vol.17, No.1, pp.76-83, 1994.

5. Haering, W.J., Ryan, R. R. and Scott, R.A., "New Formulation for General Spartial Motion of Flexible Beams", Journal of Guidance, Control, and Dynamics, Vol.18, No.1, pp.82-86, 1994.

6. Ryan, R. R., "Simulation of Actively Controlled Spacecraft with Flexible Appendages," Journal of Guidance, Vol.13, No.4, pp.691-702, 1990.

7. Tabarrok, B., Leech,C.M., and Kim, Y. I., " On the Dynamics of an Axially Moving Beam," Journal of the Franklin Institute, Vol.297, No.3, pp.201-220, 1974.

8. Downer, J.D. and Park, K.C., "Formulation and Solution of

Inverse Spaghetti Problem Application to Beam Deployment Dynamics," AIAA Journal, Vol.31, No.2, 1993.

9. Yuh, J. and Young, T., "Dynamic Modeling of an Axially Moving Beam in Rotation:Simulation and Experiment", Journal of Dynamic Systems, Measurements, Control, Vol.113, pp.34-40, 1991.

10.Yüksel, S. and Gürgoze, M., "On the Flexural Vibrations of Elastic Manipulators with Prismatic Joints", Computer and Structures, Vol.62, No.5, pp.897-908, 1997.

11.Gürgoze, M ., and Yüksel , S. ,"Transverse Vibrations of Flexible Beam Sliding Through a Prismatic Joint", Journal of Sound and Vibration, Vol.223, No.3, pp.467-482,1999.

12.Stylianou, M. and Tabarrok, "Finite Element Analysis of an Axially Moving Beam, part I:time integration," Journal of Sound and Vibration, Vol.178,No.4,pp.433-453, 1994.

13.Stylianou,M. and Tabarrok, " Finite Element Analysis of an Axially Moving Beam, part II:stability analysis," Journal of Sound and Vibration, Vol.178,No.4, pp.455-481, 1994.

14.Fung, R.F., Lu, P.Y., and Tseng, C.C.," Non-linearly Dynamic Modeling of an Axially Moving Beam with a Tip Mass", Journal of Sound and Vibration, Vol.218, No.4, pp.559-571,1998.

15.Huang, J. S., Fung, R.F., and Tseng, C.R., "Dynamic Stability of a Cantilever Beam Attached to a Translational /Rotational Base", Journal of Sound and Vibration, Vol. 224, No.2, pp.221-242, 1999.

16.Eigenhart, L., "An Introduction to Differential Geometry," Princeton University Press, 1948.

17.Kane,T.R., Likins, P. W. and Levinson, D. A., "Spacecraft Dynamics", McGraw-Hill,1983.

3E3　CLOS Guidance Performance Improvement
with Effective Glint Filtering

Taek Lyul Song[*] , and Dong Gwan Lee[**]

Hanyang University
Dept. of Control and Instrumentation Engineering
Sa 1 Dong 1271, Ansan, Kyunggido, 425-791, Korea

Key Words: CLOS Guidance, Glint Filtering

ABSTRACT

An effective filter structure is suggested for filtering of target glint in a radar-guided surface to air missile system. The proposed filter has decoupled range and angle channels so that it has a sound mathematical basis as well as computational efficiency as applied to the IMM algorithm. The proposed algorithm in conjunction with CLOS guidance is tested by a series of simulation runs and it is shown to improve system performance in a target glint environment by preventing high frequency control surface fluctuations.

I. INTRODUCTION

Glint is generated by changes in the target aspect angle relative to the radar beam, and it produces target angle fluctuations that render degraded guidance performance. The effect of glint may be negligible when tracking a small target at a long distance, however the effect may be dominant when tracking a relatively large target at a short distance. Radar-guided surface to air missile systems employing CLOS (Command to Line of Sight) guidance are also subject to target glint. Since the CLOS guidance requires multiplication of missile range to target angle in the error compensation command, the effect of the target glint on guidance performance becomes severe as the missile gets close to the target at the final engagement phase. The guidance commands generated by the guidance law become fluctuating with high frequency and large amplitude due to the glint noise. The responses of the fast responding actuators on board the missile to the guidance commands cause high frequency control surface fluctuations which not only increase air drag but also consume actuating resources and thus result in degraded system performance.

Several results have been published for glint noise modeling. Among them, [1] suggests that glint noise is a mixture of a Gaussian noise and heavy-tailed Laplacian outliers. The occurrence probabilities of two noises are different. The interacting multiple model (IMM) algorithm[2] with two extended Kalman filters (EKFs) is proposed for glint noise

filtering in target tracking with a radar[3]. In the mode probability update process of the IMM, [3] utilizes pseudomeasurements obtained by converting the original nonlinear measurements into linear measurements. However, it is known that the mode probability update of [3] lacks justification due to the assumptions that the converted measurement noises are uncorrelated and the state variables and the measurement noises are independent. A modified version of the channel-decoupled filter of [4] is used in the IMM algorithm for glint noise filtering of an active homing missile system in [5]. System dynamics of range and angle channels are linearized with the state estimates of the other channel. Measurements are linear and corrupted by the original measurement noises in this model so that the unjustified assumptions of [3] are not needed in the mode probability calculation.

In this paper, the target glint filtering used in [5] is applied to CLOS guidance performance improvement for a radar-guided surface to air missile system. Guidance performance with the proposed filter structure is compared with conventional filter structures.

II. SYSTEM DESCRIPTIONS

A. CLOS Guidance Loop

Consider a missile-target geometry depicted in Fig. 1 where the target with velocity V_T and the missile with velocity V_m are tracked simultaneously by a differential tracking radar and the missile is guided by the CLOS guidance law[6].
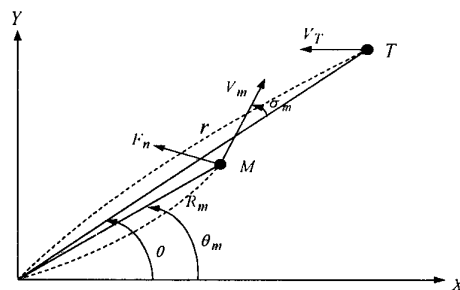

Fig. 1. Missile-target geometry for CLOS guidance

---

*　Professor
**　Graduate student

The tracking radar measures the noise-corrupted angular difference between the target and the missile. The measurements are fed through a noise filter to reduce noise contribution. A static filter is used in conventional CLOS guidance. The CLOS guidance law consists of the error angle compensation command to locate the missile on the center of the ground tracker LOS and the feedforward command to generate the required lateral acceleration under the assumption that the missile stays on the ground tracker LOS. A schematic diagram of the CLOS guidance loop is shown in Fig. 2. The error compensation command is generated by a stabilizing controller which consists of phase lead and lag networks.
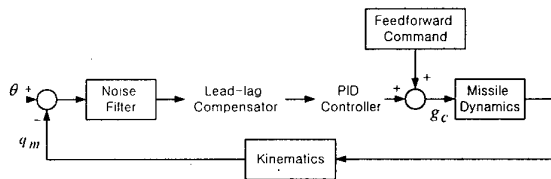

Fig. 2. CLOS Guidance Loop

B. Glint Model

The radar measurements contain target glint and radar thermal noises. Effect of the thermal noise on the CLOS guidance is not significant compared with target glint effect. It is proposed in [1] that the heavy-tailed behavior of the glint noise is more suitably modeled as the mixture of a Gaussian noise with high occurrence probability and a Laplacian noise with low occurrence probability. The probability density function of the glint noise can be written as

$$f(\upsilon) = (1-\varepsilon) f_g(\upsilon) + \varepsilon f_l(\upsilon) \qquad (1)$$

where ε is the occurrence probability of the Laplacian noise and the subscripts of the function f, g and l stand for Gaussian and Laplacian, respectively, i.e.,

$$\begin{pmatrix} f_g(\upsilon) \\ f_l(\upsilon) \end{pmatrix} = \begin{pmatrix} \dfrac{1}{\sqrt{2\pi}\sigma_g} \exp(-\dfrac{\upsilon^2}{2\sigma_g^2}) \\ \dfrac{1}{2\eta} \exp(-\dfrac{|\upsilon|}{\eta}) \end{pmatrix}. \qquad (2)$$

Laplacian parameter η is related to the Laplacian noise variance σ_l^2 as $2\eta^2 = \sigma_l^2$. Spiky character of the glint could be properly modeled with the Laplacian parameter and the occurrence probability. The IMM algorithm using two EKFs is proposed in [3] to filter the glint noise with the above characteristics.

C. Proposed Filter Structure

A modified version of the channel-decoupled filter of [4] is used in the IMM algorithm. The target state variables defined in the polar coordinates can be constructed from r and θ of Fig. 1. The state vector of the range channel x_r is composed of

r, $\dot{r}$, and A_{T_r}, target acceleration in the relative range direction. The continuous dynamics employing the Singer model for target acceleration are represented as

$$\dot{x}_r = \begin{pmatrix} 0 & 1 & 0 \\ \dot{\theta}^2 & 0 & 1 \\ 0 & 0 & -\dfrac{1}{\tau} \end{pmatrix} x_r + \begin{pmatrix} 0 \\ 0 \\ \dfrac{1}{\tau} \end{pmatrix} \omega_r \qquad (3)$$

where ω_r is a white Gaussian process noise with zero-mean and power spectral density of $2\tau\sigma_{A_r}^2$. Note that $\sigma_{A_r}^2$ is the assumed variance of the target acceleration and τ is the correlation time-constant of target maneuver. Similarly, the angle channel dynamics can de described by

$$\dot{x}_\theta = \begin{pmatrix} 0 & 1 & 0 \\ 0 & -\dfrac{2\dot{r}}{r} & \dfrac{1}{r} \\ 0 & 0 & -\dfrac{1}{\tau} \end{pmatrix} x_\theta + \begin{pmatrix} 0 \\ 0 \\ \dfrac{1}{\tau} \end{pmatrix} \omega_\theta \qquad (4)$$

where $x_\theta = (\theta, \dot{\theta}, A_{T_\theta})^T$, A_{T_θ} represents target acceleration perpendicular to the relative range direction, and ω_θ is a white Gaussian noise with zero-mean and power spectral density of $2\tau\sigma_{A_r}^2$.

The measurements from the tracking radar are noise-corrupted relative range and angle information such as

$$z_r = H x_r + \upsilon_r \qquad (5)$$

and

$$z_\theta = H x_\theta + \upsilon_\theta \qquad (6)$$

where $H = (1, 0, 0)$ and υ_r and υ_θ are independent measurement noises and each noise can be modeled as the mixture of a Gaussian noise and Laplacian noise satisfying the probability density function of (1).

For glint noise filtering, the IMM algorithm [2] is applied to each channel so that each channel requires two filters based on two modes of operation: one with a Gaussian measurement noise (M^1) and the other with a Laplacian measurement noise (M^2). The IMM algorithm proposed in [2] consists of 4 steps: interaction, filtering, mode probability update, and combination. The detailed IMM algorithm can be seen in [2].

Probability of M^j, $j = 1, 2$ at $t = k$ can be obtained from the Bayesian formula as

$$\Pr(M_k^j \mid Z_k) =$$

$$\dfrac{f(z_k \mid M_{k-1}^j, Z_{k-1}) \sum_{i=1}^{2} \pi_{ji} \Pr(M_{k-1}^i \mid Z_{k-1})}{\sum_{j=1}^{2} f(z_k \mid M_{k-1}^j, Z_{k-1}) \sum_{i=1}^{2} \pi_{ji} \Pr(M_{k-1}^i \mid Z_{k-1})} \qquad (7)$$

where π_{ji} is the transition probability from M^i at $t = k-1$ to

M^j at $t = k$. The probability density functions of the measurements z_r of (5) and z_θ of (6) conditioned on M^1 and the prior observations $Z_{k-1} = \{z_1, z_2, \cdots, z_{k-1}\}$ needed in the mode probability update process can be obtained as

$$\begin{pmatrix} f(z_r \mid M^1, Z_r) \\ f(z_\theta \mid M^1, Z_\theta) \end{pmatrix} = \begin{pmatrix} N(z_r; H \, \overline{x}_r^{(1)}, H \, \overline{P}_r^{(1)} H^T + \sigma_{r_g}^2) \\ N(z_\theta; H \, \overline{x}_\theta^{(1)}, H \, \overline{P}_\theta^{(1)} H^T + \sigma_{\theta_g}^2) \end{pmatrix} \qquad (8)$$

where the subscript k and $k-1$ indicating the time step are omitted, and $\sigma_{r_c}^2, \sigma_{\theta_c}^2$ are variances of the measurement noises v_r and v_θ under the assumption of M^1, respectively. Note that $\overline{x}^{(1)}$ and $H \overline{P}^{(1)} H^T$ for the range and the angle channels represent mean and variance of the Gaussian prior under M^1. The convolution of the Gaussian prior and the Laplacian measurement noise is required to obtain the probability density functions of the measurements z_r and z_θ based on M^2. After some work, one obtains for both z_r and z_θ,

$$f(z \mid M^2, Z) = \qquad (9)$$

$$\frac{1}{2\eta} e^{\frac{\sigma^2}{2\eta^2}} \left[e^{-\frac{z - \overline{x}_1}{\eta}} G\left(\frac{z - \overline{x}_1 - \frac{\sigma^2}{\eta}}{\sigma} \right) + e^{\frac{z - \overline{x}_1}{\eta}} G\left(-\frac{z - \overline{x}_1 + \frac{\sigma^2}{\eta}}{\sigma} \right) \right]$$

where $\overline{x}_1$ and σ^2 defined as $H \overline{x}^{(2)}$ and $H \overline{P}^{(2)} H^T$ representing mean and variance of the Gaussian prior calculated under M^2, and G is the standard normal distribution function. The above result can be used for the both range and angle channels with proper parameters. The proposed filter uses the original measurements which are linear in state variables, the mode probability update algorithm of (7) has a sound mathematical basis and computational efficiency compared with the EKF approach of [3]. The EKF approach utilizes the converted pseudomeasurements which are contaminated by the correlated state dependent noises so that the mode probability update process requires the unjustified assumptions. Moreover, it requires more memories and computations relative to the proposed filter.

III. SIMULATION RESULTS

A series of Monte Carlo simulation runs is carried out to analyze CLOS guidance performance of a surface to air missile system in a target glint environment. In this study, performance of the IMM algorithm using the proposed filter structure is compared with those of the IMM algorithm using two EKFs [3,5] and a single conventional filter.

The engagement scenario for performance evaluation is established according to Fig. 1. The initial position of the target assumed to fly straight with a constant speed $V_T = 351 m/s$ is set to be $(12.000m, 4000m)$. The radar is fixed at the origin of the coordinate system and the missile is launched from the position $(10m, 0m)$ with the initial attitude angle of $23°$. The time constant of the missile autopilot in Fig. 2 is time varying according to Mach number. Guidance is operating at 40Hz.

The power spectral densities of the process noise ω_r and ω_θ

of (3) and (4) are calculated with $\sigma_{A_T} = 1 m/s^2$ and the target maneuver time constant $\tau = 5(s)$. The initial probabilities for M^1 and M^2 for the IMM algorithm are 0.8 and 0.2 respectively, while the mode transition probility matrix satisfies

$$\pi_{ij} = \begin{bmatrix} 0.8 & 0.8 \\ 0.2 & 0.2 \end{bmatrix} . \qquad (10)$$

The variances of the Gaussian measurement noises are $\sigma_{r_g}^2 = (1m)^2$ and $\sigma_{\theta_g}^2 = (0.25 m\,rad)^2$, respectively while the variances of the Laplacian noises are 25 times larger than those of the Gaussian noises.

Fig. 3 shows guidance command history generated by using a second-order conventional noise filter inside the CLOS guidance loop of Fig. 2. The result indicates that the amplitude of fluctuating guidance command is large due to the glint noise. The guidance command generated by using the IMM algorithm with the proposed filter structure is depicted in Fig. 4. It shows that the effect of the glint noise is reduced drastically compared with the conventional filter case, which indicates that unnecessary guidance command has been removed effectively. Since surface to air missiles in general have actuators with the bandwidth of 40Hz or so for precision CLOS guidance, the actuators are likely to respond to the high frequency guidance command and generate unnecessary high frequency control surface movement. The control surface movement results in consumption of electrical power or gas storage, increase of aerodynamic drag force, and adverse effect on overall system performance. 30 runs of Monte Carlo simulation are carried out to represent such effect. Fig. 5 indicates the average value of time integral of guidance command energy of the conventional filter case, while Fig. 6 is for the proposed filter case. The average is calculated by $E\left[\int g_c(t) dt \right]$. It can be concluded from Figs. 5 and 6 that the proposed filter structure is superior in energy management aspect such that it has better system performance. It turns out that the IMM algorithm with two EKFs has similar performance to the proposed filter structure shown in Figs. 4 and 6 however, the computational requirements are heavier than the proposed filter structure[3,5]. Table 1 is a summary of 30 runs of Monte Carlo simulation carried out to evaluate the guidance performance at the final engagement phase. The results indicate that the IMM algorithms have similar guidance performance with prominent terminal accuracy.

TABLE I

Guidance Performance at the Final Phase

Filter structure	Miss Distance (m)	Variance (m^2)
Conventional filter	3.45	15.21
IMM with the proposed filter	0.86	0.16
IMM with EKFs	0.88	0.12
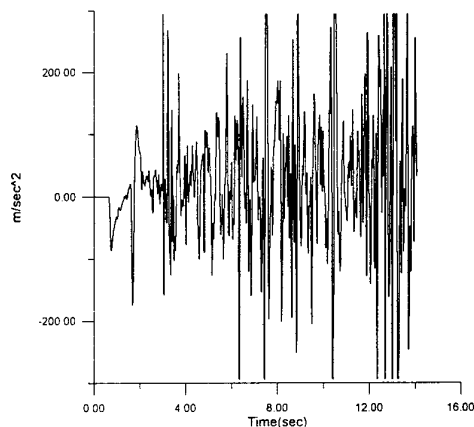
Fig. 3. Guidance command (conventional filter)
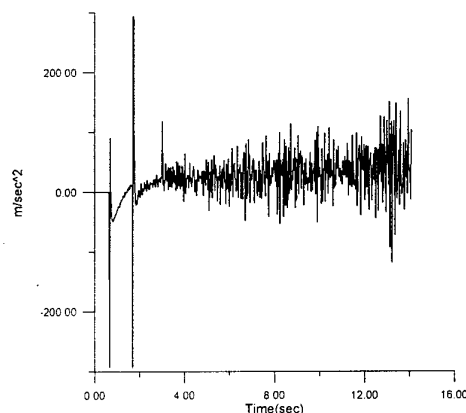
Fig. 4. Guidance command (proposed filter)
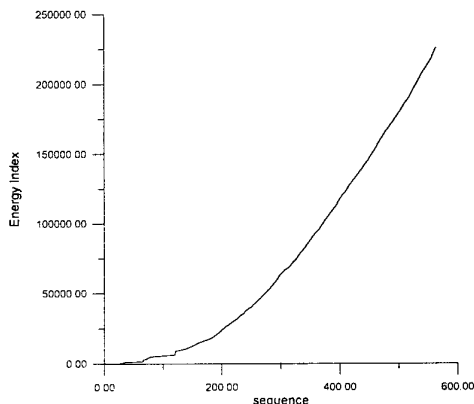
Fig. 5. Average control energy (conventional filter)
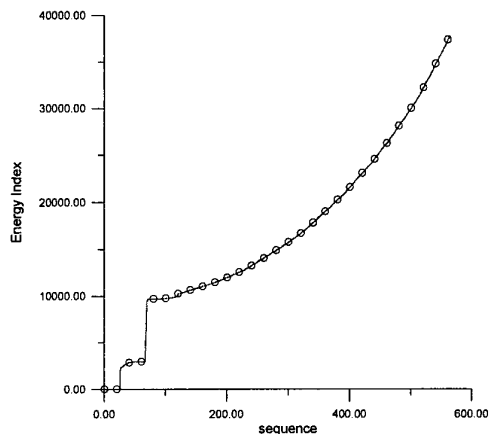
Fig. 6. Average control energy (proposed filter)

IV. CONCLUSIONS

An effective filter structure is suggested for filtering of target glint in CLOS engagements of a radar-guided surface to air missile system. Due to the decoupled range and angle channels, the proposed filter has sound mathematical basis and computational efficiency as applied to the IMM algorithm. Monte Carlo simulation in a target glint environment indicates that the proposed filter generates accurate enough guidance performance at the final engagement phase without excessive consumption of power resource and increase of aerodynamic drag during the midcourse compared with a conventional filter. Though the IMM algorithm with the EKFs has similar guidance performance, the proposed filter structure is more efficient in computational procedures.

References

[1] Wu, W., "Target tracking with glint noise" IEEE Transactions on Aerospace and Electronic Systems, Vol. 29, No. 1 (Jan. 1993), 174-185.

[2] Blom, H. and Bar-Shalom, Y., "The interacting multiple model algorithm for systems with Markovian switching coefficients," IEEE Transactions on Automatic Control, Vol. 33, No. 8, (Aug. 1988), 780-783.

[3] Daeipour, E., and Bar-Shalom, Y., "An interacting multiple model approach for target tracking with glint noise," IEEE Transactions on Aerospace and Electronic Systems, Vol. 31, No. 2 (Apr. 1994), 706-715.

[4] Pearson, J. B., and Stear, E. B., "Kalman filter applications in airborne radar tracking," IEEE Transactions on Aerospace and Electronic Systems, Vol. 10, No. 3 (May 1974), 319-329.

[5] Song, T. L. and Lee, D. G., "Effective filtering of target glint," IEEE Transactions on Aerospace and Electronic Systems, Vol. 36, No. 1 (Jan. 2000).

[6] Garnell, P. "Guided Weapon Control Systems," Pergamon Press, 1980.

3E4 Improvement of Active Homing Performance with Radome Slope Estimation

*Sang Jin Shin, **Taek Lyul Song

Hanyang University

Department of Control and Instrumentation Engineering

Sa 1 Dong 1271, Ansan, Kyunggi-do, 425-791, Korea

Keyword: Guidance and Control, Radome Slope Estimation

ABSTRACT

In this paper, a new filter structure is suggested for estimating radome slope in active homing engagements of an anti-air missile. Incorporating the IMM algorithm with a suboptimal filter to estimate radome slope and target states produces an estimation scheme that reduces the radome induced miss distance effectively. The proposed filter in conjunction with proportional navigation guidance is tested by a series of simulation runs.

1. INTRODUCTION

In this paper, a study is carried out to improve the miss distance induced by radome slope when tracking targets with microwave seekers. The radome slope may severely affect the tracking accuracy when it together with body rates are coupled into the LOS(line of sight) angular rates measured by the on-board seeker. Since typical homing guidance such as proportional navigation guidance(PNG) makes direct use of the target LOS angular rates, reduction of radome induced miss distance has attracted many researchers in the field to improve guidance performance. Miss distance and sensitivity analyses for the radome slope were investigated in [1] for various conditions for nonlinear missile systems. Seeker dynamic modeling including the radome slope was concisely explained in [2]. As the radome error can neither be precisely measured nor predicted, [3] tried to solve these problems with designing a multiple model adaptive estimator[4]. [3] assumed that the radome slope could take any of N possible discrete values in the multiple model approach. However, it is found that the radome slope can not be estimated with the method proposed in [3] unless the true target LOS angle is known, which is impossible in actual homing engagements rather than laboratory applications. The problem arises due to the lack of system observability.

A new approach using interacting multiple model(IMM)[5] is proposed in this paper. In the proposed algorithm states of filter dynamics are composed of relative position, velocity and target acceleration, unlike those of [3] where seeker dynamics was used in the filter model to estimate the radome slope. It is

conceived that target information measured from a ground radar such as a multifunction array radar is sent to the missile at a relatively low sampling frequency to help out the observability problem. The ground radar information is used only in the mode probability update of the IMM algorithm.

The proposed filter algorithm in conjunction with PNG is tested for effectiveness by a series of Monte Carlo simulation runs.

2. SYSTEM DESCRIPTIONS

2.1 Seeker Model

Consider the missile-target engagement geometry depicted in Fig. 1, where the target is tracked by an active seeker on board the missile. It denotes missile attitude angle as θ_m, seeker gimbal angle as θ_g, and target LOS angle as λ.
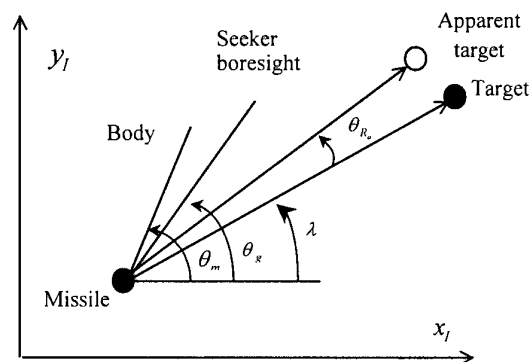
Fig. 1 Missile-target engagement

The radar wave is refracted by the radome and the target appears to be displaced from its true position by the refraction angle θ_{R_a}. The refraction angle varies with missile gimbal angle. Guidance command A_{m_c} using PNG is expressed as

$$A_{m_c} = N V_c \dot{\lambda} \tag{1}$$

where N is the navigation constant and V_c is the closing velocity. In this study, it is assumed that the transfer function from A_{m_c} to achieved missile lateral acceleration

---

* Graduate student

** Professor

A_m is second-order characterized by the natural frequency and the damping ratio. The relation between θ_m and the flight path angle γ is expressed as

$$\dot{\theta}_m = (1 + \Lambda s)\dot{\gamma}, \qquad (2)$$

where Λ is the time constant for incidence lag of which the value is large for missiles with small control surfaces and for high altitude engagements. Fig. 2 shows a block diagram of second-order seeker dynamics including the radome slope R_a.
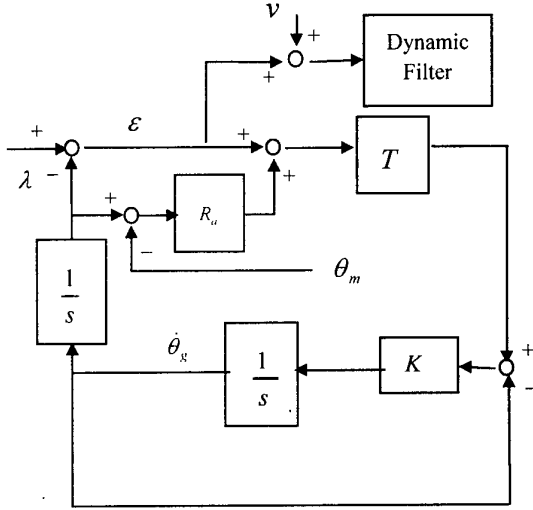
Fig. 2 Block diagram of seeker dynamics

2.2 Proposed Filter Structure

In this study, filter states are composed of relative position, velocity and target acceleration, and the Singer model[6] is used for unknown target maneuver model. The proposed filter can estimate both radome slope and state variables needed in computing guidance commands. The filter dynamic model is represented as

$$\dot{x}(t) = A\ x(t) + B\ A_m(t) + Dw(t), \qquad (3)$$

$$x(t) = (x(t), y(t), \dot{x}(t), \dot{y}(t), A_{T_x}(t), A_{T_y}(t))^T, \qquad (4)$$

$$A = \begin{bmatrix} 0 & I_2 & 0 \\ 0 & 0 & I_2 \\ 0 & 0 & -\dfrac{1}{\tau}I_2 \end{bmatrix}, \quad B = \begin{bmatrix} 0 \\ -I_2 \\ 0 \end{bmatrix}, \quad D = \begin{bmatrix} 0 \\ 0 \\ \dfrac{1}{\tau}I_2 \end{bmatrix}, \qquad (5)$$

where A_m is the missile acceleration vector, the process noise $w(t) = (w_x, w_y)^T$ is a white gaussian noise vector with zero-mean and power spectral density of $2\tau\sigma_{A_T}^2 I_2$. The measurements from the active seeker at time $t = k \cdot \Delta t$ composed of the noise-corrupted missile-target relative range and the LOS angle can be expressed as

$$\begin{pmatrix} z_R^s \\ z_\theta^s \end{pmatrix}_k = \begin{pmatrix} \sqrt{x^2 + y^2} + v_R^s \\ \tan^{-1}\dfrac{y}{x} + R_a(\theta_g - \theta_m) + v_\theta^s \end{pmatrix}_k, \qquad (6)$$

where v_R^s and v_θ^s are zero-mean white gaussian noises with variances of σ_R^{s2} and σ_θ^{s2}, respectively. The superscript 's' denotes that the quantity of the measurements is from the on-board seeker. To deal with the nonlinear measurement equation, the suboptimal filter of [7] is used in this paper. A filter bank composed of several suboptimal filters is applied to the IMM algorithm[5] to estimate radome slope and the target state variables. The interacting step of the i th suboptimal filter based on the i th mode $\widetilde{H}^i$ assuming that the magnitude of radome slope is R_a^i satisfies

$$\widetilde{x}_{k-1}^i = \frac{\sum\limits_{j=1}^{N} \hat{x}_{k-1}^j \pi_{ij} \Pr_{k-1}^j}{\sum\limits_{j=1}^{N} \pi_{ij} \Pr_{k-1}^j}, \qquad (7)$$

$$\widetilde{P}_{k-1}^i = \frac{\sum\limits_{j=1}^{N} (\hat{P}_{k-1}^j + \hat{x}_{k-1}^j \hat{x}_{k-1}^{jT})\pi_{ij} \Pr_{k-1}^j}{\sum\limits_{j=1}^{N} \pi_{ij} \Pr_{k-1}^j} - \widetilde{x}_{k-1}^i \widetilde{x}_{k-1}^{iT}, \qquad (8)$$

where $\Pr_{k-1}^j$, $j = 1,2,\cdots,N$ is the mode probability of the mode $\widetilde{H}^j$ at $t = (k-1)\cdot \Delta t$, and π_{ij} is the transition probability[5] from the mode $\widetilde{H}^j$ at $t = (k-1)\cdot \Delta t$ to the mode $\widetilde{H}^i$ at $t = k \cdot \Delta t$, and $\hat{x}_{k-1}^i$ and $\hat{P}_{k-1}^i$ are the updated estimates and the updated covariance, respectively. The propagation step of the i th suboptimal filter is expressed as

$$\overline{x}_k^i = \Phi(\Delta t)\widetilde{x}_{k-1}^i + \Gamma(\Delta t)A_m, \qquad (9)$$

$$\overline{P}_k^i = \Phi(\Delta t)\widetilde{P}_{k-1}^i \Phi(\Delta t)^T + Q_k, \qquad (10)$$

where $\Phi(\Delta t)$ and $\Gamma(\Delta t)$ are the state transition matrix and the input matrix obtained from the continuous-time dynamics of (3)-(5) with the sampling interval Δt. $\overline{x}_k^i$ and $\overline{P}_k^i$ are the predicted estimates and the predicted covariance. It is assumed that the range measurement is not affected by the radome slope in (6). The unbiased measurements used in the i th suboptimal filter based on the hypothesis $R_a = R_a^i$ are obtained as

$$\begin{pmatrix} Z_R^{si} \\ Z_\theta^{si} \end{pmatrix}_k = \begin{pmatrix} z_R^{si} \\ z_\theta^s - R_a^i(\theta_g - \theta_m) \end{pmatrix}_k$$

$$= \begin{pmatrix} \sqrt{x^2 + y^2} + v_R^s \\ \tan^{-1}\dfrac{y}{x} + (R_a - R_a^i)(\theta_g - \theta_m) + v_\theta^s \end{pmatrix}_k. \qquad (11)$$

The updated step of the i th suboptimal filter is expressed as

$$\hat{x}_k^i = \overline{x}_k^i + M^T(\overline{x}_k^i)K_k^i m(\overline{x}_k^i)(Y_k^{si} - H\overline{x}_k^i), \qquad (12)$$

$$\hat{P}_k^i = (I - K_k^i H)\overline{P}_k^i(I - K_k^i H)^T + K_k^i R_k K_k^{iT}, \qquad (13)$$

$$K_k^i = \overline{P}_k^i H^T (H\overline{P}_k^i H^T + R_k^{s^i})^{-1}, \qquad (14)$$

where $H = (I_2, 0, 0)$. $R_k^{s^i} = diag(\sigma_R^{s^2}, (\overline{x}_k^{i^2} + \overline{y}_k^{i^2})\ \sigma_\theta^{s^2})$,

and the pseudomeasurement[7] used in the i th suboptimal filter is obtained by transforming (11) as

$$Y_k^{s^i} = (Z_R^{s^i} \cos Z_\theta^{s^i}, Z_R^{s^i} \sin Z_\theta^{s^i})^T. \qquad (15)$$

The coordinate transformation matrices $m(\overline{x}_k^i)$ and $M(\overline{x}_k^i)$ in (12) are expressed as

$$m(\overline{x}_k^i) = \begin{pmatrix} \cos\overline{\theta}_L^i & \sin\overline{\theta}_L^i \\ -\sin\overline{\theta}_L^i & \cos\overline{\theta}_L^i \end{pmatrix}_k \qquad (16)$$

$$M(\overline{x}_k^i) = diag(m(\overline{x}_k^i), m(\overline{x}_k^i), m(\overline{x}_k^i)) \qquad (17)$$

$$\overline{\theta}_L^i = \tan^{-1}\left(\frac{\overline{y}_k^i}{\overline{x}_k^i}\right). \qquad (18)$$

In order to estimate the target state, the total probability theorem is used to combine the estimated values, $\hat{x}_k^i$'s, $i = 1,2,\cdots,N$ from the suboptimal filter bank such as

$$\hat{x}_k = \sum_{i=1}^{N} \hat{x}_k^i \Pr_k^i. \qquad (19)$$

It is shown that the system described with the dynamic equation of (3) and the measurement equation of (6) for radome slope estimation is not observable due to the lack of system observability. In this study, this observability problem is avoided by introducing low frequency target position information from a ground radar. The low frequency ground radar information is used only in the mode probability update step and the mode probability for each mode calculated with the ground information is kept constant in the other steps of the IMM algorithm until the next ground information is available. This implies that the mode probability update step is calculated with low frequency ground radar information and the other steps are still processed with the high frequency seeker information. If the ground information z_k^g is available at $t = k \cdot \Delta t$, the mode probability for the mode $\widetilde{H}^i$ is updated from the Bayesian formula as

$$\Pr_k^i = \frac{p^i(z_k^g)\sum_{j=1}^{N} \pi_{ij} \Pr_{k-1}^j}{\sum_{m=1}^{N} p^i(z_k^g)\sum_{n=1}^{N} \pi_{mn} \Pr_{k-1}^j}, \qquad (20)$$

where $p^i(z_k^g)$ is calculated as

$$p^i(z_k^g) =$$
$$\frac{1}{2\pi |S^i|^{1/2}} \exp\left(-\frac{1}{2}(Y_k^g - H\overline{x}_k^i)^T m(\overline{x}_k^i)^T S^{i^{-1}} m(\overline{x}_k^i)(Y_k^g - H\overline{x}_k^i)\right), \qquad (21)$$

$$S^i = H\overline{P}_k^i H^T + R_k^g,\quad R_k^g = diag(\sigma_R^{g^2}, (\overline{x}_k^{i^2} + \overline{y}_k^{i^2})\ \sigma_\theta^{g^2}), \qquad (22)$$

$$Y_k^g = (z_R^g \cos z_\theta^g, z_R^g \sin z_\theta^g)_k^T. \qquad (23)$$

Note that the superscript 'g' implies that the quantity is from the ground radar. The estimated radome slope and its covariance are obtained by using the total probability theorem as

$$\hat{R}_a = \sum_{i=1}^{N} R_a^i \Pr_k^i$$
$$\hat{P}_{R_a} = \sum_{i=1}^{N} R_a^i R_a^{i^T} \Pr_k^i - \hat{R}_a \hat{R}_a^T. \qquad (24)$$

The flow chart of the proposed algorithm is depicted in Fig. 3.
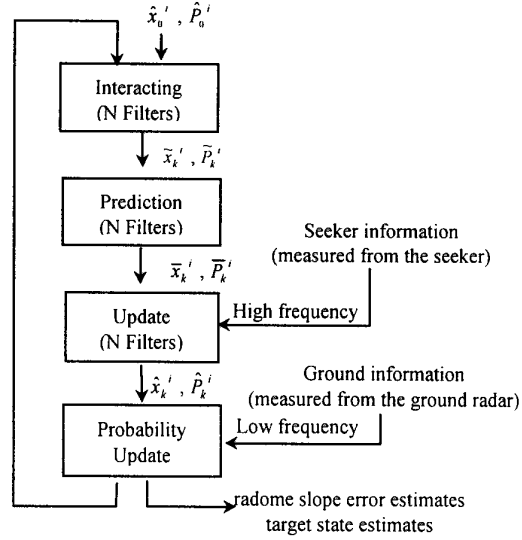
Fig. 3 Flow chart of the proposed algorithm

3. SIMULATION RESULTS

The radome slope estimation filter and the PNG of the previous section are placed in cascade to form a closed-loop to carry out a series of Monte Carlo simulation runs in order to analyze performance of the proposed filter in the terminal phase. The missile used in this planar engagement study has an speed of $500\,m/\sec$, and the target has a constant speed of $180\,m/\sec$. Initial inertial positions of the missile and the target are set to be $(0.\,m,\ 0.\,m)$ and $(10000\,m,\ 7000\,m)$. Guidance commands are limited within $200m/\sec^2$, and guidance and filter are operating at 40Hz which is the sampling frequency of a missile on-board seeker, and mode probability update step is calculated at 5Hz. Guidance and filter parameters used in this study are listed in table 1, and the time-varying radome slope is assumed to satisfy

$$R_a = 0.05\sin(0.05t). \qquad (25)$$

With the above scenario and the radome slope error, a simulation study is carried out for the active homing engagement. Fig. 4 shows missile and target trajectories generated from the active homing guidance utilizing the target state estimates of the single suboptimal filter based on the assumption of no radome slope error, while Fig. 5 shows the results with the proposed target state estimation method. The result of radome slope estimation is shown in Fig. 6 for which the following radome slope mode set is used : $\{R_a^i\}$ = $\{-0.05,\ -0.025,\ 0,\ 0.025,\ 0.05\}$. Table 2 is a summary of 15

runs of Monte Carlo simulation carried out to evaluate the performance of the proposed filter structure at the final engagement phase. It can be seen that the IMM algorithm with the proposed filter structure gives superior guidance performance at the final engagement phase over the single suboptimal filter in the presence of the radome slope.

Table 1. Missile and filter parameters

PNG	$A_{I_c} = N\,V_c\,\dot{\lambda}$	$N = 4$
autopilot transfer function	$\dfrac{w_n^{\,2}}{s^2 + 2\zeta w_n s + w_n^{\,2}}$	$w_n^{\,2} = 15\,rad/\sec$ $,\zeta = 0.6$
pitch dynamics	$\dot{\theta}_m = (1 + \Lambda s)\dot{\lambda}$	$\Lambda = 10$
power spectral density	$2\tau\sigma_{A_I}^{\,2}$, $\tau = 15(\sec)$, $\sigma_{A_I} = 2(m/\sec^2)$	
seeker	$T = 0.106$,	$K = 100$
noise	$\sigma_R^{\,s} = 2(m)$ $,\sigma_\theta^{\,s} = 0.002(rad)$ $\sigma_R^{\,g} = 2(m)$ $,\sigma_\theta^{\,g} = 0.002(rad)$	

Fig. 6 radome slope estimation

Table 2. Results of Monte Carlo simulation runs

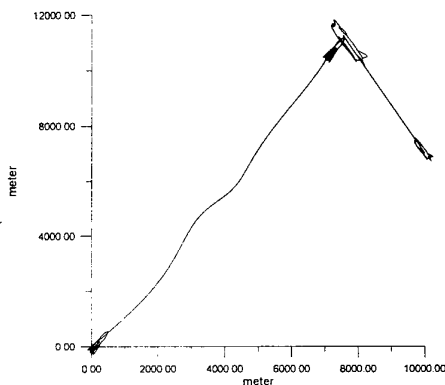| filter structure miss distance	single suboptimal filter	IMM with suboptimal filter
mean	$30(m)$	$0.8(m)$
variance	$11.6(m^2)$	$0.09(m^2)$

Fig. 4 Missile and target trajectories with the single filter
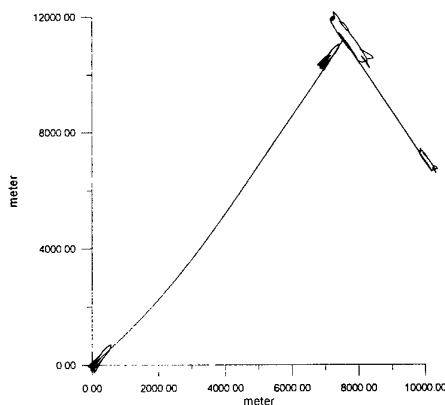
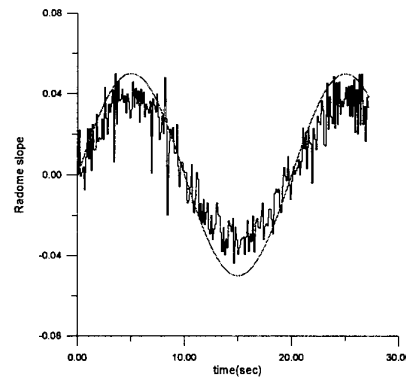Fig. 5 Missile and target trajectories with the proposed filter

4. CONCLUSIONS

An effective filter structure is proposed here for the radome slope estimation in active homing engagements of an anti-air missile. The IMM algorithm with suboptimal filter structure is tested by a series of Monte Carlo simulation runs along with a single suboptimal filter to evaluate the guidance performance. The results indicate that the proposed algorithm gives superior guidance performance over the single suboptimal filter at the final engagement phase. Target information measured from a ground radar such as a multifunction array radar is sent to the missile at a relatively low sampling frequency and used in the mode probability update step only to help out the observability problem associated with the radome slope estimation. The results show that miss distance is drastically decreased with the proposed filter.

REFERENCES

[1]Miwa, S. and Kouya, S., "Radome effect on the miss distance of a radar homing missile," AIAA GN&C Conference, 95-3285
[2]Lin, C. F. "Modern navigation, guidance and control processing," Prentice Hall , 1991.
[3]Lin, J. M. and Chau, Y. F. "Radome slope compensation using multiple-model Kalman filters," Journal of Guidance, Control, and Dynamics, Vol. 18, No. 3, pp. 637-640.
[4]Moose, R. L., Sistanizadeh, M. K. and Skagfjord,G. "Adaptive estimation for a system with unknown measurement bias," IEEE Transactions on Aerospace and Electronic Systems, AES-22, 6, pp 732-739, Nov., 1986.
[5]Blom, H. A. P. and Bar-Shalom, Y., "The interacting multiple model algorithm for systems with Markovian switching coefficients," IEEE Transactions on Automatic Control, AC-33, (8), Aug. 1988, pp 780-783.
[6]Singer, R. A., "Estimating optimal tracking filter performance for manned maneuvering target," IEEE Transactions on Aerospace and Electronic Systems, AES-6, 4, pp 473-483, Jul.,1970
[7]Song, T. L., Ahn, J. Y., and Park, C. (1988), "A suboptimal filter design with pseudomeasurements for target tracking IEEE Transactions on Aerospace and Electronic Systems, AES-24, 1(Jan. 1988), 28-39

3E6　GPS RELATIVE POSITIONING SYSTEM FOR UAVS

Genshe Chen[*] and Masatoshi Harigae[**]

Flight Division, National Aerospace Laboratory
6-13-1 OSAWA, MITAKA, TOKYO 181-0015, JAPAN

Key Words: Guidance and Control, Global Positioning System

ABSTRACT

Avoiding collisions between the Unmanned Aerial Vehicles (UAVs) and the manned aircraft in the same flight space requires accurate information on the relative position and attitude between the vehicles. An innovative Low Probability of Intercept relative positioning technology using a GPS carrier phase is developed to carry out such missions. UAV determines the precise relative position with respective to the manned aircraft based on the observable extracted from the direct GPS and GPS-like signals (which is of Low Probability of Intercept) transmitted by a transponder on the manned aircraft. All features of the GPS signal are maintained on the transmitting GPS-like signal, such as the C/A code modulation, P code modulation, navigation information modulation, etc. To improve accuracy, a faster code and carrier phase frequency (Ka-band frequency) is used in GPS-like signal.

1. INTRODUCTION

Unmanned Aerial Vehicles (UAVs) operate as terms with manned airborne system in the same general airspace and are required to perform many potential missions, such as surveillance, targeting, complex navigation, vision tasks, etc. and must accommodate input from multiple sources including person-in-the-loop tasking. Safety of the manned aircraft and the UAVs is of paramount importance in all airspace environments. Avoiding collisions between the UAVS and the manned aircraft in the same flight space is the basic necessity for autonomous operations. Many current collision avoidances are active systems requiring some form of specialized signal output to serve as part of warning system and or require a continuous line of sight between platforms. Use of active sensors such as radar or laser ranges are not desirable due to their significant power requirements and the difficulty in conducting convert missions. Therefore, some researcher proposed to exploit on board passive eletro-optical (EO) sensors such as convention TV camera and infrared imaging device to estimate the orientation, range and range rate relative to the manned aircraft [1]. Unfortunately, an EO sensor does not have all-weather capability. Its capability is affected by weather, time of day, etc.

This paper is to investigate the feasible systematic structure for the precise manned aircraft-UAV relative positioning (MURP) technology using a GPS carrier phase, in which its power radicalization is of Low Probability of Intercept and navigation information is required between the manned aircraft and the UAV. Of course, duo to the data link required between UAV and the manned aircraft, GPS is not passive. GPS techniques offer some promising method to sense the relative

positioning between spacecraft [2, 3]. In this paper the aircraft-UAVs relative positioning configuration performs autonomous positioning processing on UAVs, and determines the precise relative position with respective to the manned aircraft, based on the obsevables extracted from the direct GPS and GPS-like signals (which is of Low Probability of Intercept) transmitted by a transponder on the manned aircraft. An additional GPS antenna located on the manned aircraft receives the visible GPS satellite signals. These signals are transmitted through a transmitting antenna after a carrier frequency shift procedure. All features of the GPS signal are maintained on the transmitting GPS-like signal, such as the C/A code modulation, P code modulation, navigation information modulation, etc. On the UAVs, a corresponding receiver antenna is used to receive the GPS-like signals from the manned aircraft. Then an inverse carrier frequency shift is made on the UAVs to retrieve the signal transmitted by the manned aircraft. The retrieved signal carry the manned aircraft's position and velocity information, which can be solved on the UAVs (As shown in Figure 1). While the UAV receives the signals directly from the GPS satellites, the UAV can determine its position and velocity based on these direct measurements. Furthermore, carrier phase differential processing can be executed on the UAV to get the precise relative position between the manned aircraft and UAV.
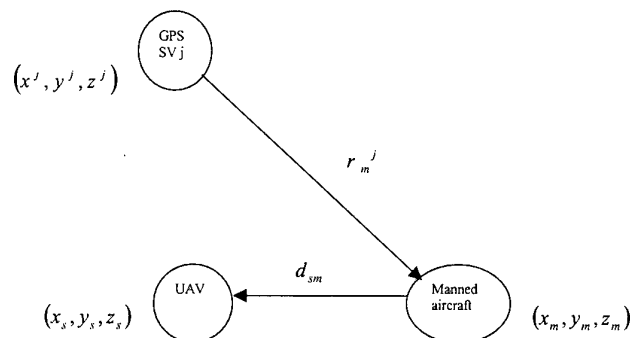

Figure 1. GPS relative positioning between manned aircraft and UAV.

2. DCP-GPS FOR RELATIVE STATE DETERMINATION

The objective of this section is to establish and motivate the data processing procedure for two aircraft using differential

phase. The result is to establish communication requirements and data processing requirement beyond the integer resolution problem independently discussed in next section.

Assuming the GPS signals received by the manned aircraft are transmitted without delay, the GPS-like signal received by the UAVs can be represented as in Figure 1.

$$\rho_{sm}^{j} = r_{m}^{j} + d_{sm} \tag{1}$$

where ρ_{sm}^{j} is the pseudorange corresponding to the j th GPS satellite signal reflecting from the manned aircraft; r_{m}^{j} is the geometrical distance between the manned aircraft and the j th GPS satellite; d_{sm} is the geometrical distance between the manned aircraft and the UAV.

In equation (1), ρ_{sm}^{j} can be derived by the GPS receiver on the UAV after a GPS signal retrieving procedure, and the GPS satellite position can be determined through the extracted ephemeris. So there are four unknowns in equation (1), the 3-dimensional coordinates (x, y, z) of the manned aircraft and the relative distance d_{sm} between the manned aircraft and the UAV. The four unknowns can be computed immediately assuming visibility to four satellites observed simultaneously by the GPS antenna on the manned aircraft. If the receiver clock bias is introduced in equation (1), one more satellite will be required for real-time positioning. Equation (1) represents the manned-UAV relative positioning algorithm.

Similarly, the velocity of the manned aircraft and the relative velocity between the manned and the UAV can be determined through the Doppler shift measurements. Time differentiation of the equation (1) gives as

$$\dot{\rho}_{sm}^{j} = \dot{r}_{m}^{j} + \dot{d}_{sm} \tag{2}$$

where $\dot{\rho}_{sm}^{j}$ is the range rate corresponding to the j th GPS satellite signal reflecting from the manned aircraft; $\dot{r}_{m}^{j}$ is the range rate between the manned aircraft and the j th GPS satellite; $\dot{d}_{sm}$ is the range rate between the manned aircraft and the UAV.

Two subsystems are included in the prototype manned aircraft-UAV relative positioning system. One is the master subsystem that will be located on the manned aircraft. The other is the slave subsystem that will be carried by the UAV, as shown in Figure 2.
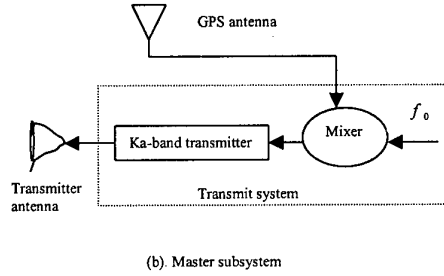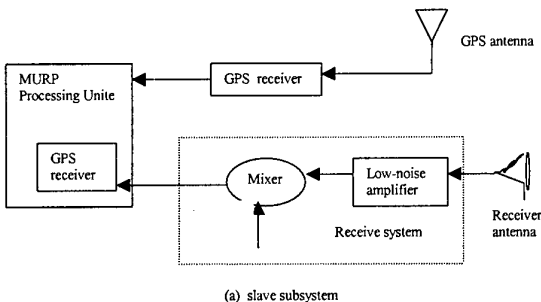

(a) slave subsystem

(b). Master subsystem

Figure 2. Prototype manned aircraft-UAVs relative Positiong system

The master subsystem, which consists of the GPS antenna, the Ka-band transmit system and the Ka-band transmit antenna, is to receive the visible GPS satellite signals, shift the carrier frequency up to the Ka-band and retransmit the GPS signal modulated on the frequency f_0. The GPS signal received by the antenna is given by:

$$s(t) = AC(t)D(t)\cos[(\omega_c + \Delta\omega)t + \Phi_0] \tag{3}$$

where A is the signal amplitude in V, C(t) is the PRN code modulation ($\pm$), D(t) is the 50bps data modulation ($\pm$), ω_c is the carrier phase frequency (L_1 or L_2) in rad/sec, $\Delta\omega$ is the frequency offset in rad/sec, and Φ_0 is the nominal carrier phase. After mixer and transmitter, the GPS signal modulated on the frequency f_0 can be represented as

$$s(t) = A A_m C(t)D(t)\cos[(\omega_c + \omega_0 + \Delta\omega)t + \Phi_0] \tag{4}$$

where $\omega_0 = 2\pi f_0$ and A_m is the gain of the transmit system. By comparing equation (3) and (4), the conclusion is made that the Ka-band signal given by (4) encompasses all messages on the original GPS signal.

The slave subsystem consists of the GPS antenna, the GPS receiver, the Ka-band receiver system and the MURP processing unit. The GPS antenna and the GPS receiver are used to receive directly the GPS signals and extract the navigation messages modulated on the GPS signals and the raw observable, such as the code pseudoranges, carrier phase measurements and Doppler shifts,etc.

The Ka-band antenna and the receiver are aimed to retrieve the GPS signal from the Ka-band signal given by (4). A GPS receiver in the MURP processing unit is used to provide the raw observable from the retrieved GPS signal. In the MURP unit, the raw measurements from the direct GPS signal and the retrieved GPS signal are processed by the MURP algorithm proposed in this paper and derive the navigation messages for collision avoidance.

The mutual relative positioning system can be obtained by combining the master and slave subsystems together and installed them on each manned aircraft and UAV in the same airspace. In

this way, any manned aircraft or UAV acts as master and slave subsystem. In the case of a manned aircraft and a UAV, each aircraft would need to carry three corner-located GPS receiver antennas, two Ka-band receiver antennas and two transmitter antennas mounted on opposing corners (Figure 3). The configuration of the Ka-band transmitter and receiver antennas would provide full sky coverage in all directions, assuming hemispherical fields of view for each antenna. The three GPS antenna mounted on a face of the aircraft provides two independent GPS interferometer to determine the aircraft's 3-dimensional attitude.
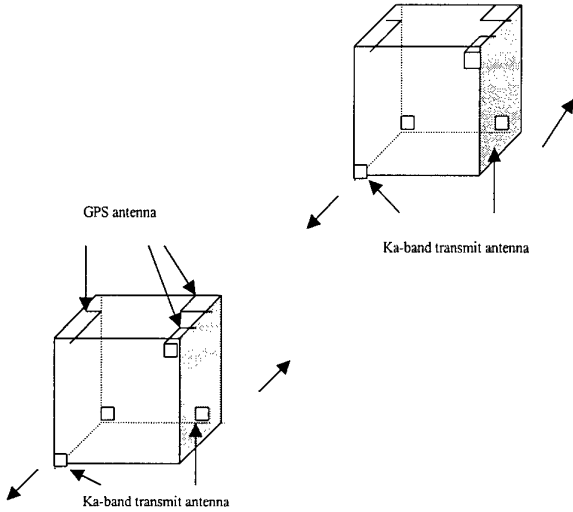

Figure 3. Configuration with a total of seven antennas.

3. INTEGER AMBIGUITY SEARCH ALGORITHMS

This section outlines two schemes for determining the initial carrier phase integer ambiguity. The first scheme was developed by Farrell [4]. This scheme has already shown success in determining relative positions to less than 2 centimeters using a static base station and a rover. The second scheme is based on the multiple model kalman filter (MMKF) [5].

The Farrell scheme uses hypothesis testing and least squares techniques to determine the initial integer ambiguity. The scheme is computationally efficient and easy to implement. The process can be broken into four steps.

The first step in this algorithm is the formulation of the single difference measurements. The code and phase measurements from satellite i at receiver A are subtracted from the measurements from the same satellite at receiver B. The result is a new measurement that eliminates the common mode errors, such as selective availability, and therefore has reduced noise characteristics. The single difference code equation is given by

$$\Delta \widetilde{\rho}^i = \Delta r^i + \frac{f_2}{f_1} \Delta I^i + \Delta M P^i + \Delta \eta^i \qquad (5)$$

The single difference carrier phase equation is likewise given by:

$$\Delta \widetilde{\theta}^i \lambda + \Delta N^i \lambda = \Delta r^i - \frac{f_2}{f_1} \Delta I^i + m p^i + \Delta \beta^i \quad (6)$$

where $\widetilde{\rho}$ is the measured pseudorange from GPS receiver in meter; f_2 is the frequency of L_1 signal; f_1 is the frequency of L_2 signal; $\frac{f_2}{f_1} I_a$ is the Ionospheric error; MP is the C/A code multipath error; η is the zero mean, Gaussian random noise; $\widetilde{\theta}$ is the measured carrier phase of GPS receiver; N is the integer number of wavelengths from satellite to the receiver, considered a constant; mp is the carrier phase multipath; β is the zero mean, Gaussian random noise.

The second step in this algorithm is to combine L_1 and L_2 measurements from both code and carrier phase in order to determine the best initial estimate of the integer ambiguity. Te recombination of the measurements makes use of wide lane and narrow lane techniques. Wide lane and narrow lane are simply a linear combination of the L_1 and L_2 carrier frequencies. The wide lane measurement wavelength is determined for subtracting the L_1 frequency from the L_2 frequency. The narrow lane wavelength is determined from adding the L_1 frequency to the L_2 frequency.

The initial integer ambiguity is found by subtracting the wide lane carrier phase measurement from the narrow lane code measurement. To form the wide lane carrier phase measurement, multiply both the L_1 and L_2 single difference carrier measurement found in (6) by λ_w and subtract one from the other to get:

$$\left(\Delta \widetilde{\theta}^i_{L_1} - \Delta \widetilde{\theta}^i_{L_2} \right) \lambda_w + \left(\Delta N^i_{L_1} - \Delta N^i_{L_2} \right) \lambda_w$$
$$= \Delta r + \Delta I^i + \Delta \gamma^i_p \qquad (7)$$

where

$$\Delta \gamma^i_{pp} = \frac{\lambda_w}{\lambda_1} \left(\Delta m p^i_{L_1} + \beta^i_{L_1} \right) - \frac{\lambda_w}{\lambda_2} \left(\Delta m p^i_{L_2} + \beta^i_{L_2} \right)$$

In a similar fashion, multiply both L_1 and L_2 single difference code measurements found in (5) by λ_n and subtract one from the other to produce the narrow lane code measurement:

$$\left(\frac{\Delta \widetilde{\rho}^i_{L_1}}{\lambda_1} + \frac{\Delta \widetilde{\rho}^i_{L_2}}{\lambda_2} \right) \lambda_n = \Delta r + \Delta I^i + \Delta \gamma^i_c \qquad (8)$$

where

$$\Delta \gamma^i_c = \frac{\lambda_n}{\lambda_1} \left(\Delta M P^i_{L_1} + \Delta \eta^i_{L_1} \right) + \frac{\lambda_n}{\lambda_2} \left(\Delta M P^i_{L_2} + \Delta \eta^i_{L_2} \right)$$

subtracting (7) from (8) and rearranging, produces

$$\left(\frac{\Delta\widetilde{\rho}^i_{L_1}}{\lambda_1} + \frac{\Delta\widetilde{\rho}^i_{L_2}}{\lambda_2}\right)\lambda_n - \left(\Delta\widetilde{\theta}^i_{L_1} - \Delta\widetilde{\theta}^i_{L_2}\right)\lambda_w \qquad (9)$$
$$= \left(\Delta N^i_{L_1} - \Delta N^i_{L_2}\right)\lambda_w + \Delta\gamma^i_p + \Delta\gamma^i_c$$

At this point, the true range and ionosphere error has been eliminated. Only one unkown is left, the integer ambiguity. In addition, the dominant code multipath error is attenuated resulting in a total error variance for this measurement of one meter. Smoothing for a short period of time will produce an initial estimate of the integer ambiguity defined as N_0. The unknown integer ambiguity is also a wide lane integer that narrows the search space from +/-3 integer on each satellite only slightly more than the variance of measurement. The total integer search space for processing data from four satellites is 4 raised to the 7th power, or 2401. This search space is too large for a residual processor to monitor all the possible integers. Therefore a hypothesis search scheme is implemented to reduce the search space.

The third step is the hypothesis test algorithm of [4]. Two key features of this algorithm produce rapid reductions in the hypothesis search space. First, the single difference carrier phase measurements are divided into primary and secondary measurements. The primary set consists of the four measurements providing the best GDOP. The secondary set must consist of at least two more measurements. For a given hypothesis on primary set, the primary measurements are used to produce an estimate of the current state. This state is then used to form a resulting estimate on the integer ambiguity of the secondary set. If this ambiguity is outside the hypothesis search space for those measurements, or the residual formed does not meet the Chi-Square test, the initial hypothesis in immediately rejected.

The second feature of the search scheme artificially sets the initial integer hypothesis on he first primary measurement to zero. The direct result is that all of the other integers and the clock bias estimate of the state are bias by the unknown integer. Indirectly, the hypothesis search space for four satellites is reduced from 4 to 7th power to 3 to 7th power because the scheme no longer needs to search the first integer. The initial integer may be recovered through smoothing the clock bias after the integer ambiguity (bias by the initial integer) is determined.

In the fourth step after the search space has been reduced, a residual processor processes the measurements for each remaining hypothesis over time. The residual error is given by:

$$e(k) = \lambda\left(\Delta\widetilde{\theta}(k) + N_0 + N_H\right) - \lambda H\Delta\hat{x}(k) \qquad (10)$$

where N_H represents the current hypothesis. The residual with the correct hypothesis will tend toward zero with time. If none of the residuals converge in a set period of time, the entire process is re-initialized starting with the determination of a new initial N_0 from equation (9). As stated previously, this algorithm is a nonlinear search algorithm.

Another algorithm is the multiple model adaptive kalman filter. The MMKF is based on the kalman filter where its hypothesized parameters are modified at each update stage as an expected value in which the probabilities used in the expected value are the probabilities of each hypothesis, conditioned on the residual history. In the integer resolution problem the hypothesized integer are added to the estimated state vectors. The complication in implementing the MMKF is that the probabilities of each hypothesis, conditioned on the residual history and having a given probability of transition, must be generated. For the integer resolution problem that means about 343 of these probabilities are generated and represents a substantial computation burden. The structure of the MMKF is given in [5].

An important aspect of reducing the computational burden is that the initial set of hypothesis can be made sparse so that the number of probabilities to be generated can be substantially reduced. It is shown that if certain conditions are satisfied and if the true hypothesis is not in a sparse set, then the probability of a hypothesis will converge to the hypothesis in the sparse set closest to the true hypothesis within a given information metric. This means that once convergence to a hypothesis in the set is obtained, the set of hypothesis can be made finer in the vicinity of converged hypothesis. This process continues until there are no hypotheses not included in the set in the region of interest.

A nice feature of this structure is that once convergence to the true hypothesis has been obtained, the probability generation should remain operable for a small set about the current hypothesis to monitor possible cycle slips. The probability generator remains sensitive to hypothesis changes since the probability of transition from one hypothesis to another is assumed.

4. CONCLUSIONS

This paper presents an innovative application of GPS technology for UAV collision avoidance. Two methods are suggested for solving the integer ambiguity problem. The Farwell method uses hypothesis testing combined with least squares processing to determine the initial integer values. A second method uses the MMKF to estimate the integers. In order to test these algorithms, a computer architecture based on the PC bus and commercial, off-the shelf components will be constructed.

Future work will also expand the GPS to combine differential carrier phase GPS and an INS system for relative positioning application in UAV collision avoidance.

REFERENCE

1. Menon, P. K. A., "Electro-Option Navigation for Aircraft," IEEE Trans. on AES, 29(3), 1993.

2. K. Lau, S. Lichen, L. Young, and B. Haines, "An innovative deep space application of GPS technology for formation flying spacecraft," Proceedings of AIAA Guidance Navigation and Control Conference, July 1996.

3. Harigae, M. et al., "GPS Relative Navigation System Using Carrier Phases for Rendezvous and Docking, " Proceedings of 19th ISTS, pp. 325-330, Yokohama, 1994.

4. Farrell, J. A., and M. Barth, "The Global Positioning System and Inertial Navigation," McGraw-Hill, 1999.

5. Maybeck, P. S., "Stochastic Models, Estimation, and Control," Arlington, VA: Navtech, 1994.

THE BA609 TILTROTOR AIRCRAFT:
A NEW WAY TO FLY IN THE 21ST CENTURY

DONALD J. BARBOUR

EXECUTIVE DIRECTOR,
SALES AND MARKETING
BELL/AGUSTA AEROSPACE COMPANY
FORT WORTH, TEXAS, USA

Abstract

The Bell/Agusta Aerospace Company BA609 civil tiltrotor aircraft is being developed as a private corporate joint venture. This precedent-setting program is expected to be the first powered-lift category VTOL aircraft to be certified for civilian and commercial operation. This paper deals initially with the product definition phase. A new precedent will also be set by the certification of the BA609, and the paper describes the evolution process to develop a basis for certification. The main body of the paper contains an overview description of the design with commentary about specific design issues that shaped the configuration. (Many of the details here-in are extracted and revised from an earlier paper, Ref.13). This discussion concludes with an overview of expected BA609 vehicle weight and performance capability addressing the specifics of typical missions in offshore, corporate, and search-and-rescue mission scenarios. Elements of supportability are included, and the paper concludes with a comment stating target BA609 program milestones, summary and conclusions.

Introduction

Over sixty years of painstaking research and development has resulted in the capability to bring the BA609 civil tiltrotor to the commercial marketplace. In the 75th Wilbur and Orville Wright Lecture given by Dr. Hans Mark (Ref. 1) and subsequently in an article (Ref. 2), a description of that development is provided. The first tiltrotor design studies, called the Baynes Heliplane, were conducted in Great Britain in 1937. A German development was started during the Second World War, the Focke-Wulf Achgelis FA 269, but this design was never built as a flying aircraft.

The first flying tiltrotor was the Model 1–G Convertiplane built by Bob Lichten at Transcendental Aircraft Company of Pennsylvania. Two aircraft were built and flown; unfortunately, one of them crashed and the financial resources of the small company were insufficient to survive it. Bob Lichten went to work for Bell and was a prime mover in the XV–3 (Ref. 2), built by Bell under contract to NASA and the U.S. Air Force. This aircraft enjoyed a number of successes, the most notable of which was the first in-flight complete conversion from helicop-ter flight to airplane flight. The Bell XV-3 performed 100 successful in-flight conversions during flight tests in the late 1950's. The flight research and subsequent full-scale wind tunnel work in the NASA Ames 40-ft × 80-ft wind tunnel performed with this aircraft unearthed a stability problem that became known as "whirl flutter."

This complex dynamic phenomenon occurs when the forces and moments resulting from deflection of the rotor elastic modes and from rotor flapping couple with the wing elastic modes in such a way that the resulting wing dynamic deflections aggravate the rotor problem. This phenomenon occurs at high speed.

The whirl flutter problem delayed tiltrotor development about twenty years, until the problem and solution was understood. During this time, a great deal of analytical development and dynamic wind tunnel testing was done to understand and predict, and thus design around, the problem. Structural dynamics engineers at Bell, Boeing, and NASA all developed analytical codes that gave similar results and were shown to have a reasonable degree of correlation with model test results. What was needed was a flying aircraft to demonstrate that the problem was truly understood and a safe tiltrotor could be designed.
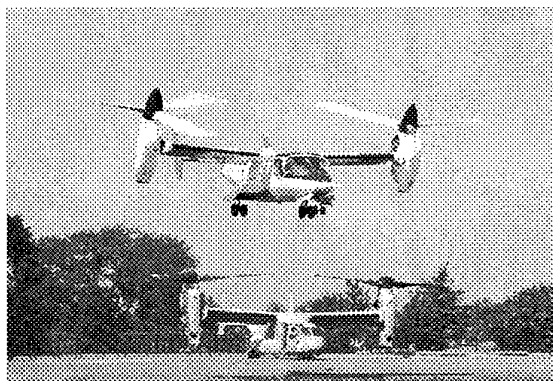

Fig. 1. The V–22 Osprey and XV-15 tiltrotor aircraft

NASA and the U.S. Army (and later the U.S. Navy), joined forces to create a program that produced the XV-15 Tiltrotor Research aircraft (Fig.1&2). Bell Helicopter won this program in open competition in 1972, and development began in earnest. The success of this vehicle is well documented (e.g., Refs. 3 to 9).
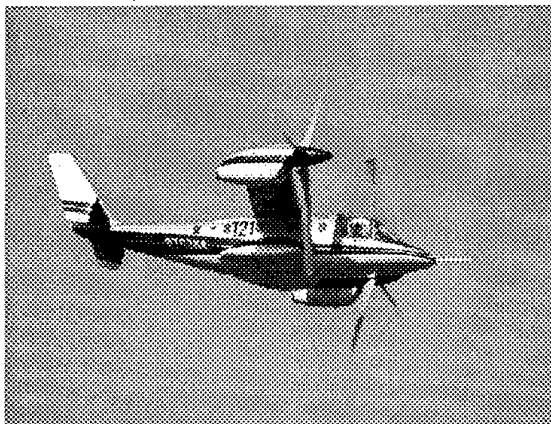
Fig. 2. The Bell XV-15 tiltrotor aircraft.

In 1981, the XV-15 was shown at the Paris Air show, and grabbed the attention of John Lehman, who, at the time, was Secretary of the Navy. The ability of the tiltrotor concept to allow a marine force to launch an attack onto the beach at much greater distances, thus protecting capital ships from land-based missiles, was the principle upon which the JVX program (later to become the Osprey) was started. The V-22 Tiltrotor program suffered many political setbacks, but the Congress and U.S. Military Services commitment to tiltrotor technology allowed this remarkable aircraft (Fig. 1) to enter into initial production in 1997. MV-22 deliveries have begun to the U.S. Marine Corps and will begin with the US Air Force soon.

Yet another lesser-known tiltrotor aircraft was built and flown in 1995. The Bell Eagle Eye (Ref. 10) is an unmanned air vehicle that was built to provide a true shipboard-compatible surveillance capability that could operate without taking up the valuable runway deck of a carrier and that could be launched without assistance.

It is apparent that the BA609 (Fig.3) is no overnight breakthrough. It rests on a long development during which many technical challenges were found and overcome, and a great deal of corporate knowledge was stored, waiting for the time to be ripe for the exploitation of this investment in technology in the civil transport market. In November 1998, the Bell/Agusta Aerospace Company was formally announced. The BA609 tiltrotor program was officially launched and the task of designing, building and certifying the world's first civil tiltrotor was underway.

Certification

One of the immediate questions that arose when we applied to the FAA for a certification basis was "What standards should be used?" Clearly the Part 29 helicopter standards were insufficient by themselves, and so were the Part 25 airplane standards. It was also equally clear

that in most cases, the language of either Part 25 or Part 29 was in fact applicable and only a few incidental issues would require new definitions. In order to facilitate the process, the FAA recommended that we certify under Part 21.17 (b), "Special Condition Aircraft," and that wherever possible, we should incorporate the existing Part 29 and Part 25 language, since the supporting material in the advisory circulars already exists, and the means of compliance are well understood by both ourselves and the regulatory agencies. For the most part, the structural and equipment paragraphs are taken from Part 29 , however, it is in the operating paragraphs that a division occurs. When the aircraft is operating as a helicopter in hover or low speed flight, the rules from Part 29 have been adopted. In airplane flight, the Part 25 rules are used. An iterative process with the FAA has produced a
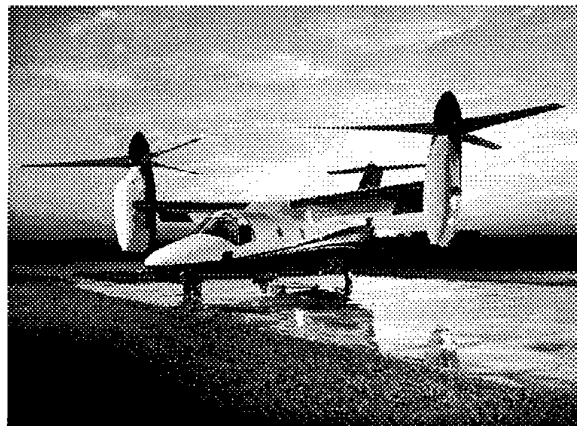

Fig. 3. The Bell/Agusta BA609 civil tiltrotor aircraft.

certification basis that is acceptable to the FAA and is accepted as reasonable by the design team. Other countries will follow the initial U.S. Certification include Italy, Canada, Australia, France, Germany, U.K., and Japan. In fact customers have been found in more than 18 countries so far, and others are pending.

Market Driven Aircraft Definition

In the initial stages of the pre-design of the BA609 tiltrotor (then known only by its Bell design number, D600), a series of high-level design requirements could be immediately identified. These were determined by extensive market research and customer interviews. This process was undertaken in an effort to be certain
"...we build the RIGHT aircraft...". First, the aircraft must be able to operate within the existing infrastructure, both on the ground and in the airspace. Second, the challenge was to develop a product with the required performance and life cycle cost parameters desired by the market , within the available corporate resources.
After a brief study of the infrastructure constraints in terms of rig sizes, hangar sizes, heliport constraints and the size of medium-class helicopters operating in this

environment, we concluded that the overall tip-to-tip dimension of the aircraft should be approximately 60 ft (18.3 m) or less. The marketing team conducted a number of market surveys and concluded that we should concentrate on a nine-passenger vehicle as the smallest and least expensive, yet capable vehicle. This size is nearly equal to the highest productivity levels being flown around the world today. It also became clear from the surveys, we should assume that each passenger and baggage weighed 220 lb (100 kg), since in many of the potential applications (e.g., offshore oil, corporate, civil government utility), this was more often the case than the lower values permitted by regulation. These requirements thus produced a need for a 1,980 lb (900 kg) payload with mission radii operating as far out as 250 nmi (463 km). This range requirement was established by a survey of current and projected offshore shuttle requirements, as new deeper-water drilling technology becomes available.

Other mission applications for corporate, search-and-rescue (SAR), and emergency medical service (EMS) roles were also studied. The Design Mission profiles are shown for the offshore oil, corporate Search and Rescue scenarios.

The BA609 design missions are shown in Figs. 4 and 5. Design studies of the corporate and search-and-rescue

Fig. 4. Offshore missions.

(SAR) missions defined details of the cabin size, layout, and baggage compartment volume.

In a hostile environment, so often encountered in offshore operations, it is clear that a requirement exists to be able to withstand an engine failure at any point in the mission, and to flyaway or land safely. This requirement was studied in the simulator for aircraft with various power-to-weight ratios; power margins were established; including the engine spoolup time, and vehicle dynamics modeled as realistically as possible. This requirement sized the rotor for the aircraft for available powerplant capability at a 30-second rating.

The passenger compartment was a compromise between the conflicting needs of a low-weight configuration and the desire to provide a spacious and comfortable cabin.
In terms of cross section, the BA609 is just a shade bigger than popular civil fixed wing aircraft (such as the Cessna Citation or the King Air), and Bell's own Model 430 helicopter. In terms of cabin length, it is not quite as long as a King Air, but significantly longer than the helicopter competition fielded by Sikorsky or Eurocopter.

The remaining definition of the aircraft came from the fuel required for the offshore 250 nmi radius mission (380 km) with IFR reserves, which defined the minimum internal wing volume. The design team requirement to clear the fuselage with the rotor at a clearance of 18 inches (45.72 cm) and provide a wing loading that would provide an acceptable low stall speed in airplane mode sized the wing, given the rotor size from the available power and projected aircraft weight. We selected the Pratt & Whitney PT6-6A engine for three fundamental reasons: reliability, available power, and economics. The PT6 family of engines has a demonstrated track record of only three flight shutdowns per million flight hours. All the known engines in the size class, and some bigger, were evaluated; but no other engine could meet our needs in terms of reliability, weight, and cost. The Pratt & Whitney PT6 series was also the most preferred by the customer surveys.
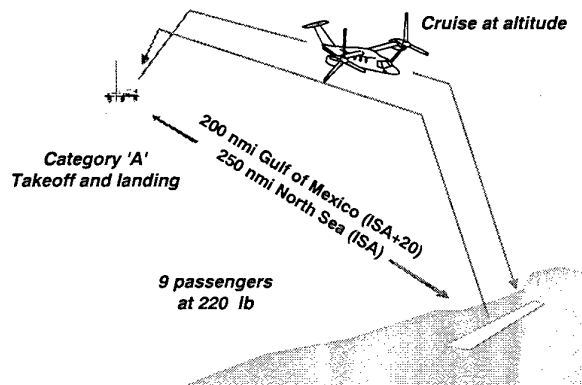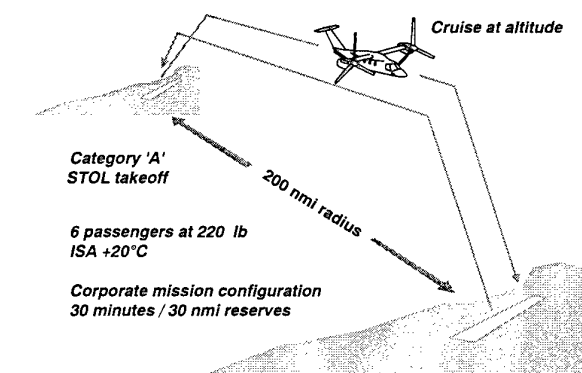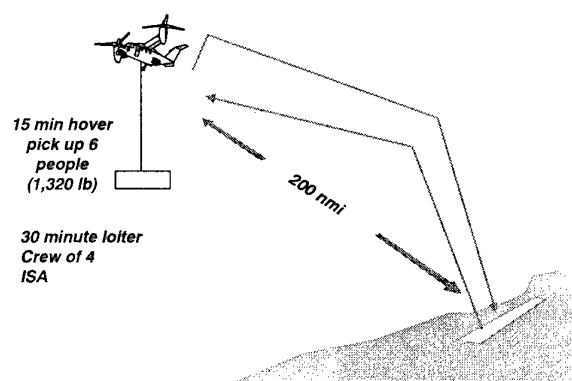

Corporate mission

Rescue mission

Fig.5. Corporate and SAR missions.

The final trade studies of various wing loading and rotor disc loading (all flying the same missions), led engineers to conclude that the 26 ft (7.92 m) diameter rotor with a wing span of 33.8 ft (10.3 m), and a design gross weight of 16,800 lb (7,260 kg) was the right combination. The BA609 sizing solution is very close in overall size to the XV–15. In a sense, this fell in line with our initial stated strategy to reduce technical risk to a minimum by using tried and proven ideas. In the XV–15, we had a ready-made data base against which to check our design parameters, loads predictions, etc.

Getting Down To Details

Once the overall geometry was established and initial performance and maneuvering capability estimates were done, the design loads were established by analyzing individual cases of "worst case" events. The design team (including members from engineering, manufacturing, marketing, and customer support) was ready to start the task of detailed layout and detail design within the new certification basis requirements.

Fuselage

The forward pressure bulkhead is just forward of the cockpit and serves also as a mounting point for the nose wheel. The bay immediately above the wheel well is where most of the avionics equipment is located. The bulkhead forward provides for a location of a weather radar. The forward structure and transparencies are designed to withstand a 4-lb (1.8-kg) bird strike while traveling at cruise speeds and altitudes below 8,000 ft (2,438 m). The transparency design problem is more difficult than usual, because of the high-speed requirement normally associated with a fixed-wing airplane and the large transparencies to provide adequate pilot visibility for vertical landing in confined areas. In addition, an operating pressure differential of 5.5 psi (37.9 kPa) must be contained to permit operation up to 25,000 ft (7,620 m) and maintain the cabin at 8,000 ft (2,438 m).

The center cabin is circular in cross section because of the pressurization requirement, and is constructed from aluminum frames and graphite skins. The frames are manufactured using high-speed machining techniques and the skins are made using fiber tow placement. The principal structural problem is to provide a load path for the crash loads to the main gear. The wing is attached through two lifting beams that are in turn supported on five frames to provide the load path. The second unusual problem is to ensure that the fuselage deflections under pressurization are accommodated and yet also provide a stiff joint in pitch to ensure that fuselage inertia is a factor in the rotor wing stability problem. The aft fuselage is not pressurized and contains the baggage bay and the structure for the tail loads and main gear. The BA609 pressurized fuselage will be produced by Fuji, in Japan.

Landing Gear

The nose gear consists of the air-oil single stage shock strut with internal centering cams, shimmy damper, downlock assembly, landing gear door assembly, and the wheel and tire assembly. The nose gear is 360-degree swiveling with an extend/retract actuation mechanism. The main landing gear consists of air-oil single stage shock struts, positioning rod, proximity switches for gear lock and weight on wheels, landing gear door driver, drag brace and up/down lock links. The extend/retract actuation has normal hydraulic function and emergency extension provisions.

The design point of the gear is to be able to withstand a 10 ft/s landing following an engine failure at the critical point and not yield the gear or its surrounding structure.

Empennage

The tail configuration selected is a T-tail design typical in appearance to many modern fixed wing airplanes. A great deal of development time was put into wind tunnel tests to ensure that the BA609 thick wing on top of the fuselage did not create undue losses in tail effectiveness at angle of attack. The vertical is designed by the Dutch roll mode at low speed and high altitude. Although this took a lot of work, the result is worth the effort since the wake-on-tail effects that were noted on the XV–15 are shown to be significantly less in the powered wind tunnel model data. As a result, a smooth ride should be possible with any quartering wind at low speed. The design of the tail is fairly conventional and must also be capable of dealing with the bird strike problem. (Initial bird strike tests were passed in Spring 2000). There is no rudder on the aircraft; yaw control is provided by differential collective pitch on the rotors when the pilot pushes the pedals .

Wing

The wing span of the BA609 is 33.83 ft (10.31 m) between the rotor centerlines with a constant chord of 65 inches (1.65 m), giving a reference wing area of 183.3 ft^2 (17.03 m^2) and an aspect ratio of 6.25. The wing setting incidence is 3 degrees with a small degree of dihedral and forward sweep. This geometry was selected based on several factors. The span is driven by the rotor diameter, the fuselage diameter, and the required blade tip clearance, which was selected to be 18 inches (45.72 cm). The chord was set by the requirement to provide enough area to allow a low stall speed. The wing thickness-to-chord ratio was calculated to give a cross sectional area for the torque box sufficient for the torsional rigidity required for aeroelastic stability and also to provide enough fuel volume to meet mission requirements. It also provides efficient slow speed flight characteristics while acceptable in high speed flight for drag considerations.

In helicopter flight, the center of gravity of the aircraft is nominally on the line between the rotor centers. As the nacelle converts to airplane flight, the center of gravity migrates forward. The forward sweep of the wing is selected in such a manner that the airplane mode nominal center of gravity coincides with the typical 25% aerodynamic mean chord location, and also is helpful in providing a greater degree of blade flapping clearance from the wing leading edge.

The 35% chord plain flaperon provides for both flap functions and airplane mode roll control. It was selected for manufacturing simplicity and adequate roll control power.

The structural design of the wing includes two spars: a main spar at mid-chord, and a forward spar at 5% chord. Three composite ribs support the spars across the center of the aircraft and three more on each side along the length of the wing. At the tip there are two special ribs on each side, which are fabricated out of aluminum forgings. These tip ribs serve the function of housing the nacelle and conversion actuator spindles; the tip ribs react all of the loads from the rotor and nacelle and distribute them into the wing structure. Upper and lower graphite skins with integral hat section stiffeners complete the torque box for proper stiffness, dynamics, and load management.

The cove aft of the main spar contains the drive system cross shaft. The bearings for this shaft are mounted off the main spar. All of the fuel for the aircraft is contained in ten crashworthy fuel cells in the wing. These cells are fitted with breakaway fittings to ensure that no fuel spillage will occur, thus reducing the chance of fire in the event of a major accident.

The leading edge section contains the conversion system cross shaft, and is designed to take a 4-lb (1.8-kg) bird strike at 240 kts(444 km/h) with no penetration of the wing torque box, thus preserving the integrity of the fuel system and enabling flight loads to be carried with no problem after the event.(The main wing bird strike tests were passed in 1999).

Pylon Conversion System

This system is unique to tiltrotor aircraft and is in the machining tool in Fig. 6. The actuator, which provides the nacelle motion, is mounted on a spindle located in the wingtip and mounted off the front wing spar. It consists of a double telescoping ballscrew that is driven through a planetary differential gearbox by either a primary hydraulic drive unit or a backup hydraulic drive unit. Each drive unit has its own hydraulic brake. An interconnecting shaft runs through the wing leading edge and provides another drive path to the actuator through a 90-deg bevel gearbox.
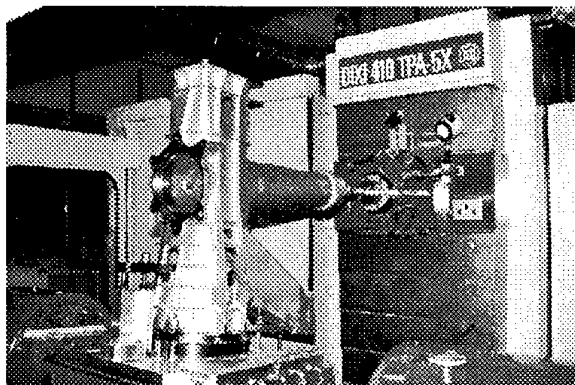

Fig. 6. BA609 Tiltrotor Conversion Pylon

The system has five angular displacement transducers on each side of the aircraft that provide nacelle position information and allow any mechanical failure to be identified and isolated. The actuators on each side of the aircraft are mechanically linked via the cross shaft and are also monitored electronically to ensure synchronous operation even if the cross shaft were to fail. The planetary gearbox design permits a hydraulic drive unit seizure to occur without preventing actuator operation, and is designed to operate without lubrication for a minimum of four complete conversion cycles.

The hydraulic power to drive the actuator can be supplied by any of three independent hydraulic systems. The electrical power is provided by triple independent systems. The fundamental design of the flight control system is triplex, so we have three independent flight control computers controlling the actuator.

This level of redundancy and the care taken to obviate or minimize the effects of mechanical failure give a system confidence level that a critical failure of this system is less than one chance in a billion. The critical sizing conditions are the cold ambient cases. At −40°F (−40°C), the actuator can operate at 10 degrees (deg) per second in normal operation and degrades to 8 deg/s after three failures have accumulated if only one primary hydraulic drive units is powering both sides. This would not be noticed by the pilot without the monitoring system, since the flight control computer would limit nacelle conversion rate to less than these values for normal operation.

The conversion system will operate normally down to − 65°F (−54°C) and is tolerant of failures at this condition, though the rate of conversion may slow to a noticeable degree.

The mechanical systems are designed to be tolerant of failure, with jam-resistant design redundant bull gears, and for example, molded elastomer wipers on both ball nuts to reduce the possibility of a jammed ballscrew.

In addition to providing nacelle motion, the actuator also preloads the nacelle onto the downstop in cruise flight.

This augments the stiffness of the pylon and provides greater margin from aeroelastic stability boundaries. After two failures in cruise flight, we will restrict the maneuver load envelope to less than 2g to ensure that the nacelle remains down, and the stability margin is assured.

This description should provide a partial answer to the often-asked question, "what happens if you cannot reconvert?" The system is designed to operate even if BA609 lost two hydraulic systems, two electrical systems, and two flight control computers—and in some cases, a simultaneous mechanical failure on a cold day. This reduces the probability of the problem to less than one in a billion. None the less, even if all of these efforts to prevent trouble are not sufficient, it is still not a catastrophic event. The airplane is still in a safe flying condition, and a clear landing site needs to be found. The problem is no worse than landing a propeller-driven aircraft with the wheels up. Many pilots have walked away from such landings, even though the propellers were bent or even torn off the aircraft. The composite design of the proprotor is an advantage in this unlikely event, since it has been shown that the blades will shatter on impact into small fragments and dust.

Drive System

The drive system is unique in the tiltrotor. The engine power comes in at the bottom of the proprotor gearbox on a 30,000 rpm engine output shaft. The first stage reduces the rpm nearly 4 to 1, at which point we have an overrunning sprag clutch. The power is then transmitted to the second stage pinion and bull gear and through a planetary set of gears to the proprotor shaft, which turns at 569 rpm at 100% shaft speed. A pylon shaft made of stainless steel, with flexible couplings on each end, provides a means of transmitting power aft to the tilt-axis gearbox. This box has two roles: (1) to turn the corner and permit power to be transmitted across the interconnect shaft, and (2) to provide a location for the accessory drives for generators for the icing system, hydraulic pumps, oil pumps, and cooler blower drive. The interconnect shaft allows the aircraft to lose an engine with no asymmetry in flight or control. In the event of a shaft failure, the control system is capable of synchronization and maintains symmetric power and

control application, provided that both engines are operating. If both an engine and a cross shaft fail, then the aircraft can survive if prompt action to shut down the remaining engine is taken, and the aircraft survives the transient condition. After that, the vehicle can be reconverted with power off, to helicopter mode and an autorotative descent entered. If two engines fail, steady state autorotation entry can be achieved without the difficulty of the transient asymmetric condition.
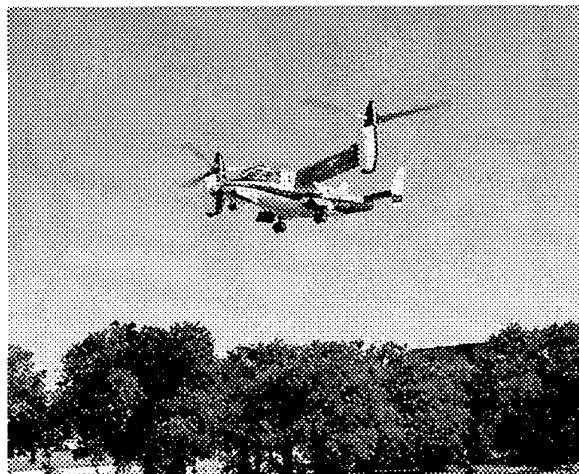This maneuver has already been flown on the XV–15 aircraft (Fig.7).

Fig. 7. Tiltrotor Hovering approach to land.

Rotor

The BA609 rotor is very similar in concept to the V–22 design and draws on some of the manufacturing experience of the Bell Model 430 helicopter. It is 26 ft in diameter (7.925 m) and has three blades, each of which has a thrust-weighted mean chord adequate to which is estimated to provide for a maximum gross weight takeoff from Denver on a hot day and allow for normal air vehicle maneuvers with a margin from rotor stall. The blade twist, 47.5 deg, was chosen to provide the best balance between hover and cruise flight. In helicopter mode, the tip speed is 775 ft/s (236.2 m/s), which is reduced to 651 ft/s (198.4 m/s) in cruise flight to increase the fuel efficiency of the aircraft and also to provide a very quiet airplane. The blade spar is made of fiberglass with carbon torsion wraps. The afterbody is made of Nomex® core with fiberglass skins. The blade has a full-length titanium abrasion strip and also has electrothermal de-ice/anti-ice protection.

The yoke assembly is also made of fiberglass and provides the necessary amount of precone to the rotor. The centrifugal force bearings, the drive links, and the hub flapping spring are all elastomeric components included in the assembly.

The design incorporates provisions for pendulum absorbers inside the blade cuff to reduce rotor-induced vibration. The pre-implementation of this design prevents the issues of icing contamination and drag penalties, since the installation is enclosed.

A slipring assembly is mounted on top of the rotor mast to permit the transfer of electrical power and icing control signals to the rotating blade system. The BA609 rotor controls are very similar to the XV–15 design, with separate collective and cyclic actuation. The whole assembly is encased in the spinner.

Nacelle

The nacelle is split into two zones by the horizontal firewall. In the upper zone a titanium casting with an integral spindle is the basic structure that collects all the rotor and nacelle loads and transmits them to the wing. The pylon support casting supports the main proprotor gearbox and the tilt-axis gearbox.

The engine is below the horizontal fire wall and is mounted with a bipod mount close to the engine center of gravity and attached to the pylon support casting. The forward mount consists of an axially soft aluminum tube to the lower proprotor gearbox input face. The coolers for transmission oil and hydraulic oil are located in the upper zone aft of the tilt-axis gearbox; the cooler blower is driven off this gearbox. Note the engine exhaust is over 7 feet above the surface for safe, friendly ground ops.

The engine inlet is located on the bottom of the nacelle and is a bypass inlet design with a plenum chamber in front of the engine face. A bypass duct augmented by a bypass blower ensures that particles do not turn the corner into the engine but are exhausted through the blower exhaust. This design also protects the engine from icing, and has been used for a number of years on the Model 412 helicopter.
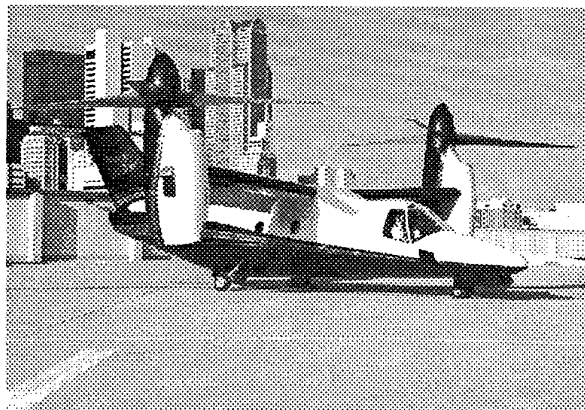

Fig. 8. Nacelle designed for ground clearance and maintainability.

Flight Controls

The cockpit controls are almost identical to those of a conventional helicopter, with a center cyclic stick and a collective/power lever. In helicopter mode, the collective input on both sides from the collective lever provides vertical ascent/descent control. Differential use of collective provides roll control and is activated by the center stick in the roll direction. Fore and aft motion of the cyclic stick provides rotor longitudinal cyclic, providing control of pitch and center of gravity as in a single-rotor helicopter. The pedals provide differential cyclic pitch input, giving yaw control of the aircraft. In airplane

mode, the longitudinal stick commands elevator as in a conventional airplane. Roll control is obtained by differential deployment of the wing flaperons. The collective lever becomes a power lever and blade pitch, is controlled by a blade angle–rpm governer as used in many turboprop aircraft. In airplane mode, the only unusual facet of the design is that the Bell/Agusta BA609 tiltrotor has no rudder. Yaw control and turn coordination is accomplished by using differential collective pitch from the pedals and from automatic turn compensation algorithms.

The transfer of control from one surface to another as the conversion proceeds is totally seamless to the pilot and does not require any special action on the pilot's part. A thumb switch on the side of the collective lever controls the conversion process itself. The pilot can command either direction and can stop the nacelles at any angle chosen, although recommended gates are provided for normal operations. Once the conversion is complete and airplane mode is established, the rpm is reduced by means of a beep switch to 84% for airplane mode flight. The heart of the system resides in triplex flight control computers.

Each computer has three processors to enable each system to be self-checking without the possibility of contamination of another system. The rotor actuators are also triplex for collective and cyclic control. In the baseline design there is no lateral actuator, as calculations do not indicate the need for one. However, provisions exist for the addition of a duplex actuator, should the need arise during the test program. The flaperon and elevator actuation is by three independent simplex actuators.

Each control input made by the pilot is converted to a digital signal by redundant sensors and transmitted through independent wiring with as much physical separation as possible to the computers, which are located so that no one event could damage all three. The computer computes the proper input to the actuator from the preprogrammed flight control laws and sends signals to each actuator to execute the pilot's desired command.

The secret of the success of this system is in its capacity for failure management through the redundancy management software that minimizes the risk to the airplane if failures occur. This system logic is complex and beyond the scope of this paper. The system is designed so that the probability of a catastrophic failure is extremely remote (i.e., less than one chance in a billion).

Hydraulics

The BA609 has three independent 3,000 psi hydraulic systems to meet the requirements of FAR 25.1435 and which are designed in accordance with the guidelines established in MIL-H-5440 for a Class II system. Each system is capable of providing power to each of the flight control subsystems and is capable of providing sufficient
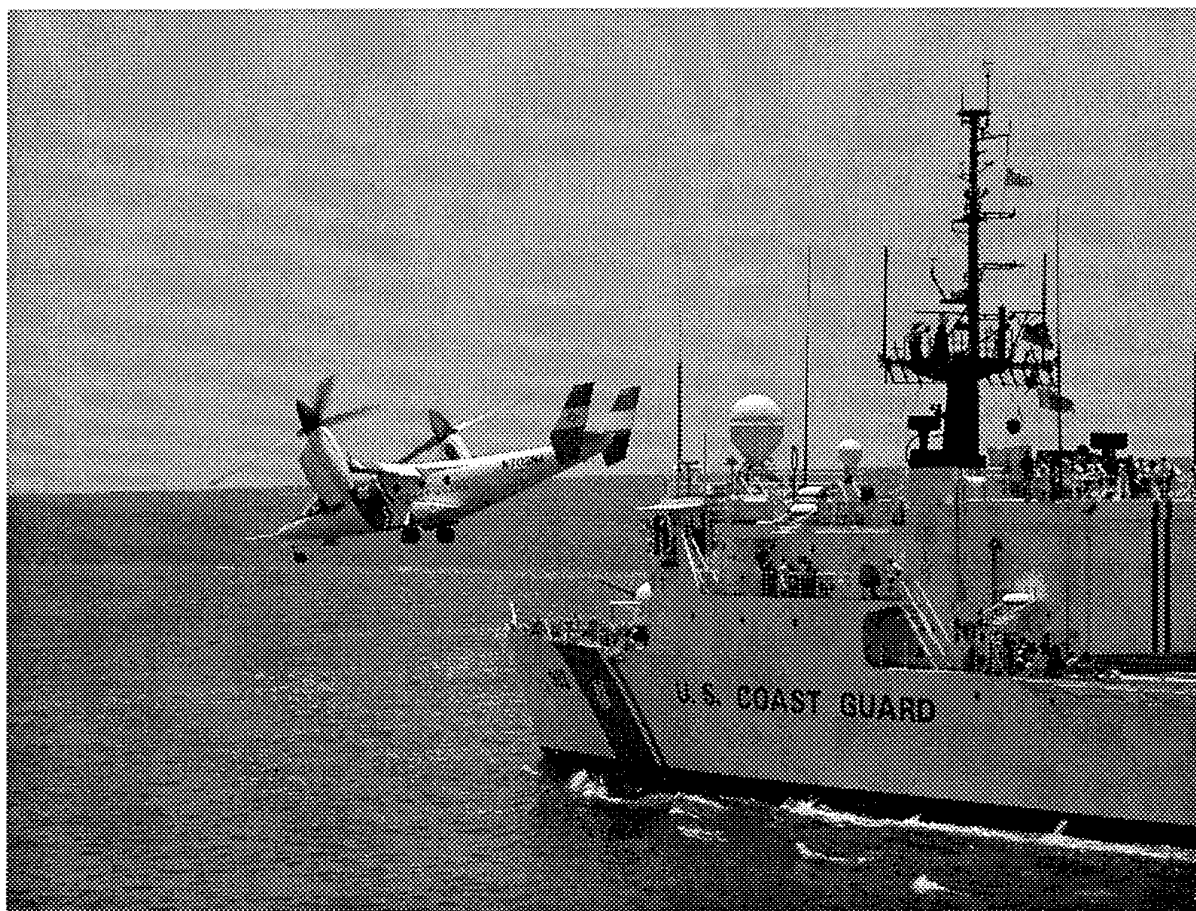
Fig. 9. Tiltrotor ideal for Coast Guard Missions; Engineering demonstration, May, 1999.

power for safe flight should the other two systems become inoperative. Ground test connections are provided to allow operation and servicing by an external power source.

Electrical

The BA609 has both an ac system and a dc system. The aircraft dc system is powered by three dc generators, a battery, and external power. Under normal conditions, the majority of the dc power is provided by a brushless 400-A generator mounted in the midwing area and driven by the interconnect drive shaft. A small amount of current is drawn from the two 300-A starter generators to help with brush wear and to allow the system to ensure the generators are functioning normally. Each generator is monitored and controlled by a generator control unit that continuously monitors the status of each generator, regulates the voltage, provides for protective features, and controls switching of the engine starter, generator line contactor, and various other distribution contactors that control the flow of power to the aircraft loads. Any one generator can provide sufficient power for safe flight and the battery is sized to permit safe emergency landing if all three generators should fail. These and other Certification conditions are of key interest to the Coast Guards (Fig.9.)

around the world as well as potential public and private tiltrotor operators.

The ac system is powered by two self-cooled variable-frequency 115-V ac generators. Each generator provides three independent sources of power: (1) an ac power source for the electrothermal ice protection and also the air conditioning unit; (2) a permanent magnet source of generator control unit primary power, and (3) a flight control permanent magnet generator providing full wave rectified power as a primary power source to a single flight control computer.

Avionics

The avionics suite that is standard in the aircraft is a Collins "Proline 21" integrated avionics system with three active matrix liquid crystal displays, as shown in Fig. 10. Two VHF communications radios and two VHF navigation radios are provided. The system includes a single DME, an ADF, and a mode S transponder. Flight director and GPS are available to complete the modern navigation systems.

Icing System
The icing system consists of (1) two 25-kVA generators powering the electrothermal anti-ice and de-ice systems
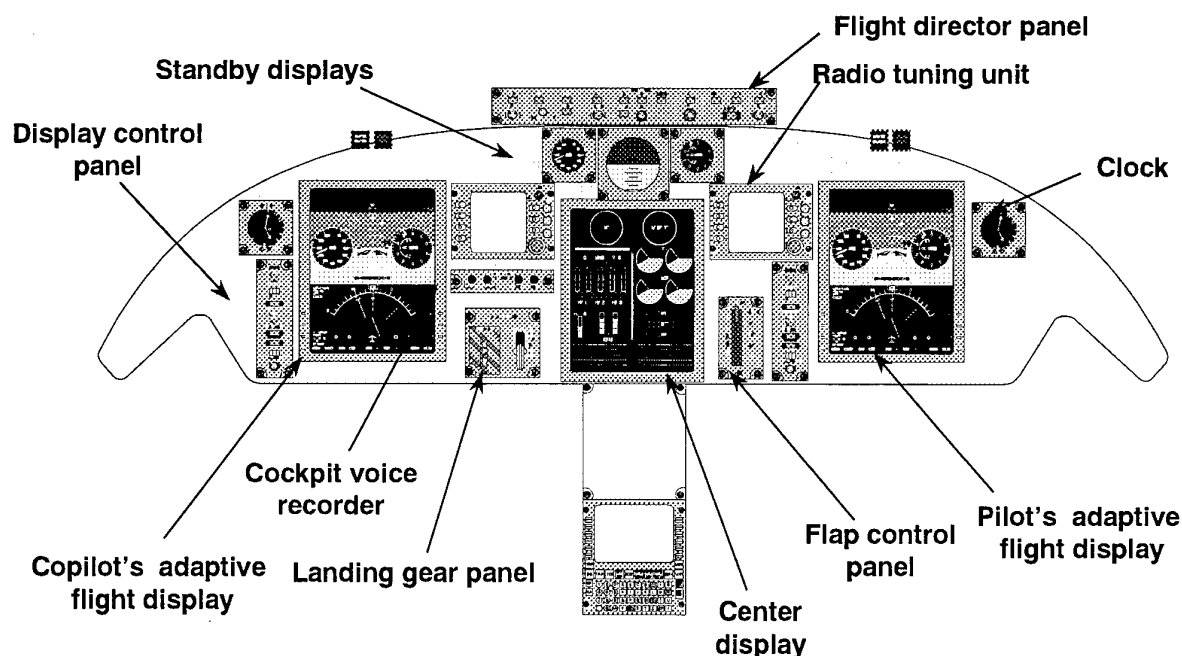
Fig. 10. Cockpit displays.

and (2) pneumatic boots used on the wing leading edge. The windshield and air data sensors are heated. Each of the six prop-rotor blades has seven heater blankets that are controlled sequentially by a dual icing controller. Icing indicators enunciate a warning to the pilot of icing conditions. The design does not include icing treatment for the tail, since experience with the V–22 and recent BA609 tunnel tests, have shown this not to be necessary.

ECS

The engine bleed port is used to provide pressurized air for the cabin. The air is precooled before reaching the nacelle swivel joint and runs down the aft cove of the wing to the fuselage. The bleed line also provides pressure for the wing leading edge de-ice boot. The bleed air is an adequate source of cabin heat and air conditioning is provided by a vapor cycle air conditioner driven by ac electrical power. The system is capable of providing 21,500 Btu/h at 103°F (39°C). Fresh air is provided by bleed air or by an additional ventilation fan.

Weight and Performance

Early marketing surveys indicated that almost all customer requirements could be met with a useful load of 5,500 lb (2,495 kg). A comparison of typical mission weights is shown in Table 1. The data in Table 1 show how various mission requirements create different mission weights. In the case of the North Sea offshore missions, we have to add a standard interior, nine crashworthy seats, and offshore kits (e.g., flotation, life rafts). With a full complement of fuel of 2,481 lb (1,125 kg) and

a payload of 1,980 lb (898 kg), At the takeoff weight, the BA609 has a significant payload margin as limited by Transport Category performance at mid-mission in a sea level ISA environment.

For a typical corporate mission we should be able to take off with six executive passengers in an executive class interior with a full load of fuel, under Transport Category conditions, at a sea level ISA+20C atmosphere. In a cargo class aircraft, we are able to handle a maximum payload of 3,093 lb (1,403 kg).

Table 2 shows some of the key performance parameters. The BA609 should be able to hover out of ground effect at maximum gross weight in excess of 5,000 ft (1,524 m) altitude on a standard day, perform a slow conversion for the comfort of the passengers, climb out at a comfortable 550 ft/min (168 m/min), and cruise at 275 kn (509 km/h) at 20,000 ft (6,096 m), or a little slower at 25,000 ft (7,620 m). On an ISA +20°C (+95°F) day, the maximum cruise speed is about 265 kn (491 km/h) at altitudes between 10,000 ft and 16,000 ft (3,048 m and 4,877 m), while economical cruise speeds are about 250kn (463 km/hr) throughout the cruise altitude range.

The North Sea mission described earlier and depicted in Fig. 4 is limited by the requirement to safely survive an engine failure at the most critical point in the mission. This occurs when the pilot has committed to land on the rig on a windless hot day. Given the remarkable in-flight reliability of the PT6 engine, the probability of this event occurring in the critical five seconds of landing, is approximately four times in a billion flight hours. The landing gear was designed to handle a 10 ft/s landing (3.05

Table 1. ESTIMATED BA609 Selected Typical Weight & Performance Elements*

Missions: (2 pilots, IFR capable, Max Ranges at Req'd Payloads)	North Sea offshore (9 pax)	Corporate (6 pax)	Rescue (+1 crew, 2 evacuees)	EMS (+2 attend, 1 patient)	Cargo (0 pax)
Useful Load (per mission configurations)	5,367 lb 2,434 kg	4,739 lb 2,150 kg	4,536 lb 2,057 kg	4,276 lb 1,939 kg	5,525 lb 2,506 kg
Interior/seats and equipment`	265 lb 120 kg	470 lb 213 kg	55 lb 25 kg	461 lb 209 kg	0
Unusable fluids	14 lb 6 kg	14 lb 6 kg	14 lb 6 kg	14 lb 6 kg	14 lb 6 kg
Kits (per mission)	227 lb 103 kg	54 lb 24 kg	976 lb 443 kg	260 lb 118 kg	0
Crew	400 lb 181 kg	400 lb 181 kg	400 lb 181 kg	400 lb 181 kg	400 lb 181 kg
Payload (minimum Required per design document)	1,980 lb 898 kg	1,320 lb 599 kg	660 lb 299 kg	660 lb 299 kg	3,093 lb 1,403 kg
Max Range (VTOL, DRY Tank, No AUX fuel, No Reserves)	750 nm	> 500nm	675 nm	675 nm	> 400nm
Speed, (economy CRUISE)	250 kts	250 kts	250 kts	250 kts	250 kts

*Based on ESTIMATED weights/performance; ALL ACTUAL BA609 tiltrotor weights/performance is Subject to FAA Certification and Approved Flight Manual requirements; targeted for 2003.

m/s) to deal with this case. Given the flight performance limits of this condition (ISA), we currently have an adequate positive payload margin with the mission flown at 25,000 ft altitude (7,620 m) at MCP.

For the Gulf of Mexico mission, we have less margin because of the ambient temperature in this case (ISA+20C). Even so, we currently calculate a positive payload margin. At this stage in development, it is necessary to have margins, since weight growth during certification, flight test has been a historical fact of life. None-

theless, we believe we have adequate margin for the task and should be able to deliver design mission performance in the production vehicle.

In a corporate mission using a Transport Category departure from a ground level helipad, we have a range capability of 675 nmi (1,205 km) on an ISA plus 20° C (95°F) day and slightly in excess of 750 nmi (1,389 km) on a standard day (59 deg F).

Table 2. Key BA609 tiltrotor selected mission performance parameters *

1. Hover AEO standard gross weight = 16,800 lb (7,620 kg), altitude = 5,000 ft (1,641 m)

2. Maximum speed = 282 kt (522 km/h) at MCP, gross weight = 15,000 lb (6,804 kg) at 20,000 ft (6,096 m)

3. Maximum rate of climb = 2,900 ft/min (884 m/min) at SLS, gross weight = 16,000 lb (7,257 kg)

4. Service ceiling OEI, standard day(ISA) = 16,000 ft (4877 m) airplane mode @ 200kts

5. Service ceiling OEI ,ISA+20°C = 13,000 ft (3,962 m) airplane model

6. Transport Category takeoff gross weight = 15,600 lb (7,076 kg) at ISA +20°C "confined area" VTOL

7. Transport Category takeoff gross weight > 16,800 lb (7,620 kg) at ISA +30°C, STOL w/ 400 ft roll

8. Range – corporate mission, standard day(ISA) = 750 nm (1,389 km)

*All BA609 tiltrotor mission performance parameters Subject to FAA Certification and Approved Flight manual conditions and requirements; targeted in 2003.

Maintenance and Supportability

Operating cost is a major factor in the operators acquisition decision process. The design reliability of each component has been estimated and each contribution to scheduled and unscheduled maintenance costs has been calculated. At this stage in the design, BA609 targeted direct operating cost of the aircraft will be in the vicinity of $850/hour (as calculated in 1996 USD), yielding a very competitive cost per seat mile capability compared to other VTOL alternatives.

Since in the first 80+ orders we have 18+ countries represented, it is clear that a worldwide network of parts and overhaul facilities is needed. It is our current plan to leverage the networks that Bell and Agusta have in place to service the more than 5,000 helicopters we have in service worldwide. Bell/Agusta Aerospace Company plans to offer warranties and spares programs competitive in the medium class fixed wing and VTOL industry.

Training

The FAA has determined that a new pilot rating will be required for "powered lift" pilots, and the training syllabus for this rating is still a matter of discussion between our pilot staff, who have had most of the tiltrotor pilotage experience to date, and the regulatory agencies. We will provide pilot training sufficient to satisfy the requirements of this new rating. Initially we will provide a syllabus for dual fixed wing and helicopter rated pilots who should be able to transition to a powered lift rating relatively easily. It is believed for these individuals that about twenty hours of instruction in flight should be sufficient after ground school and simulator time. We will also provide a syllabus for helicopter pilots and one for fixed-wing rated pilots, however, the requirement in terms of flight time is currently not published by the FAA as of this writing. Pilots will be trained to proficiency.

Development Program

The development program of the BA609 civil tiltrotor was officially announced on November 16, 1996 at the Smithsonian Museum. Since then, much of the engineering definition and design release of the aircraft has been accomplished. Bell/Agusta Aerospace Company has completed the critical design reviews and are well into the tooling and part fabrication phase of the program. At the time of writing this paper, the program schedule shows First flight in Summer 2001, including four BA609 aircraft. BA609 dual pilot IFR certification and deliveries are then scheduled to begin in 2003.

For further updated information, please visit our web site: www.bellagustaaerospace.com

Summary and Conclusions

The development of the BA609 tiltrotor represents a new threshold of technology being implemented as a civil aviation alternative for the 21st century. The paper has shown the results of work over the past 50+ years and concludes that the technology is understood, the systems are designed to be safe and comply with new FAA certification criteria, the materials are tailored for the design, and the performance and design characteristics have been determined by the market. The confidence is high for the civil applications of tiltrotor because of its large and unique operating envelope offering customers the ability to hover, takeoff vertically, fly IFR 275kts up to 25,000 feet, and land up to 675nm away, vertically. Obviously today's airports may be used, but the real growth potential is in off-airport operations. Missions including offshore shuttles, hospitals transfers, corporate itineraries, as well as other civil government utility roles like Search and Rescue, are ideal for this newly applied technology. We anticipate, just as the world has seen the birth of airplane and helicopter flight in the 20th century, we will all experience the choice of more convenient, cost effective, fast hybrid VTOL flight in the 21st century.

The BA609 tiltrotor is the first civil certified alternative for this new way to fly.

References

1. Dr. Hans Mark, "Aircraft without Airports: The tiltrotor concept and VTOL aviation," 75th Wilbur and Orville Wright Lecture, given at the Royal Aeronautical Society,11 December 1986.

2. Dr. Hans Mark and R. R. Lynn, "Aircraft without airports: Changing the Way Men Fly," *Vertiflite*, Vol. 34, Number 3 , May/ June.

3. W. H. Deckert and R. G. Ferry," A Limited Flight Evaluation of the XV–3 Aircraft," AFFTC-TR-60-4, May 1960.

4. H. K. Edenborough, T. M. Gaffey, and J. Weiberg, "Analyses and Tests Confirm Design of Proprotor Aircraft," presented at AIAA 4th Aircraft Design, Flight Test and Operations Meeting, AIAA Paper No. 72-803 ,Los Angeles California, August 1972.

5. K. Wernicke and J. P. Magee, "XV–15 Flight Test Results Compared with Design Goals," presented to the AIAA Aircraft systems and Technology Meeting, Paper No. 79-1839, New York, NY, August 20, 1979.

6. J. P. Magee and K. Wernicke, "XV–15 Tiltrotor Research Aircraft: Program Report" presented at the Atlantic Aeronautical Conference, Williamsburg, Vir-

ginia, March 1979.

7. L. Schroers," Dynamic Structural Aeroelastic Stability Testing of the XV–15 Tiltrotor Research Aircraft," NASA TM 84293,USA AVRADCOM 82-A-17, December 1982.

8. J. M. Bilger, R. C. Marr, and A. Zahedi; "Results of Structural Dynamic Testing of the XV–15 Tiltrotor Research Aircraft," presented at The American Helicopter Society 37th Annual Forum, Paper No. 81-53, May 1981.

9. G. B. Churchill and D. C. Dugan, "Simulation of the XV–15 Tiltrotor Research Aircraft," NASA TM 84222, USA AVRADCOM TR 82-A-4, March 1982.

10. J. P. Magee, "Tiltrotor Technology Thrusts," presented at the SAE Aerospace Congress and Exhibition, Long Beach, California, Paper No. 831537, October 1983.

11. W. Tharp, R. Morgan, and J. P. Magee, "Design of a Tiltrotor Unmanned Air Vehicle for Maritime Applications," presented at the AIAA–AHS–ASEE Aeropace Design Conference, Paper No AIAA 93-1040, February,1993.

12. D.J.Barbour, 609 Core Team, et.al., Design Requirements and Objectives; internal, "unpublished" document defining BA609 mission requirements and customer design preferences; July, 1996.

13. John Magee, "609 Tiltrotor Design", paper presented and published, Royal Aeronautical Society, London, October, 1998.